

**Design, Development, and Prelaunch Calibration of a Low
Cost 118.75 GHz Temperature Sounding Radiometer for
CubeSat Missions**

by

Lavanya Periasamy

B.Tech., Madras Institute of Technology, Anna University, 2005

M.S., Texas Tech University, 2007

A thesis submitted to the
Faculty of the Graduate School of the
University of Colorado in partial fulfillment
of the requirements for the degree of
Doctor of Philosophy
Department of Electrical, Computer and Energy Engineering

2019

This thesis entitled:
Design, Development, and Prelaunch Calibration of a Low Cost 118.75 GHz Temperature
Sounding Radiometer for CubeSat Missions
written by Lavanya Periasamy
has been approved for the Department of Electrical, Computer and Energy Engineering

Prof. Albin J. Gasiewski

Prof. Dejan Filipovic

Prof. Zoya Popovic

Prof. Frank S. Barnes

Prof. Scott Palo

Date _____

The final copy of this thesis has been examined by the signatories, and we find that both the content and the form meet acceptable presentation standards of scholarly work in the above mentioned discipline.

Lavanya Periasamy, (Ph.D., Electromagnetics and Remote Sensing)

Design, Development, and Prelaunch Calibration of a Low Cost 118.75 GHz Temperature Sounding Radiometer for CubeSat Missions

Thesis directed by Prof. Albin J. Gasiewski

The 118.75 GHz eight-channel, double-side-band scanning temperature sounding radiometer “MiniRad” for CubeSat missions is intended to serve as a demonstrator for a constellation of low cost, quick turn-around millimeter wave and higher frequency passive sounders and imagers for weather forecasting at high spatial and temporal resolution. This radiometer payload, built at the Center for Environmental Technology in partnership with the Colorado Space Grant Consortium and the National Snow and Ice Data Center at the University of Colorado at Boulder, can provide a 3D temperature map from the earth’s surface to an altitude of 18 km. For precise prelaunch antenna calibration, an HE_{11} mode full wave electromagnetic field analysis was developed in Matlab for determination of an optimal feed horn and offset paraboloidal reflector geometry such that the main beam and spillover efficiencies of the system are maximized, and these and the antenna phase center location that maximizes phase efficiency are precisely known. Results from this analysis were also compared with HFSS and GRASP simulations of the antenna subsystem. The efficacy of employing a 3D-printed corrugated conical horn, operable between 110 and 127 GHz, as the feed for the reflector was addressed due to its very low cost and rapid manufacturability. Horn measurements indicated a reflection coefficient below -15 dB and an 89.08% average spillover efficiency at the main reflector subtending a 16° half-angle. The need for a compact intermediate frequency spectrometer for operation between 50 MHz and 7 GHz resulted in the design and development of an eight-channel lumped element filterbank with bandwidths between 250 MHz and 2.2 GHz. Laboratory experiments implemented to characterize the MiniRad helped in achieving radiometer sensitivities close to theoretical limits. Initial performance obtained from airborne measurements over Antarctica during the NASA Operation IceBridge experiment in Oct-Nov 2016

suggested a well-focused scanning antenna subsystem and good separation between radiometer channels. After final system integration, measurements obtained from prelaunch experiments indicated the antenna 3-dB beamwidth to be broader by $\sim 0.1^\circ$ compared to the idealized simulated pattern, and radiometer sensitivities that agreed to better than 0.5 K with theoretical estimates across all eight channels.

Dedication

*To my grandparents Unnamalai, Perundevi, Balaiyan and Nallamuthu,
my parents Mangala and Periasamy, my spouse Parag,
and all the teachers in my life.*

Acknowledgements

I would like to express my sincere gratitude to my advisor, Prof. Albin J. Gasiewski for his invaluable technical guidance that has helped me investigate any research problem with both theoretical and experimental thoroughness.

I also acknowledge all members of my doctoral committee: Prof. Frank Barnes, Prof. Dejan Filipovic, Prof. Zoya Popovic, and Prof. Scott Palo. I am especially grateful to Dr. Filipovic and Dr. Popovic for their support over the years.

My sincere gratitude to David Kraft at the Center for Environmental Technology for helping me with a myriad of mechanical issues I faced as part of my PhD work. Thanks to several students at the Colorado Space Grant Consortium who contributed to the PolarCube satellite mission including Michel Dieml, Evan Schoemer, Manuel Bukart, Joaquin Castillo, Robert Belter, and Glenda Alvarenga. Acknowledgements are due to David Galagher at NSIDC, Fred Solheim at Radiometrics, and Brian Sanders, Michael Hurowitz, Roger Carter, and Bill Hosack at Orbital Micro Systems. Thanks to NIST scientists Dr. Joshua Gordon and David Novotny for providing measurements of the 3D-printed horn, and Dr. Axel Murk at the University of Bern for simulating the MiniRad antenna model in GRASP.

Financial support for my graduate studies through the NASA Earth and Space Science fellowship and the NIST PREP assistantship is acknowledged. I am also thankful to Dr. Robert Kursinki for providing me a merit scholarship for the ATOMMS project at LASP.

Finally, I am immensely grateful to my few friends, both at CU and around the globe, who have been there for me during this phase of life.

Contents

Chapter		
1	The MiniRad CubeSat Radiometer	1
1.1	Planned MiniRad CubeSat Missions	2
1.2	Science and Technology Precedents	2
1.3	Microwave Absorption and Radiative Transfer in the Atmosphere	4
1.4	Instrument Specifications	8
1.4.1	MiniRad Theoretical Weighting Functions and Error Covariance	12
1.5	Radiometer Calibration	16
1.5.1	MiniRad Hybrid Two-point Calibration	20
2	Radiometer Antenna System	25
2.1	Full Wave Fourier Field Analysis	27
2.1.1	Power Conservation	32
2.2	Feed and Reflector Geometry	33
2.3	Antenna Phase Center	36
2.4	Estimated Antenna System Performance	40
3	3D Printed Feed Horn	45
3.1	Design	45
3.2	Fabrication	46
3.3	Performance	47

4	IF Spectrometer	55
4.1	Two-stage Amplification	58
4.2	Cascaded Diplexer Based Filterbank	60
4.3	Linear Zero Bias Power Detection	65
4.4	Video Amplification Post Detection	69
4.4.1	Video Amplifier Noise Contribution	72
4.5	Data Digitization and Acquisition	76
5	Prelaunch Testing and Calibration	78
5.1	Airborne Experiments over Antarctica	78
5.2	Radiometer Final Assembly	85
5.3	Radiometer Laboratory Measurements	87
5.3.1	Power Supply Noise Rejection	87
5.3.2	Characterization of Inherent System Noise	87
5.3.3	Thermal and Pressure Testing	93
5.3.4	Y-Factor Testing	94
5.3.5	RF Passband Measurements	94
5.4	Calibration Chamber Assembly	95
5.5	Radiometric Data Calibration	98
5.6	Radiometer Performance	101
5.6.1	Radiometer Antenna Step Response	104
5.6.2	Radiosonde-based Radiative Transfer Inter-comparisons	107
5.6.3	PIN Diode Noise Temperature Calibration	112
6	Conclusion	114
6.1	Summary of Thesis	114
6.2	Future CubeSat Radiometer Constellations	118

Bibliography	119
 Appendix	
A List of Symbols	126
B List of Acronyms	129
C 118.75 GHz Polar Atmosphere Weighting Functions	131
D Antenna System Analytic Geometry	135
D.1 Main Beam Scan Geometry	137
E The Polar Fourier Transform	138
F Selected “First Light” Images from the OIB Experiment	139
G Component Datasheets	141

Tables

Table

1.1	Theoretical estimates of receiver noise temperature and radiometer sensitivity (for 4.096 ms integration time and 290 K antenna temperature) across the desired 8 radiometric channels have been calculated using the insertion losses and noise figures of the RF front end components.	13
2.1	Key geometrical parameters of the MiniRad feed horn and offset reflector (wavelength λ is 2.53 mm).	34
2.2	Summary of measured and computed spillover efficiencies obtained from the CROMMA far field measurement of the 3D-printed horn, the HE ₁₁ mode full wave analysis, and the GRASP [1] and HFSS simulations.	44
3.1	Tabulated here are the far field phase center locations computed by application of a spherical fit to the phases of (i) the CROMMA measured far field pattern of the 3D printed horn, (ii) the HE ₁₁ mode based far field, and (iii) the HFSS simulation of the corrugated horn. $ \theta_{lim} $ indicates the elevation angle range used in the analysis.	53
4.1	Approximate noise powers at the IF module input estimated from the theoretical receiver noise temperature and measured MITEQ LNA gain for earth and cold space views.	59
4.2	Fixed attenuators installed before the tunnel diodes and the detected output voltage.	70

4.3	Thermal noise voltage (referred to the output) contributions due to the source resistances ($\pm 0.1\%$ tolerance).	72
4.4	Noise contributions due to the op-amp's inherent noise sources.	73
5.1	Locations and types of external resistive temperature devices (RTDs) installed inside the calibration chamber to monitor temperatures of targets/components used for instrument calibration. The last two columns summarize measured temperature extremes during the bridge-scan and Marshall field experiments (respectively). . . .	98
A.1	Table of constants.	126
A.2	Table of Greek symbols.	127
A.3	Table of Roman symbols.	128

Figures

Figure

- | | | |
|-----|---|----|
| 1.1 | Atmospheric opacity spectrum [2, 3, 4] illustrating range of microwave frequencies appropriate for imaging from CubeSats. The green arrow indicates <15 km surface resolution from ~425 km LEO altitude using the CubeSat form factor. The red box highlights the oxygen absorption line at 118.7503 GHz. | 8 |
| 1.2 | The MiniRad radiometer inside the PolarCube 3U CubeSat: (a) after final assembly (the multi-layer insulation that shields the reflector motor assembly is also seen), (b) during final assembly with the mirror in its deployed configuration, (c) during final assembly with the mirror in its stowed configuration, and (d) rendition of the 3U CubeSat with deployed reflector and solar panels. | 9 |
| 1.3 | Functional block diagram of the 118.75 GHz MiniRad CubeSat radiometer. | 10 |
| 1.4 | Assuming a satellite altitude of 350 km, the MiniRad instrument specifications were used with the NOAA88b radiosonde data set for winter, clear-air polar latitudes to compute (a) the theoretical temperature weighting functions and surface weights for nadiral 118 GHz observations over ocean, and (b) the error covariance or the RMS temperature error profile. | 16 |
| 1.5 | Calibration cycle of the space-borne MiniRad radiometer | 21 |
| 2.1 | Antenna system geometry used in the HE ₁₁ mode full wave Fourier Bessel electromagnetic field analysis. | 26 |

2.2	Normalized aperture illumination (in dB) on the (a) reflector surface, and (b) main aperture obtained using the HE_{11} mode full wave analysis. The illuminations are not centered due to the offset reflector geometry.	31
2.3	Fractional power intercepted by a constant z -plane immediately behind the reflector for increasing reflector half-angle computed using the HE_{11} mode full wave analysis (blue) and a Gaussian beam mode analysis (red). The Gaussian mode overestimates the spillover efficiency by $\sim 2\%$ at the MiniRad reflector half-angle ($\sim 16^\circ$).	32
2.4	Comparisons between the spillover efficiencies obtained using (a) the full wave and far field HE_{11} mode analyses, and (b) HE_{11} and Gaussian mode far field analyses.	34
2.5	2D-renditions of the reflector Poynting flux power density for various motor shaft scan angles computed using the HE_{11} mode full wave analysis.	36
2.6	For the design frequency 118.75 GHz, the plots show (a) electric field phase distribution across the main aperture assuming the reflector focus is at the center of the horn aperture, and (b) phase centers computed using the HE_{11} mode full wave and far field, and Gaussian beam-mode analyses for various feed horn lengths L_h and diameters D_h at a plane passing through the center of the reflector. The ordinate is the phase center location z_{pc} with respect to the horn's aperture. Negative values of z_{pc} indicate a phase center within the horn body (see Figure 2.1.	37
2.7	Phase distributions of the x -component of the electric field E_x along the two principal perpendicular diameters of the main aperture for various reflector axial displacements: (a) $x = \text{constant}$, and (b) $y = \text{constant}$	39
2.8	Phase efficiencies η_{ph} , and phase standard and maximum deviations at the main aperture as a function of reflector axial displacement z'_{pc} computed at three key frequencies (112 GHz, 118.75 GHz and 125 GHz).	39
2.9	The HFSS antenna model including the corrugated horn, reflector and strut.	41

2.10	Comparisons between the HE_{11} mode full wave (blue) and Ansys [®] HFSS (red) total far field radiation patterns for several azimuthal cuts are shown. Spillover lobes are most prominent closer to $\phi = 0^\circ$	42
2.11	Co-polarized and cross-polarized far field simulated patterns for principal azimuthal cuts obtained using the HE_{11} mode full wave Fourier analysis, Ansys [®] HFSS, and Ticra [®] GRASP [1] at 118.75 GHz are depicted.	43
2.12	Overall main aperture far field beam efficiencies $\eta_b(\theta)$ as a function of elevation θ computed using both full wave and HFSS models are plotted. Also shown for comparison, are beam efficiencies due to uniform, quadratic, and quartic tapers. The gray vertical lines mark the first null for a uniformly illuminated aperture and the MiniRad antenna.	44
3.1	The 3D-printed corrugated horn design with the 17.28° bent rectangular to circular waveguide transition.	46
3.2	Optimization of the corrugated horn design parameters: Variations in $ S_{11} $ due to (a) changes in diameter a_2 for a fixed diameter a_1 , and (b) changes in corrugation depth d for fixed diameters a_1 and a_2	47
3.3	Mechanical assembly details of the 3D-printed corrugated feed horn: (a) mounting holes and alignment pins to securely fasten the horn to the satellite chasis, (b) printed horn (unpolished) cross-section depicting the filleted corrugations, and (c,d) the horn WR8 waveguide section bolted to the PIN diode.	48
3.4	Far field patterns of the corrugated feed horn at 118.75 GHz: (a) measured at the NIST CROMMA facility, and (b) simulated using the HFSS model.	50
3.5	(a) Measured and simulated horn reflection coefficient magnitudes are shown. (b) Measurements of the normalized far field directivities for the 3D printed horn at three key frequencies indicate a small asymmetry in the main beam but low side-lobe levels.	50

3.6	(a) Time domain analysis of the measured reflection coefficient indicates reflections (≤ -25 dB) close to the horn throat and loft. (b) Reference planes used in the measurement of the reflection coefficient are indicated.	51
3.7	3D-printed feed horn beam efficiencies $\eta_{bh}(\theta)$ as a function of boresight angle obtained using the measured (in magenta) and simulated far field horn patterns are depicted. The inset is a plot of the measured and computed normalized far field directivity patterns for the $\phi = 0^\circ$ plane.	52
3.8	Measured and computed E-plane far field phases show good agreement within an 80° angular spread.	53
3.9	Surface profile of the bent WR-8 to WC-8 waveguide transition obtained with a DektakXT Stylus Profiler	54
4.1	Parameters used in the design of the CPW-ground transmission line on a 0.5 oz 20 mil RO4350B TM Rogers Duroid in NI AWR	56
4.2	Pictures of the (a) original four-channel IF and VA PCBs, (b) top side (IF) of the designed 4-layer hybrid PCB within its metal carrier, (c) bottom side (VA) of the PCB (this is a test setup image and includes a Samtec cable that mates with the digital board), (d,e) sideview of the IF and digital carriers, and (f) backside of digital carrier with Samtec connector that mates with the VA side of the hybrid PCB. . . .	57
4.3	Two-stage MMIC amplification on the IF module providing a tapering ~ 40 dB to ~ 20 dB gain between 50 MHz and 6.5 GHz.	58
4.4	Procedure to design the eight-channel cascaded diplexer-based filterbank.	61
4.5	Figures represent (a) schematic of the eight-channel cascaded diplexer-based filterbank (including detector circuitry), and (b) circuit model of a single diplexer used in designing the filterbank.	63
4.6	Schematic of the IF filterbank, detector circuitry and video amplifiers (excluding the two-stage gain and ADC circuitry) implemented as a four-layer hybrid PCB. . . .	64

4.7	Comparison between the simulated and measured spectral passband responses of the IF filterbank on the two-layer RO4350B PCB. Measurements were taken using the setup shown in Figure 4.8c.	65
4.8	For the two-layer IF PCB: Weighting functions generated using IF passband responses from the AWR simulation and (a) boxcar response, (b) measurement; (c) setup for filterbank response measurement, and (e) IF thermal response measurement setup using thermoelectric Peltier chips.	66
4.9	The four-layer IF filterbank: (a) normalized spectral response of the MiniRad IF spectrometer module measured via a slow frequency sweep between 50 MHz and 8 GHz, (b) convolutional bandwidths and theoretical ΔT_{rms} ($\tau_i = 4.096$ ms) for the eight IF channels, and (c) measured ($ S_{21} ^2$) spectral responses on three additional identical IF PCBs with a high frequency calibrated probe connected to a vector network analyzer.	67
4.10	Tunnel diode sensitivities and reflection coefficients measured with sinusoidal inputs of varying frequency and power.	70
4.11	Schematic of the ADC circuitry (including the Samtec connector) on the VA side of the IF spectrometer is shown. The unity gain amplifier and the ADC negative inputs are also shown.	71
4.12	Noise analysis of the dual op-amp ADA4528-2 for a single radiometric channel. . . .	73
4.13	Annotated layout diagrams of the top and bottom layers of the digital board are shown: (a) the top layer includes power regulation and radiometric data acquisition circuitry, and (b) the bottom layer mainly consists of mirror motor control circuitry and motor encoder data acquisition.	75
4.14	Configuration of a preliminary rooftop test against the backdrop of the Flatirons at the University of Colorado, Boulder.	77

5.1	Time series data of sky scans from the roof-top test (Oct 2016) before the OIB experiment are shown. The limb brightening effect for scan angles away from nadir, anticipated spectral behavior of the opaque and transparent channels and, scattering from the strut can be discerned from the plot. The higher level of noise in channels 2 and 3 (between 700 MHz and 1200 MHz) are possibly due to EMI or RFI. These issues were corrected after the OIB experiment.	80
5.2	Prior to the OIB experiment in Oct-Nov 2016: (a) the end-to-end radiometer system was assembled and tested in the 1.5 U CubeSat envelope for the first time, (b) a rooftop test was executed with LN ₂ and ambient absorber as calibration targets, and (c) in the calibrated sky scans for each channel, the red curve is the mean antenna temperature averaged over 2100 scans (~40 minutes). The RMS error per 5 ms sample is illustrated by the blue upper and lower curves. (Channels 2 and 3 showed performance degradation and were subsequently rectified after OIB).	81
5.3	Antenna temperature map of the Tierra del Fuego, an archipelago off the southern most tip of South America, observed by the transparent channels of the airborne instrument on October 26, 2016.	82
5.4	Antenna temperature maps with scan bias removed of (a) an ice edge (W57°, S75°30') and, (b) a land-water boundary (W70°54', S53°26') imaged by channels 5-8 are shown. The cooling present in (b) close to the boundary indicates a drop in the antenna temperature for a 3 km wide region just before the coast line. (The aircraft Rexolite [®] window effect is also present.).	83
5.5	Comparisons of along track nadir scans extracted from an ice edge and land ocean boundary (Figures 5.4a and 5.4b) respectively with theoretical estimates.	84
5.6	Pictures of the final assembled radiometer hardware are shown here: (a) RF chain and leaded NTC thermistor locations, (b) low noise amplifier (LNA), (c) dielectric resonant oscillator (DRO), (d) RF chain and IF spectrometer in carrier, (e) side view inside the 1.5U CubeSat, and (f) top view including reflector and strut.	86

5.7	Plots (a-g) are measurements depicting the impact of drift in IF, LNA, and DRO regulated supply voltages on the detected output voltage. The red lines are best linear fits to the measurements (blue curves). Table (h) provides sensitivity coefficients calculated using the best line fits.	88
5.8	Histograms of the radiometer noise measurements during PIN diode OFF/ON states over ~ 23 epochs (~ 59 s each) detrended to first order. Data kurtosis estimates indicate excellent Gaussian distribution across all channels.	91
5.9	Measured radiometer noise statistics over multiple epochs (~ 59 s each) during PIN OFF/ON states: (a) Allan deviation for PIN OFF state, (b) kurtosis and skewness per epoch (PIN OFF), (c) Allan deviation for PIN ON state, (d) kurtosis and skewness per epoch (PIN ON) and, (e) Allan deviations computed at 1 s, the time duration between calibrations. Radiometer gains used in this table were obtained using calibrated data from the Marshall field test.	92
5.10	Pressure cycling of the radiometer inside a bell jar: (a) experimental setup, and (b) measured temperatures of the RF components (upper plot) and voltage regulators, microcontrollers and the mirror motor (lower plot) as a function of pressure inside the bell jar.	93
5.11	Plots depicting the stability of radiometer gain are shown for measurements taken over a 10 minute time period when the ambient temperature dropped from (a) -5 °C to -10 °C, and (b) -13 °C to -17 °C. (Low sensitivity on channel 2 was fixed after the test.	94
5.12	Bench-top Y-factor measurements with absorber and LN ₂ , and the PIN switch toggling states every 5 s.	95
5.13	Comparisons between the measured IF passband response on PolarCube's MiniRad (solid line) and the RF passband response on the GEMS-01A's MiniRad (dashed line) radiometers.	96

5.14	Top view of the calibration chamber used for prelaunch calibration of the MiniRad radiometer.	97
5.15	(a) Motor encoder counts and derived angular velocity before (blue curves) and after (red curves) optimum Weiner filtering, and (b) histograms of the noisy (upper plot) and filtered (lower plot) angular velocities.	100
5.16	The calibration chamber housing the radiometer and calibration targets rests on a trailer as the radiosonde, seen in the background, is ready for launch [5] at the Marshall field.	102
5.17	Radiosonde measurements of relevant atmospheric parameters taken at the NCAR Marshall field site in Boulder, CO (N39.9491°, W105.1973°, 1743 MASL) [5] are shown. The location is at an altitude of 1.743 km where the atmospheric pressure is 825.15 mb. Above 27.1 km, the sonde data has been appended with the TIGR mid latitude winter atmospheric profile [6] ensuring no discontinuity in pressure.	103
5.18	Step responses of the 8-channel radiometer measured during the bridge-scan experiment show excellent agreement with the simulated antenna-pattern-convolved step function.	105
5.19	In this set of plots, derived impulse responses of the eight-channel radiometer antenna subsystem obtained from the measured step responses are compared with the simulated far field main beam. Data on either side of the main beam are <i>not</i> antenna side lobes but simply antenna temperature differences across the bridge (on the left side) and the sky (on the right side) away from the “step”.	106
5.20	Comparisons between the average estimates of the radiometer ΔT_{rms} obtained from the sum-of-squares measurements and the theoretical calculations.	107
5.21	(a,b) Calibrated radiometric sky scan and sum-of-squares measurements obtained at the Marshall field experiment during the third 30-minute epoch.	108
5.22	Comparisons between the unitary passband weights of the IF spectral response measured on the PolarCube MiniRad, and the RF spectral response measured on the GEMS-01A MiniRad instruments are depicted.	110

5.23	Antenna temperature discrepancies as a function of zenith angle (main beam pointing direction) are shown for skyscan measurements taken over three ~ 30 minute epochs for ~ 1.5 hours after the radiosonde launch.	111
5.24	Plots of the second-order statistics of the brightness discrepancies for the eight radiometric channels.	113
5.25	These set of plots combine data from the bridge-scan and Marshall field experiments in order to determine an estimate of noise reflected off the PIN diode as a function of physical temperature of front-end components.	113
C.1	Theoretical atmospheric temperature weighting functions for the four most opaque channels of the MiniRad 118 GHz space-borne radiometer over Polar land and ocean during summer and winter for $\{0^\circ, 30^\circ, 60^\circ\}$ zenith angles.	132
C.2	Theoretical atmospheric temperature weighting functions for the four most transparent channels of the MiniRad 118 GHz space-borne radiometer over Polar land and ocean during summer and winter for $\{0^\circ, 30^\circ, 60^\circ\}$ zenith angles.	133
C.3	Theoretical surface weights for the eight channels of the MiniRad 118 GHz space-borne radiometer over Polar land and ocean during summer and winter for $\{0^\circ, 30^\circ, 60^\circ\}$ zenith angles.	134
D.1	The sampling schemes used on (a) the elliptic aperture, and (b) the reflector in order to determine the electromagnetic fields on their surfaces using the full wave Fourier transform method.	136

F.1	Few antenna temperature maps obtained by the most transparent channel of the airborne MiniRad instrument aboard the NASA DC8 during the IceBridge experiment over Antarctica between Oct 24 and Nov 02, 2016. The effect of the aircraft Rexolite [®] window has not been removed. After this experiment, electrical and mechanical hardware corrections/improvements were made to the radiometer before its final integration in Feb 2018 (see Chapter 5)	140
-----	---	-----

Chapter 1

The MiniRad CubeSat Radiometer

The prediction of weather and climate from meso to global scales necessitates the use of precision satellite data, closely sampled in both temporal and spatial extent. Atmospheric temperature variations of 0.1 K or smaller over a decade are relevant to the detection and prediction of global change in climate and weather patterns. The importance of acquiring meteorological data at high spatial and temporal resolution has been emphasized in the U.S NRC Decadal Survey's [7, 8] Precipitation, Atmospheric, Temperature and Humidity (PATH) mission requirements, and arises from a need for weather forecasting to cope with rapidly evolving weather patterns. The positive impact of passive microwave observations of tropospheric temperature, water vapor and surface variables on short-term weather forecasts has been clearly demonstrated in recent forecast anomaly growth studies. The development of a fleet of passive microwave sensors especially at V-band and higher frequencies in low earth orbit using 3U and 6U CubeSats [9] could help accomplish the aforementioned objectives at low system cost and risk as well as provide for regularly updated radiometer technology [10, 11, 12, 13]. A constellation of precisely inter-calibrated spectrometers would provide time-resolved global coverage of temperature, humidity and precipitation with lower overall sensor system noise for improved forecasting based on numerical weather prediction (NWP) models. The 118.75 GHz eight-channel, double-side-band scanning temperature sounding radiometer "MiniRad" for CubeSat missions is intended to serve as a demonstrator for such a fleet of low cost, quick turn-around millimeter wave (MMW) and higher frequency passive sounders and imagers.

1.1 Planned MiniRad CubeSat Missions

The MiniRad spectrometer is the payload for the University of Colorado (CU) at Boulder's PolarCube 3U CubeSat mission. This mission was developed by the CU Center for Environmental Technology (CET) in partnership with the CU National Snow and Ice Data Center (NSIDC) and the Colorado Space Grant Consortium (COSGC). It is scheduled for launch on a Virgin Galactic vehicle in mid 2019 through NASA's Educational Launch of Nanosatellites (ELaNa) program. An evolved version of the MiniRad radiometer is also the payload for the Global Environmental Monitoring System (GEMS) In-Orbit Demonstrator (IOD) mission jointly developed by Orbital Micro Systems Inc. (OMS) and CU CET. The GEMS-IOD mission is scheduled to deploy from the International Space Station (ISS) also in mid 2019.

The PolarCube mission is focused primarily on sounding in Arctic and Antarctic regions with the following key remote sensing science and engineering objectives: (i) collect coincident tropospheric temperature profiles above sea ice, open polar ocean, and partially open-water areas to develop joint sea ice concentration and lower tropospheric temperature mapping capabilities in clear and cloudy atmospheric conditions. This goal will be accomplished in conjunction with data from existing passive microwave sensors operating at complementary bands; and (ii) assess the capabilities of small passive microwave satellite sensors for environmental monitoring in support of the future development of inexpensive Earth science missions and (possibly) operational satellites supporting the NRC PATH and Aerosol/ Cloud/ Ecosystem (ACE) goals.

1.2 Science and Technology Precedents

With cuboid dimensions 10 cm x 10 cm x 30 cm and weighing $\lesssim 4$ kg, advantages of CubeSats include a standardized payload/bus envelope, availability of frequent space access via launches of opportunity, and facilitation of on-orbit verification of evolving space hardware due to low launch costs. A recent example of such a technology demonstration were the twin communications-relay CubeSats MARCO [14], built by NASA's Jet Propulsion Laboratory (JPL) riding along with the

InSight lander to Mars. However, due to volume and power constraints, CubeSats can limit the overall science mission objectives.

The MiniRad radiometer is based on an established design with extensive suborbital aircraft flight heritage [15, 16, 17, 18]. This low cost instrument has been developed at the University of Colorado, Boulder on a budget of < 0.25 million. Still, it can provide comparable clear-air temperature profiling capabilities to those of the Advanced Technology Microwave Sounder (ATMS) on JPSS-1 (NPP/Suomi) [19], but at nearly twice the spatial resolution. Other relevant CubeSat radiometer missions for atmospheric sounding that have either been launched or are in progress include the TEMPEST-D carrying a radiometer payload developed by the NASA Jet Propulsion Laboratory (JPL) [20] operating at five channels between 89 and 182 GHz, the MIT Lincoln Laboratory’s MicroMAS-2 and MiRaTA [21] [22] hosting radiometers sensing near 89, 118, 183 and 207 GHz, NASA Goddard Space Flight Center’s IceCube hosting an 883 GHz cloud ice radiometer, and the TWICE mission [23] in collaboration between Colorado State University, NASA JPL, and the Northrop Grumman corporation.

In polar environments with low moisture and comparatively lower amounts of cloud liquid water compared to the tropics and middle latitudes, the 118 GHz band will provide high sensitivity to surface features such as sea ice and leads. Well accepted propagation models [24] infer that there is < 3 dB opacity to the surface at frequencies ~ 5 GHz from the 118.7503 GHz line center in the polar regions, and thus high sensitivity to sea ice/ocean fraction. The response of the radiometer’s highest intermediate frequency channel to sea ice and clouds will be similar to that provided by the 89 GHz channel on the NASA Aqua AMSR-E sensor, which provides current high-resolution data for sea ice concentration mapping. However, the additional channels closer to the 118 GHz line center will provide a coincident temperature profiling capability (Figure 1.4a) to be used for correlating sea ice state with the tropospheric temperature variations, specifically within the lower troposphere. While several studies point to recent increases in tropospheric water vapor over the Arctic, obtaining accurate and consistent data on warming and water vapor in the polar regions is an ongoing challenge due to strong seasonal and spatial heterogeneity. Upper snow-pack properties

are detectable by the 118 GHz sensor due to the very dry atmosphere present during clear-sky conditions over central Greenland and Antarctica. Past studies of passive microwave emission variations at the high end of satellite frequencies currently available (e.g., 89 GHz on AMSR-2) suggest that there is as strong variation in passive microwave emission after snowfall events and in the thermal evolution of the snow-pack in autumn.

1.3 Microwave Absorption and Radiative Transfer in the Atmosphere

All matter at temperatures above absolute zero emit, absorb or reflect electromagnetic radiation due to kinetic motion of particles within them. The spectral density of radiation from a perfect *blackbody* (emissivity $\epsilon = 1$) at physical temperature T for one of two orthogonal modes i.e., the thermal power it radiates per unit area of radiating surface per unit solid angle Ω and per unit frequency f is given by Planck's law:

$$B_f(f, T) = \frac{2hf^3}{c^2} \frac{1}{e^{hf/k_B T} - 1} = \frac{2}{\lambda^2} \frac{hf}{e^{hf/k_B T} - 1} \quad (\text{Wm}^{-2}\text{Hz}^{-1}\text{st}^{-1}) \quad (1.1)$$

where k_B , h and c are the Boltzmann constant, the Planck constant, and the speed of light in the medium respectively [25]. The function $B_f(f, T)$, representative of blackbody radiation, is called the Planck function. Examples of natural emitters of electromagnetic radiation at microwave frequencies are (a) the ground with equivalent temperature of about 300 K, (b) the sky with equivalent temperature of about 5 K when looking toward zenith and about 100 K to 150 K toward the horizon, and (c) the cosmic microwave background with equivalent temperature of 2.73 K. In cases where $hf \ll k_B T$ (known as the Rayleigh-Jeans law), the Planck function reduces to $B_f^{RJ}(f, T) \simeq \frac{2k_B T f^2}{c^2} = \frac{2k_B T}{\lambda^2}$. On the other hand, for higher frequencies where $hf \gg k_B T$ (known as the Wein approximation), $B_f^W(f, T) \simeq \frac{2hf^3}{c^2} e^{-hf/k_B T}$. The Rayleigh-Jeans approximation results in a linear relationship between the spectral intensity and physical temperature, and is generally applied in remote sensing at microwave frequencies ($1 \text{ GHz} \leq f \leq 300 \text{ GHz}$) and lower, and terrestrial temperatures. In this context, the intensity can be linearly scaled to an equivalent *brightness* temperature less than ~ 0.1 K error. However, this approximation is not valid when the

cosmic microwave background is a cold-temperature reference or a background brightness [26] (as is the case for space-borne microwave radiometers).

Radiative transfer theory describes the intensity of electromagnetic radiation propagating in media that absorb, emit and scatter this radiation [27, 25, 28, 29, 30, 31]. It is fundamental to passive remote sensing instruments such as radiometers that measure radiant energy. In general, an arbitrarily polarized electromagnetic radiation field can be described by a four-component modified Stokes' vector:

$$\bar{I}(f, T) = \lim_{\substack{\Delta f \rightarrow 0 \\ \Delta \Omega \rightarrow 0}} \begin{bmatrix} \langle |E_v|^2 \rangle \\ \langle |E_h|^2 \rangle \\ \text{Re}\langle E_v E_h^* \rangle \\ \text{Im}\langle E_v E_h^* \rangle \end{bmatrix} = \begin{bmatrix} I_v \\ I_h \\ U \\ V \end{bmatrix} \quad (\text{Wm}^{-2}\text{Hz}^{-1}\text{st}^{-1}) \quad (1.2)$$

where I_v and I_h are the spectral intensities of the vertically and horizontally polarized field components, and U and V are the in-phase and quadrature covariances between the vertical and horizontal field components. Using the Rayleigh-Jeans approximation, the spectral intensity vector can be scaled to a brightness temperature vector \bar{T}_B :

$$\bar{T}_B \equiv \frac{\lambda^2}{k} \bar{I} = \begin{bmatrix} T_{Bv} \\ T_{Bh} \\ T_U \\ T_V \end{bmatrix} \quad (\text{K}) \quad (1.3)$$

The solution to the differential radiative transfer equation (DRTE) is referred to as a *forward transfer* problem in contrast to the inverse, or *retrieval* problem. For a non-scattering, planar-stratified atmosphere, the DRTE is simplified to (in the Rayleigh-Jeans approximation):

$$\cos \theta \frac{d\bar{T}_B(h, \theta, f)}{dh} = -\kappa_a(h)\bar{T}_B(h, \theta, f) + \kappa_a(h)T(h) \quad (1.4)$$

where h is the height, θ is the angle of the direction of propagation with respect to zenith, and κ_a is the total (scalar) absorption coefficient (or equivalently, the total extinction coefficient since scattering has been neglected). For a specularly reflecting surface, (1.4) can be integrated

between $-\pi/2 \leq \theta \leq +\pi/2$ to obtain the integrated radiative transfer equation for a non-scattering atmosphere [31]:

$$\begin{aligned}
T_{B\beta}(h, \theta, f) &= \int_0^h T(h') \kappa_a(h', f) \sec \theta e^{-\int_{h'}^h \kappa_a(h'', f) \sec \theta dh''} dh' \\
&+ e^{-\int_0^h \kappa_a(h', f) \sec \theta dh'} \left[T_S (1 - r_\beta(\theta)) \right. \\
&+ r_\beta(\theta) \left(\int_0^\infty T(h') \kappa_a(h', f) \sec \theta e^{-\int_0^{h'} \kappa_a(h'', f) \sec \theta dh''} dh' \right. \\
&\left. \left. + T_{CB} e^{-\int_0^\infty \kappa_a(h', f) \sec \theta dh'} \right) \right] \quad (1.5)
\end{aligned}$$

where the polarization index β is either v (vertical) or h (horizontal), $r_\beta(\theta)$ is the surface reflectivity, T_S is the surface temperature, T_{CB} is the cosmic microwave background temperature (~ 2.73 K), and κ_a is the total absorption coefficient (including attenuation caused by small non-scattering hydrometeors). The integral term in the exponential is the integrated opacity τ :

$$\tau(h', h, \theta) = \int_{h'}^h \kappa_a(h'') \sec(\theta) dh'' \quad (1.6)$$

For scattering (non-specularly) reflecting surfaces, the reflected brightness temperature term in (1.5) will also include contributions from all downwelling angles weighted by the bistatic scattering coefficient of the surface. For $|\theta| \geq \pi/2$, the brightness consists of only the downwelling and cosmic background contributions:

$$\begin{aligned}
T_{B\beta}(h, \theta, f) &= \int_0^\infty T(h') \kappa_a(h', f) \sec \theta e^{-\int_{h'}^h \kappa_a(h'', f) \sec \theta dh''} dh' \\
&+ T_{CB} e^{-\int_0^\infty \kappa_a(h', f) \sec \theta dh'} \quad (1.7)
\end{aligned}$$

Integrals in equations (1.5) and (1.7) can be re-cast as an integral of the product of atmospheric temperature (or any atmospheric parameter) and a *temperature weighting function* over atmospheric altitude [2] [3]. Using the temperature weighting function set $\{\overline{W}(h', h, \theta), \overline{W}_S(h, \theta), \overline{W}_{CB}(h, \theta)\}$

that specifies the relationship between the brightness temperature vector $\bar{T}_B(h, \theta)$ and the atmospheric temperature profile $T(h)$, the surface temperature T_S , and the cosmic background temperature T_{CB} , the microwave radiative transfer equation can be written as:

$$\bar{T}_B(h, \theta) = \int_0^{\infty} T(h') \bar{W}(h, h', \theta) dh' + \bar{W}_S(h, \theta) T_S + \bar{W}_{CB}(h, \theta) T_{CB} \quad (1.8)$$

In reality, a radiometer has a finite number of spectral channels, each with a fixed center frequency and bandwidth. Hence, the weighting function must incorporate the passband response of the system in addition to the physical parameters of the atmosphere. This function is therefore representative of the spatial response of the instrument to a particular atmospheric parameter, in this case temperature. It defines relative contributions of the thermodynamic temperatures from various atmospheric levels to the integrated brightness temperature sensed within a given spectral bandwidth (channel) of the radiometer. Using the equations described in this section, weighting functions and expected brightnesses can be computed for a known instrument spectral response, and atmospheric profile and surface (such as one obtained from a radiosonde).

The total gaseous absorption coefficient κ_a is the sum of absorption due to all constituent molecules in the atmosphere. The primary gaseous absorbers in the troposphere and stratosphere for frequencies below 300 GHz are diatomic oxygen (O_2) and water vapor (H_2O). Carbon dioxide (CO_2), carbon monoxide (CO) and ozone (O_3) exhibit resonant absorptions, and nitrogen (N_2) exhibits a weak resonant absorption at microwave frequencies. Figure 1.1 depicts total clear-air zenith opacity spectra from 2 GHz to 1 THz for representative atmospheric conditions [4]: summer low latitude, annual mid latitude and winter high latitude. Opacity spectra for dry (i.e. no water vapor) annual mid latitude conditions are also shown for ozone, nitrogen and oxygen individually. These calculations were based on the Liebe MPM87+ [24] absorption model and include only non-isotopic species.

The absorption lines that play a dominant role in the remote sensing of temperature profiles are the oxygen absorption lines near 60, 118.75, 368.50, 424.76, and 487.25 GHz. The density of O_2 is well known within the troposphere and stratosphere. Water vapor generally accounts for $\lesssim 3\%$ of

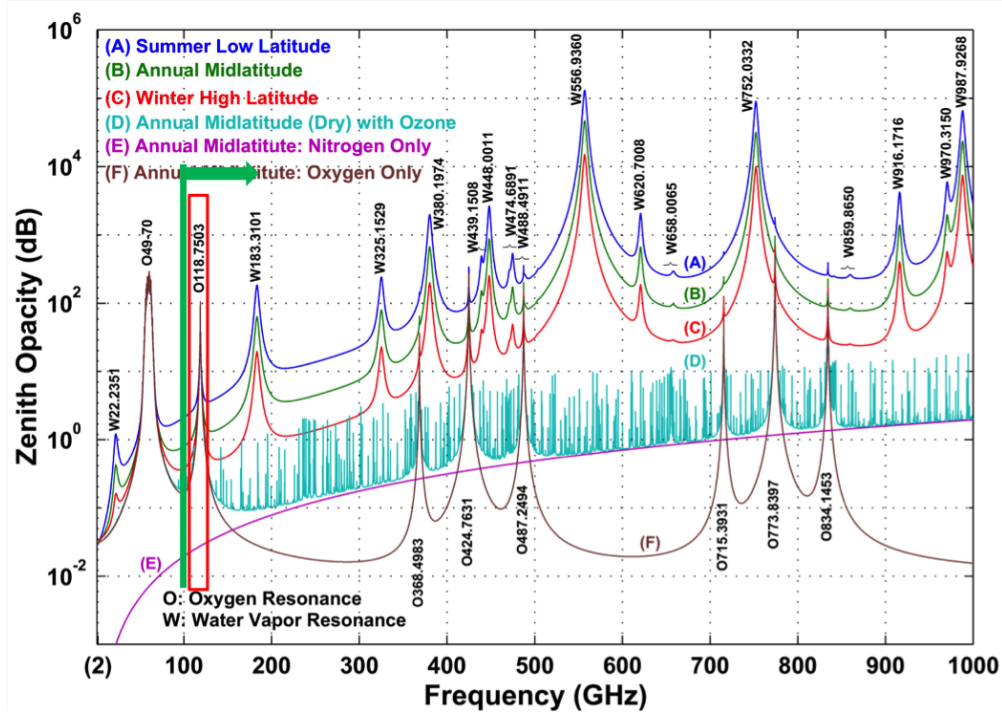


Figure 1.1: Atmospheric opacity spectrum [2, 3, 4] illustrating range of microwave frequencies appropriate for imaging from CubeSats. The green arrow indicates <15 km surface resolution from ~ 425 km LEO altitude using the CubeSat form factor. The red box highlights the oxygen absorption line at 118.7503 GHz.

the atmospheric mass density, but exhibits a highly variable mixing ratio, and contributes a small but significant amount of absorption at 118 GHz. Non-opaque clouds also contribute to brightness perturbations at 118 GHz [3] [31]. Hence, their temperature weighting functions are deterministic for hydrometeor-free profiles provided the water vapor profile and surface reflectivity are known, and the atmospheric absorption model is accurate.

1.4 Instrument Specifications

The 3U CubeSat payload, MiniRad is an eight channel, double side band 118.75 GHz scanning passive microwave temperature sounder with an antenna subsystem comprising a scanning offset paraboloidal main reflector and a stationary corrugated feed (Figure 1.3). The reflector (including motor assembly), supported by a single strut, is in a stowed configuration and deployed after launch

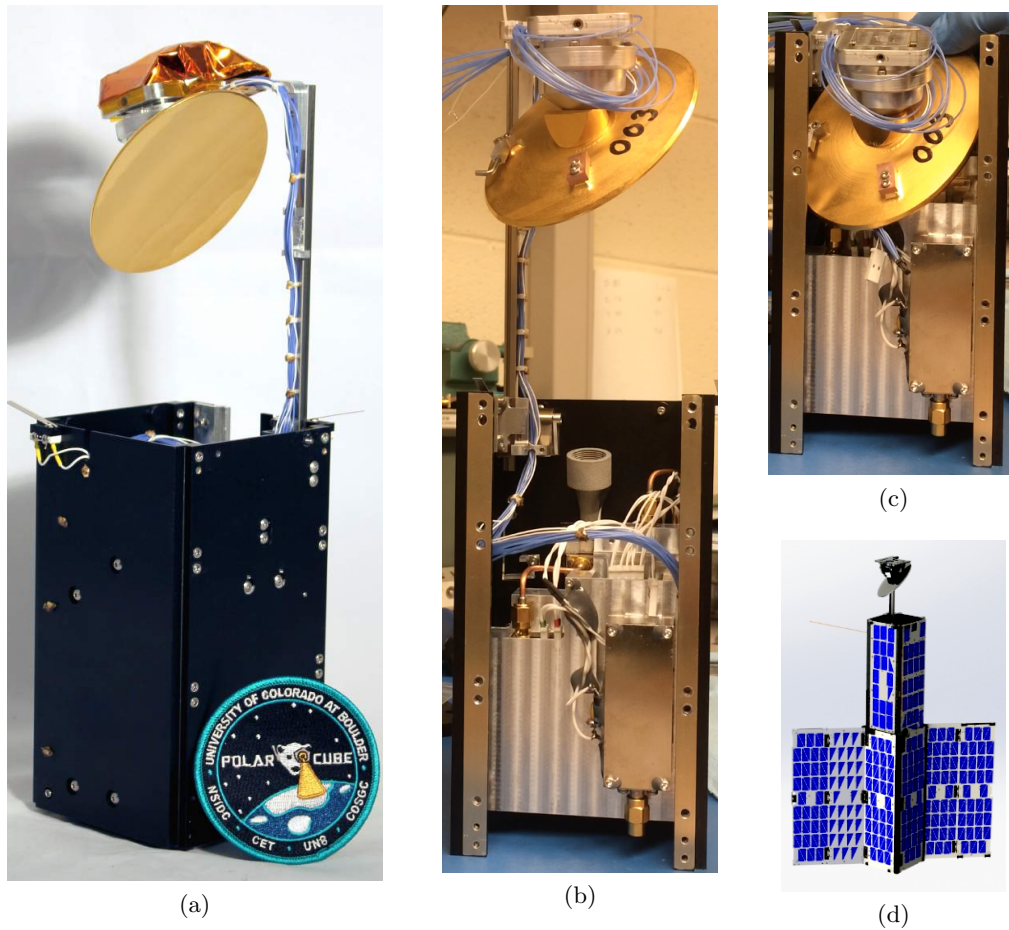


Figure 1.2: The MiniRad radiometer inside the PolarCube 3U CubeSat: (a) after final assembly (the multi-layer insulation that shields the reflector motor assembly is also seen), (b) during final assembly with the mirror in its deployed configuration, (c) during final assembly with the mirror in its stowed configuration, and (d) rendition of the 3U CubeSat with deployed reflector and solar panels.

(Figure 1.2).

The WR8 waveguide-based radio frequency (RF) front end of the total power radiometer includes a double side band (DSB) sub-harmonic mixer and tripler, dielectric resonator oscillator (DRO) and intermediate frequency (IF) low noise amplifier (LNA). The peak power draw of the payload (including mirror motor) is ~ 5 W. It is to be noted that the LNA and IF surface mount MMIC amplifiers are operated in a power starved mode to minimize their power consumption. Due to the \sim symmetric nature of the 118.75 GHz resonance and the DSB mixer, small drifts in the

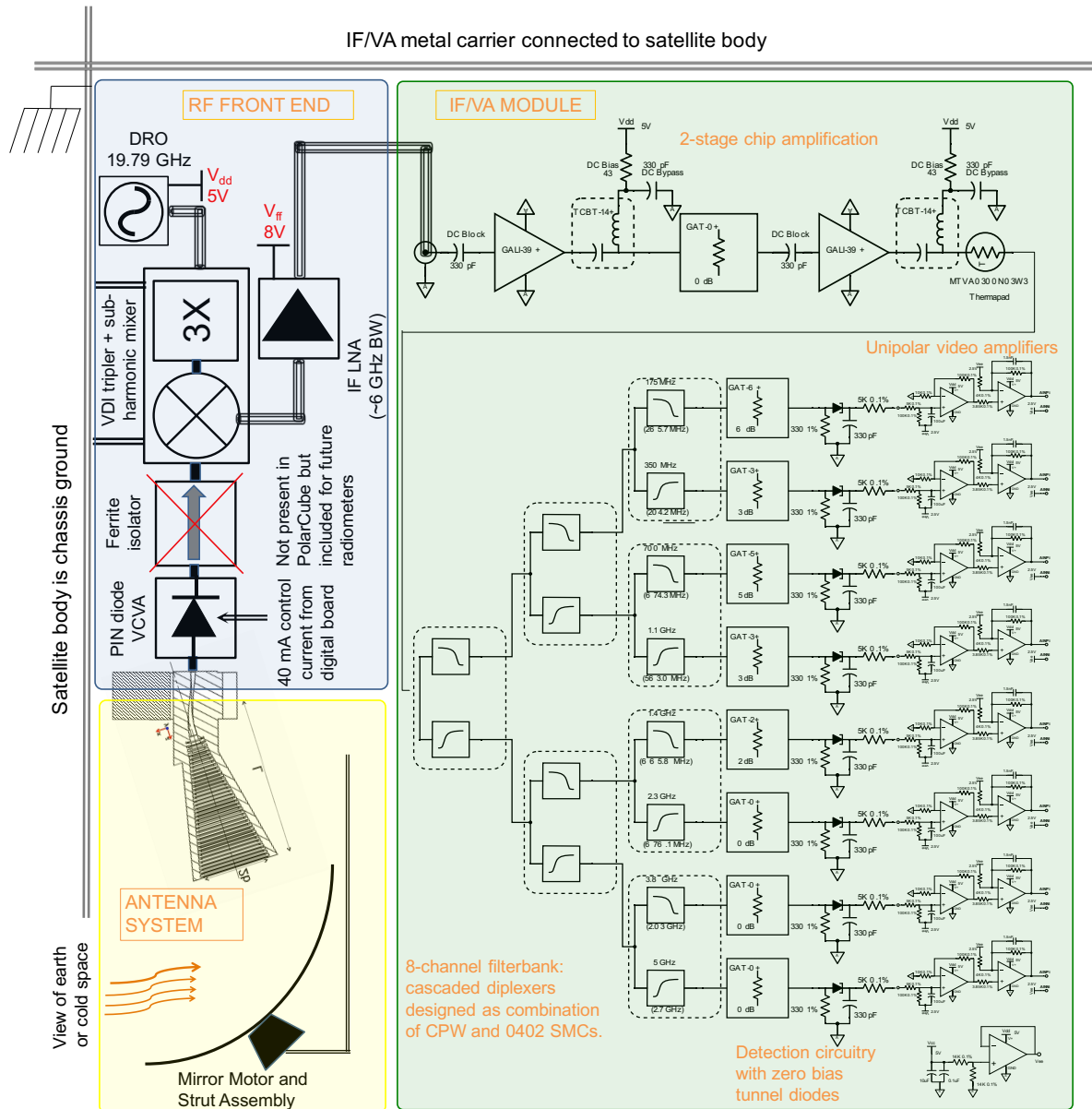


Figure 1.3: Functional block diagram of the 118.75 GHz MiniRad CubeSat radiometer.

local oscillator frequency are manifested as second-order errors.

The IF spectrometer module comprises of an eight channel filterbank whose center frequencies were selected to provide sensitivity from the upper troposphere (including tropopause) down to the surface with as much bandwidth as available to reduce integration noise to levels of $\sim 0.5\text{-}3$ K per 3-dB sampled pixel [4]. The channel center frequencies were selected such that their weighting functions peaked from close to the surface to an altitude of ~ 18 km. The spectrometer has a nonuniform vertical resolution of ~ 1 km close to the surface, and ~ 5 km in the upper troposphere and lower stratosphere.

The theoretical system temperature T_{SYS} across the eight channels (Table 1.1) can be computed using the Friis formula as:

$$T_{SYS} = T_A + T_{REC} = T_A + (L_S L_I - 1)T_o + L_S L_I (T_M + L_M T_G) \quad (1.9)$$

where T_o is 290 K, T_{REC} is the receiver temperature, T_A is the antenna temperature (chosen as 290 K here), and L_S, L_I and L_M are the switch, isolator and mixer losses respectively. Mixer and IF LNA noise temperatures, T_M and T_G , are obtained from their specified noise figures. The theoretical radiometer sensitivity values are based on ~ 4 msec samples aggregated at the 3-dB footprint resolution of MiniRad.

A 3D-printed corrugated feed horn illuminates an ~ 8 cm offset scanning parabolic reflector to achieve a $\sim 2.2^\circ$ 3-dB beam width with nominal one second scan period. With its crosstrack scanning (at ~ 1 Hz) mirror, the radiometer achieves Nyquist spatial sampling at ~ 18 km 3-dB spatial resolution and measures useful scene data $\pm 60^\circ$ about nadir. One disadvantage of a crosstrack scan is that the main beam's incidence angle and footprint size vary with scan angle due to the offset geometry. Previous space-borne instruments employing crosstrack scanning include the Microwave Sounder Units (MSUs) on TIROS-N, and Scanning Microwave Spectrometers (SCAMSs) on Nimbus-5.

The mirror is deployed on a simple extendable mechanism that has been prototyped (Figure 1.2) and reviewed favorably during the Air Force's University Nanosat Program (UNP) Critical

Design Review of February 2014. This configuration maximizes aperture size without impinging on the internal bus volume needed for electronics. The deployment system consists of a rail mounted to one panel that slides along a linear bearing during deployment, and is stopped by a stopping plate. Two adjustment plates on the mirror motor assembly enable its translational motion for precise optical alignment [32] [33]. The deployment itself is implemented with a frangibolt assembly. The design of the mirror motor assembly and deployment are described in detail in [32].

The crosstrack scan enables the radiometer to implement a two-point calibration (c.f. §1.5.1) using an internal PIN diode switch and view of cold space (Figure 1.5). The scan rate itself is chosen so that Nyquist spatial sampling can be achieved in the cross track direction. Spatial Nyquist sampling requires 50% overlap between adjacent 3 dB footprints on earth. While Nyquist sampling in the along track direction is a function of the 3 dB beam width θ_{3dB} , and the altitude of the satellite, cross track Nyquist sampling additionally depends on the reflector scan rate. If the main beam dwell time is assumed to equal radiometer integration time τ_i , the angular time period is $2\pi\tau_i/\theta_{3dB}$. Considering a nominal 2.3° 3-dB beam width (based on the maximum aperture diameter of the reflector in the CubeSat) and 5 ms integration time, a reflector scan rate of ~ 1 -1.2 Hz was chosen during the design phase.

1.4.1 MiniRad Theoretical Weighting Functions and Error Covariance

Antenna temperatures expected from an instrument for a given atmospheric profile and surface can be computed using the radiative transfer equations described in §1.3. The observation equation can be expressed in matrix form [34] as:

$$\bar{T}_A = \bar{\bar{W}} \cdot \bar{T} + \bar{W}_S T_S + \bar{W}_{CB} T_{CB} + \bar{n} \quad (1.10)$$

where $\bar{\bar{W}}$ is an $M \times P$ observation (or weighting) matrix, \bar{W}_S and \bar{W}_{CB} are the instrument's response to the surface and cosmic background temperatures (respectively), $\bar{T} \triangleq [T_1, T_2, \dots, T_P]^t$, and $\bar{T}_A \triangleq [T_{A_1}, T_{A_2}, \dots, T_{A_M}]^t$. The system noise \bar{n} , which is uncorrelated among channels and successive observations, is modeled as a zero-mean Gaussian observation noise - it is equivalent to

Ch	#	1	2	3	4	5	6	7	8
Lower side band	f_{low}^{LSB} (GHz)	118.6004	118.4504	118.2504	117.8504	117.4504	117.0504	116.2504	115.0504
	f_{high}^{LSB} (GHz)	118.5004	118.2504	117.8504	117.4504	117.0504	116.2504	115.0504	112.4504
Upper side band	f_{low}^{USB} (GHz)	118.9004	119.0504	119.2504	119.6504	120.0504	120.4504	121.2504	122.4504
	f_{high}^{USB} (GHz)	119.0004	119.2504	119.6504	120.0504	120.4504	121.2504	122.4504	125.0504

Ch	PIN Switch			Isolator			Mixer			LNA		
	Loss (dB)	Loss (lin)	Temp (K)	Loss (dB)	Loss (lin)	Temp (K)	NF (dB)	L_M (lin)	Temp (K)	NF (dB)	L_G (lin)	Temp (K)
1	0.6	1.15	42.96	0.6	1.15	42.96	5.6	3.39	692.65	2.2	1.66	191.28
2	0.6	1.15	42.96	0.6	1.15	42.96	5.5	3.87	831.75	2.0	1.58	169.62
3	0.6	1.15	42.96	0.6	1.15	42.96	5.5	3.61	756.88	1.7	1.48	138.94
4	0.6	1.15	42.96	0.6	1.15	42.96	5.4	3.55	738.96	1.7	1.46	134.03
5	0.6	1.15	42.96	0.6	1.15	42.96	5.5	3.47	715.54	1.7	1.46	134.03
6	0.6	1.15	42.96	0.6	1.15	42.96	5.6	3.55	738.96	1.6	1.45	129.18
7	0.7	1.17	50.72	0.6	1.15	42.96	5.9	3.55	738.96	1.5	1.41	119.64
8	0.9	1.23	66.78	0.6	1.15	42.96	5.3	3.63	762.93	1.5	1.40	114.95

Ch	#	1	2	3	4	5	6	7	8
with Isolator	T'_{SYS} (K)	2013.6	1859.8	1716.3	1648.2	1693.3	1704.8	1847.5	1648.2
	$\Delta T'_{rms}$ (K)	3.60	2.38	1.57	1.51	1.55	1.10	0.96	0.59
without Isolator	T_{SYS} (K)	1716.3	1582.4	1457.4	1398.1	1437.4	1447.4	1571.6	1398.1
	ΔT_{rms} (K)	3.13	2.07	1.37	1.32	1.35	0.96	0.84	0.52

Table 1.1: Theoretical estimates of receiver noise temperature and radiometer sensitivity (for 4.096 ms integration time and 290 K antenna temperature) across the desired 8 radiometric channels have been calculated using the insertion losses and noise figures of the RF front end components.

the standard deviation of the radiometer noise. The high degree of linearity of (1.10) with respect to temperature allows the use of a linear minimum mean-square-error (LMMSE) statistical operator to estimate the vertical atmospheric temperature profile in clear air. In this method, an estimate of the discretized temperature profile $\hat{\bar{T}}$ is computed from the measured antenna temperature perturbations $\bar{T}_A - \langle \bar{T}_A \rangle$ using the LMMSE retrieval operator $\bar{\bar{D}}$ as:

$$\hat{\bar{T}} = \langle \bar{T} \rangle + \bar{\bar{D}} \cdot (\bar{T}_A - \langle \bar{T}_A \rangle) \quad (1.11)$$

where $\langle \cdot \rangle$ denotes ensemble averaging. Atmospheric temperature profile fluctuations can be modeled as jointly Gaussian random processes where the *a priori* temperature profile covariance $\bar{\bar{R}}_{TT}$ is:

$$\bar{\bar{R}}_{TT} = \langle (\bar{T} - \langle \bar{T} \rangle)(\bar{T} - \langle \bar{T} \rangle)^t \rangle \quad (1.12)$$

The retrieval operator $\bar{\bar{D}}$ can be calculated from a purely statistical basis, incorporating no information on the underlying physics of the observation process and requires only an ensemble of coincident temperature profile and radiometric antenna temperature measurements:

$$\bar{\bar{D}} = \bar{\bar{R}}_{TTA} \bar{\bar{R}}_{T_A T_A}^{-1} \quad (1.13)$$

where $\bar{\bar{R}}_{T_A T_A}$ is the antenna temperature covariance matrix, and $\bar{\bar{R}}_{TTA}$ is the cross-covariance between the atmospheric and antenna temperatures. From (1.11) and (1.13), the error covariance of the retrieved profile $\bar{\bar{R}}_{EE} = \langle (\hat{\bar{T}} - \langle \bar{T} \rangle)(\hat{\bar{T}} - \langle \bar{T} \rangle)^t \rangle$ can be expressed as

$$\bar{\bar{R}}_{EE} = \bar{\bar{R}}_{TT} - \bar{\bar{R}}_{TTA} \bar{\bar{R}}_{T_A T_A}^{-1} \bar{\bar{R}}_{T_A T_A}^t \quad (1.14)$$

For the linear observation process defined by (1.10), $\bar{\bar{R}}_{T_A T_A}$ and $\bar{\bar{R}}_{TTA}$ can be written in terms of $\bar{\bar{R}}_{TT}$, $\bar{\bar{W}}$ and $\bar{\bar{R}}_{nn}$, the instrument noise covariance (note that the noise covariance matrix is a diagonal matrix as the noise is uncorrelated between channels):

$$\bar{\bar{R}}_{TTA} = \bar{\bar{R}}_{TT} \bar{\bar{W}}^t \quad (1.15)$$

$$\bar{\bar{R}}_{T_A T_A} = \bar{\bar{W}} \bar{\bar{R}}_{TT} \bar{\bar{W}} + \bar{\bar{R}}_{nn} \quad (1.16)$$

and thus,

$$\bar{D} = \bar{R}_{TT} \bar{W}^t (\bar{W} \bar{R}_{TT} \bar{W}^t)^{-1} \quad (1.17)$$

$$\bar{R}_{EE} = (\bar{I} - \bar{D} \bar{W}) \bar{R}_{TT} (\bar{I} - \bar{D} \bar{W})^t + \bar{D} \bar{R}_{nn} \bar{D}^t \quad (1.18)$$

To determine a theoretical understanding of instrument performance based on specifications (Table 1.1), previously generated atmospheric profiles for clear air conditions can be used to compute the expected atmospheric weighting functions and error covariance. The National Oceanic and Atmospheric Administration NOAA88b radiosonde/rocketsonde data set comprises 7547 profiles that are globally distributed seasonally and geographically. It provides atmospheric temperature as well as moisture and ozone content measurements at 100 discrete predefined pressure levels. Profiles obtained during summer and winter months in the earth's polar region i.e. at $|\text{latitude}| \geq 60^\circ$ have been used. With this criteria, the data set for the statistical temperature profile retrieval analysis comprised a total of 824 profiles for winter (Dec, Jan, Feb) and 594 profiles for summer (Jun, Jul, Aug). The surfaces (land and ocean) that the radiometer would observe were constructed based on the following conditions: for land, a surface reflectivity of 5% has been assumed and for ocean, a wind speed of 7 km/s and ocean salinity of 35 ppt (fraction by weight) has been assumed. Weighting matrices and error covariance matrices were computed for an observation altitude of 350 km for eleven cases (Appendix C) obtained from a combination of observation season, surface and angle: {summer, winter} x {land, ocean} x {0°, 30°, 60°}. An in-house microwave radiative transfer (MRT) program [31] that assumes a planar stratified atmosphere was used. Figure 1.4a shows the instrument's eight theoretical weighting functions for clear-air nadir observation over ocean during a polar winter. The root-mean-squared errors in temperature retrieval and the *a priori* standard deviations in temperature are depicted in Figure 1.4b. Between 1.5 km and 22.5 km altitude, the standard deviation errors over ocean are between 1.3-3 K for summer and winter.

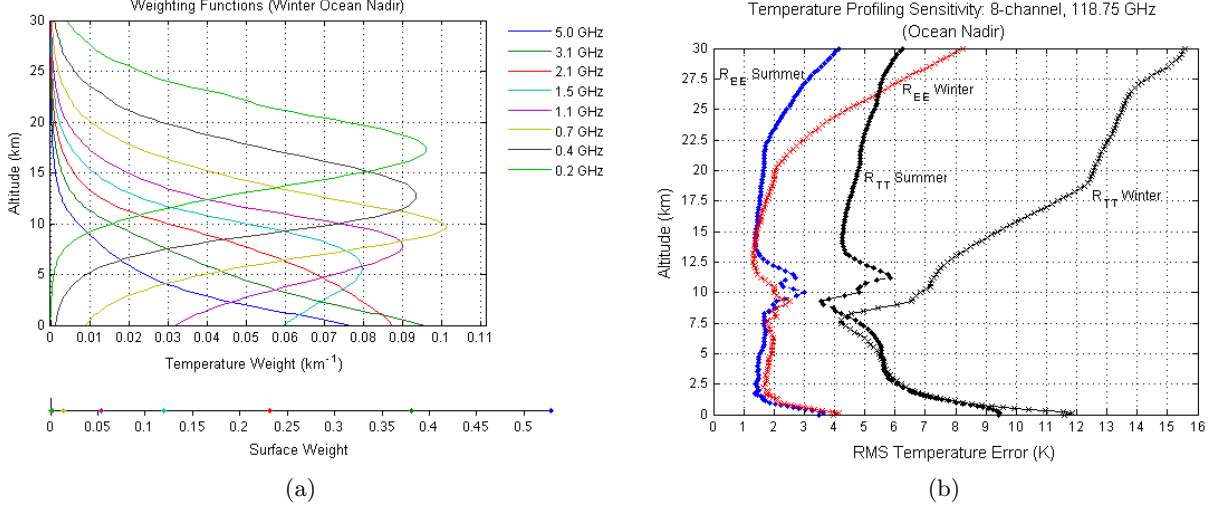


Figure 1.4: Assuming a satellite altitude of 350 km, the MiniRad instrument specifications were used with the NOAA88b radiosonde data set for winter, clear-air polar latitudes to compute (a) the theoretical temperature weighting functions and surface weights for nadiral 118 GHz observations over ocean, and (b) the error covariance or the RMS temperature error profile.

1.5 Radiometer Calibration

Estimation with sub-Kelvin level accuracy of the Level-1 brightness temperatures measured by a space-borne radiometer requires precise knowledge of the end-to-end spatial and spectral responses and noise temperature and gain spectrum of the instrument as a function of the physical payload temperature. Precise estimation also requires a repeatable calibration procedure with minimal calibration error [35].

The power received by the MiniRad total power radiometer at the feed horn aperture P_R can be defined in terms of the elements of the modified Stokes vector \bar{I} , and the antenna subsystem far field power gain matrix $\bar{\bar{G}}_p$ [29] [36] as:

$$P_R = \int_0^\infty \frac{\lambda^2}{4\pi} |H_{SYS}(f)|^2 \oint_{4\pi} \left(G_{p_{vv}} I_v + G_{p_{hh}} I_h + G_{p_{hv}} U + G_{p_{vh}} V \right) d\Omega df \quad (1.19)$$

where

$$\bar{\bar{G}}_p = \begin{bmatrix} G_{p_{hh}} & G_{p_{hv}} \\ G_{p_{vh}} & G_{p_{vv}} \end{bmatrix} \quad (1.20)$$

and $H_{SYS}(f)$ is the radiometer spectral response referred to the feed horn aperture. Note that the

antenna power gain includes the effects of the main reflector ohmic loss and feed horn spillover loss. Cross-polarization in predominantly linearly polarized radiometers used for atmospheric sounding can generally be accommodated in data processing. Accordingly, (1.19) can be simplified by considering a single modified Stokes parameter $I_\alpha = I_v = I_h$ and associated unpolarized gain $G_p = G_{p_{vv}} + G_{p_{hh}}$ of the antenna. For a non-isothermal environment where the intensity exhibits spatial variation, the co-polarized intensity at frequency f is defined by the Planck function as $I_\alpha(\Omega, f, T_B) = \frac{hf^3}{c^2} \frac{1}{e^{hf/k_B T_B(\Omega, f)} - 1}$ where k_B is Boltzmann's constant, h is Planck's constant, c is the speed of light, and $T_B(\Omega, f)$ is the spatially varying brightness temperature inclusive of the absorption, scattering, and emission properties of the medium and source distribution.

The integrated received power is dependent on the main beam pointing direction Ω' which for scanning antenna systems is a function of the reflector scan angle ψ_S . For continuous (vs. stepped) scanning antenna systems, a scan-integrated antenna gain pattern [37, 38] inclusive of feed spillover, reflector loss, and scattering from the strut and satellite body needs to be considered to determine the time-averaged power observed within each radiometer integration time interval τ_i :

$$G'_p(\Omega, f, t) = \frac{1}{\tau_i} \int_{t-\tau_i/2}^{t+\tau_i/2} G_p(\Omega, f, \Omega'(t')) dt' \quad (1.21)$$

where $\Omega'(t')$ is the direction in which the main beam points at time t' .

The total power received at the feed horn aperture of the MiniRad radiometer can thus be written as:

$$\begin{aligned} P_R(t) = & \frac{1}{2} \int_0^\infty \frac{\lambda^2}{4\pi} |H_{SYS}(f)|^2 \left[\oint_{\Omega_M(f)} G'_p(\Omega, f, t) I_\alpha(\Omega, f, T_B) \right. \\ & + \left. \oint_{4\pi - \Omega_M(f)} G'_p(\Omega, f, t) I_\alpha(\Omega, f, T_B) \right] d\Omega df \\ & + \int_0^\infty \frac{hf}{e^{hf/k_B T_{MR}} - 1} |H_{SYS}(f)|^2 \left(1 - \frac{1}{4\pi} \oint_{4\pi} G'_p(\Omega, f, t) d\Omega \right) df \end{aligned} \quad (1.22)$$

In (1.22), the first term represents intensity contributions from the main lobe. Note that the main lobe solid angle $\Omega_M(f)$ is in general slightly frequency dependent. Contributions from stray sources picked up by the antenna side lobes and spillover lobes are contained in the second term. This term

includes background radiation from the environment (e.g., cosmic background contributions). The last term represents thermal emission from the reflector where T_{MR} is its physical temperature. If a thermal model of the reflector is available, a temperature distribution can be used instead of a single physical reflector temperature.

Commonly, for $hf \ll k_B T$, the Rayleigh-Jeans approximation to the Planck function is used along with aggregate measures of ohmic, spillover, and main beam efficiencies. In this case (1.22) is approximated by:

$$P_R(t) \simeq k_B \int_0^\infty |H_{SYS}(f)|^2 [\eta_l \eta_{bm} T_{B,ML} + \eta_l (1 - \eta_{bm}) T_{B,SL} + (1 - \eta_l) T_{MR}] df \quad (1.23)$$

$$\simeq k_B T_A(t) B_{NE} \quad (1.24)$$

where η_{bm} and η_l are the main beam and ohmic efficiencies (respectively). The source terms $T_{B,ML}$ and $T_{B,SL}$ are brightness temperatures of the main antenna lobe and side and spillover lobes (respectively). In (1.24), $T_A(t)$ is the antenna temperature referred to the feed horn aperture and B_{NE} is the effective noise bandwidth of the radiometric channel. Hence, in its simplified form, the corrected effective main lobe brightness temperature estimated using the radiometer measurements is [29]:

$$\hat{T}_{B,ML} = \frac{T_A}{\eta_l \eta_{bm}} - \frac{T_{B,SL}(1 - \eta_{bm})}{\eta_{bm}} - \frac{T_{M,R}(1 - \eta_l)}{\eta_l \eta_{bm}} \quad (1.25)$$

Thus, the interpretation of radiometric measurements is strongly affected by the magnitudes of the various antenna efficiencies [36] such as spillover efficiency η_s , taper efficiency η_t , phase efficiency η_{ph} , and cross-polarization efficiency η_x that impact the main beam efficiency η_{bm} , as well as the *accuracy* with which these efficiencies can be determined. To emphasize this point, it is noted that a space-borne radiometer of the MiniRad scanning architecture observing a 300 K scene in a cold space background requires that the error in the estimation of the spillover efficiency be $\sim 0.03\%$ or smaller in order to obtain a corrected brightness temperature measurement bias of 0.1 K or better.

In two-point calibration, a radiometer is assumed to be a linear (causal) system between two calibration cycles. It is generally desired that a radiometric calibration target emulates

a blackbody (within the frequency range of interest) with minimal thermal variation across its structure. The design, analysis and standardization of calibration targets for radiometry is by itself a widely researched area [39, 40]. When two external targets are used for calibration, their physical temperatures need to be monitored precisely and continuously using resistive temperature devices (RTDs). Their physical temperatures are first converted to brightnesses using the target emissivity and subsequently to antenna temperatures using (1.24). During the time interval when the antenna main beam scans either calibration target, linear fit curves between antenna temperatures of the calibration target, and measured powers are determined. Generally, a linear power detector in the radiometer converts the detected power into voltage, and thereafter an analog-to-digital converter (ADC) converts these voltages to digital counts. Calibration equations for determining estimates of the radiometer gain \hat{m} or slope (counts/K) and system noise temperature \hat{b} or offset (counts) are as follows:

$$\hat{m} = \frac{N_{R,H} - N_{R,C}}{\hat{T}_{A,H}^f - \hat{T}_{A,C}^f} \quad (1.26)$$

$$\hat{b} = \frac{N_{R,C}\hat{T}_{A,H}^f - N_{R,H}\hat{T}_{A,C}^f}{\hat{T}_{A,H}^f - \hat{T}_{A,C}^f} \quad (1.27)$$

where $N_{R,H}$ and $N_{R,C}$ are radiometer counts measured when viewing the hot and cold target, respectively. $\hat{T}_{A,H}^f$ and $\hat{T}_{A,C}^f$ are estimates of the hot and cold target antenna temperatures referred to the feed horn aperture, obtained using:

$$\hat{T}_{A,C}^f = \eta_s \hat{T}_{B,C}^m + (1 - \eta_s) \hat{T}_{B,BG}^m \quad (1.28)$$

$$\hat{T}_{A,H}^f = \eta_s \hat{T}_{B,H}^m + (1 - \eta_s) \hat{T}_{B,BG}^m \quad (1.29)$$

where $\hat{T}_{B,C}^m$, $\hat{T}_{B,H}^m$ and $\hat{T}_{B,BG}^m$ are brightness temperatures of the hot and cold calibration targets referred to the main aperture of the antenna. Their brightnesses are derived by scaling their physical temperatures (measured using resistive temperature devices) with best estimates of their emissivities. Scene observations (in counts) are converted to calibrated scene antenna temperature estimates using:

$$\hat{T}_{A,S}^f = N_{R,S} - \hat{b}/\hat{m} \quad (1.30)$$

where again $N_{R,S}$ represents radiometer counts detected when viewing the scene, and $\hat{T}_{A,S}^f$ is the estimated scene antenna temperature referred to the feed horn aperture.

1.5.1 MiniRad Hybrid Two-point Calibration

The two-point calibration method employed by MiniRad is not end-to-end i.e., while the cold calibration source, the cosmic microwave background, is external to the radiometer, its second calibration source, the reflective PIN diode switch, is an internal waveguide-based diode that switches states as the reflector scans over cold space. In this hybrid calibration scheme, the PIN diode reflects power incident at both its ports when it is switched ON, and when OFF, behaves almost like a through waveguide section. The following comments can be made on the noise temperature $\hat{T}_{B,H}^{pin}$ measured during the PIN diode ON state:

- $\hat{T}_{B,H}^{pin}$ is the noise temperature referred to the PIN diode output port.
- Since the diode's reflection coefficient is ~ 40 dB at both ports, $\hat{T}_{B,H}^{pin}$ consists mainly of noise power generated by the mixer (NF $\simeq 5.5$ dB) reflected from the noise diode receiver port.
- Inherent loss of the PIN diode (~ 0.7 dB) also contributes to $\hat{T}_{B,H}^{pin}$.
- Without an isolator between the PIN switch and the mixer, $\hat{T}_{B,H}^{pin}$ could contain some local oscillator signal leaking out through the mixer.
- $\hat{T}_{B,H}^{pin}$ does not include effects of the antenna far field pattern, radiation loss, feed horn spillover and loss, scattering due to the strut/satellite, reflector loss and emission, and cold space intrusions. This limitation makes accurate determination of the effective scan-integrated antenna spatial and spectral response especially critical as the afore-mentioned effects cannot be calibrated out.

Characteristics of the expected noise power during the PIN diode ON state can be determined as a function of physical temperature from prelaunch measurements using two external targets. Details

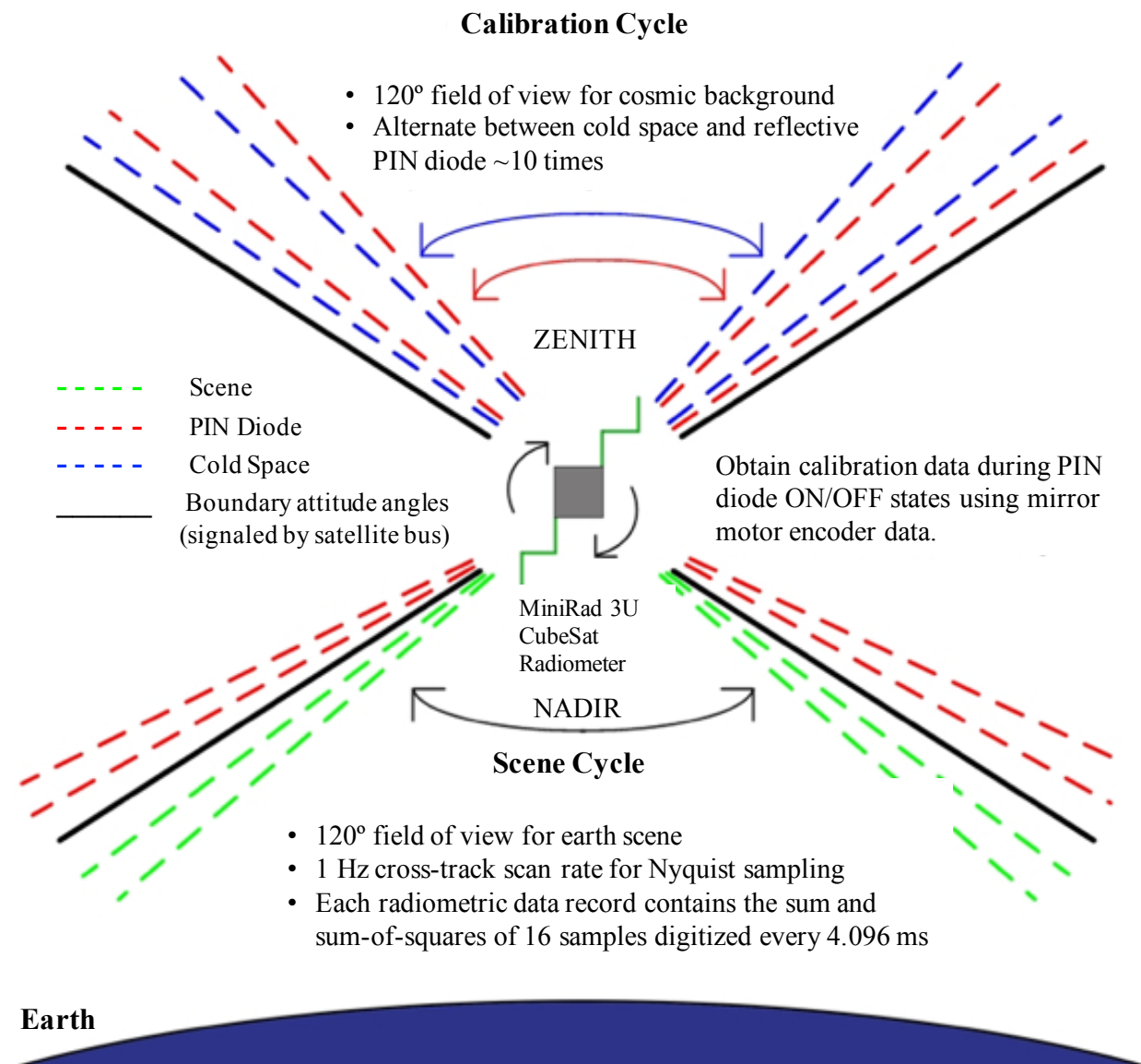


Figure 1.5: Calibration cycle of the space-borne MiniRad radiometer

of this experiment are described in 5.6.3. This noise power model can be used to calibrate scene measurements captured by the radiometer post launch.

Prelaunch calibration is the process of acquiring precise knowledge of an instrument's spectral and thermal response before it is launched into space [35, 41, 42]. It enables accurate estimation of radiometric brightness temperatures before the application of inversion algorithms to extract desired environmental/geophysical parameters. This procedure is absolutely critical to passive spectrometers that detect noise power below a nanowatt (< -90 dBW). Thereby, in order to obtain precisely calibrated radiometric measurements (brightness temperatures) with negligible uncertainties due to instrument, it is imperative to have accurate knowledge of:

- (1) Antenna system efficiencies for frequencies between 112 GHz and 125 GHz as a function of reflector scan angle:
 - (a) Three-dimensional antenna pattern, possibly measured in an antenna chamber inclusive of satellite body and strut assembly.
 - (b) Location of spillover lobes to compute brightness temperature contributions due to known stray sources.
 - (c) Estimation of the phase center at the center frequency 118.7503 GHz to within $1/10^{th}$ of the wavelength.
 - (d) Reflector loss and thermal emission.
- (2) Spectral response of the instrument for frequencies between 112 GHz and 125 GHz that enables knowledge of atmospheric weighting functions, surface weights and cosmic background weights:
 - (a) Ohmic loss due to feed horn, and insertion losses due to front-end RF components, that is, the PIN diode during both OFF and ON states, the short WR-8 waveguide section, the mixer and tripler waveguide component, and the IF LNA.
 - (b) Passband response of the IF and VA module.

- (3) Calibrated noise power measurements during the PIN diode ON state as a function of physical temperature ideally spanning the temperature range the satellite will experience in orbit.
- (4) Variations in the instrument's spectral response (gain, loss and noise temperature) with respect to thermal fluctuations.

The following chapters in this dissertation provide an in-depth discussion of the author's work on the end-to-end electrical design, development and prelaunch calibration of the low-cost MiniRad 118 GHz radiometer built for the PolarCube and the GEMS-1A 3U CubeSats:

- Chapter 2 describes the quasi-optical design of a feed horn and (near-field) offset reflector antenna system. This includes the development of an electromagnetic analysis software suite in MATLAB to compute near field radiated fields for a HE_{11} mode primary aperture field distribution that permits precise prelaunch antenna calibration of the radiometer.

- Chapter 3 discusses the 3D-printed 118.75 GHz corrugated feed. This includes the design of a 3D-printable conical corrugated horn with bent WR-8 to WC-8 waveguide transition for operation between 110 GHz and 127 GHz. The corrugations have been modified to enable the metal laser sintering process.

- Chapter 4 provides an in-depth discussion of the low-cost, compact intermediate frequency spectrometer. This includes the design of an eight channel filterbank (50 MHz to 7 GHz, bandwidths between 250 MHz and 2.2 GHz) with seven contiguous cascaded diplexers implemented as coplanar waveguide and lumped element combinations. The four layer RO4350B and FR4 hybrid stack-up PCB also includes two-stage chip amplification and power detector diodes and, chopper-stabilized op-amp circuitry and analog-to-digital conversion for each channel.

- The first half of Chapter 5 discusses sensor noise and other laboratory measurements. Results from several laboratory experiments conducted for fine-tuning of power into detectors; thermal noise, gaussianity and $1/f$ noise; impact of voltage supply and ambient temperature fluctuations are delineated.

- The last part of Chapter 5 describes final system integration in the CubeSat and prelaunch radiometric characterization. This includes implementation of field experiments with two external calibration targets for comparison of radiometer sky scans with coincident radiosonde data and microwave radiative transfer models, determination of antenna radiation pattern and main beam efficiency and, estimation of reflective diode switch on-state fit coefficients for post-launch calibration.

Chapter 2

Radiometer Antenna System

Radiometric sounding measurements are strongly affected by the main-beam, ohmic, and spillover efficiencies of the optics, as well as inhomogeneities in the scene and background radiation fields. For antenna systems using lenses or reflectors, the main beam efficiency is a function of amplitude taper, phase variation, and polarization of the main aperture fields. Surface errors in the focusing element(s) can produce a random phase non-uniformity. The interpretation of radiometric data is also affected by the accuracy with which these efficiencies can be determined. To emphasize this point, it is to be noted that a space-borne radiometer observing a 300 K scene in cold space requires that the error in the estimation of spillover efficiency be 0.03% or smaller in order to obtain corrected brightness temperature measurement accuracy of 0.1 K or better.

The Gaussian (paraxial) beam mode approximation [43] is a commonly used method for optical analysis of antenna subsystems with limited off-axis accuracy for millimeter and sub-millimeter wavelength diffracted fields. Its use stems from the computational burdens and inaccuracies associated with full solutions to Maxwell's equations over a volume that may be up to hundreds of wavelengths on a side. However, subtle changes in the feed horn design parameters, including changes that induce feed horn mode phasing such as corrugation depth or step diameters, produce pattern changes at the reflector that are not captured by the Gaussian approximation.

To provide a more precise determination of the requisite efficiencies for radiometry, a full wave Fourier field study [44] [45] [36] was implemented that focuses on the precise numerical analysis of the complex diffracted field produced by an offset feed at the focal point of a reflector (or lens)

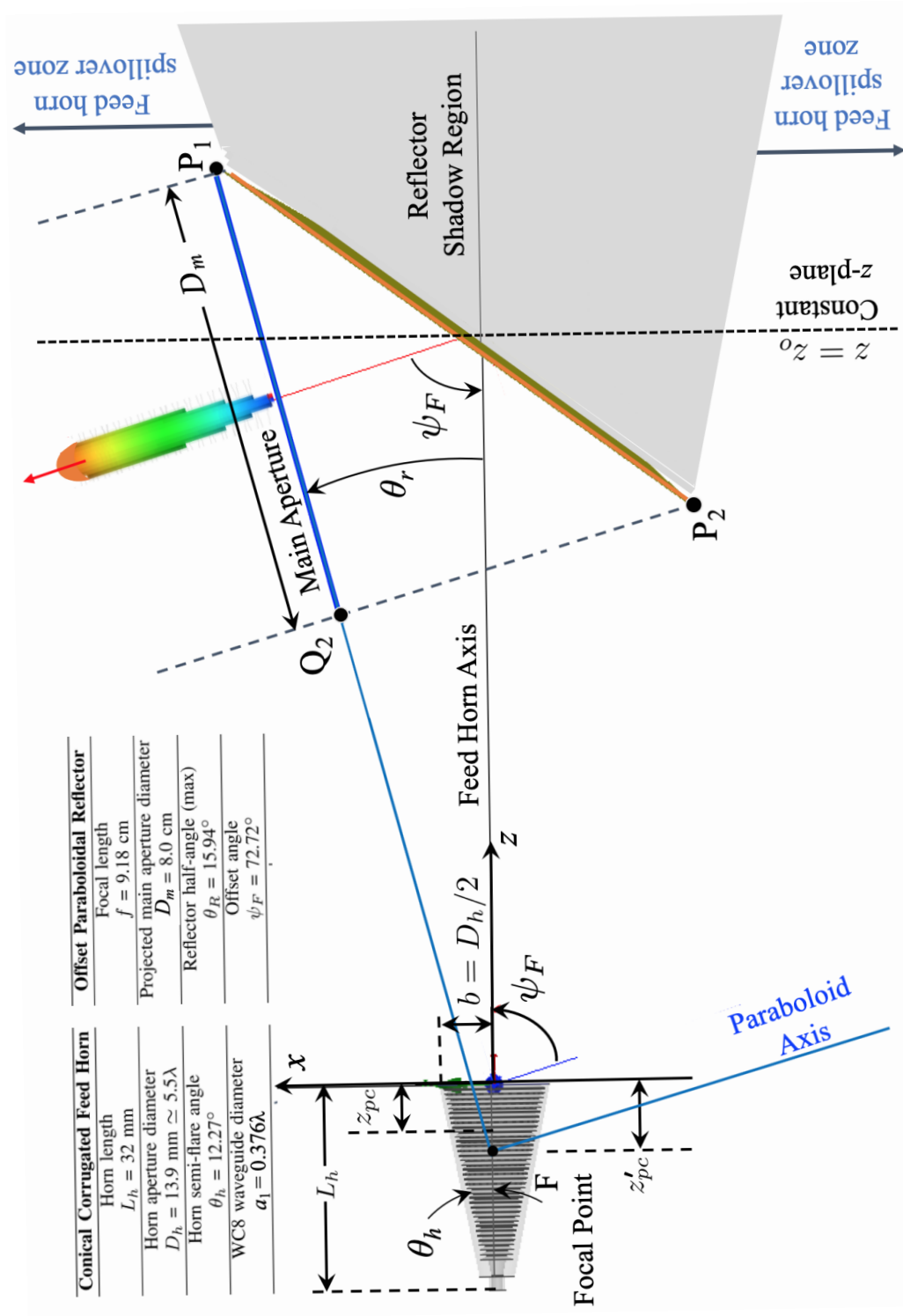


Figure 2.1: Antenna system geometry used in the HE_{11} mode full wave Fourier Bessel electromagnetic field analysis.

focusing element. The analysis leads to the determination of an optimal feed horn and reflector geometry such that the main beam and spillover efficiencies of the system are maximized, and that these and the ohmic efficiency are precisely known. This analysis is applied to the antenna subsystem of the 3U CubeSat (PolarCube or GEMS-01A) 118.75 GHz MiniRad radiometer payload which comprises a spinning offset paraboloidal main reflector and a stationary corrugated feed horn.

2.1 Full Wave Fourier Field Analysis

The full wave Fourier field analysis is used to determine with high precision the antenna system spillover, main beam, and radiation efficiencies, and feed horn phase center location. This information is needed for a scanning reflector/fixed-feed system at all scan angles. It is also used to optimize reflector and feed geometry before (low cost) fabrication as well as enable precise knowledge of the antenna's spatial radiometric response before launch. This is especially critical for radiometers that do not permit end-to-end external calibration such as the PolarCube and GEMS-01A 118.7503 GHz MiniRad radiometers. MiniRad uses a hybrid calibration scheme with cold space as one (external) calibration source and a reflective PIN diode as the second (internal) calibration target. One advantage of using an internal calibration source is that the effects of antenna beam spillover as well as thermal gradients over the external calibration target's surface need not be accounted for during antenna temperature calibration procedures.

Owing to its high beam efficiency, good cross-polarization characteristics, low ohmic loss, well-defined phase center, and good return loss over a large bandwidth, the corrugated feed horn is widely used in sub-millimeter wavelength (SMMW) radiometry [46] [47]. Ideally, it is of interest that the corrugated feed horn be designed such that it supports only the HE_{11} mode at its aperture. Any higher order mode compromises the main beam efficiency function of the horn. Hence, a theoretical analysis of the feed and reflector antenna subsystem assuming a pure HE_{11} mode at the feed aperture can be used as a benchmark for performance analyses.

The HE_{11} mode couples with $\sim 98\%$ efficiency to the fundamental Gaussian mode [48]. The $\sim 2\%$ power present in higher order Gaussian modes contributes to minor side lobes in the far field

of the horn. Note that ultra Gaussian [49] [50] corrugated horns were not used in MiniRad since they required too large a length for the available space within the 3U CubeSat envelope constraints. Additionally, the Potter horn [51] [52] that is designed to approximate the HE₁₁ mode by excitation of the TE₁₁ and TM₁₁ modes with appropriate amplitudes and phases does not have the bandwidth required for the eight-channel double side band MiniRad radiometer.

The aperture fields of corrugated horns for a given set of design parameters are well represented mathematically using Bessel functions. This representation allows the application of the Fourier transform to the analysis of these antennas for determination of the radiated fields, and subsequently spillover, cross-polarization, and other parameters of interest at the reflector aperture with the precision needed in radiometry for weather forecasting applications. Consider a conical corrugated horn whose axis is along the z -coordinate and aperture is in the $z = 0$ plane (Figure 2.1). Expressions for the HE₁₁ mode electric and magnetic aperture fields \vec{E}_a and \vec{H}_a of this horn of length L_h and aperture radius b have been determined by Clarricoats [48] using the surface impedance method, and are reproduced here:

$$\begin{aligned} E_{ax}(\rho, \phi) &= -j \frac{A_o k}{2K} \left[(\bar{\Lambda} + \bar{\beta}) J_0(K\rho) + (\bar{\Lambda} - \bar{\beta}) J_2(K\rho) \cos(2\phi) \right] e^{-j \frac{k\rho^2}{2L_h}} \\ E_{ay}(\rho, \phi) &= -j \frac{A_o k}{2K} (\bar{\Lambda} - \bar{\beta}) J_2(K\rho) \sin(2\phi) e^{-j \frac{k\rho^2}{2L_h}} \\ E_{az}(\rho, \phi) &= A_o J_1(K\rho) \cos(\phi) e^{-j \frac{k\rho^2}{2L_h}} \end{aligned} \quad (2.1)$$

$$\begin{aligned} H_{ax}(\rho, \phi) &= -j \frac{A_o k}{2\eta_o K} (1 - \bar{\Lambda} \bar{\beta}) J_2(K\rho) \sin(2\phi) e^{-j \frac{k\rho^2}{2L_h}} \\ H_{ay}(\rho, \phi) &= -j \frac{A_o k}{2\eta_o K} \left[(1 + \bar{\Lambda} \bar{\beta}) J_0(K\rho) - (1 - \bar{\Lambda} \bar{\beta}) J_2(K\rho) \cos(2\phi) \right] e^{-j \frac{k\rho^2}{2L_h}} \\ H_{az}(\rho, \phi) &= \frac{A_o \bar{\Lambda}}{\eta_o} J_1(K\rho) \sin(\phi) e^{-j \frac{k\rho^2}{2L_h}} \end{aligned} \quad (2.2)$$

The aperture fields are a weighted sum of zeroth and second order Bessel functions with a spherical wave phase factor $e^{-j \frac{k\rho^2}{2L_h}}$. Here, η_o is the free space impedance, k the free space wave number, A_o the field amplitude, and $\bar{\Lambda}$ the normalized hybrid factor. The balanced hybrid condition occurs when the surface admittance tends to zero and requires that $\bar{\Lambda} = +1$ for the HE₁₁ mode [53] [54]. The transverse wave number $K = \sqrt{k^2 - \beta^2}$, where β is the phase change coefficient,

and $\bar{\beta} = \beta/k$ is the normalized phase change coefficient. In equations (2.1) and (2.2), it is noted that terms multiplying the second order Bessel function have a second harmonic dependency on the azimuthal coordinate ϕ . Ideally, this term cannot be zero for the balanced hybrid case because $\bar{\beta}$ can never be equal to 1 [48]. Therefore, this non-zero term will result in a small azimuthal variation of the nominally x -polarized aperture field as well as a non-zero cross-polarized field component. These properties are also applicable to the radiated fields derived from the aperture fields using the Fourier transform analysis. Many analyses such as [55] do not take the effects of this asymmetry into account when considering the radiated fields from a corrugated horn with an HE_{11} mode aperture field distribution.

Consider a horn whose axis is along the z -coordinate and aperture is along the $z = 0$ plane (Figure 2.1). The radiated electromagnetic fields along any plane parallel to the feed's aperture at a distance $z = z_o$ can be obtained by using the two dimensional polar Fourier transform method (Appendix E). The transverse components of the Fourier Bessel transformed electromagnetic fields [56] can be derived as:

$$\begin{aligned}
f_x(k_\rho, \psi) &= \frac{-jA_o k}{2K} \left[(\bar{\Lambda} + \bar{\beta}) F_0(k_\rho) - \pi(\bar{\Lambda} - \bar{\beta}) e^{j2\psi} F_2(k_\rho) \right] \\
f_y(k_\rho, \psi) &= \frac{\pi A_o k}{2K} (\bar{\Lambda} - \bar{\beta}) e^{j2\psi} F_2(k_\rho) \\
g_x(k_\rho, \psi) &= \frac{\pi A_o k}{2K \eta_o} (1 - \bar{\Lambda} \bar{\beta}) e^{j2\psi} F_2(k_\rho) \\
g_y(k_\rho, \psi) &= \frac{-jA_o k}{2K \eta_o} \left[(1 + \bar{\Lambda} \bar{\beta}) F_0(k_\rho) - \pi(1 - \bar{\Lambda} \bar{\beta}) e^{j2\psi} F_2(k_\rho) \right]
\end{aligned} \tag{2.3}$$

where $\vec{f}_t = f_x \hat{x} + f_y \hat{y}$ is the transverse component of the transformed electric field and $\vec{g}_t = g_x \hat{x} + g_y \hat{y}$ is the transverse component of the transformed magnetic field, and the functions $F_0(k_\rho)$ and $F_2(k_\rho)$ are defined as:

$$F_0(k_\rho) = \int_0^b J_0(k'_\rho \rho') J_0(K \rho') e^{-j \frac{k \rho'^2}{2L}} \rho' d\rho' \tag{2.4}$$

$$F_2(k_\rho) = \int_0^b J_2(k'_\rho \rho') J_2(K \rho') e^{-j \frac{k \rho'^2}{2L}} \rho' d\rho' \tag{2.5}$$

The z -components of the Fourier transformed fields can be obtained by Gauss' laws and the plane wave dispersion relationship.

Using a plane wave phase propagation factor and the polar inverse Fourier transform, the radiated electromagnetic fields on any plane at a distance z_o from the feed's aperture can be determined. Expressions for the transverse components of the fields in polar coordinates are:

$$\begin{aligned} E_x(\rho, \phi; z_o) &= -j \frac{A_o k}{2K} [(\bar{\Lambda} + \bar{\beta}) L_0(\rho; z_o) + \pi(\bar{\Lambda} - \bar{\beta}) e^{j2\phi} L_2(\rho; z_o)] \\ E_y(\rho, \phi; z_o) &= -\frac{\pi A_o k}{2K} (\bar{\Lambda} - \bar{\beta}) e^{j2\phi} L_2(\rho; z_o) \end{aligned} \quad (2.6)$$

$$\begin{aligned} H_x(\rho, \phi; z_o) &= -\frac{A_o k}{2K \eta_o} \pi e^{j2\phi} (1 - \bar{\Lambda} \bar{\beta}) L_2(\rho; z_o) \\ H_y(\rho, \phi; z_o) &= -j \frac{A_o k}{2K \eta_o} \left[(1 + \bar{\Lambda} \bar{\beta}) L_0(\rho; z_o) - \pi e^{j2\phi} (1 - \bar{\Lambda} \bar{\beta}) L_2(\rho; z_o) \right] \end{aligned} \quad (2.7)$$

where:

$$L_0(\rho; z_o) = \frac{1}{2\pi} \int_{k_\rho=0}^k F_0(k_\rho) J_0(k_\rho \rho) e^{-jz_o \sqrt{k^2 - k_\rho^2}} k_\rho dk_\rho + \frac{1}{2\pi} \int_{k_\rho=k}^{\infty} F_0(k_\rho) J_0(k_\rho \rho) e^{-z_o \sqrt{k_\rho^2 - k^2}} k_\rho dk_\rho \quad (2.8)$$

$$L_2(\rho; z_o) = \frac{1}{2\pi} \int_{k_\rho=0}^k F_2(k_\rho) J_2(k_\rho \rho) e^{-jz_o \sqrt{k^2 - k_\rho^2}} k_\rho dk_\rho + \frac{1}{2\pi} \int_{k_\rho=k}^{\infty} F_2(k_\rho) J_2(k_\rho \rho) e^{-z_o \sqrt{k_\rho^2 - k^2}} k_\rho dk_\rho \quad (2.9)$$

Once these functions are computed, the full wave aperture source fields can be accurately obtained on the reflector's surface using physical optics as well as in the main aperture plane using the aperture distribution method [44] [36]. It is noted that if the secondary focusing element was entirely in the far zone of the feed, the Fourier transform of the aperture fields (2.3) evaluated at the asymptotic points $k_x = k \sin \theta \cos \phi$, $k_y = k \sin \theta \sin \phi$ (i.e., the points of stationary phase) can be directly used to determine the radiated fields impinging on its surface. However, for MiniRad the precise full wave fields are necessary since the reflector is decidedly not in the far zone of the feed.

Using equations (2.3)-(2.9), fields along any constant z -plane can be rapidly computed. However, for curved surfaces such as the paraboloidal reflector, only elliptic arcs of points on the

reflector will lie on the same z -plane (Appendix D). The meshing technique required to discretize the reflector surface thus involves a number of finely spaced z -plane contours bounded by the rim of the reflector. In such cases, the field calculations are much more time consuming since the radial integrals need to be reevaluated for each such z -plane. However, an important economy is that the integrals in (2.8) and (2.9) are one-dimensional, thus considerably reducing computational burden. Mathematical details of the antenna geometry, surface meshing techniques, and integration procedures used are described in Appendix D.

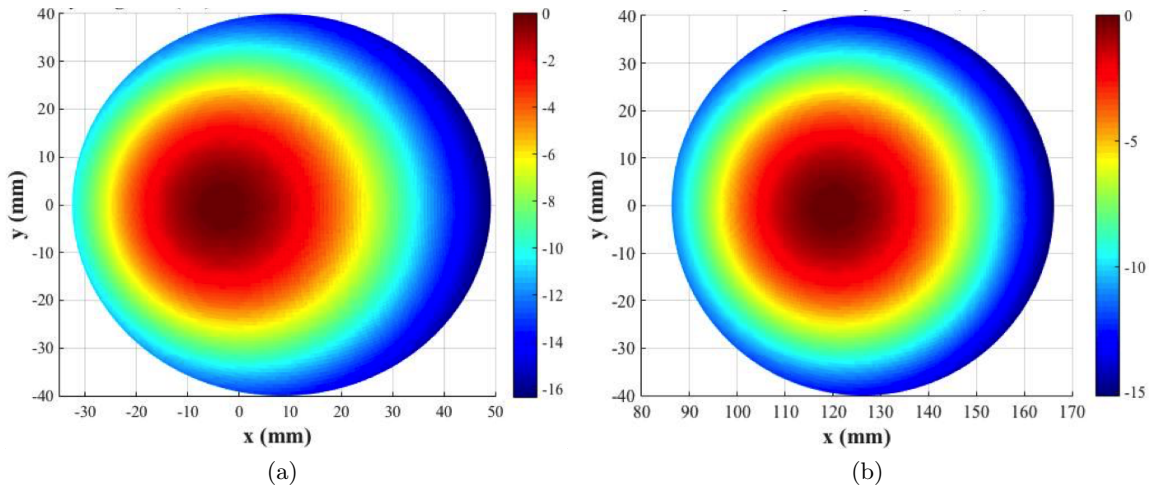


Figure 2.2: Normalized aperture illumination (in dB) on the (a) reflector surface, and (b) main aperture obtained using the HE_{11} mode full wave analysis. The illuminations are not centered due to the offset reflector geometry.

The well-understood aperture distribution method is used to determine fields reflected from the surface of the paraboloidal mirror and subsequently, the far zone fields radiated by the main “primary” aperture but excluding spillover lobes. In order to include spillover lobes in the overall radiation pattern, the electromagnetic fields radiated from the feed horn and *not* occulted by the reflector are computed at a constant z -plane through P_1 (Figure 2.1) and nulled in the shadow region behind the reflector. This plane is assumed to be a “secondary” aperture and radiated fields from it are easily computed using a far-zone Fourier transform method. The total far field directivity, inclusive of spillover lobes, can subsequently be approximated as an incoherent sum

of the primary and secondary radiated field power flux densities. Ignoring far field phases, the directivity of the antenna subsystem becomes:

$$D(\Omega, f) = \eta_l \eta_s D_M(\Omega, f) + (1 - \eta_l \eta_s) D_S(\Omega, f) \quad (2.10)$$

$$\simeq \eta_l \eta_s D_M(\Omega, f) + w(\Omega)(1 - \eta_l \eta_s) D_F(\Omega, f) \quad (2.11)$$

where $D_M(\Omega, f)$, $D_S(\Omega, f)$, and $D_F(\Omega, f)$ are the far field directivities computed from the primary, secondary, and feed horn apertures (respectively), and $w(\Omega)$ is a window function set to zero in the angular region occulted by the reflector and unity elsewhere. The spillover efficiency η_s is the ratio of the Poynting power flux intercepted by the reflector (or an equivalent surface) and the total power radiated by the feed. Equation (2.10) is preferred since it models diffraction from the main reflector edges.

2.1.1 Power Conservation

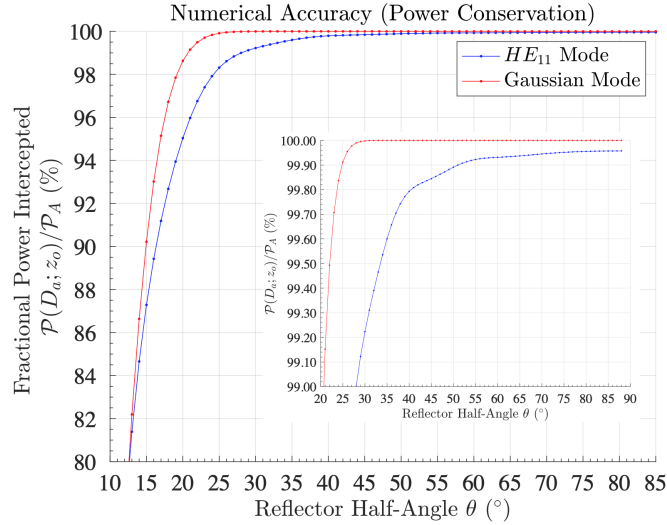


Figure 2.3: Fractional power intercepted by a constant z -plane immediately behind the reflector for increasing reflector half-angle computed using the HE_{11} mode full wave analysis (blue) and a Gaussian beam mode analysis (red). The Gaussian mode overestimates the spillover efficiency by $\sim 2\%$ at the MiniRad reflector half-angle ($\sim 16^\circ$).

For precise calculations of antenna efficiencies such as spillover, it is imperative that the Poynting power flux transmitted from the feed horn aperture is conserved at any constant z -plane.

Using (2.1) and (2.2), an analytical expression for the total real power \mathcal{P}_F radiated from the feed horn is:

$$\begin{aligned} \mathcal{P}_F &= \frac{1}{2} \operatorname{Re} \left\{ \int_{-b/2}^{b/2} \int_{-b/2}^{b/2} \left[\vec{E}_a(x, y; z=0) \times \vec{H}_a^*(x, y; z=0) \right] dx dy \right\} \\ &= \frac{\pi}{\eta_o} \left(\frac{A_o k}{2K} \right)^2 \left\{ b^2 \bar{\beta} (1 + \bar{\Lambda}^2) [J_0^2(Kb) + J_1^2(Kb)] + \frac{2(\bar{\Lambda} - \bar{\beta})(1 - \bar{\Lambda}\bar{\beta})}{K^2} J_1^2(Kb) \right\} \end{aligned} \quad (2.12)$$

Similarly, using (2.6) and (2.7), an expression for the total real power intercepted by a circular aperture of radius R_z at any z -plane is:

$$\mathcal{P}(R_z; z_o) = \frac{\pi}{\eta_o} \left(\frac{A_o k}{2K} \right)^2 \left\{ (\bar{\Lambda} + \bar{\beta})(1 + \bar{\Lambda}\bar{\beta}) \int_{\rho=0}^{R_z} \rho L_0 L_0^* d\rho - 2\pi^2 (\bar{\Lambda} - \bar{\beta})(1 - \bar{\Lambda}\bar{\beta}) \int_{\rho=0}^{R_z} \rho L_2 L_2^* d\rho \right\} \quad (2.13)$$

In order to verify numerical accuracy of the computations, the fractional power intercepted $\mathcal{P}(R_z; z_o)/\mathcal{P}_F$ at a constant z -plane immediately behind the reflector's location was computed for increasing half angle θ subtended by this circular aperture (Figure 2.3). With a generic desktop computer, power conservation to a level of 99.996% ($\lesssim 4 \times 10^{-4}$ dB) was achieved using a 64-point Gauss-Lobatto quadrature scheme with $\Delta\rho \simeq \lambda/50$ mesh size (Appendix D). Due to their slowly decaying oscillatory nature, numerical integration of the Poynting flux integrands in (2.13), and specifically the contribution from (2.9), does not converge rapidly using Gaussian quadrature. Quadrature methods that take into account such oscillatory integrals could be used to further improve precision [57] [58] [59].

2.2 Feed and Reflector Geometry

Due to their limited volume, CubeSats are highly suitable for passive microwave instruments operating at frequencies higher than ~ 90 GHz with small antennas that can be contained (or stowed in the case of deployable reflectors) within the satellite envelope. In a highly directive antenna system incorporating scanning reflectors or lenses, the aperture area of the primary reflecting element is generally maximized to provide for a narrow beamwidth, and hence improved spatial resolution.

The MiniRad antenna feed horn was designed under the constraints of the $\sim 1.5U$ CubeSat payload volume available using a commercial fixed-length waveguide-based mixer front-end from Virginia Diodes Inc. To optimize the horn dimensions, spillover efficiencies were computed at a plane passing through the center of the reflector and perpendicular to the horn axis using the full wave Fourier method (§2.1). A parametric sweep of horn length and aperture diameter enabled maximization of spillover efficiency) (Figure 2.4). These simulations were carried out at the 118.75 GHz band center frequency with an initial assumption that the reflector focal point was located at the center of the horn aperture.

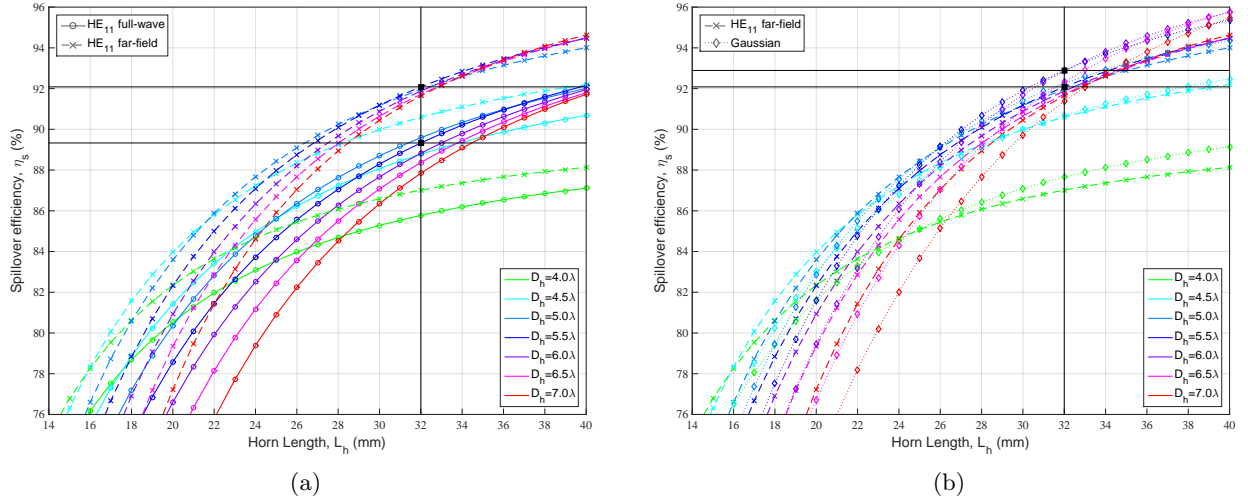


Figure 2.4: Comparisons between the spillover efficiencies obtained using (a) the full wave and far field HE_{11} mode analyses, and (b) HE_{11} and Gaussian mode far field analyses.

Offset Paraboloidal Reflector	Conical Corrugated Feed Horn
Focal length $f = 9.18$ cm	Horn length $L_h = 32$ mm
Projected main aperture diameter $D_m = 8.0$ cm	Horn aperture diameter $D_h = 2b = 13.9$ mm $\simeq 5.5\lambda$
Reflector half-angle (max) $\theta_R = 15.94^\circ$	Horn semi-flare angle $\theta_h = 12.27^\circ$
Offset angle $\psi_F = 72.72^\circ$	WC8 waveguide diameter $a_1 = 0.376\lambda$

Table 2.1: Key geometrical parameters of the MiniRad feed horn and offset reflector (wavelength λ is 2.53 mm).

Spillover has a direct impact on the main beam and aperture efficiencies of the antenna [36]. Precise knowledge of the spillover efficiency is also essential for accurate radiometric calibration as seen in (1.22)-(1.25). Comparisons between spillover efficiencies computed using the HE₁₁ full wave near zone, the HE₁₁ far field, and Gaussian mode far field analyses are shown in Figures 2.4a and 2.4b. When the reflector lies within the feed horn Fresnel zone, accurate spillover calculations require the full wave radiated fields rather than either the HE₁₁ or Gaussian mode far fields. From these comparisons, the feed horn length L_h (from the apex of the cone of the horn to its aperture) was selected to be 32 mm. Considering main aperture efficiency at the reflector, a horn diameter of 5.5λ was selected (c.f. §2.4). Other considerations are the need to restrict the horn flare angle to $\lesssim 20^\circ$ causing it to fall within the category of a narrow flared corrugated horn that exhibits minor spherical phase variation across its aperture, and that contributions from the parasitic HE₁₂ mode at the horn aperture which decrease with increasing feed length are minimized [48].

The MiniRad radiometer's offset paraboloidal reflector has a projected circular main aperture of diameter 8 cm which results in an ~ 18 km 3 dB footprint at nadir from an orbit altitude of 450 km. This reflector is stowed within the CubeSat envelope and deployed after launch. It is held by a single strut in its deployed configuration and includes a motor assembly behind the reflector for crosstrack scanning (Figure 1.2). Its focal length $f_m = 9.18$ cm was finalized based on the fixed length and position of the radiometer RF chain, the theoretical estimate of the antenna phase center location \hat{z}'_{pc} (§2.3), and use of a moderately large $F\#$ to constrain main aperture phase aberration. The reflector itself has an elliptic periphery with major and minor axes of 10.04 cm and 8 cm (respectively). These dimensions, chosen based on the volume available for stowing the mirror inside the CubeSat envelope, necessitate a reflector offset angle ψ_F (i.e., the angle between the paraboloid axis and horn axis) of 72.72° (Figure 2.1). Note that due to its offset geometry, the reflector scans in a shallow cone with apex angle 72.72° rather than in a plane. Since the RF front-end components are comprised of split-block waveguide and mount to an inner wall of the payload, this offset geometry incurs a 17.28° (i.e, $90^\circ - \psi_F$) bend in the WR-8 rectangular waveguide (with dimensions $a = 2.032$ mm, $b = a/2$) to WC-8 circular waveguide (with radius

optimized to 0.953 mm) transition. The geometry of the circular waveguide and corrugations were optimized by modeling the horn using the Ansys[®] HFSS FEM solver. Details of the horn design parameters, manufacturing method and performance are described in Chapter 3.

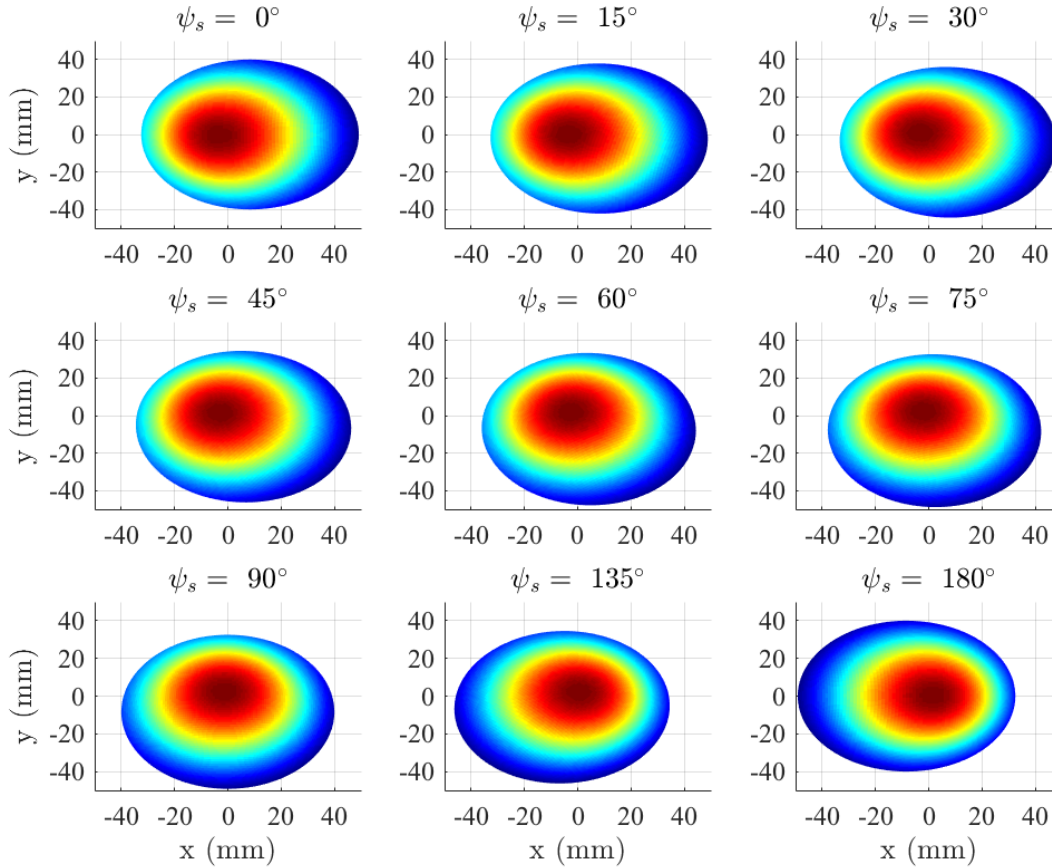


Figure 2.5: 2D-renditions of the reflector Poynting flux power density for various motor shaft scan angles computed using the HE_{11} mode full wave analysis.

2.3 Antenna Phase Center

In order to minimize phase error [55] [60] across the reflector's radiating aperture, the virtual phase center of the feed horn needs to coincide with the focal point of the parabolic reflector. Phase errors in the main aperture serve to lower the phase efficiency η_{ph} , which in turn lowers the main

beam efficiency η_{bm} (in addition to incurring loss in on-axis antenna gain). If unknown, these phase errors directly contribute to errors in the estimation of main-lobe brightness temperature.

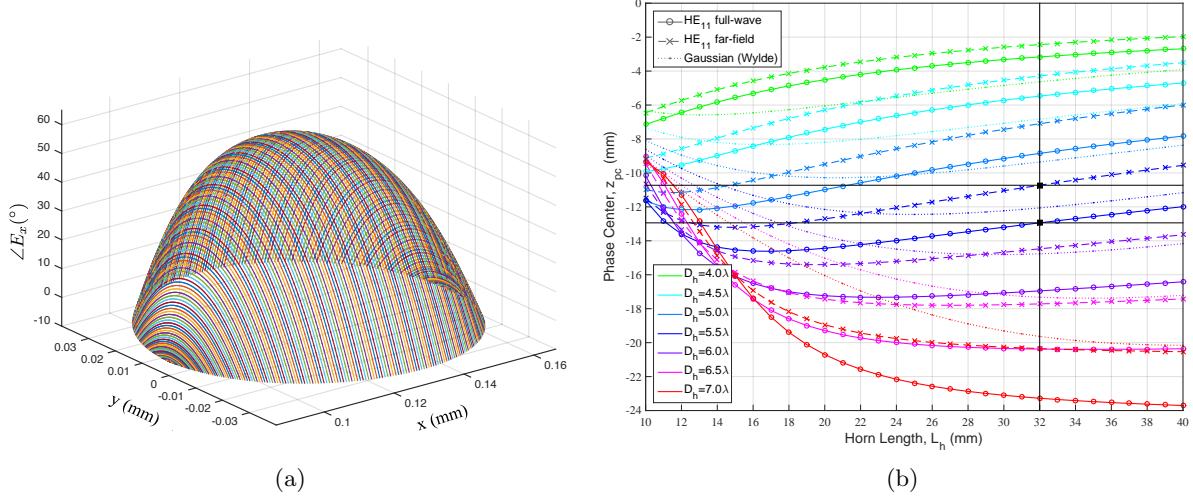


Figure 2.6: For the design frequency 118.75 GHz, the plots show (a) electric field phase distribution across the main aperture assuming the reflector focus is at the center of the horn aperture, and (b) phase centers computed using the HE_{11} mode full wave and far field, and Gaussian beam-mode analyses for various feed horn lengths L_h and diameters D_h at a plane passing through the center of the reflector. The ordinate is the phase center location z_{pc} with respect to the horn’s aperture. Negative values of z_{pc} indicate a phase center within the horn body (see Figure 2.1).

Phase centers were initially computed using full wave fields evaluated at a plane passing through the center of the reflector by fitting spherical wavefronts to the electric field phases found from the HE_{11} mode full wave, HE_{11} mode far field, and Gaussian beam mode analyses. The Gaussian beam mode method uses the well-known Gaussian-Laguerre field decomposition technique to determine the beam phase center [43]. Figure 2.6b shows computed phase center locations z_{pc} at 118.75 GHz for several horn lengths and diameters. These curves provide an initial estimate of the phase center and bound the range of reflector focal lengths given constraints of the CubeSat envelope and length of the strut that supports the deployable reflector. For example, the spillover efficiency curves in Figure 2.4a indicate that an increase in feed length by ~ 2 mm will improve η_s by $\sim 1\%$. Therefore, an accurate estimate of the phase center location will help ensure that L_h (and thus η_s) is maximized. Note that the phase centers differ by ~ 2 mm between the near field

and far field analyses, thus revealing the importance of the full wave analysis for compact scanning antennas. Since initial estimates of the spillover efficiency and phase center were acceptable for the mission goals, the focal length f_m was left unchanged from its initial value of 9.18 cm.

The final location of the focal point of the reflector was determined using the phase distribution of the HE_{11} mode full wave electromagnetic fields propagated to the reflector's main aperture (Figures 2.7a and 2.7b). Phase deviations and efficiencies across this aperture were computed as a function of reflector axial displacement (Figure 2.8). The phase efficiency has been computed using:

$$\eta_{ph} = \left| \int_{A_m} \vec{E}(x, y) dA \right|^2 / \left[\int_{A_m} |\vec{E}(x, y)| dA \right]^2 \quad (2.14)$$

where A_m is the area of the reflector's main aperture. The displacement that maximized main aperture phase efficiency η_{ph} at the design center frequency was used to fix the reflector's focal point. This location (z'_{pc} in Figure 2.1) was chosen to be 13.5 mm so that the phase efficiency was maximized at 118.75 GHz (Figure 2.8). The final location z'_{pc} is close to but 0.6 mm further into the horn flare than the computed full wave value of 12.9 mm (Figure 2.6b). For zero axial displacement of the horn (i.e., $z'_{pc} = 0$ mm), the maximum phase deviation at the main aperture plane exceeded 60° (Figure 2.6a), thus illustrating the importance of precise focusing. Note that the calculated far field phase center is 10.97 mm behind the horn aperture (Table 3.1). By application of a spherical fit to the E -plane cut obtained from laboratory far field measurements of the 3D-printed feed horn (see Chapter 3), the computed phase center was 12.02 mm behind the horn.

Phase distributions across the main aperture for the final 13.5 mm reflector axial displacement are shown in Figures 2.7a and 2.7b. The peak phase deviation of 8° (i.e., $\lambda/50$) could be reduced to some extent by shaping of the reflector. However, shaping of a scanning paraboloidal reflector could affect phase distributions for multiple scan angles ψ_S differently. Such shaping needs further study and has not been attempted for the MiniRad reflector.

The loss in gain due to the main aperture phase error can be roughly estimated using the Ruze factor $e^{(-k\sigma_{ph})^2}$ [61] where σ_{ph} is the RMS main aperture phase error (Figure 2.8). For the

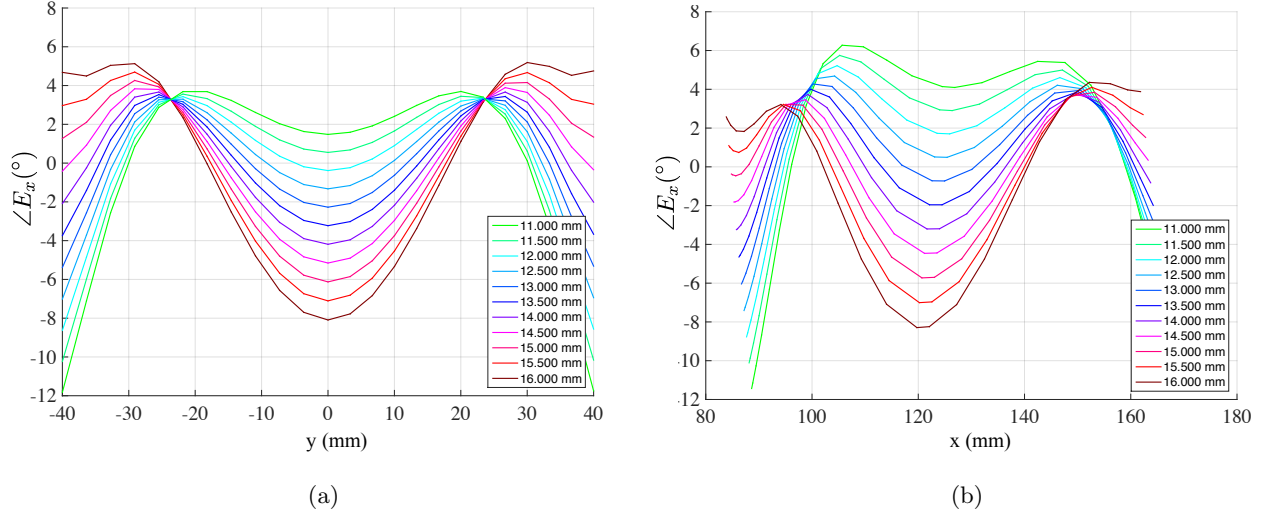


Figure 2.7: Phase distributions of the x -component of the electric field E_x along the two principal perpendicular diameters of the main aperture for various reflector axial displacements: (a) $x = \text{constant}$, and (b) $y = \text{constant}$.

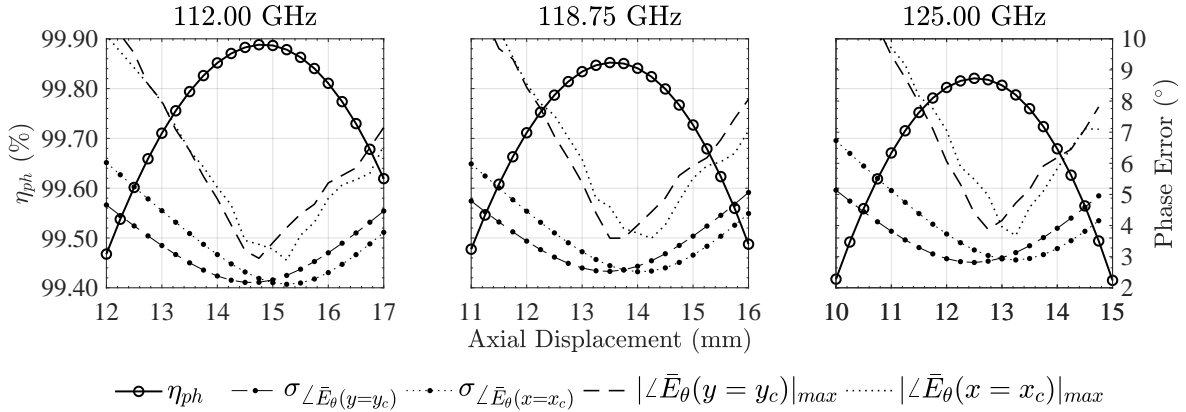


Figure 2.8: Phase efficiencies η_{ph} , and phase standard and maximum deviations at the main aperture as a function of reflector axial displacement z'_{pc} computed at three key frequencies (112 GHz, 118.75 GHz and 125 GHz).

RMS phase error of 2.6° at the center frequency, the Ruze factor is 99.79% which is close to the computed phase efficiency $\eta_{ph} = 99.85\%$. A 0.2% uncalibrated loss in far field gain (i.e., ~ 0.01 dB) results in a 0.6 K error (0.2% of 300 K) that would be significant for a weather satellite, and more so for climate applications. Note that a ~ 2 mm uncertainty in the phase center estimation

and/or focal point displacement of the MiniRad antenna system will result in a $\sim 0.25\%$ error in the knowledge of the antenna phase efficiency. Such an error results in a worst-case 0.75 K error in the estimated main beam brightness temperature. Alignment precision and phase efficiency thus need to be considered during radiometer design and development. Figure 2.8 also indicates that the optimum phase center depends weakly on frequency. For the 13.5 mm displacement, the phase efficiency is 1% lower at 112 GHz and 0.5% lower at 125 GHz than that at 118.75 GHz. Phase efficiency thus contributes to slightly lower gain and main beam temperature error more so at the transparent wings of the 118.7503 GHz oxygen resonance.

2.4 Estimated Antenna System Performance

After focusing (i.e., axial displacement of the reflector by 13.5 mm towards the feed horn), the spillover efficiency was computed to be $\eta_s = 91.79\%$ at the center frequency, 118.7503 GHz. The spillover was computed by integrating the real Poynting flux over the surface of the elliptic aperture formed by the rim of the reflector. This spillover calculation closely corroborates the efficiency of 91.79% obtained from Ticra[®] GRASP [1] simulations.

The taper efficiency η_t of the main aperture illumination at 118.75 GHz was computed using the full wave analysis to be $\eta_t = 77.62\%$. This efficiency is a measure of how uniformly the main aperture area is illuminated but is less relevant in passive microwave sensing than the other antenna efficiencies. Taper efficiency has been computed using:

$$\eta_t = \left| \int_{A_m} \vec{E}(x, y) dA \right|^2 / \left[\int_{A_m} |\vec{E}(x, y)| dA \right]^2 \quad (2.15)$$

where A_m is the area of the reflector's main aperture.

Overall directivity obtained using the HE₁₁ mode full wave analysis (2.10) are plotted in Figures 2.10 and 2.11. Analogous Ansys[®] HFSS and Ticra[®] GRASP [1] simulation results of the antenna system with corrugated feed, reflector, and strut are also included. The HFSS model for the reflector and feed (Figure 2.9) used a hybrid model with a finite element boundary integral (FEBI) boundary for the corrugated horn and an integral equation (IE) boundary for the reflector

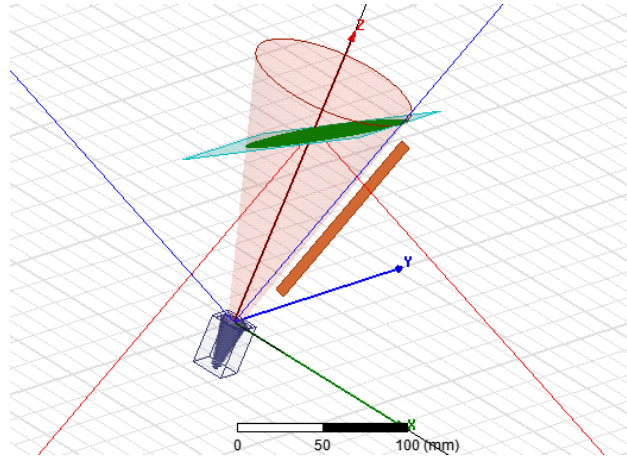


Figure 2.9: The HFSS antenna model including the corrugated horn, reflector and strut.

and strut. All simulations were run on a desktop computer with 16 GB RAM.

The simulated far field patterns obtained using the HE_{11} mode full wave analysis and the HFSS model were used to estimate the main beam efficiency η_{bm} of the MiniRad antenna system. The extent of the main beam is customarily defined as the null-to-null beamwidth. The main beam efficiency is the energy contained within the first null of the main beam and is a measure of the spatial selectivity of the antenna. For example, an ideal pencil beam will have a main beam efficiency of 100%. This efficiency is an important design parameter for applications such as earth remote sensing where contributions from side lobes and spillover lobes contaminate the brightness temperature estimate of the scene (§1.5). Figure 2.12 indicates that an overall simulated main beam efficiency η_{bm} of $\sim 89.49\%$ is expected. It is important to keep in mind that this number includes the simulated spillover efficiency loss of 91.79% which is a principal mechanism in reducing the main aperture main beam efficiency.

The true radiation pattern of the MiniRad antenna subsystem could not be measured due to cost and time constraints. However, the antenna performance was verified during two field experiments: airborne experiments over Antarctica during NASA’s Operation IceBridge mission [62] [63] (October 24 to November 02, 2016) (c.f. §5.1), and bridge-scan experiments conducted at the University of Colorado at Boulder. In the bridge-scan experiment, the MiniRad operated

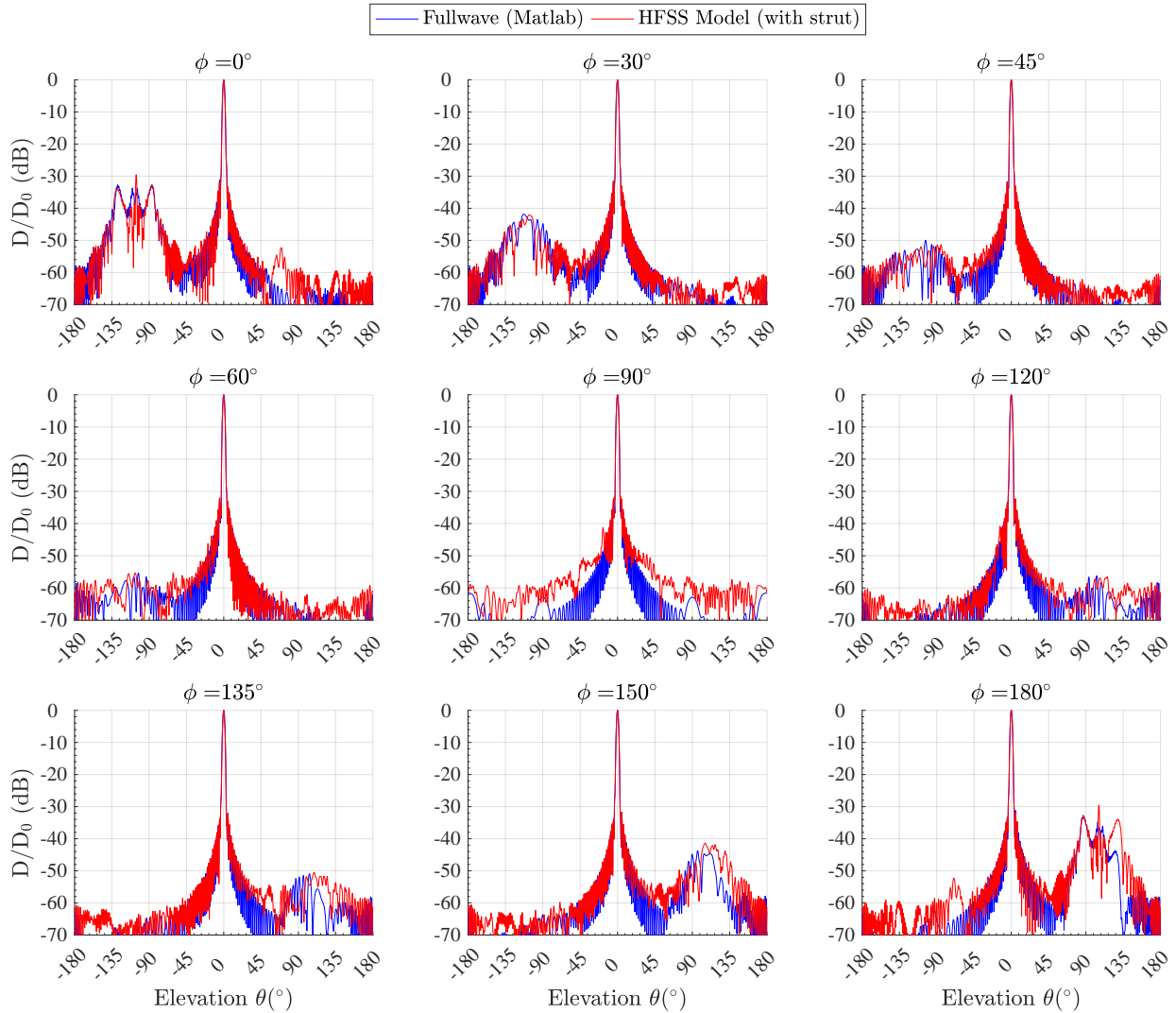


Figure 2.10: Comparisons between the HE_{11} mode full wave (blue) and Ansys[®] HFSS (red) total far field radiation patterns for several azimuthal cuts are shown. Spillover lobes are most prominent closer to $\phi = 0^\circ$.

as an upward looking radiometer scanning across open clear-sky occulted by a far zone half-space concrete obstruction (§5.6.1).

The feasibility of using a 3D-printed corrugated horn operating between 110 GHz and 126 GHz as the feed for MiniRad was investigated primarily due to the very low cost and fast turn-around time of 3D printed components. Precise measurements of the far field radiation patterns

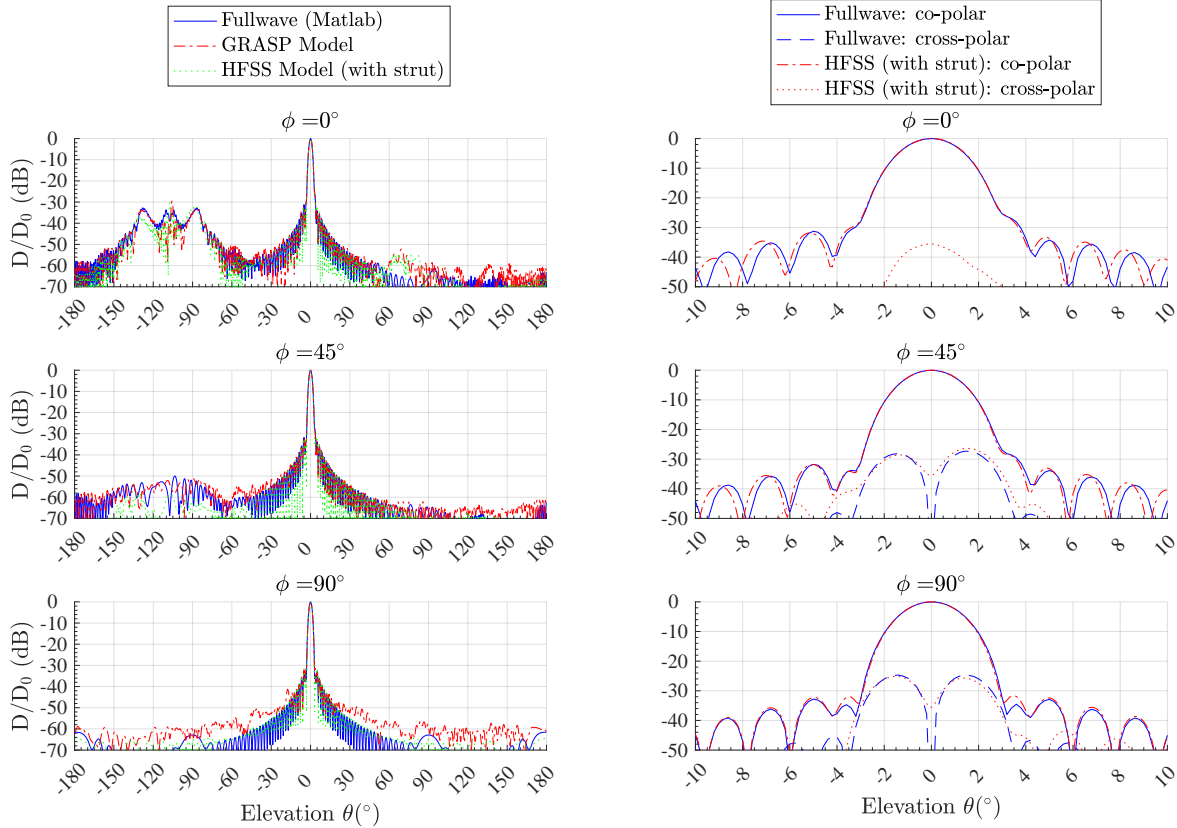


Figure 2.11: Co-polarized and cross-polarized far field simulated patterns for principal azimuthal cuts obtained using the HE₁₁ mode full wave Fourier analysis, Ansys[®] HFSS, and Tica[®] GRASP [1] at 118.75 GHz are depicted.

of the 3D-printed corrugated horn were made at the NIST CROMMA antenna range facility in Boulder [64] (Chapter 3). These measurements were used to determine the 3D-printed horn far field beam efficiency η_{bh} at the 16° reflector half-angle that can provide a good empirical estimate of the expected spillover of the horn-reflector antenna subsystem. Figure 3.7 shows that if the reflector were in the far field of the feed horn, $\sim 89.08\%$ of the feed's total energy will be contained within its aperture. This number is lower than the theoretical estimate of spillover efficiency by $\sim 2.8\%$. However, as the reflector is in the near zone (~ 14.3 cm average distance from phase center) of the feed horn (horn far zone $\gtrsim 2D_h^2/\lambda = 15.31$ cm at 118.75 GHz), a slightly higher near zone spillover efficiency could be expected since the beam will remain partly collimated in the near zone.

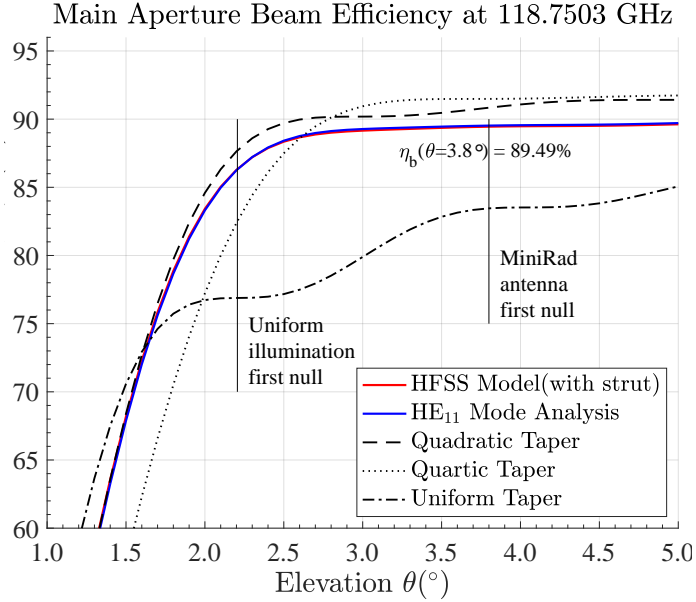


Figure 2.12: Overall main aperture far field beam efficiencies $\eta_b(\theta)$ as a function of elevation θ computed using both full wave and HFSS models are plotted. Also shown for comparison, are beam efficiencies due to uniform, quadratic, and quartic tapers. The gray vertical lines mark the first null for a uniformly illuminated aperture and the MiniRad antenna.

These measurements also indicate some asymmetry in the aperture field distribution (Figures 3.4 and 3.7). But, the reflector is symmetric with respect to its focal point, and hence the spillover efficiency will not depend on scan angle.

Method	$\eta_s(\%)$	Notes
CROMMA	88.93	far zone measurement
HE ₁₁ full wave	91.79	near zone analysis
Ticra [®] GRASP	91.79	near zone simulation
Ansys [®] HFSS	91.33	far zone simulation

Table 2.2: Summary of measured and computed spillover efficiencies obtained from the CROMMA far field measurement of the 3D-printed horn, the HE₁₁ mode full wave analysis, and the GRASP [1] and HFSS simulations.

Chapter 3

3D Printed Feed Horn

The feasibility of using a 3D-printed corrugated horn operating between 110 GHz and 126 GHz as feed for the 118.75 GHz 3U CubeSat temperature sounding radiometer was investigated primarily due to the very low cost and fast turn-around time of 3D printed components. In addition to the complexity of sub-millimeter size corrugations, the horn includes a rectangular to circular waveguide transition with a 17.28° bend to accommodate an offset paraboloidal reflector with maximum aperture area. A directly machined or electroformed corrugated horn at sub-millimeter wave frequencies is quoted higher than 10,000 USD with a turn-around time of several months. In comparison, a batch of five printed horns were procured at one-tenth this price in less than a week.

3.1 Design

The PolarCube feed horn has a diameter $D_h = 2b = 5.5\lambda$ and length $L_h = 32 \text{ mm} \simeq 2.3D_h$ where λ is 2.53 mm (Figure 3.1). The procedure used to determine these horn dimensions was explained in §2.2. The horn's circular waveguide diameter a_1 was chosen to prevent propagation of the TM_{11} mode but kept large enough to minimize attenuation in the waveguide. Circular waveguide diameter a_2 , and corrugation depth d were optimized using HFSS simulations to minimize reflection coefficient (Figures 3.2a, 3.2b). The length of the rectangular to circular waveguide transition was chosen to be slightly greater than twice the maximum operating guide wavelength. A longer, smoother transition helps minimize reflections and generation of higher order modes; however, its length was constrained by the space available for the payload within the CubeSat.

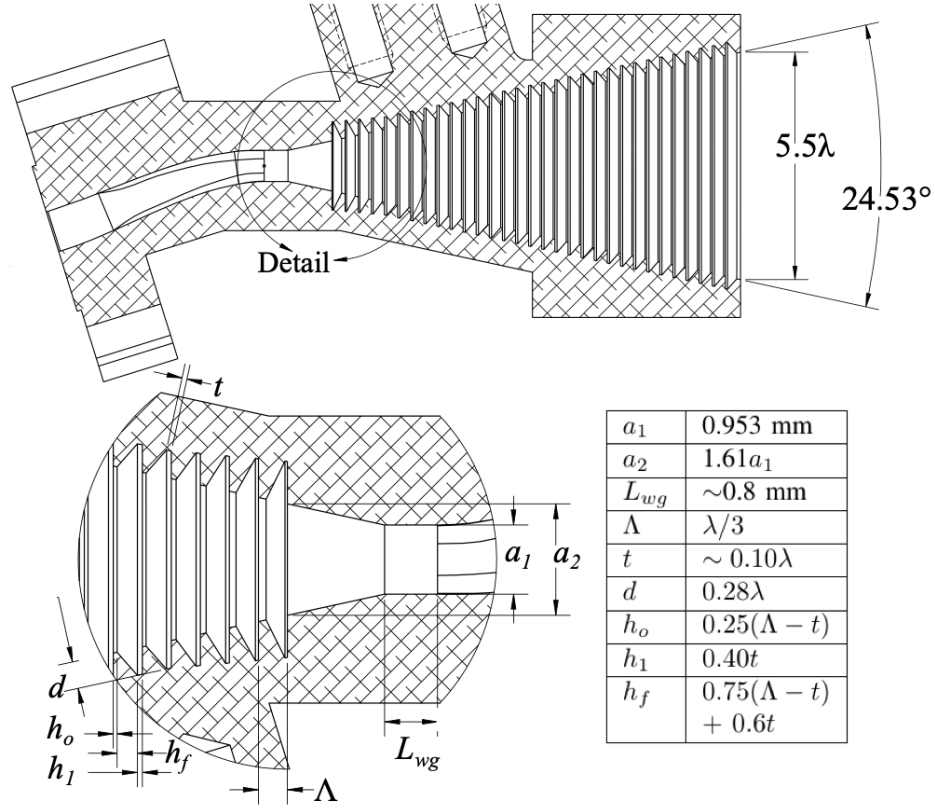


Figure 3.1: The 3D-printed corrugated horn design with the 17.28° bent rectangular to circular waveguide transition.

3.2 Fabrication

The horn was built with an EOS GmbH EOSINT M 280 printer [65] that utilizes a direct metal laser sintering (DMLS) process in an inert argon atmosphere. DMLS is an additive manufacturing (AM) technique [66] where a high intensity laser beam, guided by a CAD model of the desired object, sinters a metal-alloy powder bed, layer by layer, to build the object [67, 68]. The EOS printer achieves a $380 \mu\text{m}$ minimum feature size and $20\text{-}30 \mu\text{m}$ layer thickness with a typical part accuracy of $100 \mu\text{m}$ which depends on the powder material. The metal powder used is an aluminium casting alloy AlSi10Mg [69], a commercial alloy specifically optimized for use by this printer that has good casting properties for thin-walled and complex parts. The total weight percentage of the alloying elements is $\sim 12\%$ with silicon comprising $9\text{-}11\%$ weight. The powder is melted by a 200 W

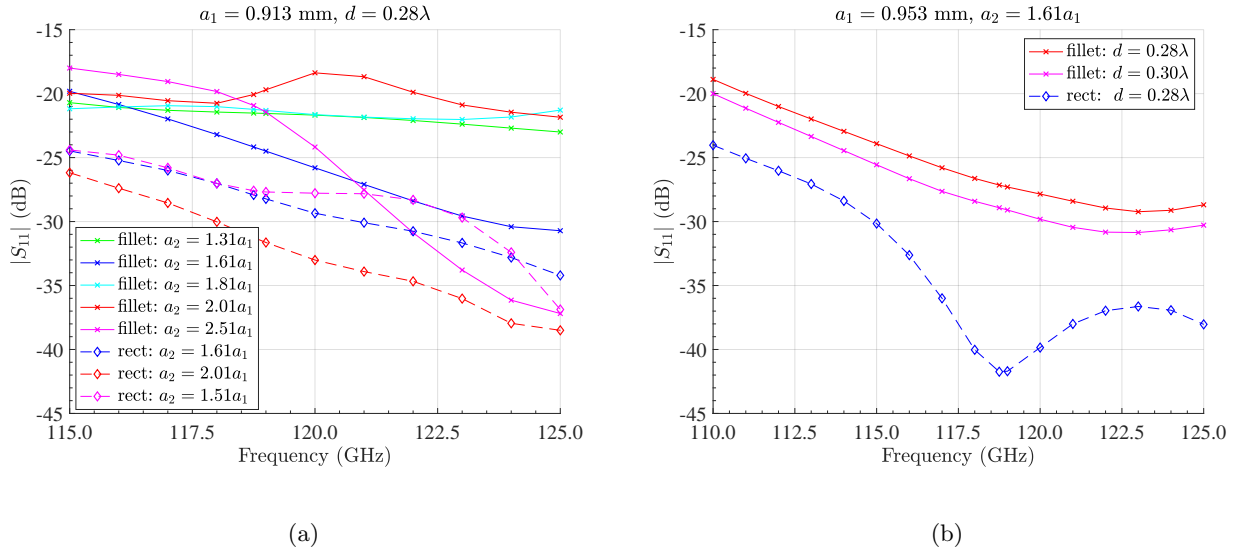


Figure 3.2: Optimization of the corrugated horn design parameters: Variations in $|S_{11}|$ due to (a) changes in diameter a_2 for a fixed diameter a_1 , and (b) changes in corrugation depth d for fixed diameters a_1 and a_2 .

Ytterbium (Yb) fiber laser with a 200 μm beam diameter.

Standard corrugation parameters [48, 54] for rectilinear corrugations were modified to support filleted corrugations (Figure 3.1) to avoid downward facing surfaces during the build process. Such filleted corrugations are self supporting and can be printed (without support) by the metal laser sintering process. Overhangs up to an angle of $\sim 25^\circ$ can be built without requiring a support structure [70]. The horn has a non-standard flange as it is directly mated to a waveguide-based PIN diode switch (with a UG-387 flange) at the radiometer front-end. Hence, a short rectangular waveguide section with a standard flange at one end is used to interface the horn with a vector network analyzer or frequency synthesizer during measurements (Figure 3.6b).

3.3 Performance

The performance of the 3D-printed horn has been evaluated from near-field measurements made at the NIST (National Institute of Standards and Technology) Configurable Robotic Millimeter-wave Antenna facility (CROMMA) in Boulder, CO [71, 64]. Far-field patterns were obtained at

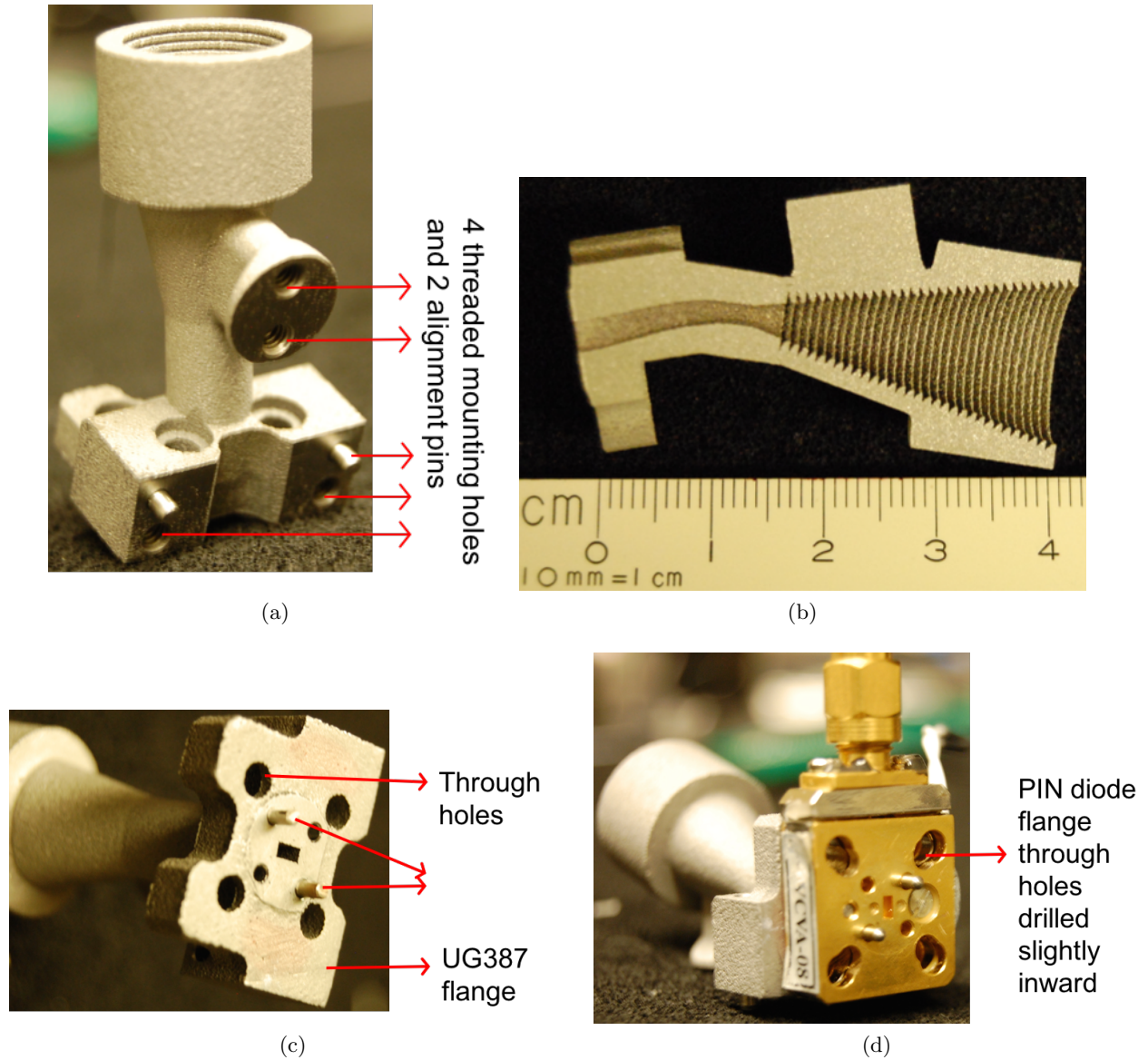


Figure 3.3: Mechanical assembly details of the 3D-printed corrugated feed horn: (a) mounting holes and alignment pins to securely fasten the horn to the satellite chassis, (b) printed horn (unpolished) cross-section depicting the filleted corrugations, and (c,d) the horn WR8 waveguide section bolted to the PIN diode.

three key frequencies pertinent to the 118 GHz radiometer (with a 7 GHz bandwidth): 118.7503 GHz, 112 GHz and 125 GHz. A comparison between the measured and simulated far field patterns (Figures 3.4a, 3.4b) indicates some asymmetry within the 10 dB contour. This degree of asymmetry, if known precisely, is acceptable for this linearly polarized temperature sounding radiometer.

Using the CROMMA measurements, the peak power gain of the 3D-printed horn was determined to be 20.32 ± 0.5 dB at 118.75 GHz by an extrapolation method, which is ~ 1.9 dB lower than the HFSS simulated (with an aluminium material) value of 22.18 dB [64]. But, the horn directivity obtained from a re-interpolated measured gain pattern was ~ 23.8 dB. In comparison, the theoretical directivity calculated by assuming a pure HE_{11} mode aperture distribution, with 68.8% taper efficiency, is 23.14 dB at the center frequency. So, in addition to an ohmic loss, there is reduction in horn main lobe energy and consequently an increase in side-lobe energy (Figure 3.4a). This pattern asymmetry and the presence of larger side lobes suggests that the aperture field distribution could contain higher order modes (such as HE_{21}) in addition to the primary HE_{11} mode. Although the slot style is not critical to corrugated horn performance [48], inconsistencies in the dimensions of corrugations along the length of the horn due to the 3D printing process could result in generation and propagation of higher order modes. The measured reflection coefficient of the 3D printed horn (Figure 3.5a) is lower than -15 dB in the frequency band of interest (110 GHz to 126 GHz). However, there are significant spectral variations in the band that could be due to inconsistencies in the printed corrugations especially close to the feed horn throat and the bent waveguide section. A time domain analysis of the measured reflection coefficient helps gain a better understanding of the $|S_{11}|$ spectral variations. The reflection coefficient $S_{11}(f)$ is defined as the ratio of a reflected wave $V^-(f) = \mathcal{F}\{v^-(t)\}$ and an incident wave $V^+(f) = \mathcal{F}\{v^+(t)\}$. Cross-correlation of the incident and reflected waves in time-domain determines distances from the reference plane at which reflections occur and their magnitudes. Assuming that the incident wave $v^+(t) = \delta(t)$, this cross-correlation function $R_{v^+v^-}(\tau)$ is the inverse Fourier transform of the cross-spectral density between $v^+(t)$ and $v^-(t)$ or product of the measured reflection coefficient and a box car filter over the band of interest (110 GHz to 125 GHz) (3.1). Figure 3.6b indicates the horn

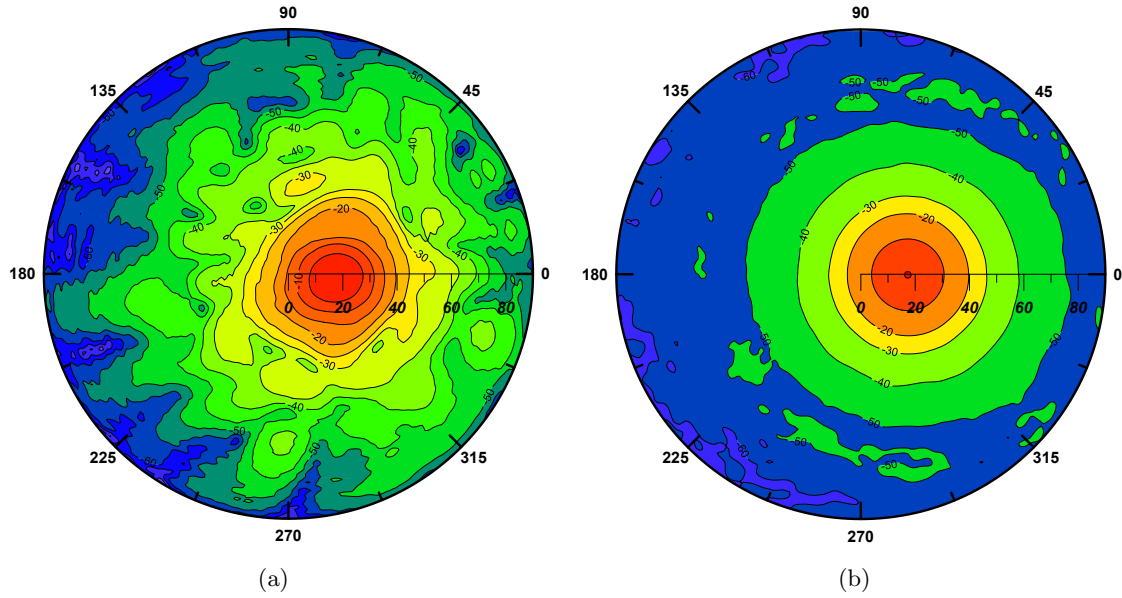


Figure 3.4: Far field patterns of the corrugated feed horn at 118.75 GHz: (a) measured at the NIST CROMMA facility, and (b) simulated using the HFSS model.

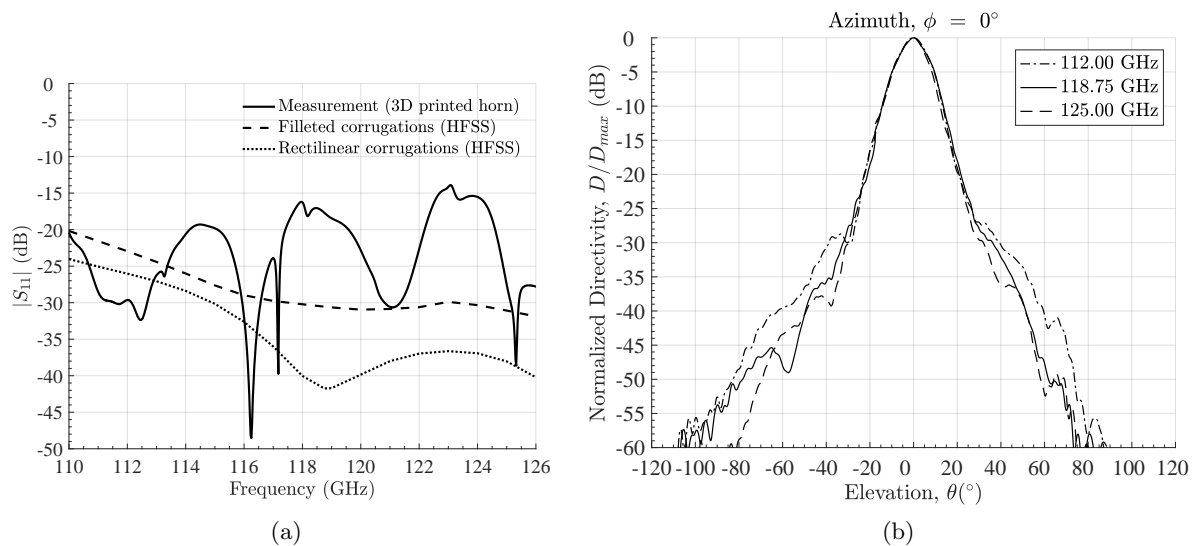


Figure 3.5: (a) Measured and simulated horn reflection coefficient magnitudes are shown. (b) Measurements of the normalized far field directivities for the 3D printed horn at three key frequencies indicate a small asymmetry in the main beam but low side-lobe levels.

under test and planes of interest. The WR8 waveguide adapter is 2.5 cm in length and connects the VNA output to the horn. The 17.28° bent waveguide section in the feed horn is ~ 2 cm long. It is

noted (Figure 3.6a) that maximum reflections occur in the bent rectangular to circular waveguide transition and close to the throat of the horn. However, the reflections are below -25 dB. Also shown for comparison are measured reflections due to a short placed at the input to the waveguide adapter and the reference plane.

$$\begin{aligned}
 |R_{v^+v^-}(\tau)| &= |\mathcal{F}^{-1}\{S_{v^+v^-}(f)\}| = |\mathcal{F}^{-1}\{V^+(f)V^{-*}(f)\}| \\
 &= \left| \mathcal{F}^{-1}\{S_{11}^*(f)\} \left[W\left(\frac{f-f_c}{B/2}\right) + \left(\frac{f+f_c}{B/2}\right) \right] \right| \\
 &= |S_{11}(-\tau) \text{sinc}(\pi B\tau) \cos(2\pi f_c\tau)|
 \end{aligned} \tag{3.1}$$

As the corrugated horn is feed for an ~ 8 cm offset paraboloidal reflector, its beam efficiency

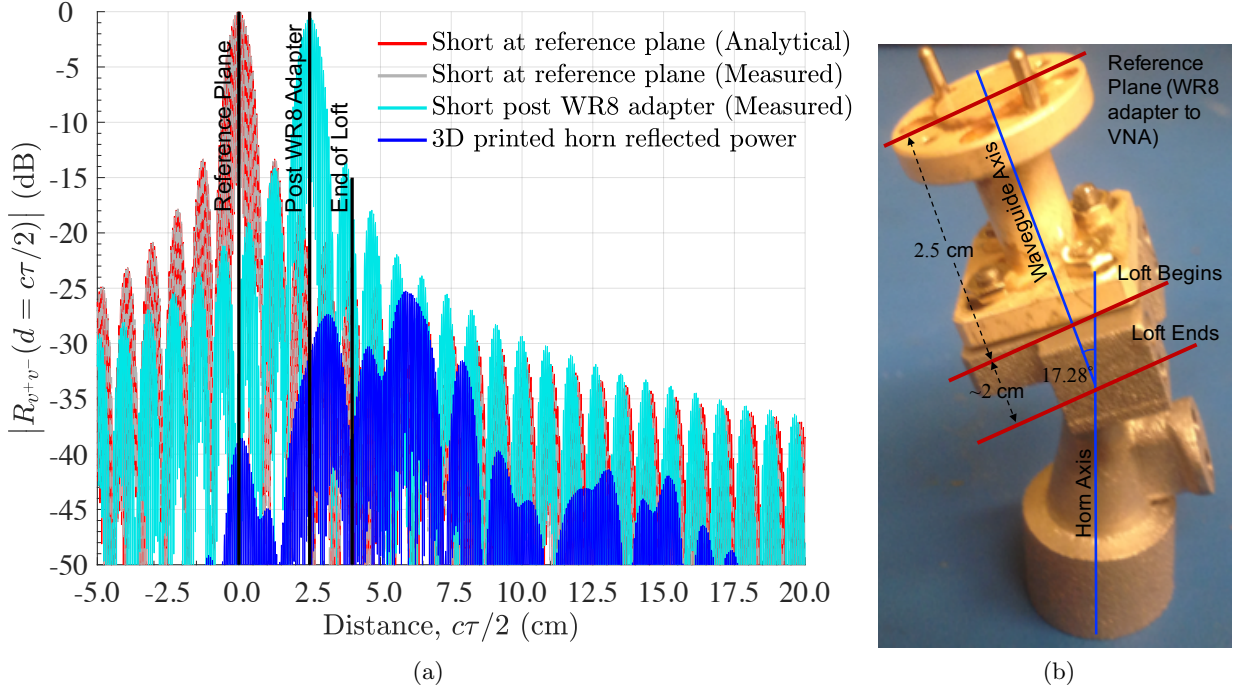


Figure 3.6: (a) Time domain analysis of the measured reflection coefficient indicates reflections (≤ -25 dB) close to the horn throat and loft. (b) Reference planes used in the measurement of the reflection coefficient are indicated.

calculated from the measured far field pattern at the reflector half-angle ($\sim 16^\circ$) gives a rough estimate of the spillover efficiency of horn-reflector antenna system. As seen in Figure 3.7, the horn beam efficiency function $\eta_{bh}(-16^\circ \leq \theta \leq 16^\circ)$ for the 3D-printed horn is $\sim 3\%$ lower than that for the HE_{11} mode aperture field distribution or the HFSS model of the corrugated horn. This

reduction in beam efficiency is consistent with observations from Figure 3.4 that show increased side lobe energy in the measured far field. However, as the reflector is in the near zone (~ 14.3 cm average distance from phase center) of the feed horn (horn far zone $\gtrsim 2(2b)^2/\lambda = 15.31$ cm at 118.75 GHz), a higher near zone spillover efficiency could be expected since the beam will remain partly collimated in the near zone. Note that the dashed and dotted magenta curves in the figure are beam efficiencies computed using measurements *either* in the left or right sectors of the hemisphere, and are indications of the degree of beam asymmetry.

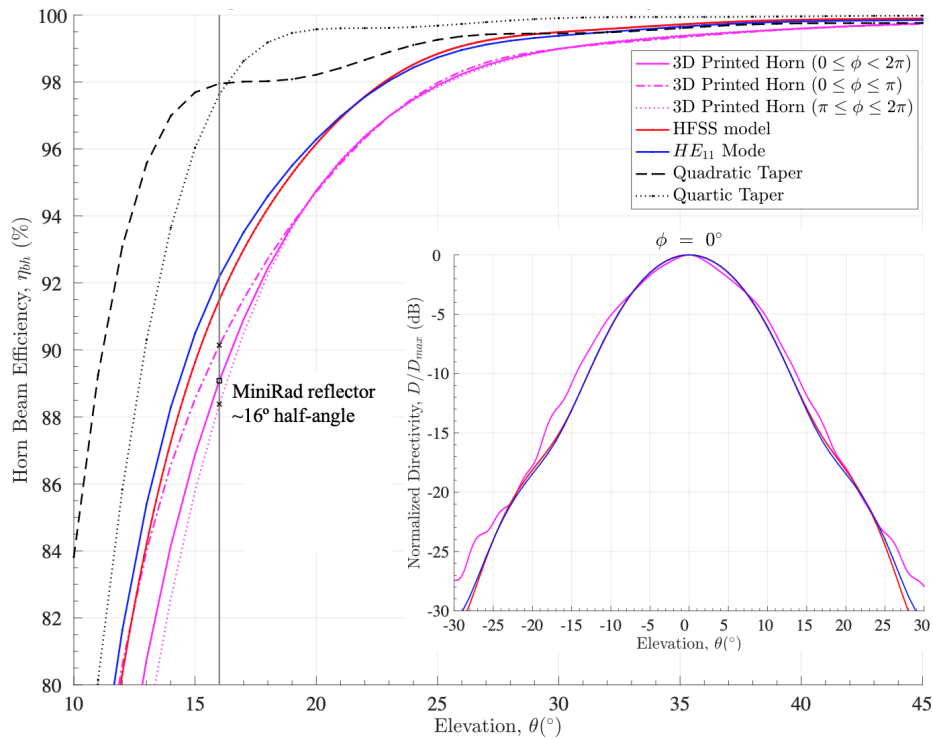


Figure 3.7: 3D-printed feed horn beam efficiencies $\eta_{bh}(\theta)$ as a function of boresight angle obtained using the measured (in magenta) and simulated far field horn patterns are depicted. The inset is a plot of the measured and computed normalized far field directivity patterns for the $\phi = 0^\circ$ plane.

Alignment of PolarCube main reflector requires precise knowledge of the feed horn's phase center. The apparent phase center of a horn is a function of the distance of the analysis region (e.g main aperture) from the horn aperture, angular spread in elevation and azimuth used for the analysis (i.e., 3 dB or 10 dB beam contour), plane cut (i.e., E or H plane) and frequency. Hence, there is a locus of phase centers obtained for the above conditions [72]. The measured far field

phase agrees reasonably with simulations within an 80° angular spread but shows some asymmetry (Figure 3.8). The far field phase center has been calculated by a spherical fit of the measured far field phase for 60° and 90° angular spreads. A comparison with phase centers obtained from simulated patterns is shown in Table 3.1.

Range	$ \theta_{lim} \leq 30^\circ$			$ \theta_{lim} \leq 45^\circ$		
Freq (GHz)	Msr (mm)	HE ₁₁ (mm)	HFSS (mm)	Msr (mm)	HE ₁₁ (mm)	HFSS (mm)
112.00	-11.32	-10.88	-12.35	-10.02	-9.83	-9.58
118.75	-12.02	-10.97	-10.76	-10.48	-9.99	-8.18
125.00	-12.68	-13.52	-11.58	-10.82	-11.71	-11.66

Table 3.1: Tabulated here are the far field phase center locations computed by application of a spherical fit to the phases of (i) the CROMMA measured far field pattern of the 3D printed horn, (ii) the HE₁₁ mode based far field, and (iii) the HFSS simulation of the corrugated horn. $|\theta_{lim}|$ indicates the elevation angle range used in the analysis.

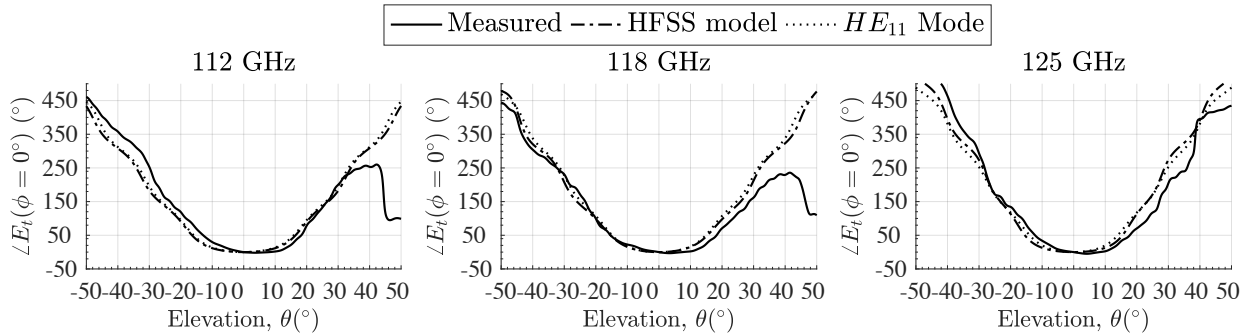


Figure 3.8: Measured and computed E-plane far field phases show good agreement within an 80° angular spread.

In order to better understand the surface roughness of the 3D-printed horn, its axial cross-section (Figure 3.3b) was studied with a profilometer. With no post-polishing procedures applied to the DMLS horn, its average surface roughness R_a was measured to be $\sim 19.5 \mu\text{m}$. Measurements were made with a DektakXT Stylus Profiler. It is to be noted that the metal alloy powder AlSi10Mg has a $\sim 100 \mu\text{m}$ particle size and after microblasting, the average surface roughness is expected to

reduce to $\sim 11 \mu\text{m}$ [69]. This measurement was carried out on the surface of a cube per ISO 4287 [73]. However, surfaces of the corrugations will also have a stepped effect due to the layered sintering process and some improvement in ohmic loss may be expected after careful polishing. Far field measurements indicate that there is $\sim 1\text{-}2$ dB reduction in gain and hence, it is worthwhile to investigate the affect of post-processing methods such as micro shot-peening on (sub)millimeter wave corrugated feeds.

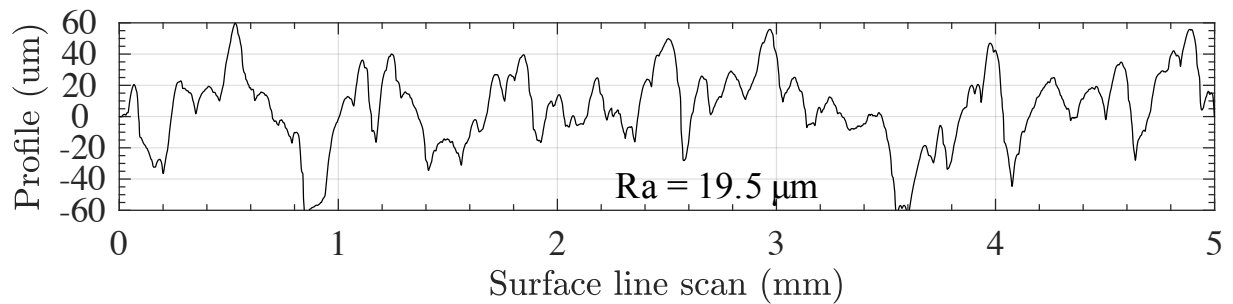


Figure 3.9: Surface profile of the bent WR-8 to WC-8 waveguide transition obtained with a DektakXT Stylus Profiler

Since the 3D-printed horn is part of a space-borne radiometer, it will be subjected to temperature extremes and fluctuations every ~ 90 minute LEO orbit. Thermal analyses of the satellite are indicative of payload temperatures between -20°C and $+45^\circ\text{C}$ in orbit. The MiniRad's performance has been successfully verified during laboratory and field tests inside thermal and vacuum chambers as well as airborne measurements over Antarctica. During such tests, the physical temperature of the feed horn has been as low as -40°C and no degradation in radiometric performance was observed.

Chapter 4

IF Spectrometer

As described in Chapter 1, the PolarCube radiometer is a total power superheterodyne radiometer with a waveguide-based RF front end (Figure 1.3). Following downmixing of electromagnetic radiation received over a 13 GHz bandwidth about the 118.75 GHz O₂ resonance with a Virginia Diodes Inc. (VDI) double sideband sub-harmonic mixer, and intermediate frequency (IF) power amplification with a 6.5 GHz bandwidth MITEQ IF low noise amplifier (LNA), an IF spectrometer detects, amplifies and digitizes this IF power over eight spectral bands. This chapter describes the design and performance of this microwave and audio frequency circuitry that comprises of an intermediate frequency (IF) and video amplifier (VA) module on a four-layer hybrid printed circuit board (PCB) connected to the output of the IF LNA via a short 3.5 mm coaxial (SMA) cable. The PCB is described as hybrid because:

- the top two IF layers (microwave frequency signal and analog ground) are etched on a 20 mil RO4350BTM Rogers Duroid high frequency hydrocarbon ceramic laminate [74], and
- the bottom two layers (audio frequency signal and analog+digital ground) are etched on the commonly used FR-4 glass epoxy copper-clad laminate.

The RO4350BTM is a low loss substrate with a dielectric constant ϵ_r of 3.48 and dissipation factor $\tan \delta$ of 0.0037 at 10 GHz/23°C. The substrate height is 0.508 mm (20 mil) and thickness of the copper cladding is 17 μm (0.67 mil). The 50 Ω transmission line is designed as a coplanar waveguide (CPW) ground in the NI AWR RF/Microwave circuit design simulator [75] (Figure 4.1).

The IF comprises of an 8-channel filterbank designed with cascaded duplexers, two-stage MMIC (Monolithic Microwave Integrated Circuit) chip amplification and detector circuitry (Figure 4.2b). Vias are stitched on either side (resembling fence posts) of the transmission lines to minimize mutual coupling between the quasi-TEM (transverse electromagnetic) fields on transmission lines. The original IF and VA circuit boards (with four channels) were built using power dividers and hermetically sealed discrete component LORCH bandpass filters. Although such filters provide excellent bandpass characteristics, two such boards, each requiring a separate metal carrier, are bulky (and heavy), and cannot be supported within the 1.5U CubeSat volume (Figure 4.2a) along with the RF waveguide front-end. The VA section includes two-stage chopper-stabilized operational amplifiers for the eight radiometric channels and analog to digital conversion circuitry. Also located on this side of the four layer PCB is a Samtec LHSM 0.5 mm connector (Figure 4.2c) that mates with a second digital board (Figures 4.2e and 4.2f).

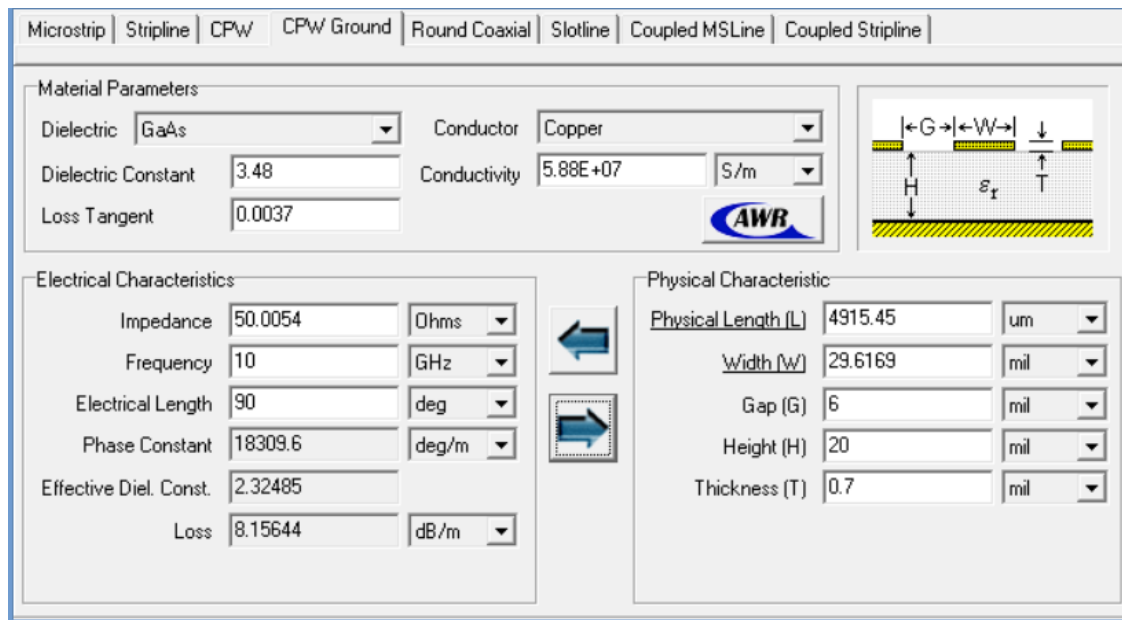
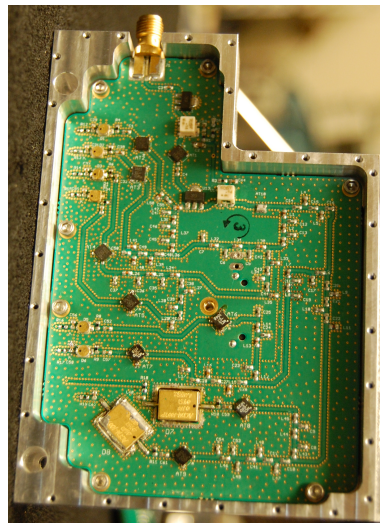


Figure 4.1: Parameters used in the design of the CPW-ground transmission line on a 0.5 oz 20 mil RO4350BTM Rogers Duroid in NI AWR

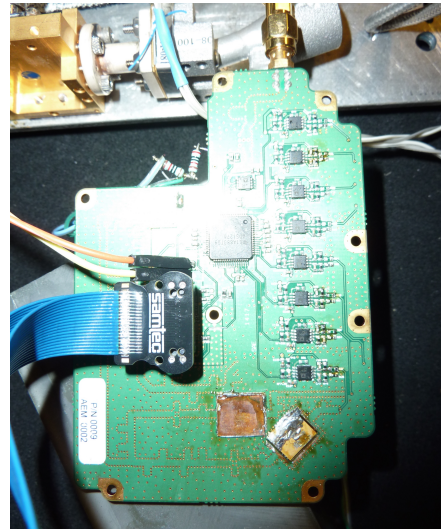
The IF spectrometer and the digital board are enclosed in two separate Aluminum carriers that connect back to back (Figures 4.2d and 4.2e). The carrier body is milled from a single block



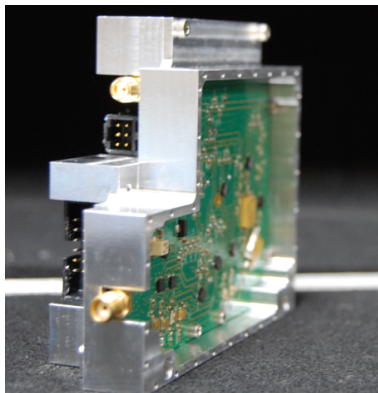
(a)



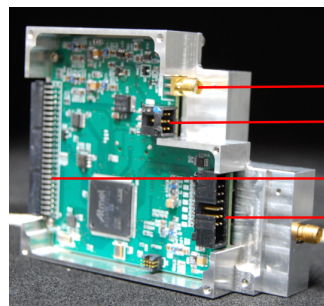
(b)



(c)



(d)



(e)

- 40 mA switching current to PIN diode
- 8V and 5V regulated DC outputs to LNA and DRO
- To satellite BUS
- Thermistor inputs



(f)

Figure 4.2: Pictures of the (a) original four-channel IF and VA PCBs, (b) top side (IF) of the designed 4-layer hybrid PCB within its metal carrier, (c) bottom side (VA) of the PCB (this is a test setup image and includes a Samtec cable that mates with the digital board), (d,e) sideview of the IF and digital carriers, and (f) backside of digital carrier with Samtec connector that mates with the VA side of the hybrid PCB.

of aluminum and includes bosses at the corners to support the PCB. Both carriers have an ~ 1 inch slot for the Samtec connectors. The IF carrier also has an opening for the SMA connector that connect to the LNA while the digital carrier has openings for an SMA connector that connects to the PIN diode, 8 V and 5 V regulated voltage supplies and 50-pin connector to the CubeSat bus. Metal enclosures for these boards precludes coupling of external electromagnetic radiation (i.e) electromagnetic interference (EMI) or radio frequency interference (RFI) with fields generated by the IF, VA or digital PCBs. Aluminum lids are secured to the carriers with metal screws, spaced ~ 1 cm apart, around the carriers' rims. The highest frequency of interest in the IF determines separation between screws. These metal screws act as boundaries for electric fields (forcing them to zero at such points) and hence preclude coupling through the tiny slot (air gap) between the carrier rim and lid.

4.1 Two-stage Amplification

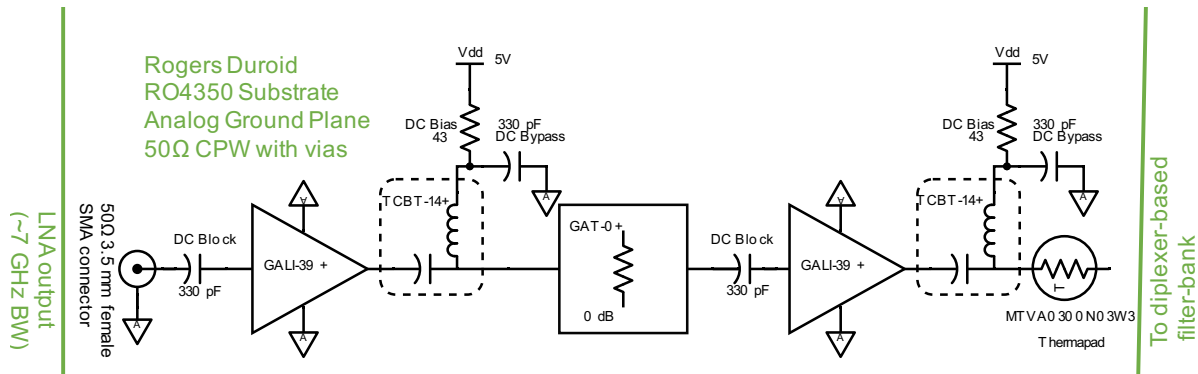


Figure 4.3: Two-stage MMIC amplification on the IF module providing a tapering ~ 40 dB to ~ 20 dB gain between 50 MHz and 6.5 GHz.

The SMA connectorized MITEQ low noise amplifier provides ~ 29 dB power gain over a bandwidth of 6 GHz when operated at 8 V (and ambient temperature). The IF module provides additional power amplification so that the total noise power detected by the tunnel detector diode for each channel falls within the power detector's linear range of operation (maximum sensitivity). Theoretical estimates of the noise power into the IF module can be determined from Table 4.1. Two

Ch #	B_C (MHz)	G_{LNA} (dB)	T_{SYS} (est) (K)	P_N (earth) (dBm)	P_N (cold sky) (dBm)
1	265.72	27.9	2013.6	-80.7	-81.3
2	204.22	28.1	1859.8	-82.2	-82.8
3	674.29	28.3	1716.3	-77.3	-78.0
4	563.00	28.7	1648.2	-78.2	-78.9
5	665.85	29.2	1693.3	-77.4	-78.1
6	676.14	29.9	1704.8	-77.3	-78.0
7	2031.0	30.8	1847.5	-62.3	-62.9
8	2708.7	29.9	1648.2	-71.4	-72.1

Table 4.1: Approximate noise powers at the IF module input estimated from the theoretical receiver noise temperature and measured MITEQ LNA gain for earth and cold space views.

cascaded stages of the Gali-39+ MMIC amplifier (Figure 4.3), each providing ~ 22 dB to ~ 16 dB gain between 50 MHz and 7 GHz, have been used to achieve the additional gain necessary after the MITEQ IF LNA (Figure 4.3) for linear power detection. Note that the gain of the Gali-39+ chip rolls off at higher frequencies, as observed in the measurement of the filterbank response (Figure 4.2). In order to minimize power dissipation in the bias resistor (R_b), the amplifiers are biased at 5 V (V_{dd}) for a 3.5 V device operating voltage (V_d) and 35 mA device operating current (or bias current I_b). The value of the bias resistor needed can be easily determined using:

$$R_b = (V_{dd} - V_d(T, I_b))/I_b \quad (4.1)$$

It is noted that the device operating voltage V_d is a function of the bias current I_b and component temperature T . If V_o is the y-intercept in a plot between device operating voltage and bias current at room temperature T_o , then:

$$V_d(I_b, T) = V_o + \frac{\Delta V_d}{\Delta I_b} I_b + \frac{\Delta V_d}{\Delta T} (T - T_o) \quad (4.2)$$

By substituting (4.1) in (4.2),

$$I_b = \frac{V_{dd} - V_o - \frac{\Delta V_d}{\Delta T} (T - T_o)}{R_b + \frac{\Delta V_d}{\Delta I_b}} \quad (4.3)$$

An expression for the variation of bias current with temperature is determined by differentiating

(4.3) with respect to temperature (4.4):

$$\frac{\Delta I_b}{\Delta T} = (\frac{\Delta V_d}{\Delta T}) / (R_b + \frac{\Delta V_d}{\Delta I_b}) \quad (4.4)$$

Substituting values for $\frac{\Delta V_d}{\Delta T}$ (-2.5 mV/°C) and $\frac{\Delta V_d}{\Delta I_b}$ (2.9 mV/mA) from the specification sheet for the Gali-39+ (at 35 mA bias current and 25 °C), the change in bias current with temperature $\frac{\Delta I_b}{\Delta T}$ is found to be -0.055 mA/°C. (The negative sign means that the bias current and hence, amplifier gain decreases with increasing temperature.) Over an operating temperature range of -40 °C to +55 °C, the bias current varies by 5.2 mA. This causes the gain to decrease by ~0.5 dB at the highest temperature and a similarly increase by ~0.5 dB at the lowest temperature. To compensate for such gain variation due to temperature fluctuations as well as bias resistor tolerance and supply voltage fluctuations, a temperature variable chip attenuator (thermapad) with a negative temperature coefficient of attenuation is installed after the two-stage chip amplification circuitry.

The DC bias circuit for the amplifier uses the TCBT-14+ bias tee. The equivalent inductance of such a wideband choke is 1 μ H at 100 mA. While a commercially available inductor of such small inductance has a series resonant frequency (SRF) <100 MHz, the RF choke can be used upto 8 GHz. The DC blocking capacitor at the input to the Gali-39+ must have low effective series resistance (ESR) and no parasitic resonance upto the highest operating frequency. The precautionary bypass capacitor prevents stray coupling between the bias line and other components. It is emphasized that manufacturer footprints for such MMICs have been optimized for best performance and these layouts have been exactly followed to obtain optimum gain and prevent parasitic oscillations.

4.2 Cascaded Diplexer Based Filterbank

The eight channel filterbank (50 MHz to 7 GHz, bandwidths between 250 MHz and 2.2 GHz) is designed with seven contiguous cascaded diplexers implemented as coplanar waveguide/lumped element combinations. The lumped elements used were inductors and capacitors available as 0402 surface mount components (SMC) in the market. All diplexers are designed [76] as parallel connected, partly complementary structures with foreshortened, doubly terminated second order

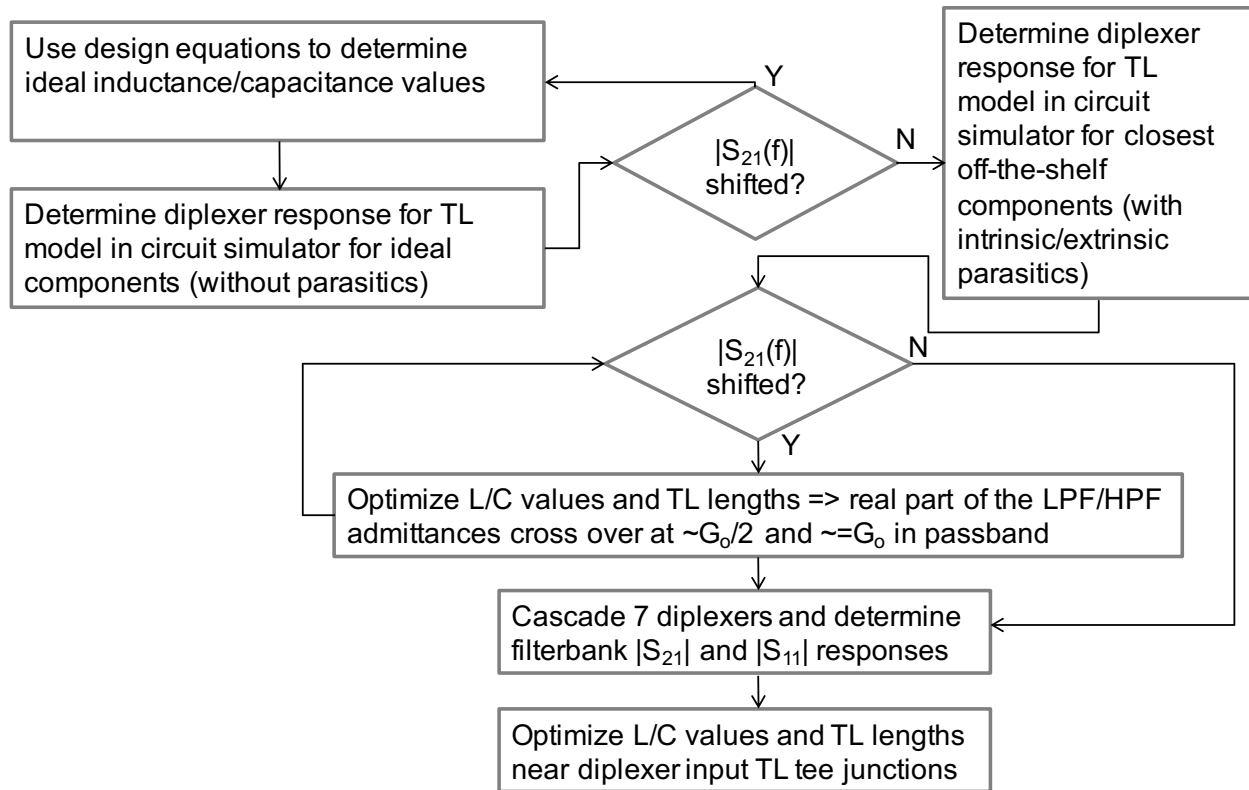


Figure 4.4: Procedure to design the eight-channel cascaded diplexer-based filterbank.

Chebyshev low and high pass filters (LPF and HPF). A complementary diplexer is one where the low and high pass filters are connected in parallel and have complementary input admittances (i.e., the sum of their input admittances is real and constant for all frequencies). It should be noted that only minimum reactance and minimum susceptance networks can be made complementary. A minimum reactance network is one whose input impedance is finite for all real frequencies while for a minimum susceptance network, its input admittance is finite for all real frequencies. An important property of minimum reactance and susceptance networks is that there exists a mathematical relationship between the real and imaginary parts of the input impedance (or susceptance). The component values for the diplexers are chosen such that the real part of the admittances of the low and high

pass filters cross over at approximately one-half the source conductance G_o and are \sim equal to G_o within its passband. So, as the input admittance is nearly constant within the passband, the input reactance is approximately zero [77]. The diplexer is hence matched to the source for all frequencies of interest. The true component values were obtained using an iterative process as delineated in the flowchart shown in Figure 4.4 because of the following reasons:

- presence of unavoidable intrinsic parasitic inductances and capacitances of the off-the-shelf 0402 SMCs,
- inductances and capacitances associated with the short lengths of coplanar waveguides between the lumped elements on the RO4350 substrate,
- availability of SMCs of specific denominations only- for e.g., the smallest value of an 0402 inductor that CoilCraft manufactured at the time of design was 1 nH, and
- tolerance of SMCs available in the market.

A model of a single diplexer simulated in the NI AWR microwave circuit simulator [75] is shown in Figure 4.5b. The ModeLithics[©] library [78] was used to model the SMCs. After achieving a reasonable simulated response for the filterbank, the design was first implemented on the 4350B[™] Rogers Duroid substrate as a two layer PCB. Measured and simulated responses of the IF filterbank are shown in Figure 4.2. Although not perfect, the filterbank responses have good separation between channels and acceptable bandwidths. Thermal tests (-18 °C to +50 °C) to determine the sensitivity of the IF board to temperature variations indicated responses that were stable and gain variations within acceptable limits that could be corrected with thermopads. A comparison between the atmospheric temperature weighting functions [3] over polar ocean for nadir observation (Figure 4.8b) (computed with an in-house microwave radiative transfer program [31] using both measured and simulated filterbank responses indicates close agreement between the two cases. The weighting functions sample from the surface to \sim 18 km in altitude and can hence subsequently enable retrieval of a 3D temperature map of the earth's lower atmosphere from the

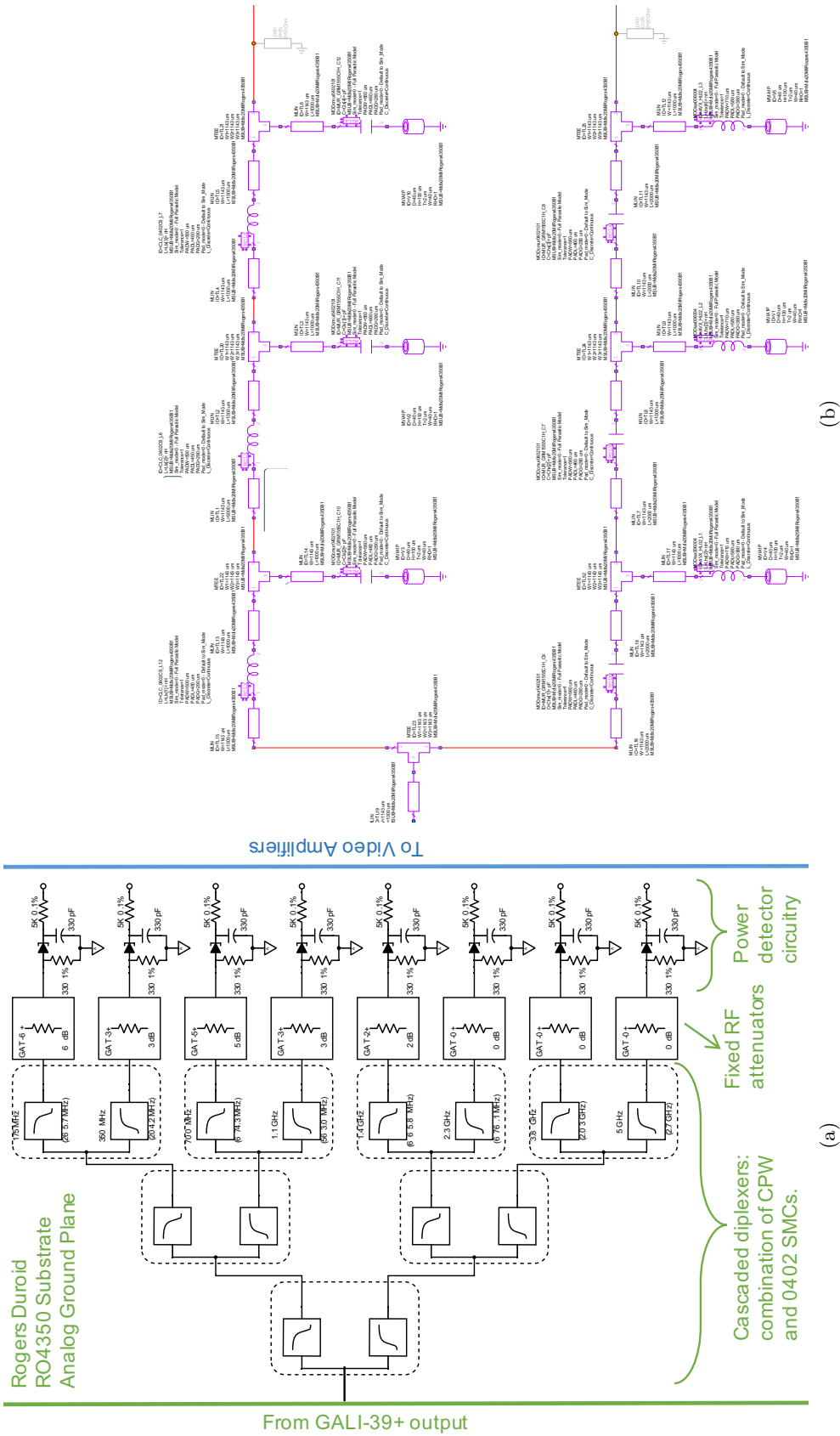


Figure 4.5: Figures represent (a) schematic of the eight-channel cascaded diplexer-based filterbank (including detector circuitry), and (b) circuit model of a single diplexer used in designing the filterbank.

instrument brightness temperature measurements. The convolutional bandwidths (4.14) for the eight radiometric channels are tabulated in Table 4.9b. These bandwidths have been estimated using the measured frequency response (Figure 4.9a) and theoretical estimates of the system noise temperature (Table 4.1).

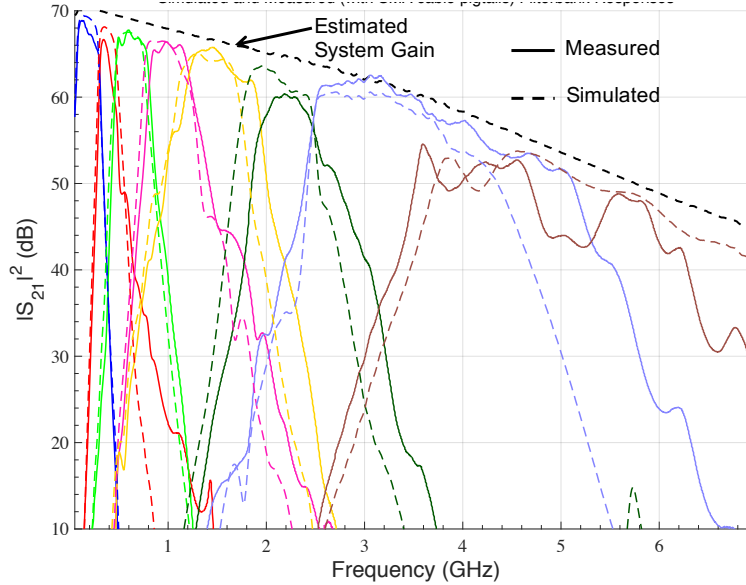


Figure 4.7: Comparison between the simulated and measured spectral passband responses of the IF filterbank on the two-layer RO4350B PCB. Measurements were taken using the setup shown in Figure 4.8c.

4.3 Linear Zero Bias Power Detection

Total noise spectral power at the output of each channel of the IF filterbank is detected by a zero-bias tunnel detector diode. Let $v_B(t)$ be the voltage signal at the diode input. The voltage at the output of the tunnel diode power detector circuit before low pass filtering is $v_D(t) = v_B(t)v_B(t)$. Its autocorrelation function $R_{v_D}(\tau)$ can be derived (assuming $v_B(t)$ to be a continuous, zero-mean Gaussian random variable) as [79]:

$$R_{v_D}(\tau) = R_{v_B}^2(0) + 2R_{v_B}^2(\tau) = \left[\int_{-\infty}^{+\infty} S_{v_B}(f)df \right]^2 + 2R_{v_B}^2(\tau) \quad (4.5)$$

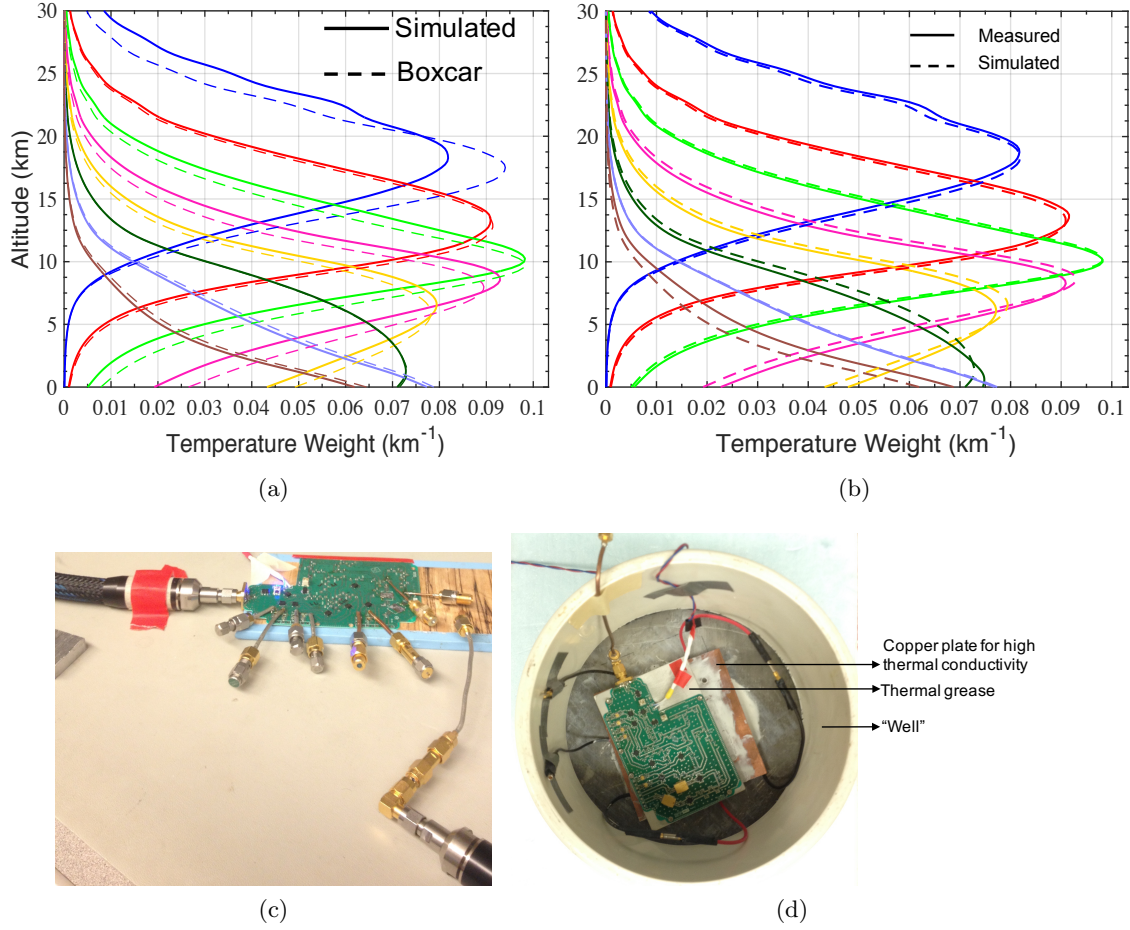


Figure 4.8: For the two-layer IF PCB: Weighting functions generated using IF passband responses from the AWR simulation and (a) boxcar response, (b) measurement; (c) setup for filterbank response measurement, and (e) IF thermal response measurement setup using thermoelectric Peltier chips.

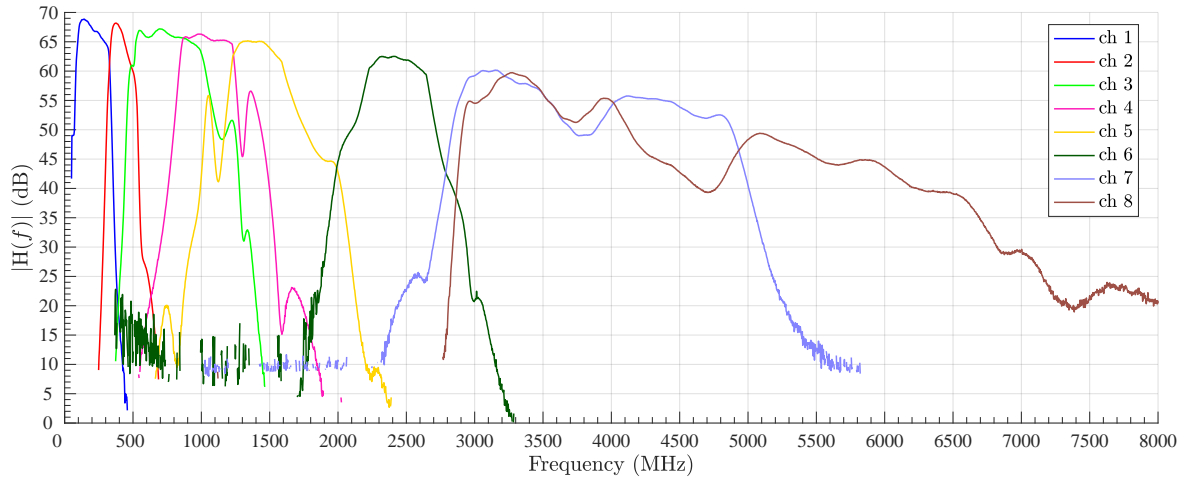
Applying the Weiner-Khinchine theorem, the two-sided power spectral density at the detector output is:

$$S_{v_D}(f) = \left[\int_{-\infty}^{+\infty} S_{v_B}(f) df \right]^2 \delta(f) + 2S_{v_B}(f) * S_{v_B}(f) \quad (4.6)$$

where,

$$S_{v_B}(f) = \frac{1}{2} k_B T_{SYS}(f) G_{SYS}(f) |H_{BPF}(f)|^2 \quad (4.7)$$

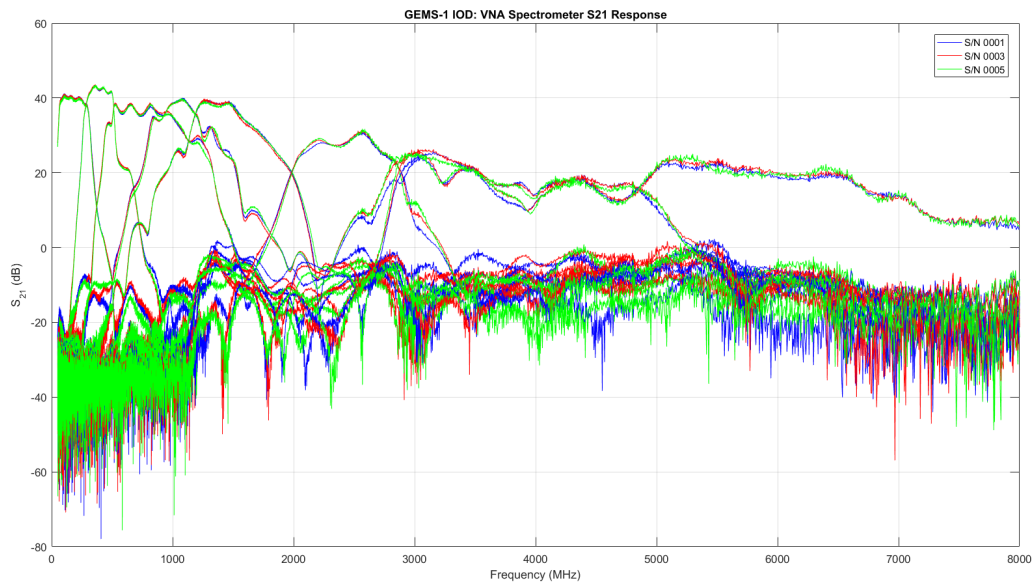
$T_{SYS}(f)$ and $G_{SYS}(f)$ are system noise temperature and gain. $|H_{BPF}(f)|$ indicates the spectral response of a radiometric channel after the IF LNA, while $G_{SYS}(f)$ includes the all front-end gains



(a)

Ch #	1	2	3	4	5	6	7	8
B_C (MHz)	265.72	204.22	674.29	563.00	665.85	676.14	2031.0	2708.7
ΔT_{rms} (K) (theoretical)	2.22	2.36	1.21	1.28	1.21	1.20	0.74	0.58

(b)



(c)

Figure 4.9: The four-layer IF filterbank: (a) normalized spectral response of the MiniRad IF spectrometer module measured via a slow frequency sweep between 50 MHz and 8 GHz, (b) convolutional bandwidths and theoretical ΔT_{rms} ($\tau_i = 4.096$ ms) for the eight IF channels, and (c) measured ($|S_{21}|^2$) spectral responses on three additional identical IF PCBs with a high frequency calibrated probe connected to a vector network analyzer.

and losses as a function of frequency. A first order RC low pass filter is part of the detector circuit with an RC time constant τ_D chosen such that its cutoff frequency is much less than the convolutional bandwidth of the IF filter. Therefore, due to low pass filtering, the tunnel diode output voltage v_o only includes spectral content in the audio frequency range (bandwidth < 10 kHz). The spectrum of v_o (assuming a box car filter) is then:

$$\begin{aligned}
S_{v_o}(f) &= S_{v_D}(f)|H_{BPF}(f)|^2 \simeq S_{v_D}(f)[\tau_D^2 \text{sinc}^2(f\tau_D)] \\
&= \left[\int_{-\infty}^{+\infty} \frac{1}{2} k_B T_{SYS}(f) G_{SYS}(f) |H_{BPF}(f)|^2 df \right]^2 [\tau_D^2 \text{sin}^2(f\tau_D)] \delta(f) \\
&\quad + 2 \left\{ \frac{1}{2} k_B T_{SYS}(f) G_{SYS}(f) |H_{BPF}(f)|^2 \right\} [\tau_D^2 \text{sin}^2(f\tau_D)] \\
&\quad * \left\{ \frac{1}{2} k_B T_{SYS}(f) G_{SYS}(f) |H_{BPF}(f)|^2 \right\} [\tau_D^2 \text{sin}^2(f\tau_D)] \tag{4.8}
\end{aligned}$$

The mean and standard deviation of the low pass filtered detected output voltage $\langle v_o(t) \rangle$ and σ_{v_o} can be approximated as:

$$\begin{aligned}
\langle v_o(t) \rangle &= (\text{DC power in } S_{v_o}(f))^{1/2} \tag{4.9} \\
&= \frac{1}{2} k_B \tau_D \int_{-\infty}^{+\infty} T_{SYS}(f) G_{SYS}(f) |H_{BPF}(f)|^2 df
\end{aligned}$$

$$\begin{aligned}
\sigma_{v_o} &= (\text{AC power in } S_{v_o}(f))^{1/2} \tag{4.10} \\
&= \sqrt{\langle (v_o(t) - \langle v_o(t) \rangle)^2 \rangle} \\
&= \sqrt{\frac{1}{2} k_B^2 \tau_D \int_{-\infty}^{+\infty} T_{SYS}^2(f) G_{SYS}^2(f) |H_{BPF}(f)|^4 df}
\end{aligned}$$

Thus, the relative sensitivity of the direct detection radiometer is

$$\frac{\sigma_{v_o}}{\langle v_o(t) \rangle} = \sqrt{\frac{2 \int_{-\infty}^{+\infty} T_{SYS}^2(f) G_{SYS}^2(f) |H_{BPF}(f)|^4 df}{\tau_D \left(\int_{-\infty}^{+\infty} T_{SYS}(f) G_{SYS}(f) |H_{BPF}(f)|^2 df \right)^2}} \quad (4.11)$$

$$= \sqrt{\frac{\int_0^{+\infty} T_{SYS}^2(f) G_{SYS}^2(f) |H_{BPF}(f)|^4 df}{\tau_D \left(\int_0^{+\infty} T_{SYS}(f) G_{SYS}(f) |H_{BPF}(f)|^2 df \right)^2}} \quad (4.12)$$

$$= \frac{1}{\sqrt{B_C \tau_D}} \quad (4.13)$$

where B_C , the convolutional bandwidth of any radiometric channel is defined as

$$B_C = \frac{\left(\int_0^{+\infty} T_{SYS}(f) G_{SYS}(f) |H_{BPF}(f)|^2 df \right)^2}{\int_0^{+\infty} T_{SYS}^2(f) G_{SYS}^2(f) |H_{BPF}(f)|^4 df} \quad (4.14)$$

Off-the-shelf zero-bias tunnel diodes have been used for IF power detection. The M-Pulse MP1004 detectors were chosen for channels 1 to 6 while for channels 7 and 8, the ACTM-1007P detectors by Advanced Control Components Inc. which have a higher broadband sensitivity at frequencies ≥ 2 GHz were used. The approximate sensitivities of these diodes were estimated from specifications and laboratory tests to be $\sim 1000 \mu\text{V}/\mu\text{W}$ (narrow band, ≤ 2 GHz) and $\sim 750 \mu\text{V}/\mu\text{W}$ (broadband, ≥ 2 GHz) respectively. These tunnel diodes exhibit a narrow linear range of operation around the -23 dBm ($\sim 5 \mu\text{W}$) input power level (Figure 4.10) for which the mean detected output voltage expected is expected to be between 4 mV and 7 mV. A fixed attenuator is hence installed just before the tunnel diode for each channel that needs to be carefully tuned to optimize the input power to the diode.

4.4 Video Amplification Post Detection

The video amplifier side of the PCB (Figures 4.6 and 4.12) is essentially a low noise, signal conditioning operational amplifier (op-amp) circuit that provides voltage amplification to the microvolt level detected voltage in each channel with minimal noise contribution. The op-amp

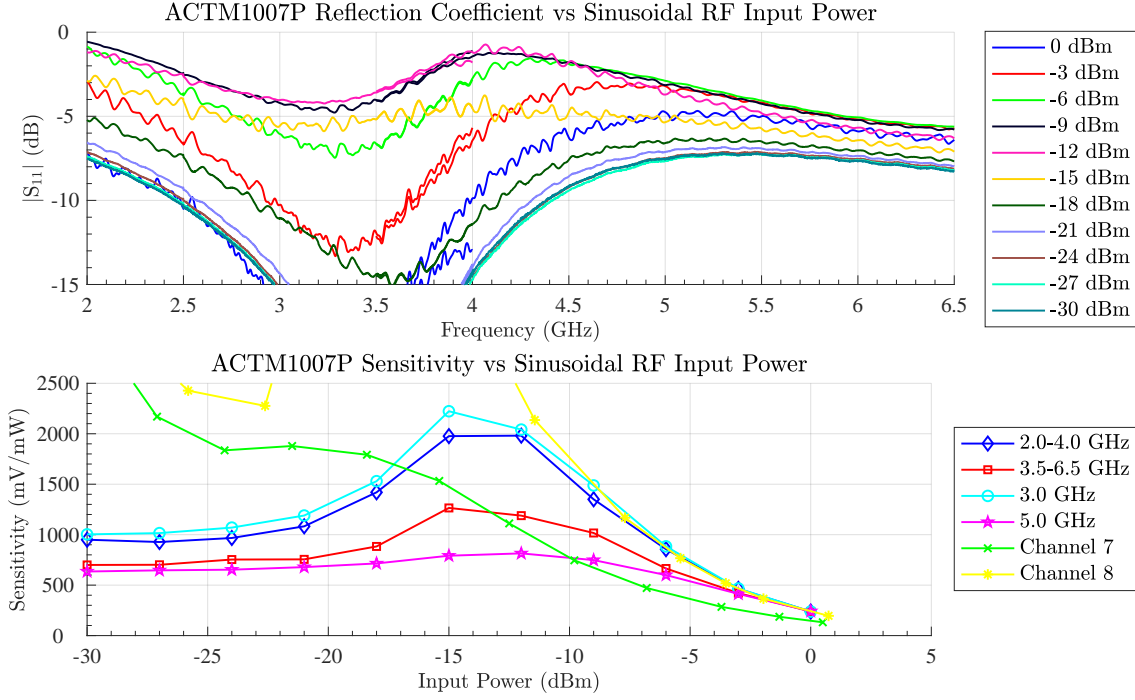


Figure 4.10: Tunnel diode sensitivities and reflection coefficients measured with sinusoidal inputs of varying frequency and power.

Channel	1	2	3	4	5	6	7	8
Attenuation (dB)	6	3	5	3	2	0	0	0
Measured detected output voltage $\langle v_o(t) \rangle$ (mV)	-4.982	-6.442	-6.632	-6.183	-7.06	-6.082	+5.465	+4.002
Estimated power into diode (dBm)	-23.0	-22.8	-21.7	-22.0	-21.5	-22.0	-22.6	-24.0

Table 4.2: Fixed attenuators installed before the tunnel diodes and the detected output voltage.

is designed as a unipolar differential op-amp that converts the single-ended input voltage to a differential signal in order to connect to the differential input of an analog to digital converter (ADC). Reference voltages V_{ee} for all eight op-amps is provided by a unity gain amplifier. The same 5 V regulated supply V_{cc} that powers the ADC also powers the op-amps. This design step ensures that any small fluctuations in the supply voltage also manifests itself on the op-amp reference voltages as well as the negative inputs of the ADC (Figure 4.11). In addition to providing a total

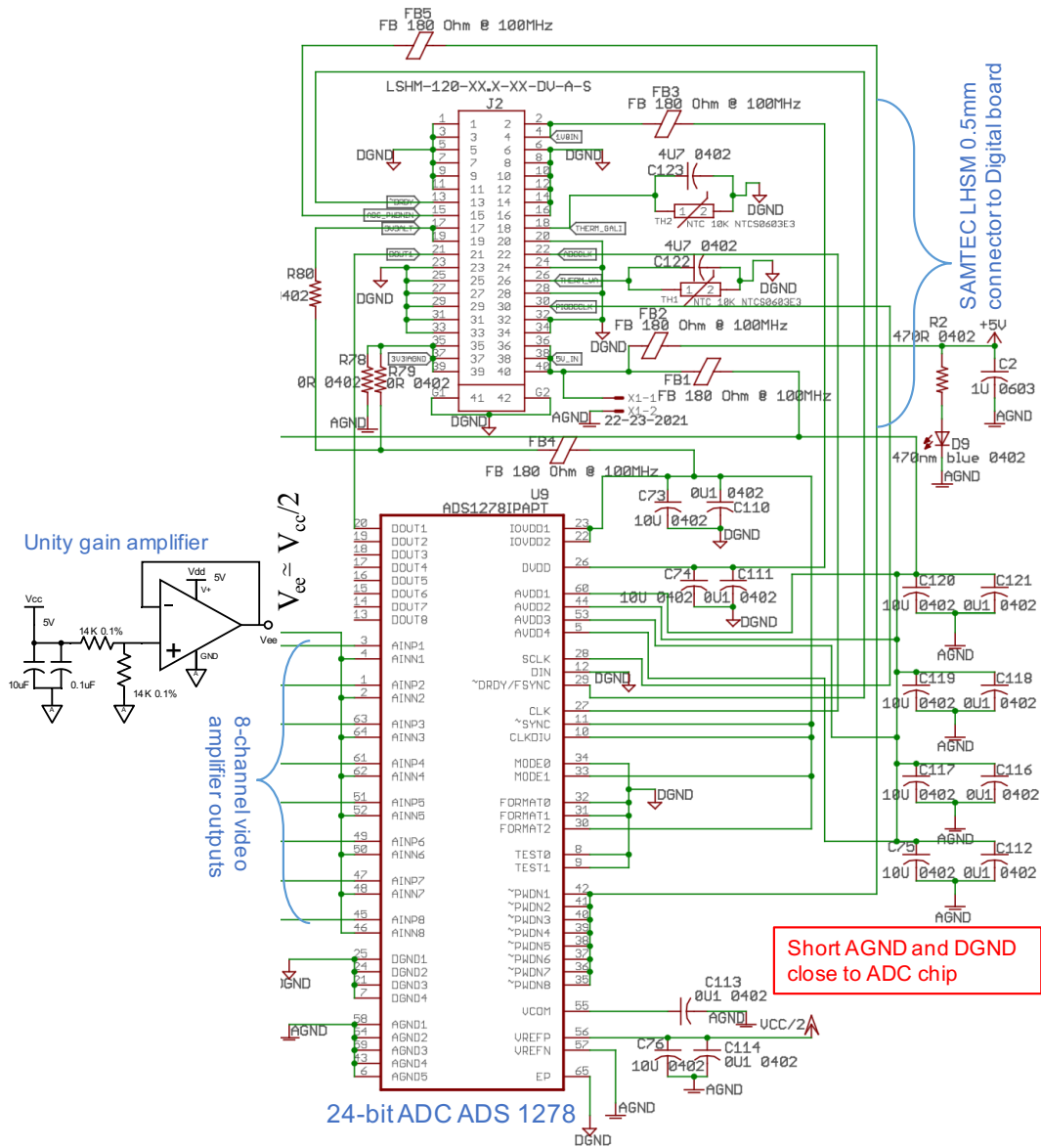


Figure 4.11: Schematic of the ADC circuitry (including the Samtec connector) on the VA side of the IF spectrometer is shown. The unity gain amplifier and the ADC negative inputs are also shown.

voltage gain of ~ 100 , the second-stage of the video amplifier includes a first order RC low pass filter whose time constant τ_D determines the extent to which adjacent samples are correlated after digitization. The op-amp selected to build this signal conditioning circuitry is the ADA4528-2 [80], a two-stage chopper-stabilized op-amp with a chopping frequency of 200 kHz (well above the low bandwidth of the input signal). This chopper architecture suppresses unwanted offset voltage and $1/f$ noise without perturbing the desired input baseband signal. As the satellite will experience temperatures between $-25\text{ }^\circ\text{C}$ and $+40\text{ }^\circ\text{C}$ in orbit, it is necessary to ensure that the op-amp output voltage remains well within operating range with minimal drift between these temperature extremes. With an offset voltage drift of $2\text{ nV}/^\circ\text{C}$, the op-amp's offset voltage will drift by $\sim 0.13\text{ }\mu\text{V}$ over the $65\text{ }^\circ\text{C}$ temperature range.

4.4.1 Video Amplifier Noise Contribution

Due to the chopping technique, the ADA4528-2 [80] has low $1/f$ voltage and current noise levels: $\langle v_n^{pp} \rangle$ and $\langle i_{nn}^{pp} \rangle$ (or $\langle i_{np}^{pp} \rangle$) of 99 nV and 10 pA peak to peak respectively, measured between 0.1 Hz and 10 Hz. Otherwise, its typical voltage and current noise densities, v_n and i_{nn} (or i_{np}) are $5.9\text{ nV}/\sqrt{\text{Hz}}$ and $0.5\text{ pA}/\sqrt{\text{Hz}}$ respectively (measured at 1 kHz). It is essential to consider the Johnson thermal noise generated within the external input source resistances in addition to input voltage or current noise in order to maintain low total output noise introduced due to the video amplifier circuit [81].

Source	R_1	R_2	R_3	R_4	R_5	R_6	R_7
(k Ω)	10	100	10	100	4	100	3.85
(μV)	136.14	43.05	136.14	13.61	8.28	1.66	8.45

Table 4.3: Thermal noise voltage (referred to the output) contributions due to the source resistances ($\pm 0.1\%$ tolerance).

Consider the schematic in Figure 4.12. The circuit diagram depicts thermal noise due to resistors as voltage noise sources. It also indicates the op-amp's inherent voltage and current noise sources at the input of the op-amp. Its input offset voltage and current are depicted as

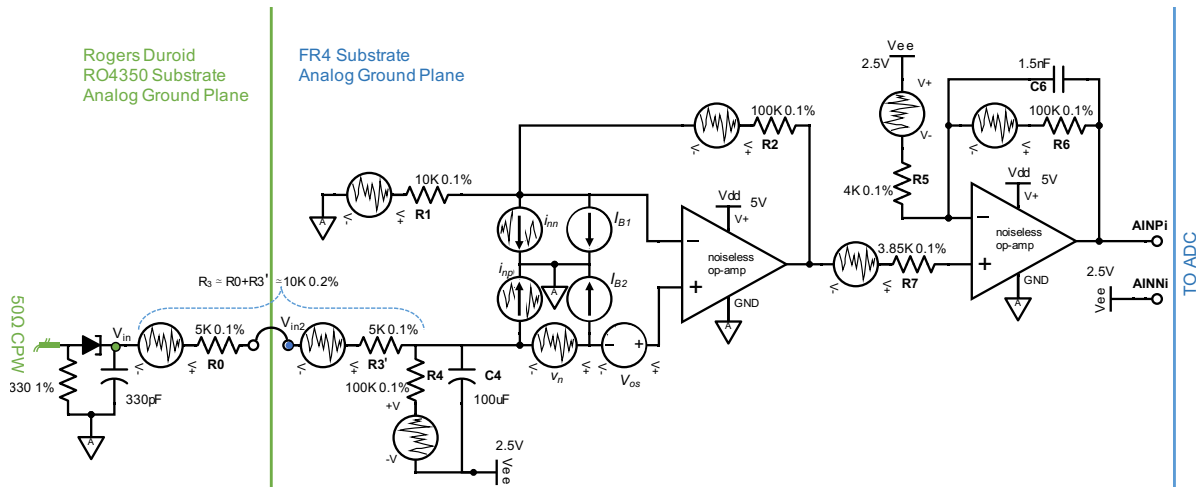


Figure 4.12: Noise analysis of the dual op-amp ADA4528-2 for a single radiometric channel.

Noise type	Noise source	Specification	Integrated noise voltage
Broadband white noise	v_n	5.9 nV/ $\sqrt{\text{Hz}}$	68.89 μV
	i_{nn}	0.5 pA/ $\sqrt{\text{Hz}}$	53.07 μV
	i_{np}	0.5 pA/ $\sqrt{\text{Hz}}$	53.07 μV
Low frequency noise (0.1-10 Hz)	$\langle v_n^{pp} \rangle$	99 nV	28.31 μV
	$\langle i_{nn}^{pp} \rangle$	10 pA	26.0 μV
	$\langle i_{np}^{pp} \rangle$	10 pA	26.0 μV

Table 4.4: Noise contributions due to the op-amp's inherent noise sources.

DC voltage and DC current sources (respectively). The standard deviation of the thermal noise voltage generated by a resistor of resistance R_o at temperature T_o is given by $\sqrt{4k_B T B R}$ where k_B is the Boltzmann constant and B the signal bandwidth. Noise due to each source resistance can be calculated separately and all contributions added using the superposition theorem used in DC network analysis of circuits. If the first and second stage inverting and non-inverting gains are

represented as G_{1m} , G_{1p} , G_{2m} and G_{2p} , the total voltage noise due to all noise sources is:

$$\begin{aligned}
V_o^n = & \left\{ 4k_B T_o B_{NE} \left[R_1 (G_{1m} G_{2p})^2 + R_2 G_{2p}^2 + R_3 \left(\frac{R_4}{R_3 + R_4} G_{1p} G_{2p} \right)^2 \right. \right. \\
& + R_4 \left(\frac{R_3}{R_3 + R_4} G_{1p} G_{2p} \right)^2 + R_5 G_{2m}^2 + R_6 + R_7 G_{2p}^2 \left. \right] \\
& + 4k_B T_o B_{NE} \left[(v_n G_{1p} G_{2p})^2 + (i_{nn} R_2 G_{2p})^2 + \left(i_{np} \frac{R_3 R_4}{R_3 + R_4} G_{1p} G_{2p} \right)^2 \right] \\
& + (\langle v_n^{pp} \rangle G_{1p} G_{2p})^2 + (\langle i_{nn}^{pp} \rangle R_2 G_{2p})^2 + \left. \left(\langle i_{np}^{pp} \rangle \frac{R_3 R_4}{R_3 + R_4} G_{1p} G_{2p} \right)^2 \right\}^{1/2} \quad (4.15)
\end{aligned}$$

The effective noise bandwidth (B_{NE}) of the op-amp (with a first order RC filter) for white noise is $\frac{\pi/2}{(2\pi R_6 C_6)}$. The $1/f$ noise bandwidth is approximated as $f_{nc} \ln(B_{NE})$ where f_{nc} is the op-amp corner frequency. Using the first seven terms in equation (4.15), the total thermal noise voltage (referred to the output) contributed by the source resistances ($\pm 0.1\%$ tolerance) is estimated to be $227.6 \mu\text{V}$. For nominal radiometer sensitivity of $\sim 0.8 \text{ mV/K}$, the noise temperature contribution is $\sim 0.3 \text{ K}$. Note that this number is required to be lower than the radiometer noise ΔT_{rms} . Noise voltage (referred to the output) contributions due to the inherent op-amp noise voltage and current sources can be calculated from the last six terms of equation (4.15). The total broadband noise contribution $\sim 175 \mu\text{V}$ is lower than the total thermal noise generated by the source resistances ($227.6 \mu\text{V}$) by $\sim 52 \mu\text{V}$. Also, due to the chopper stabilization, the total low frequency noise is only $80.3 \mu\text{V}$. Assuming an approximate radiometer gain of 0.8 mV/K , noise temperature contribution due to the op-amp's inherent noise is $\sim 0.32 \text{ K}$. Tables 4.3 and 4.4 summarize the noise voltage contributions (referred to the output) due to the various noise sources. It is noted that the thermal noise due to the source resistances in series with the op-amp inputs contribute more than twice the internal noise voltage generated by the chopper stabilized op-amp itself. Hence, values chosen for these source resistances should be kept in mind when designing the video amplifier so that their noise contributions are not higher than the inherent op-amp noise.

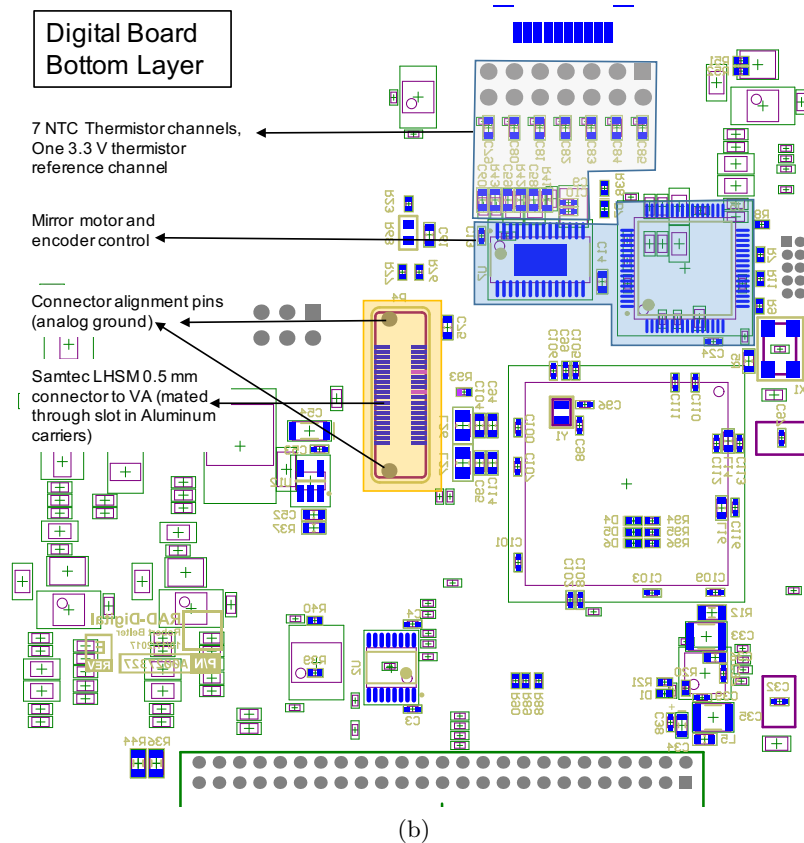
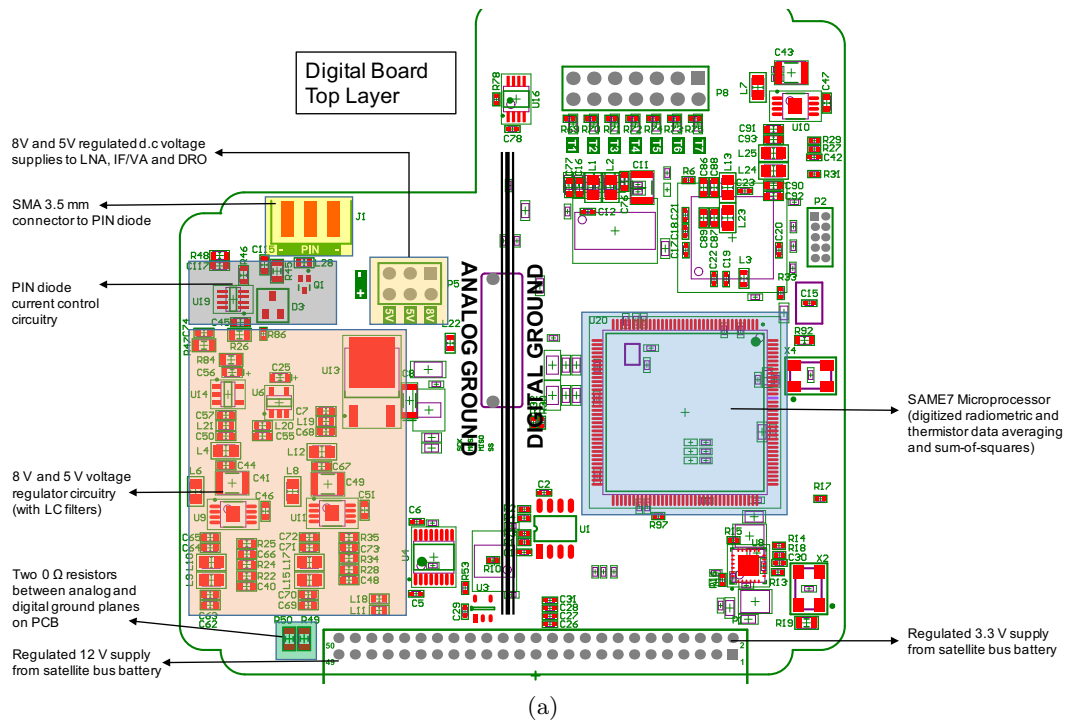


Figure 4.13: Annotated layout diagrams of the top and bottom layers of the digital board are shown: (a) the top layer includes power regulation and radiometric data acquisition circuitry, and (b) the bottom layer mainly consists of mirror motor control circuitry and motor encoder data acquisition.

4.5 Data Digitization and Acquisition

After amplification and low-pass filtering, the detected analog voltage samples are digitized using TI's ADS 1278, a 24-bit analog-to-digital converter. The digitized samples are transmitted to a microprocessor on the digital board (Figure 4.13) via the Samtec connector. The primary functions of the digital board are as follows:

- (1) Provision of regulated supply voltage/current from 12 V satellite bus battery:
 - (a) 5 V and 8 V supply voltages (referred to analog ground) to the dielectric resonator oscillator and the low noise amplifier respectively.
 - (b) Stable 40 mA switching current to the PIN diode during calibration.
 - (c) 5 V supply voltage (referred to analog ground) to the ADC, video amplifiers and IF MMIC amplifiers through the Samtec connector.
 - (d) 3.3 V and 1.8 V supply voltages (referred to digital ground) to the ADC through the Samtec connector.
 - (e) Lowpass LC π -section filters at the inputs and outputs of the Buck regulator ICs to filter transients introduced due to the switching operation.
- (2) Data acquisition with an Atmel 32-bit SAM E70 microprocessor:
 - (a) Acquire digitized data across all radiometric channels from the ADC (via the Samtec connector) and obtain 16-sample sums and sum-of-squares radiometric data records.
 - (b) Acquire thermistor data from six leaded NTC thermistors (Figure 5.6a) and three chip NTC thermistors (routed via the Samtec connector).
 - (c) Acquire 3.3 V reference voltage measurements across a 10 k Ω power divider along with thermistor samples for calibrating the NTC thermistor measurements.
- (3) Mirror motor control and motor encoder data acquisition: The Faulhaber brushless DC motor with a 12-bit absolute encoder is controlled with a second slave microcontroller and

motor driver circuit that aims to maintain mirror spin rate at ~ 1 rps.

The digital acquisition and motor control circuitry, and microprocessor programming were implemented by several undergraduate students at the Colorado Space Grant Consortium. The author was extensively involved with the power supply regulation circuitry design and output voltage accuracy, and the thermistor circuitry development. A considerable amount of time was also spent in debugging grounding issues at the ADC and digital board that caused milli-volt level fluctuations between the analog and digital ground levels.

A single data record output from the microprocessor comprises of the system time, GPS time, 24-bit 16-sample radiometric sum and sum-of-squares counts for the eight radiometric channels, 12-bit thermistor counts for the nine thermistors, one 12-bit count of the thermistor reference voltage, the PIN diode switch state, and the motor encoder count indicating mirror angular position.

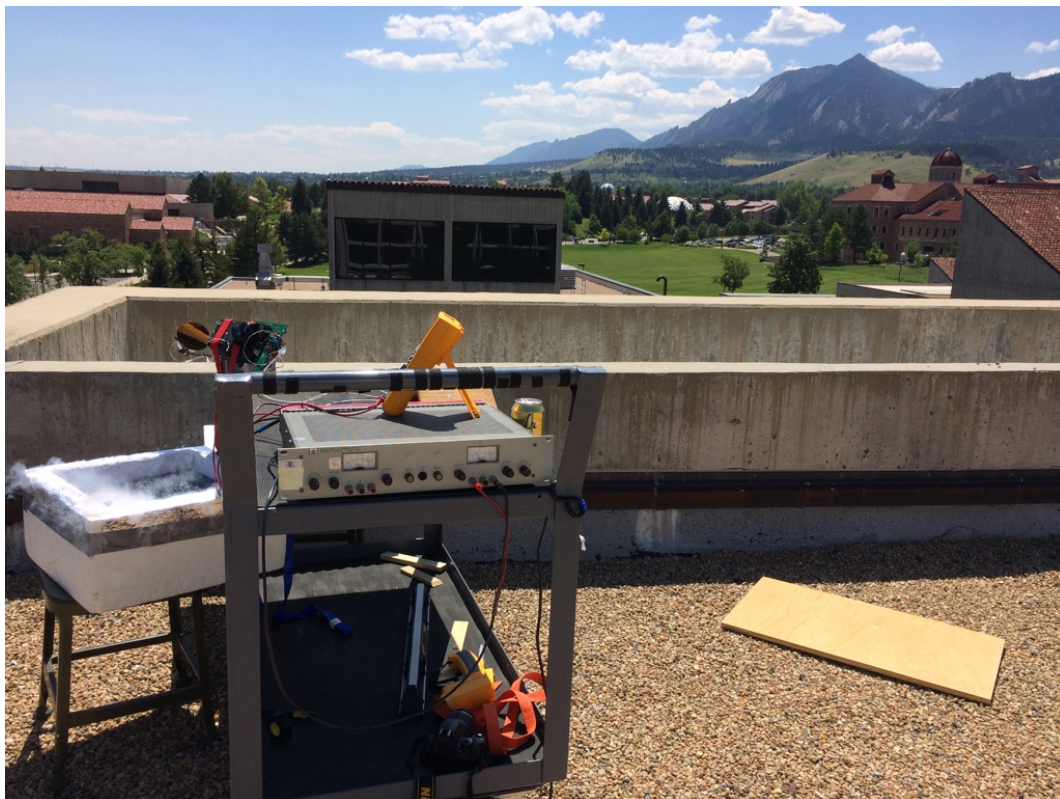


Figure 4.14: Configuration of a preliminary rooftop test against the backdrop of the Flatirons at the University of Colorado, Boulder.

Chapter 5

Prelaunch Testing and Calibration

The necessity for and, the theory behind prelaunch calibration has been detailed in §1.5. This chapter describes several measurements and experiments that were conducted on the 118 GHz radiometer to ensure its precise prelaunch calibration that will enable accurate retrieval of Level-1 calibrated brightness temperature data from instrument measurements.

5.1 Airborne Experiments over Antarctica

The MiniRad radiometer was provided with a last-minute opportunity to be part of NASA's IceBridge (OIB) experiment [62] as a "piggyback" airborne instrument aboard the NASA DC-8. The mission comprised of multiple flights over the Antarctic continent between October 24 and November 02, 2016. The purpose of the IceBridge program itself was to permit measurements at the poles by multiple airborne remote sensing instruments to fill in a crucial gap left between the end of the ICESat-1 mission and the launch of ICESat-2. In order to avail this opportunity, all sub-systems of the radiometer (which was in a bench-top configuration at the time) had to be assembled and tested for the first time in a duration of six weeks. The primary objective of this experiment was to demonstrate the imaging capabilities of the low-cost MiniRad radiometer including the millimeter wave 3D-printed horn (for the first time) with a scanning reflector, and an in-house designed IF spectral filterbank built with off-the-shelf surface mount components. For the OIB experiment, each recorded radiometric measurement is a sum of 20 digital samples where a sample is digitized every $256 \mu\text{s}$ and data is recorded on an SD card.

After Y-factor tests in the laboratory for gain and offset tuning, the integrated system (Figure 5.2a) was tested atop the roof of the university’s engineering building (Figure 5.2b) that would permit $\sim \pm 70^\circ$ unobstructed views of the Boulder sky for the spinning reflector. Two external targets, an absorber at ambient and liquid nitrogen, were used for estimating an average gain of the instrument. (It is to be kept in mind that the scan trajectory of the paraboloidal reflector is a shallow cone with apex angle 72.72° due to the offset angle between the horn and paraboloid axes). The LN₂ target is a rectangular Styrofoam container lined with pyramidal microwave absorber at the bottom and aluminum foil on the sides. The metal foil reflects stray radiation back into the container.

Sky scans were obtained by the upward-looking radiometer for ~ 40 minutes. A short segment (with two scans) extracted from the uncalibrated raw time-series data is shown in Figure 5.1. Diode detectors on channels 1 through 6 produce an increasingly positive voltage output with decreasing input power and vice versa in the case of channels 7 and 8. Strong changes in the voltages are observed as the mirror scans over the boiling LN₂. Scattering of radiation from the strut can also be discerned towards the right side of the scan. It is expected that the exposed Aluminum strut is colder than the ambient temperature. The higher level of noise in channels 2 and 3 (between 700 MHz and 1200 MHz) is possibly due to electromagnetic or radio frequency interference (EMI or RFI).

A Level-1a calibration algorithm (see c.f. §5.5 for details) was applied to obtain estimates of the antenna temperatures from the raw digital counts. The mean and variance of these calibrated antenna temperatures were obtained by averaging the data over ~ 2100 scans (Figure 5.2c). For the upward-looking radiometer, the 118.7503 ± 0.2 GHz channel (channel 1) is most opaque, and observes closest to the surface, that is, the atmospheric weighting function peaks near the surface at this frequency. The 118.7503 ± 5.0 GHz channel (channel 8) is most transparent and senses deeper into the atmosphere measuring much colder brightness temperatures. Note that the antenna temperature observed by any channel at a given reflector scan angle ψ_S is truly a band-averaged antenna temperature. The incremental warming of brightness temperatures for scan angles away

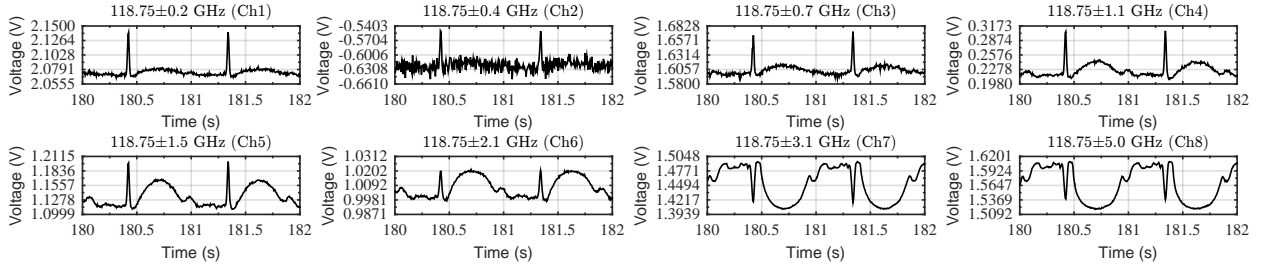


Figure 5.1: Time series data of sky scans from the roof-top test (Oct 2016) before the OIB experiment are shown. The limb brightening effect for scan angles away from nadir, anticipated spectral behavior of the opaque and transparent channels and, scattering from the strut can be discerned from the plot. The higher level of noise in channels 2 and 3 (between 700 MHz and 1200 MHz) are possibly due to EMI or RFI. These issues were corrected after the OIB experiment.

from zenith is the familiar limb brightening effect caused by increasing optical path length for larger zenith angles (i.e., the dependence of integrated opacity on $\sec(\psi_S)$), and is more pronounced for channels that can probe deeper into the atmosphere.

Measurements from the airborne experiment were critical in demonstrating performance of the 3D-printed corrugated feed horn and the IF diplexer based filter bank. Section §5.5 describes in detail the procedure to obtain antenna temperatures i.e., Level-1a calibrated data from the raw measurements. First light images with resolution better than 380 m were captured by the 118 GHz spectrometer from an aircraft altitude of $\sim 33,000$ ft. These images indicate the instrument’s ability to discern surface features with good accuracy. Antenna temperature signatures obtained from six of eight channels demonstrated the ability of the compact lumped element filter bank to separate spectral content around the 118.7503 GHz oxygen resonance.

Figures 5.4a, 5.4b and 5.3 are examples of antenna temperature maps imaged by the instrument’s four transparent channels (Ch# 5-8). The vertical stripe seen in the map at the ~ 10 km cross-section is a known scan bias caused by a Rexolite[®] window port through which MiniRad viewed. All measurements include the effect of this dielectric window as a function of scan angle. This effect, which has not been calibrated out, can be seen along both edges of the images, and is especially prominent over water. Since the most transparent channels have weighting functions peaking near

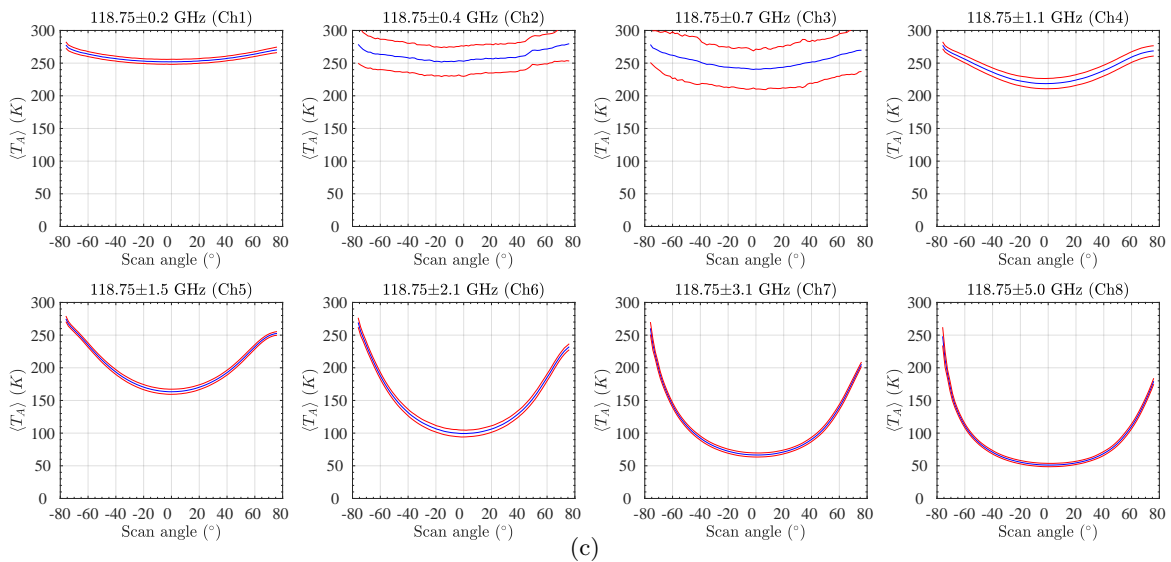
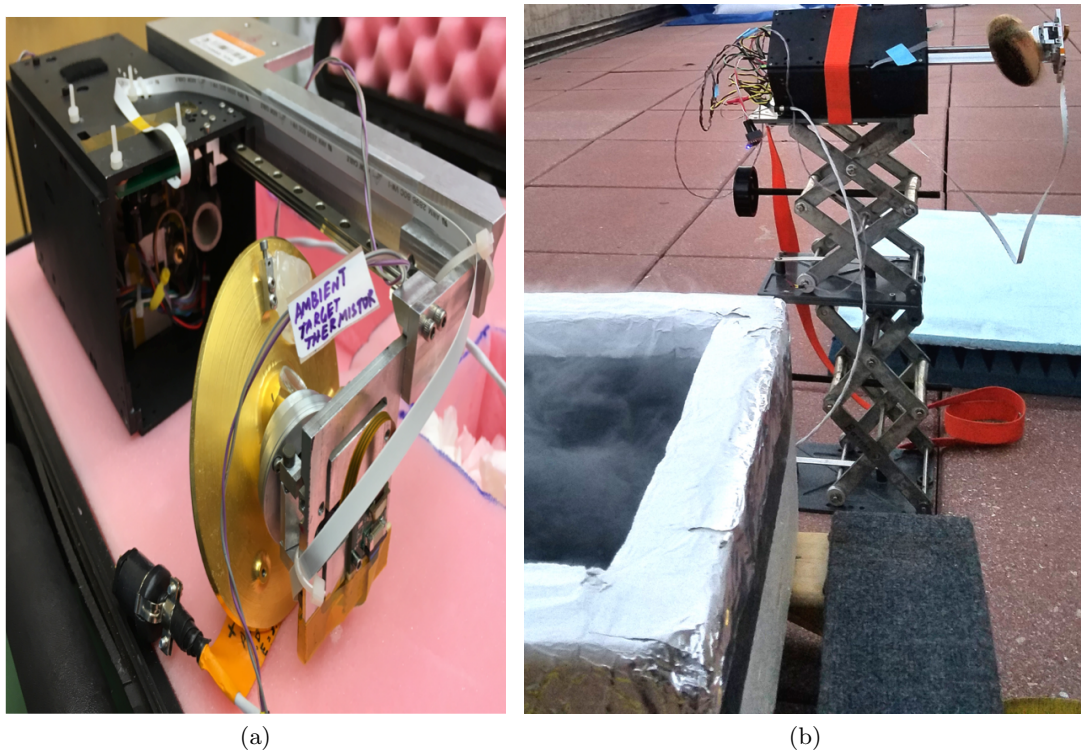
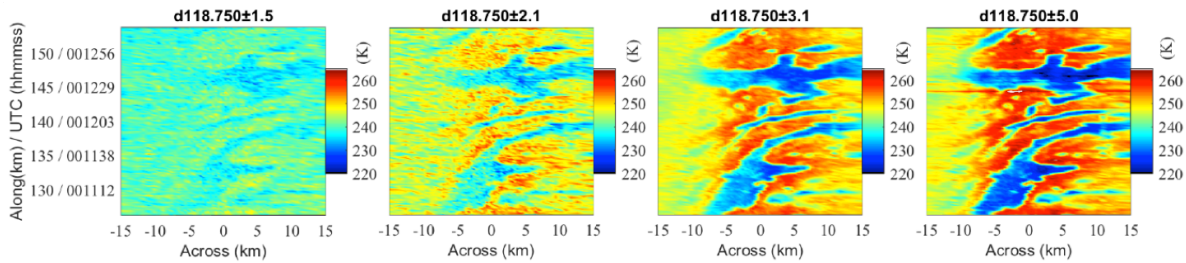
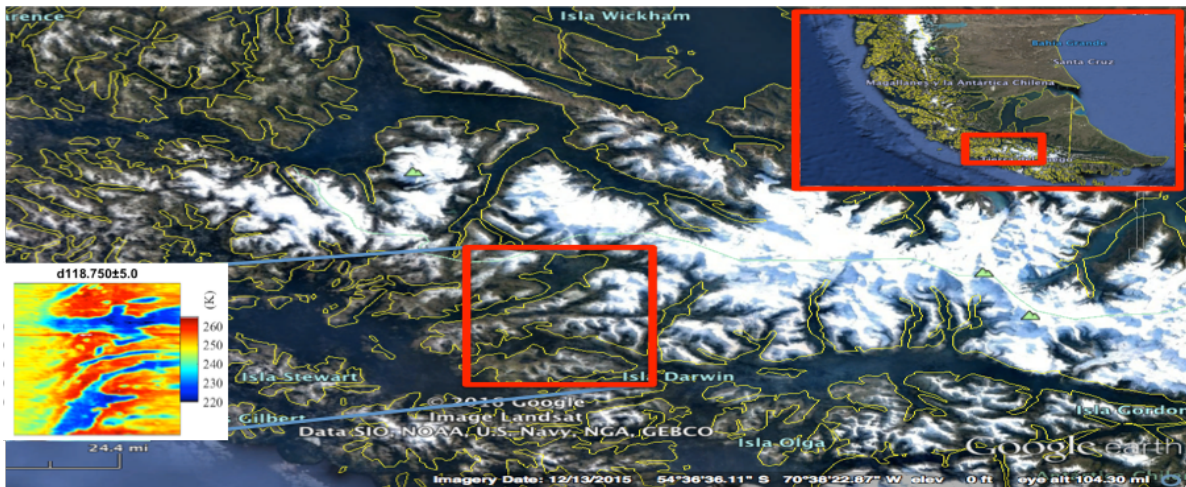


Figure 5.2: Prior to the OIB experiment in Oct-Nov 2016: (a) the end-to-end radiometer system was assembled and tested in the 1.5 U CubeSat envelope for the first time, (b) a rooftop test was executed with LN₂ and ambient absorber as calibration targets, and (c) in the calibrated sky scans for each channel, the red curve is the mean antenna temperature averaged over 2100 scans (~ 40 minutes). The RMS error per 5 ms sample is illustrated by the blue upper and lower curves. (Channels 2 and 3 showed performance degradation and were subsequently rectified after OIB).



(a)



(b)

Figure 5.3: Antenna temperature map of the Tierra del Fuego, an archipelago off the southern most tip of South America, observed by the transparent channels of the airborne instrument on October 26, 2016.

the surface, the surface emission, which is polarized (unlike atmospheric emission), has a stronger impact due to the dielectric window.

Along-track nadir scans extracted from these images (Figures 5.5a and 5.5b) show that the rate of change in antenna temperature as a function of the along track distance, is rapid, and coincides with simulated antenna temperature curves obtained by spatially convolving the computed total far field antenna pattern obtained using the HFSS simulation including the antenna strut with a two-dimensional spatial step-function in brightness temperature. Such sharp swings in antenna temperatures along land and water boundaries or ice edges confirm a well focused scanning reflector antenna system whose phase center closely coincides with the paraboloidal reflector's focus. These results are also indicative of an antenna system with high main beam efficiency, that is, the antenna

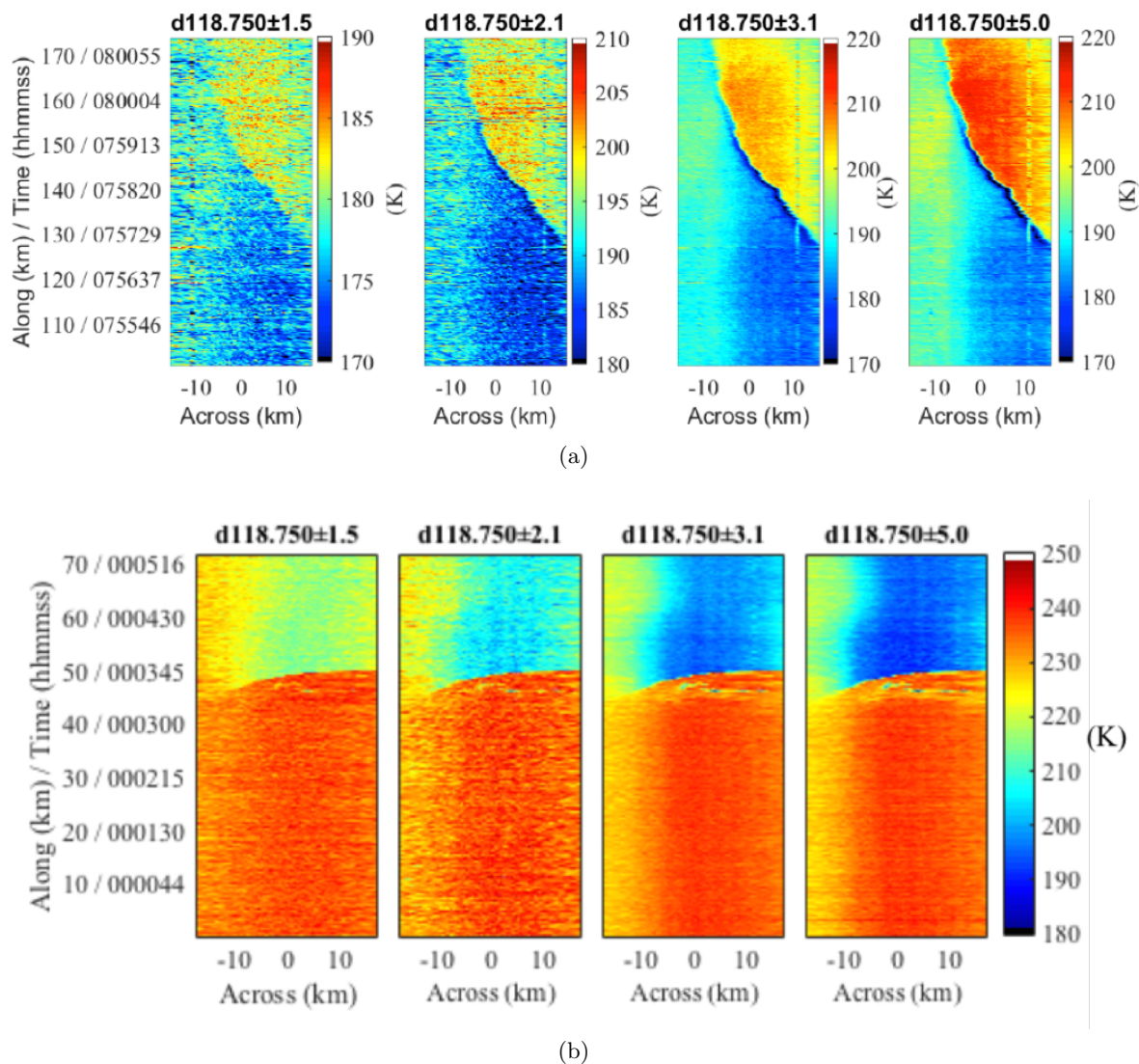


Figure 5.4: Antenna temperature maps with scan bias removed of (a) an ice edge ($W57^\circ$, $S75^\circ30'$) and, (b) a land-water boundary ($W70^\circ54'$, $S53^\circ26'$) imaged by channels 5-8 are shown. The cooling present in (b) close to the boundary indicates a drop in the antenna temperature for a 3 km wide region just before the coast line. (The aircraft Rexolite[®] window effect is also present.).

pattern has low energy in its side lobes and spillover lobes.

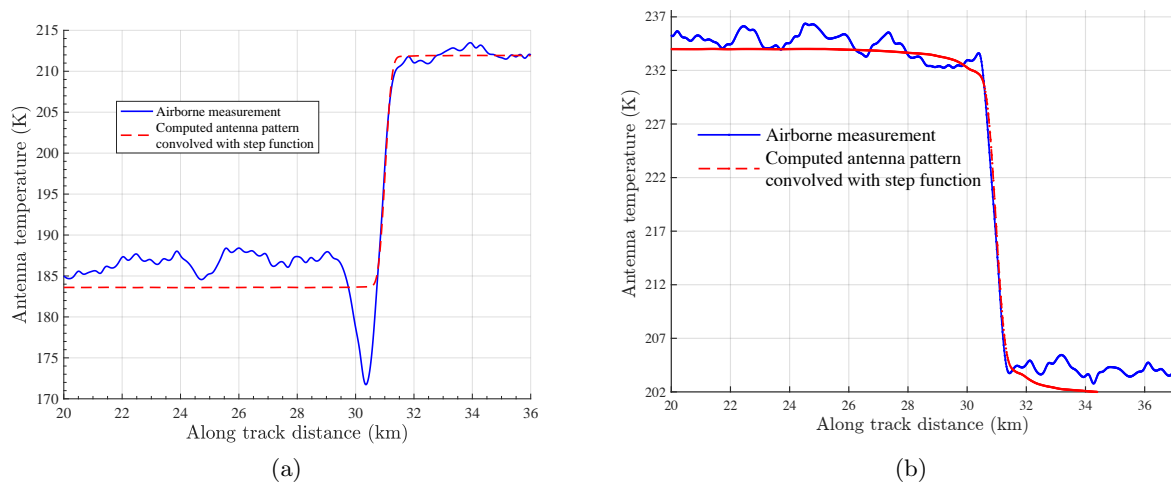


Figure 5.5: Comparisons of along track nadir scans extracted from an ice edge and land ocean boundary (Figures 5.4a and 5.4b) respectively with theoretical estimates.

Figure 5.5a reveals interesting cooling in brightness temperature over open ocean over a ~ 5 km wide. This cooling is hypothesized to be caused by cold air outflow from the Antarctic ice sheet, and is not seen elsewhere during high contrast land-water crossings. We thus see a potential application of high resolution passive microwave temperature sounding in identifying such cold air features [82].

Although the radiometer performance was verified during the airborne experiment, there were important outstanding electrical and mechanical issues that needed to be addressed before a fully packaged instrument could be delivered for integration with the CubeSat bus:

- (1) From lab tests, it was determined that the analog ground voltage level fluctuated by a few millivolts when the PIN diode, driven by a 40 mA current driver circuit in the digital board, switched states. This caused the switching voltage noise to manifest itself on the radiometric signal as well. The PIN switch hence remained switched off during the experiment and was not used for calibration. An external absorber at ambient temperature, whose temperature was monitored with a single thermistor, was used instead.

- (2) Channels 2 and 3 were noisy possibly due to EMI or RFI pickup by the IF PCB. Also, this experiment used individual two-layer IF and VA PCBs. These were integrated into a single four-layer hybrid PCB for final assembly (Figure 4.2).
- (3) An external motor driver board was mounted on the chassis as this circuitry was not part of the digital board at this stage. There were also occasional dropouts in radiometric as well as motor encoder data. The digital board was updated with motor driver circuitry before final assembly.
- (4) The motor bearing was not optimum and seemed to provide too much resistance to the motor shaft which caused the mirror to stall occasionally.
- (5) There were also several mechanical issues with the carrier design that prevented the mirror from being stowed inside the body of the satellite.
- (6) The mirror deployment could not be verified. However, it is to be noted here that the deployment has been successfully verified by the Colorado Space Grant Consortium team in a zero gravity environment at a NASA facility.

The above shortcomings were identified during the airborne experiment (Nov 2016) and rectified before the final assembly of the instrument (Feb 2018).

5.2 Radiometer Final Assembly

Before final assembly, the radiometer IF and VA four layer boards were carefully tested and tuned for optimum sensitivities across all channels. Some relevant lab experiments conducted to measure instrument performance are described in §5.3. A detailed analysis of the mirror mechanical assembly, structural analysis and alignment procedures are provided in [32] [33].

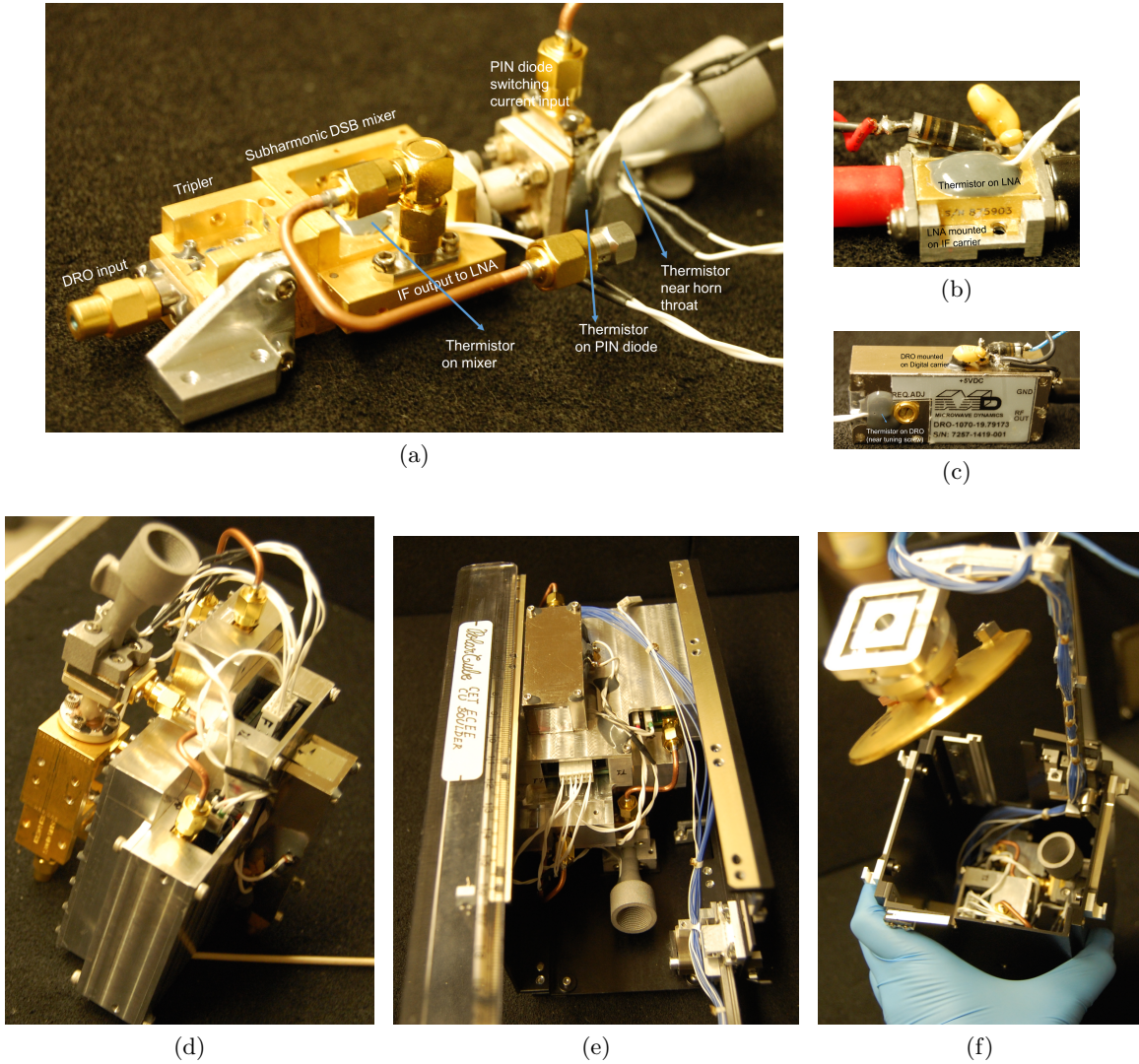


Figure 5.6: Pictures of the final assembled radiometer hardware are shown here: (a) RF chain and led NTC thermistor locations, (b) low noise amplifier (LNA), (c) dielectric resonant oscillator (DRO), (d) RF chain and IF spectrometer in carrier, (e) side view inside the 1.5U CubeSat, and (f) top view including reflector and strut.

5.3 Radiometer Laboratory Measurements

This section describes pertinent laboratory experiments conducted during and after final system integration. Measurements obtained from such tests were used to evaluate and quantify the radiometer performance prior to outdoor sky scan experiments.

5.3.1 Power Supply Noise Rejection

Figure 5.3.1 depicts a series of measurements showing the impact of drift in the IF, LNA, and DRO regulated supply voltages on the detected output voltage. Measurements were taken manually at the differential output of the op-amps. Channel 2 was saturated at the time of this test and excluded. For IF and LNA supply voltage drifts of ~ 0.5 V lower than the nominal operating voltage, the effect on the output voltage is predominantly linear across all channels. A change in the DRO supply voltage impacts its output power which in turn affects the operation of the nonlinear mixer diode. The dependence of the output voltage on DRO supply voltage is hence nonlinear. MiniRad digital circuitry does not have voltage/current sensing circuits to track or compensate for drifts in supply voltages; however, these measurements can help understand possible fluctuations in radiometer outputs, especially during calibration cycles. Sensitivity coefficients computed using best linear fits to the measurements are tabulated in Table 5.7h. For a given channel, the sensitivity to IF supply voltage is more than thrice than that to LNA supply voltage. This indicates that the MMIC chip amplifiers on the IF board are much more susceptible to gain fluctuations with supply voltage drift than the LNA. Additionally, the MMIC amplifiers are biased very close to their device operating voltage, 3.5 V (§4.1).

5.3.2 Characterization of Inherent System Noise

It is desired that radiometer system noise (that is essentially inherent thermal noise of the instrument) is purely white. The widely used central limit theorem in probability theory states that the arithmetic mean of a sufficiently large number of iterations of independent random

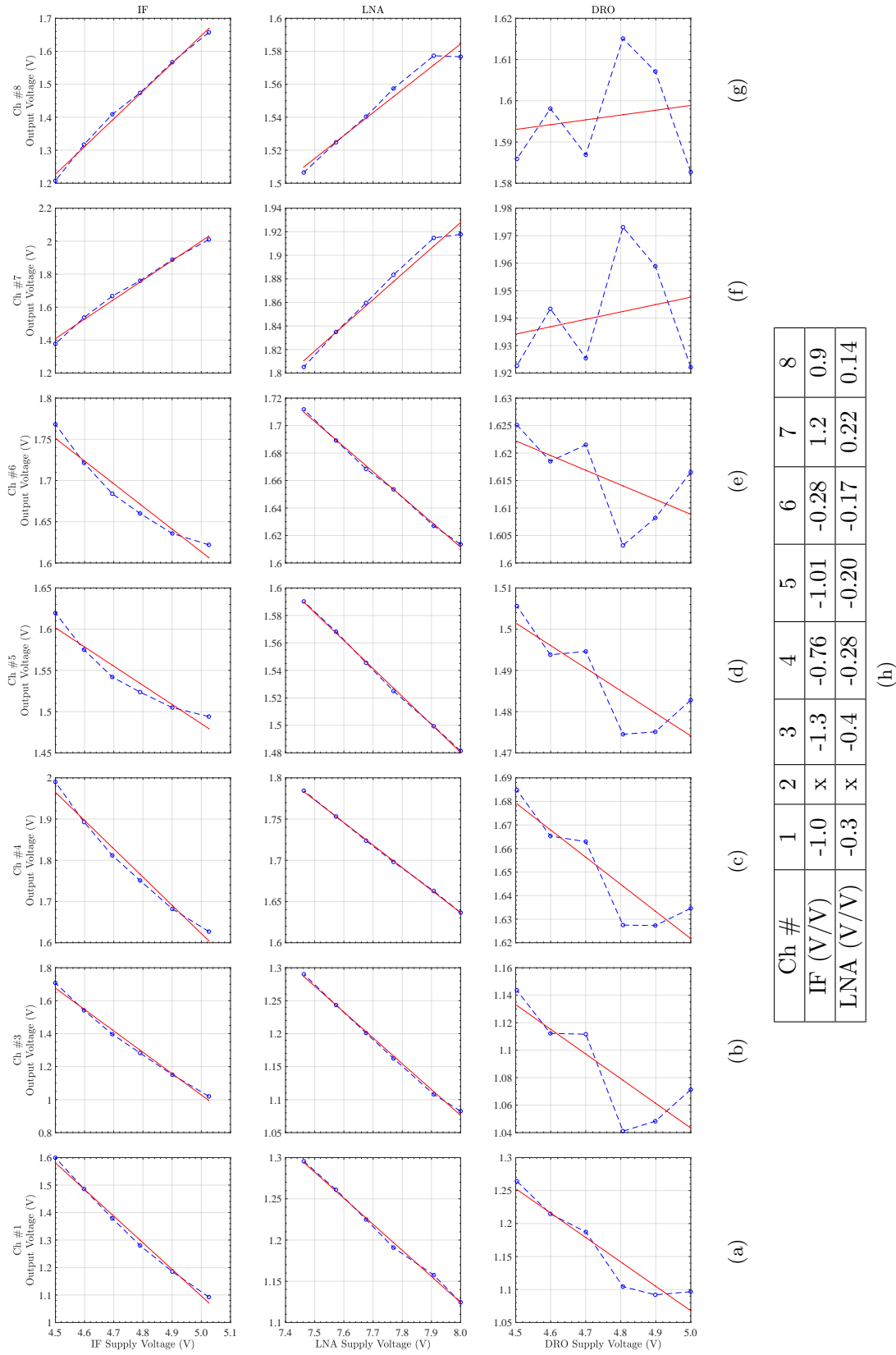


Figure 5.7: Plots (a-g) are measurements depicting the impact of drift in IF, LNA, and DRO regulated supply voltages on the detected output voltage. The red lines are best linear fits to the measurements (blue curves). Table (h) provides sensitivity coefficients calculated using the best line fits.

variables, each with a well-defined expected value and variance, will be approximately normally distributed [83]. Hence, skewness (5.2) and kurtosis (5.3), the third and fourth central moments of a Gaussian random variable (respectively) can provide quantitative measures of the system's noise characteristics. If x is a Gaussian random variable with normal probability distribution $p(x)$ (5.1) and standard deviation σ , the mathematical identities for skewness and kurtosis are as follows:

$$p(x) = \frac{1}{\sqrt{2\pi\sigma^2}} e^{-\frac{(x - \langle x \rangle)^2}{2\sigma^2}} \quad \text{where} \quad \int_{-\infty}^{\infty} p(x) dx = 1 \quad (5.1)$$

$$m_3 = E[(x - \langle x \rangle)^3] = \int_{-\infty}^{\infty} (x - \langle x \rangle)^3 p(x) dx = 0 \quad (5.2)$$

$$m_4 = E[(x - \langle x \rangle)^4] = \int_{-\infty}^{\infty} (x - \langle x \rangle)^4 p(x) dx = 3\sigma^4 \quad (5.3)$$

The moment coefficient of skewness, $g_1 = m_3/\sigma^3$ is an indicator of the symmetry of the distribution. If the moment coefficient of kurtosis, $g_2 = m_4/\sigma^4$ equals 3, then the distribution is truly normal. Now, as the normality/Gaussianity of any distribution is dependent on the number of samples, the skewness and kurtosis of this distribution will themselves have associated variances [84]. For a N -sample normal random variable distribution, the standard deviation of the skewness σ_{g_1} and, the standard deviation of the kurtosis σ_{g_2} are estimated using equations (5.4) and (5.5):

$$\sigma_{g_1} = \sqrt{\frac{6N(N-1)}{(N-2)(N+1)(N+3)}} \simeq \sqrt{\frac{6}{N}} \quad \text{for large } N \quad (5.4)$$

$$\sigma_{g_2} = \sqrt{\frac{24N(N-1)^2(N+1)}{(N-3)(N-2)(N+1)(N+3)(N+5)}} \simeq \sqrt{\frac{24}{N}} \quad \text{for large } N \quad (5.5)$$

Noise characteristics of the 118 GHz radiometer were determined using measurements taken inside a Faraday cage, a metal enclosure with absorber on all the inside walls. The feed horn aperture was covered with a small microwave absorber but the reflector was left spinning at ~ 1 Hz. For this test, the PIN diode toggled states once every minute in order to obtain datasets over longer epochs. A ~ 45 minute (uncalibrated) radiometric dataset logged over multiple epochs (~ 59 s each) was segregated per PIN diode switching state. Each epoch was detrended to the first order before estimating its skewness and kurtosis for all eight radiometric channels (Figures 5.9b and 5.9d. Two

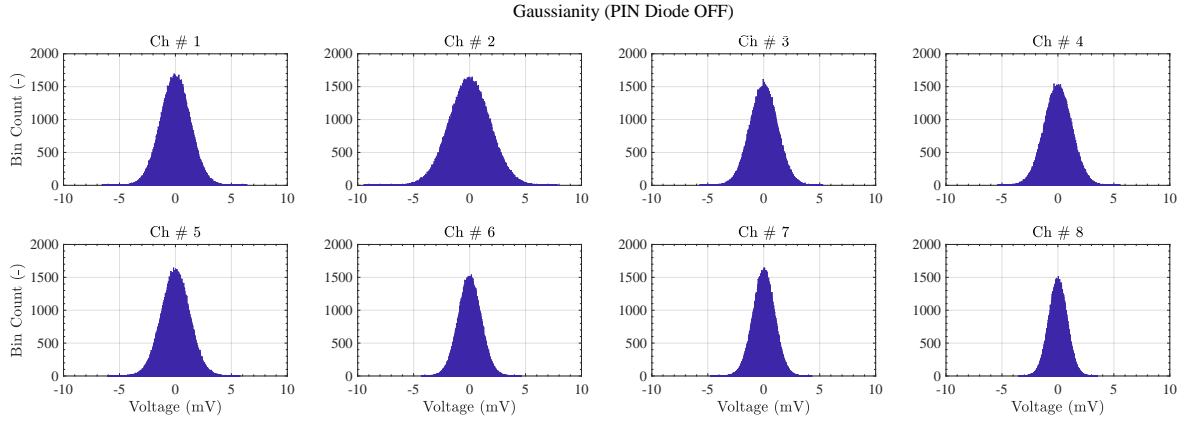
detrended datasets were obtained by combining multiple epochs for the PIN diode ON and OFF states to analyze their probability distribution. Histograms with bin resolution $25 \mu\text{V}$ (Figures 5.8a and 5.8c) and, skewness and kurtosis estimates (Tables 5.8b and 5.8d) of these composite datasets indicate unimodal, approximately symmetric [85] and normal distributions across all channels.

Very low frequency noise is a nonstationary random process whose power spectral density has a $1/|f|^\gamma$ characteristic where $1 < \gamma < 2$ and is usually ~ 1 [86]. In radiometers, its presence indicates slow time varying fluctuations (usually much longer than the system integration time) in the system gain (RF/IF amplifiers) and offset i.e., system noise temperature (due to drift of the physical temperature of the instrument). Being a nonstationary process, $1/f$ noise has a variance and power spectral density that varies with time. Allan variance $\sigma_A(\tau)$, a differential variance computed over time τ is a widely used indicator of $1/f$ noise and drift in instruments:

$$\sigma_A(\tau) \cong \frac{1}{2(N-2k)(kT_o)^2} \sum_{j=1}^{N-2k+1} [-y(j+2k) + 2y(j+k) - y(j)]^2 \quad (5.6)$$

where $T_o \simeq \tau_i = NT_s = 4.096$ ms is the time interval between samples (or equivalently, the integration time), $T_s = 256 \mu\text{s}$ is the sampling time of the ADC and $N = 16$ is the number of digitized samples averaged per recorded radiometric sample.

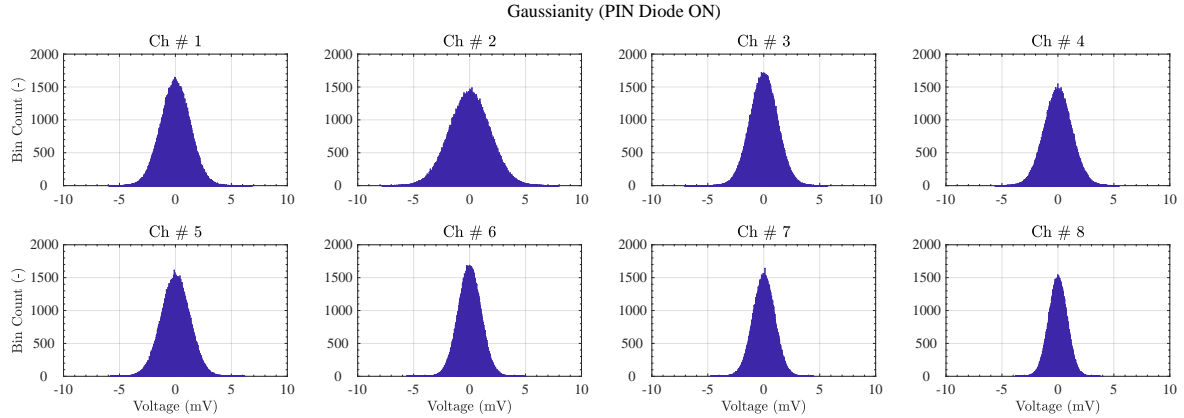
Allan deviations were computed for radiometric data per epoch for PIN diode ON and OFF states. (Note that the data samples were not detrended for Allan variance calculations). It is clear that there is negligible drift over a period of one minute and $1/f$ noise is quite white (slope $\simeq -1$ and $\gamma = 0$). As we calibrate every second, it can be inferred that the system gain and offset are stable between calibrations. With measurements of average channel response (taken during the Marshall field test 5.6.2) and computed Allan deviations at 1 s (as calibrations occur every second 5.9e), the radiometer noise standard deviation ΔT_{rms} for each channel is evaluated. The knee of the curve i.e., the time beyond which the instrument drift dominates is not evident in these plots as the time duration per epoch is a minute. It is to be noted that the use of chopper-stabilized operational amplifiers (§4.4) are quite essential to minimize $1/f$ noise between calibrations.



(a)

Ch #	1	2	3	4	5	6	7	8	σ (theoretical)
Skewness g_1	0.006	0.005	0.001	-0.002	-0.004	0.002	-0.032	-0.009	$\sigma_{g_1} = 0.0204$
Kurtosis g_2	3.001	2.999	2.997	2.999	3.015	3.001	3.029	2.992	$\sigma_{g_2} = 0.0408$

(b)

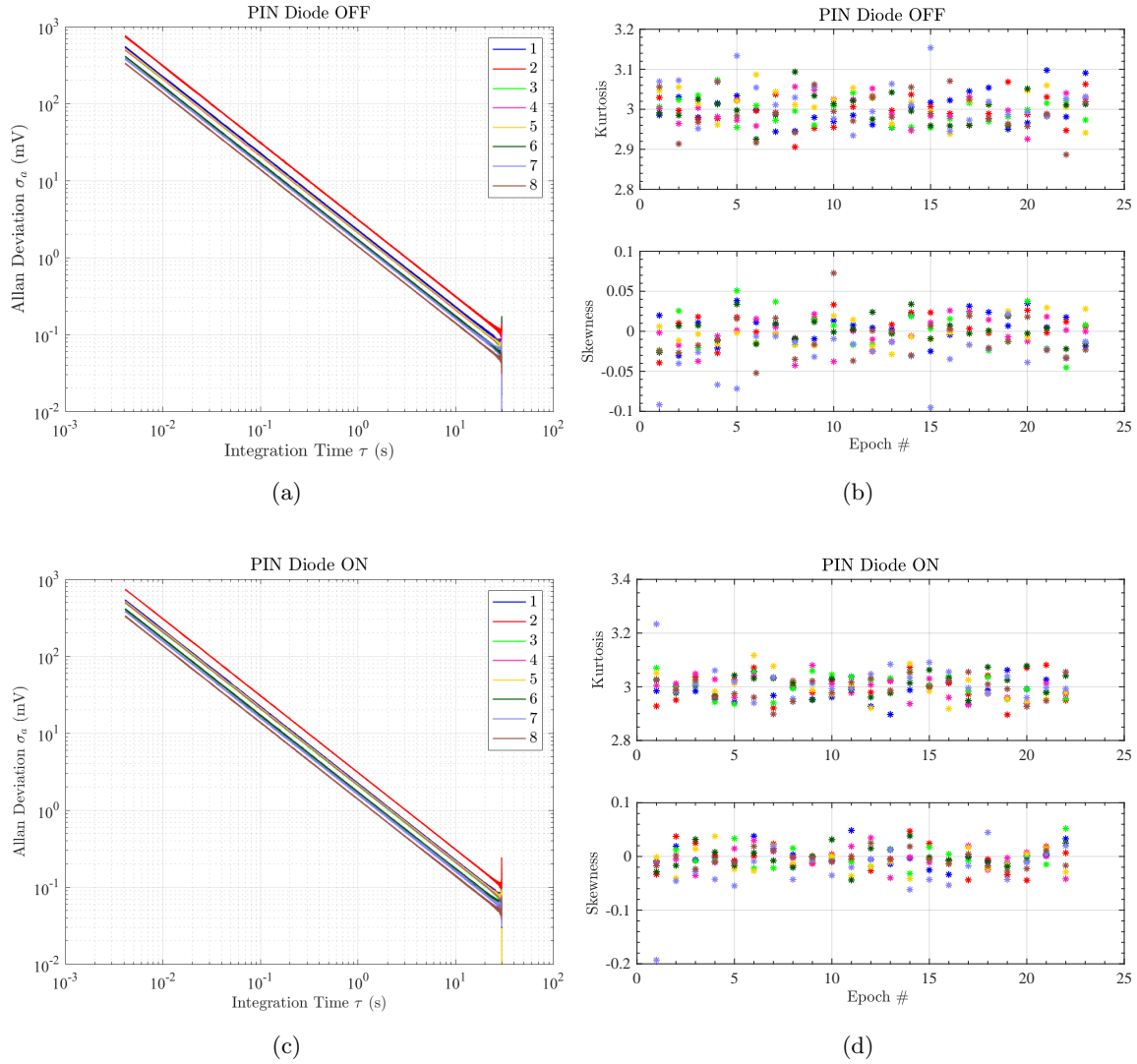


(c)

Ch #	1	2	3	4	5	6	7	8	σ (theoretical)
Skewness g_1	0.001	-0.002	-0.002	-0.004	-0.008	0.000	-0.031	-0.004	$\sigma_{g_1} = 0.0204$
Kurtosis g_2	2.985	3.001	3.008	2.999	2.998	3.012	3.039	2.996	$\sigma_{g_2} = 0.0408$

(d)

Figure 5.8: Histograms of the radiometer noise measurements during PIN diode OFF/ON states over ~ 23 epochs (~ 59 s each) detrended to first order. Data kurtosis estimates indicate excellent Gaussian distribution across all channels.



Ch #	1	2	3	4	5	6	7	8
σ_A at 1s (mV) PIN Diode OFF	2.265	3.107	2.095	2.101	2.135	1.712	1.626	1.385
σ_A at 1s (mV) PIN Diode ON	2.233	3.075	2.084	2.104	2.149	1.721	1.627	1.379
Measured Response S (mV/K)	0.45	0.67	0.84	0.77	0.88	0.62	0.90	0.65
σ_A/S (K)	4.99	4.61	2.49	2.73	2.43	2.77	1.81	2.13

(e)

Figure 5.9: Measured radiometer noise statistics over multiple epochs (~ 59 s each) during PIN OFF/ON states: (a) Allan deviation for PIN OFF state, (b) kurtosis and skewness per epoch (PIN OFF), (c) Allan deviation for PIN ON state, (d) kurtosis and skewness per epoch (PIN ON) and, (e) Allan deviations computed at 1 s, the time duration between calibrations. Radiometer gains used in this table were obtained using calibrated data from the Marshall field test.

5.3.3 Thermal and Pressure Testing

The radiometer was subjected to pressure and temperature extremes with available lab equipment, a bell jar (Figure 5.3.3) and a freezer was conducted on the instrument using a bell jar. As part of the bell jar test, additional leaded thermistors were carefully installed atop the microcontroller and voltage regulator ICs on the digital board as well as the mirror motor (with thermal grease and epoxy) in order to monitor the temperatures of these active components at low pressure and ascertain that they stayed within operating temperature range ($< 55^{\circ}\text{C}$). When

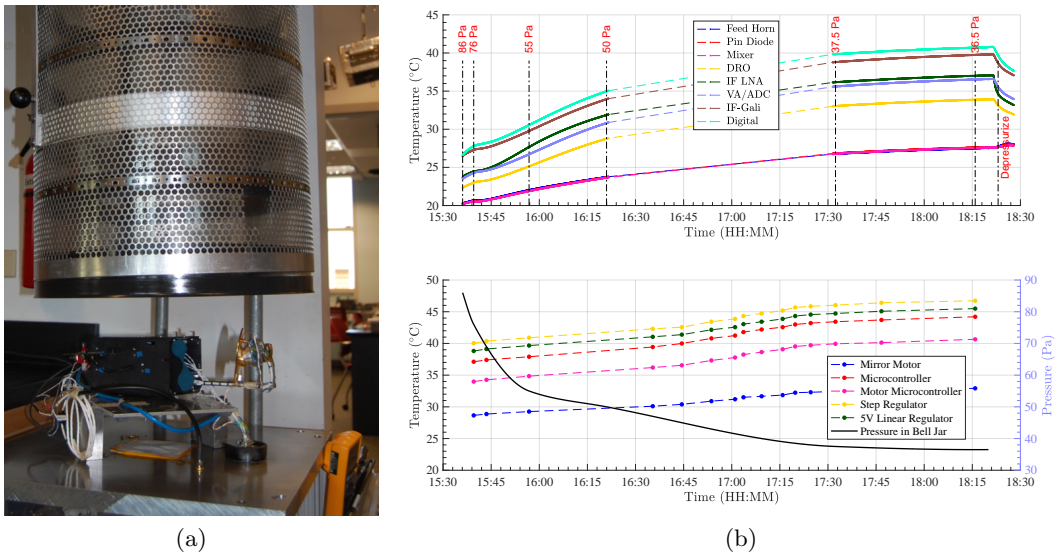


Figure 5.10: Pressure cycling of the radiometer inside a bell jar: (a) experimental setup, and (b) measured temperatures of the RF components (upper plot) and voltage regulators, microcontrollers and the mirror motor (lower plot) as a function of pressure inside the bell jar.

the instrument was tested inside the freezer, ambient absorber and liquid nitrogen were used for external two-point calibration. Radiometer gains computed over two ~ 10 minute intervals as the temperature inside the freezer dropped are shown in Figures 5.11a and 5.11b. The low sensitivity observed on channel 2 was due to a malfunctioning GAT chip attenuator before the tunnel diode - this issue was rectified after the test.

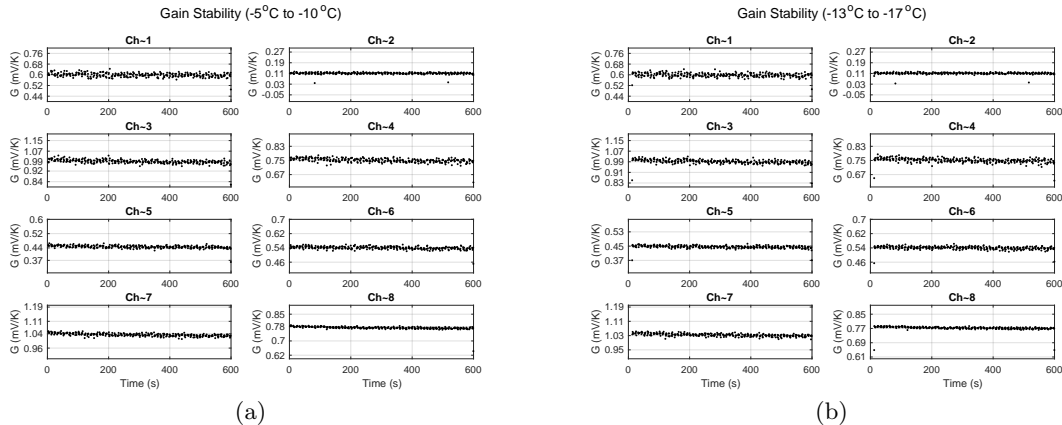


Figure 5.11: Plots depicting the stability of radiometer gain are shown for measurements taken over a 10 minute time period when the ambient temperature dropped from (a) -5°C to -10°C , and (b) -13°C to -17°C . (Low sensitivity on channel 2 was fixed after the test.)

5.3.4 Y-Factor Testing

Results from the final bench-top Y-factor testing of the instrument are shown in Figure 5.12. This test, which did not include the scanning reflector, involved manually alternating the source right in front of the feed horn aperture between a small absorber and LN_2 (in a styrofoam cup) once every minute. The measurements with ambient absorber indicate that the diode was set to switch states every 5 s. An important observation from ambient absorber measurements (such as for channels 2 and 4) is that the internal noise reflected off the PIN diode during its ON state has a frequency dependence.

5.3.5 RF Passband Measurements

It is necessary to measure accurately the spectral response of the spectrometer in order to compute the atmospheric weighting functions and brightness temperatures using a microwave radiative transfer algorithm. An RF sweep that spans both upper and lower side bands about the 118.75 GHz O_2 resonance would also be indicative of the extent of local oscillator drift albeit the use of a double side band mixer helps alleviate the impact of this drift. Due to lack of resources, only an IF spectral response of the PolarCube’s MiniRad radiometer could be obtained using a frequency

sweep between 50 MHz and 8 GHz at the input to the IF LNA. A few months later, an RF passband response was obtained on the GEMS-01A's MiniRad radiometer (built for Orbital Micro Systems Inc.) that uses an identical IF spectrometer as PolarCube's MiniRad, and an RF chain that includes an isolator and short waveguide section. This RF response has also been used in this dissertation to make inter-comparisons between the predicted and measured antenna temperatures. A comparison between the two responses (Figure 5.13) indicates that although they exhibit similar spectral characteristics, their relative channel gains are dissimilar. As such dissimilarities can cause significant errors in radiative transfer brightness temperature computations, it is essential to obtain accurate RF passband response measurements for each radiometer during its prelaunch calibration procedure.

5.4 Calibration Chamber Assembly

A measurement can be only as accurate as the measurement setup and the process used in obtaining the measurement. In order to have a precise knowledge of the instrument's characteristics during prelaunch calibration, a low budget measurement chamber was designed and built in the laboratory with an existing freezer re-purposed to house the packaged instrument, as well as the hot

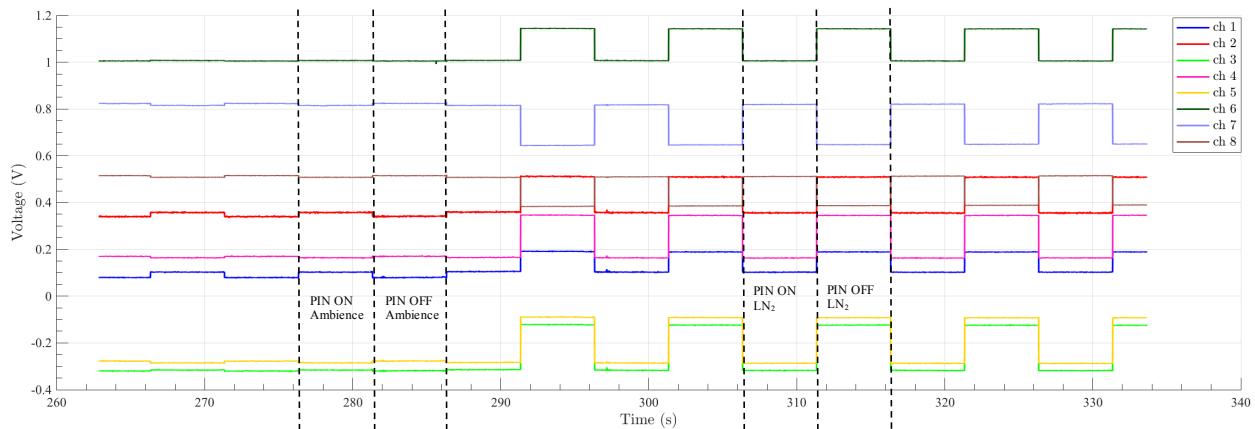


Figure 5.12: Bench-top Y-factor measurements with absorber and LN₂, and the PIN switch toggling states every 5 s.

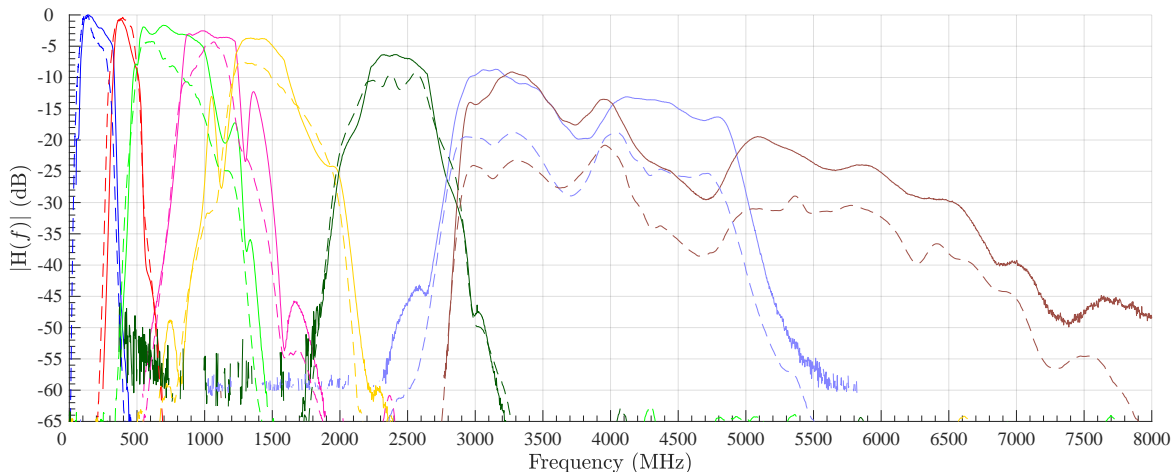


Figure 5.13: Comparisons between the measured IF passband response on PolarCube’s MiniRad (solid line) and the RF passband response on the GEMS-01A’s MiniRad (dashed line) radiometers.

and cold external calibration targets (Figure 5.14). This chamber was used to take measurements in the laboratory (Section 5.3.4) and outdoors (§5.6.1 and §5.6.2). A description of various components inside the calibration test chamber is provided below:

- (1) *Cold target*: Liquid nitrogen (LN_2) is the cold calibration source inside the chamber. The LN_2 is contained in a NIST aqueous blackbody calibration (ABC) container [87]. This styrofoam container has a geometry that minimizes reflectance of radiation incident on its front wall. The side walls are covered with microwave absorber. A triangular piece of styrofoam with aluminum foil on the inside wall rests on top of the ABC container.
- (2) *Hot target*: An unpolarized array of canted pyramidal iron-epoxy absorbing wedges at ambient temperature approximate a blackbody target used as the hot calibration source. This target has been used on the Polarimetric Scanning Radiometer (PSR) [88]. The absorbing pyramids, arranged in a two-faced L-shaped configuration, are laid on top of a thermally-conducting substrate of aluminum pyramids. The target is contained within a closed-cell styrofoam insulating jacket [88]. The physical temperature of the entire structure remains homogeneous to within 1-2 K and thus, its microwave emission temperature is

assessed using measurements of its physical temperature. The aluminum plates include heating elements to heat the target if desired.

- (3) *Sky view*: The main antenna beam has unobstructed view of the sky over a $\pm 60^\circ$ scanning range. A ~ 3 mm thick sheet of S/MMW transparent Zotefoam ([89] [90] [91]) on the top of the chamber aids in reasonable stabilization of air draft and temperature within the chamber. Zotefoam has low scattering at millimeter wavelengths due to its small cell size and low density.
- (4) *Absorber*: All exposed walls of the chamber are covered with pyramidal microwave absorber to minimize reflections off these surfaces. The mounting that supports the integrated radiometer is covered with flexible foam sheet broadband microwave absorber.

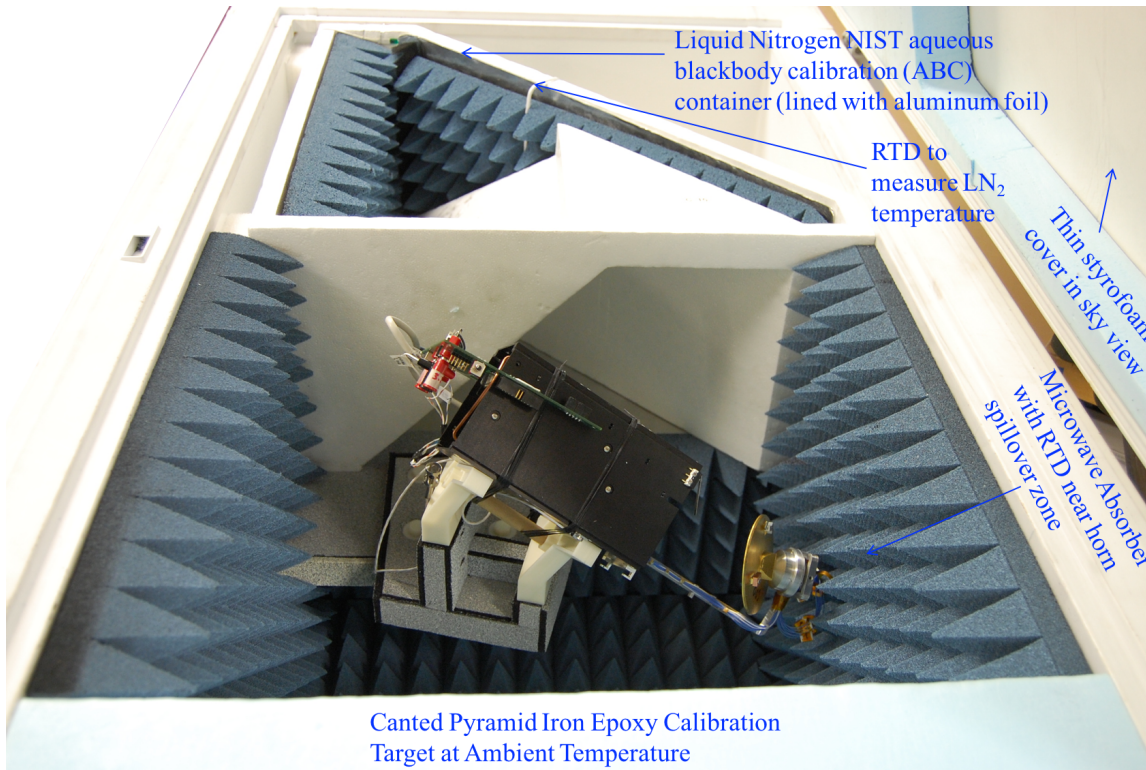


Figure 5.14: Top view of the calibration chamber used for prelaunch calibration of the MiniRad radiometer.

- (5) *External RTDs*: Eight external resistive temperature devices (RTDs) have been installed to monitor the temperatures of the hot target, LN₂, absorber, chamber air and instrument chassis during an experiment. The temperatures are monitored/recorded using an OMEGA OM-DAQXL data logger. The RTDs used, their locations and the range of temperatures measured during the field experiments are summarized in Table 5.1.

RTD Specification	RTD Type	RTD Location	Measured Temp. Ranges (°C)	
			Bridge Test	Marshall Test
3-wire 100 Ω Pt	Thin film	Hot target	[0.0, 5.0]	[6.3, 10.3]
3-wire 100 Ω Pt	Thin film	Hot target	N/A	N/A
3-wire 100 Ω Pt	Thin film	Hot target	[0.0, 4.0]	[6.4, 10.8]
3-wire 100 Ω Pt	Thin film	Hot target	[0.2, 4.5]	[6.7, 11.5]
4-wire 100 Ω Pt	Flexible hermetic-sealed	Abs spillover zone	[-34.1, -3.0]	[-14.8, 5.4]
4-wire 100 Ω Pt	Pt in ceramic tube	LN ₂ target	[-196, -195.6]	[-195.78]
3-wire 100 Ω Pt	Exposed in vented housing	Chamber air	[-43.5, -21.1]	[-22.3, -5.3]
3-wire 100 Ω Pt	Bolt-on surface	Radiometer Chassis	[-33.2, -10.4]	[-10.4, 6.0]

Table 5.1: Locations and types of external resistive temperature devices (RTDs) installed inside the calibration chamber to monitor temperatures of targets/components used for instrument calibration. The last two columns summarize measured temperature extremes during the bridge-scan and Marshall field experiments (respectively).

5.5 Radiometric Data Calibration

In this section, a detailed description of the procedure used to convert raw measurements (in ADC counts) obtained during field experiments (§5.1, §5.6.1 and §5.6.2) to calibrated antenna temperatures T_A and, subsequently brightness temperatures T_B is provided. An in-house legacy Matlab based software module “Viewrad” [92], written for Level-1 radiometric data calibration and used in previous airborne missions such as the PSR, has been modified for this purpose. An outline of the data calibration procedure is delineated below:

- (1) Convert the 24-bit, 16 sample radiometric sum and sum-of-squares counts to voltages.
- (2) Preprocess motor encoder counts and convert to angular displacements.
- (3) Use filtered encoder signal to partition measurements into the following data sets: {hot

calibration target}, {cold calibration target}, {PIN Diode ON state} and {scene}.

- (4) Convert 12-bit thermistor counts to temperatures, and subsequently preprocess thermistor and external RTD temperatures (Table 5.1) and re-interpolate to radiometer time grid.
- (5) Use filtered RTD temperatures of the hot target, LN₂ and background (antenna main beam spillover area) to obtain hot and cold target brightness temperatures.
- (6) Estimate gain and offset for each scan and, obtain scene radiometric and sum-of-squares antenna temperatures from voltages assuming linear system behavior between calibration cycles.
- (7) Form cross-track scan images from Level-1 calibrated scene data.
- (8) Estimate radiometer ΔT_{rms} using calibrated sum-of-squares measurements.
- (9) Estimate noise reference (PIN diode) characteristics as a function of physical temperature of the PIN diode (and other RF front-end components) for each channel.

The AESM-4096 encoder used in combination with the Faulhaber mirror motor is a magnetic absolute encoder with a resolution of 4096 steps per revolution. As the encoder is absolute, it implies that each shaft position is assigned to a unique angular value per revolution and hence, it is straightforward to determine the angular extents of various scan segments inside the calibration chamber. However, the motor encoder data is noisy and requires some preprocessing before it can be used. The red plots in Figure 5.15a show the noisy unwrapped unfiltered encoder counts and derived angular velocities. After basic data clean-up that involves correcting anomalous encoder values, resampling to a uniform time grid and detrending to second order, an optimal harmonic low-pass Wiener filter is applied to the unwrapped encoder data. The output of this optimal Wiener filter provides a minimum-mean-squared-estimate (MMSE) of the true angular position of the mirror under the assumption that the signal and noise are uncorrelated [93] [94] [95]. This filtering reduces discrepancy between adjacent encoder counts thus providing an instantaneous angular velocity ω_S of 1 ± 0.2 rps (Figure 5.15b).

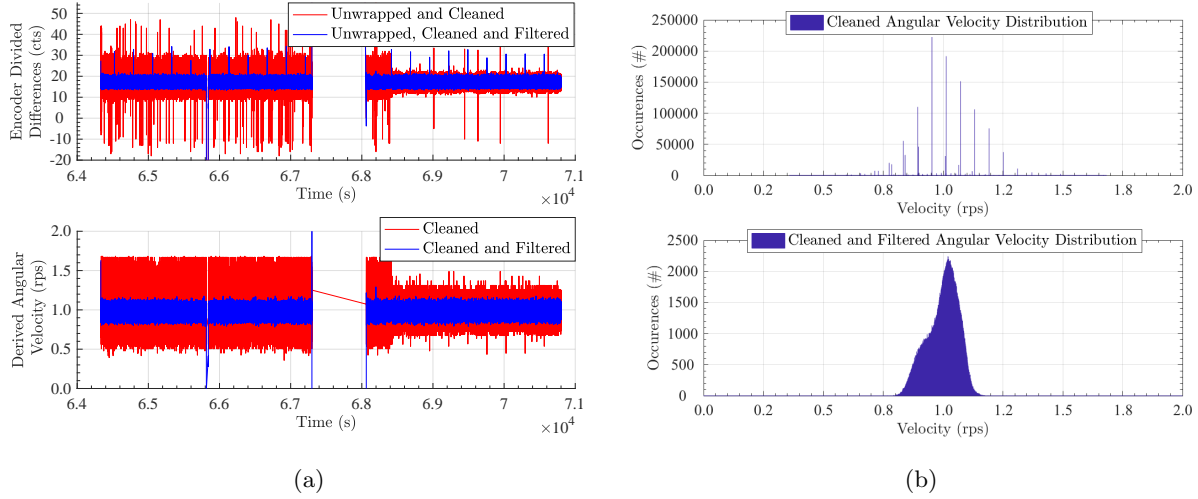


Figure 5.15: (a) Motor encoder counts and derived angular velocity before (blue curves) and after (red curves) optimum Weiner filtering, and (b) histograms of the noisy (upper plot) and filtered (lower plot) angular velocities.

There are 6 leaded NTC thermistors (§4.5) epoxied on the surfaces of the scan motor, feed horn, PIN diode, mixer, DRO, and IF LNA to monitor their physical temperatures. Additionally, 3 chip NTC thermistors are present on the IF, VA, and digital PCBs. There is also a dedicated channel to measure the ~ 3.3 V reference voltage and hence compensate for fluctuations in its value. The Stein-Hart equation (5.7) is used to convert from voltage readings to temperatures where $T_o = 298.15$ K, β is a characteristic of the thermistor procured from its specifications, V_{ref} is the measured reference voltage (in counts) and, V_T is the measured thermistor voltage (in counts):

$$\frac{1}{T} = \frac{1}{T_o} - \frac{1}{\beta} \ln \left(\frac{V_{ref}}{V_T} - 1 \right) \quad (5.7)$$

Temperature measurements from both the thermistors and RTDs are resampled to a uniform time grid, median filtered to remove spurious noise, low-pass (moving-average) filtered and re-interpolated back to radiometric time grid.

In this first order calibration scheme, physical temperatures of the hot and cold external calibration targets are converted to antenna temperatures referred to the feed horn aperture, $\hat{T}_{A,C}^f$ and $\hat{T}_{A,H}^f$ (hence the superscript 'f') by including background brightness contributions from the

horn spillover zone:

$$\widehat{T}_{A,C}^f = \eta_s \widehat{T}_{B,C}^m + (1 - \eta_s) \widehat{T}_{B,BG}^m \quad (5.8)$$

$$\widehat{T}_{A,H}^f = \eta_s \widehat{T}_{B,H}^m + (1 - \eta_s) \widehat{T}_{B,BG}^m \quad (5.9)$$

where $\widehat{T}_{B,C}^m$, $\widehat{T}_{B,H}^m$ and $\widehat{T}_{B,BG}^m$ are brightness temperatures of the cold LN₂, the hot blackbody target and the absorber near the horn spillover zone, all referred to the main aperture of the antenna (hence the superscript ‘*m*’). The spillover efficiency η_s is obtained from the HE₁₁ mode based full wave simulations (2.4). Note that as an approximation, the emissivities of the calibration sources and the microwave absorber have been assumed to be unity. Equations (1.26) and (1.27) are used to estimate the radiometer gain \widehat{m} and offset \widehat{b} per scan. Subsequently, equation (1.30) enables determination of the scene antenna temperature, referred to the feed horn aperture $\widehat{T}_{A,S}^f$. Main aperture scene antenna temperature estimates can then be calculated using:

$$\widehat{T}_{A,S}^m = \frac{1}{\eta_s} \widehat{T}_{A,S}^f - \frac{(1 - \eta_s)}{\eta_s} \widehat{T}_{B,BG}^m \quad (5.10)$$

Hence, as a first order approximation, the calibrated scene antenna temperatures referred to the main aperture are independent of spillover and background temperature. In general, the calibration target and background temperatures and emissivities will have a spatial variation that necessitates a spatial convolution of their brightnesses with the antenna gain pattern.

Finally, the behavior of the reflective PIN diode (during diode ON state) across the eight radiometric channels has to be determined as a weighted function of physical temperatures of the RF front-end components. Statistics of this internal reflected noise are critical to post-launch calibration of the instrument, where the PIN diode itself is the second calibration source.

5.6 Radiometer Performance

Two outdoor experiments were conducted after final instrument assembly to evaluate the radiometer’s performance as well as acquire prelaunch calibrated noise temperature measurements of the internal reflective PIN diode (§1.5.1): the bridge-scan and the Marshall experiments during

which the MiniRad was installed in the calibration test chamber providing two-point external radiometric calibration using ambient and LN₂-cooled targets, and operated as an upward looking radiometer performing zenith scans observing through a thin transparent foam window.

During the bridge-scan experiment, the instrument was positioned beneath the edge of an elevated walkway between buildings of the Engineering Center at the University of Colorado. This test was conducted on a particularly cold and dry cloud-free winter evening (Feb 1, 2018, ~5:00 PM to 6:30 PM MST) for ~1.5 hours. During this observation period the temperature of the radiometer chassis inside the prelaunch calibration test chamber dropped steadily from -10.5 °C to -33 °C. Note that the boiling liquid nitrogen within the chamber caused it to be much colder than the outside environment. The objective of this experiment was the verification of the step response of the radiometer's antenna system.



Figure 5.16: The calibration chamber housing the radiometer and calibration targets rests on a trailer as the radiosonde, seen in the background, is ready for launch [5] at the Marshall field.

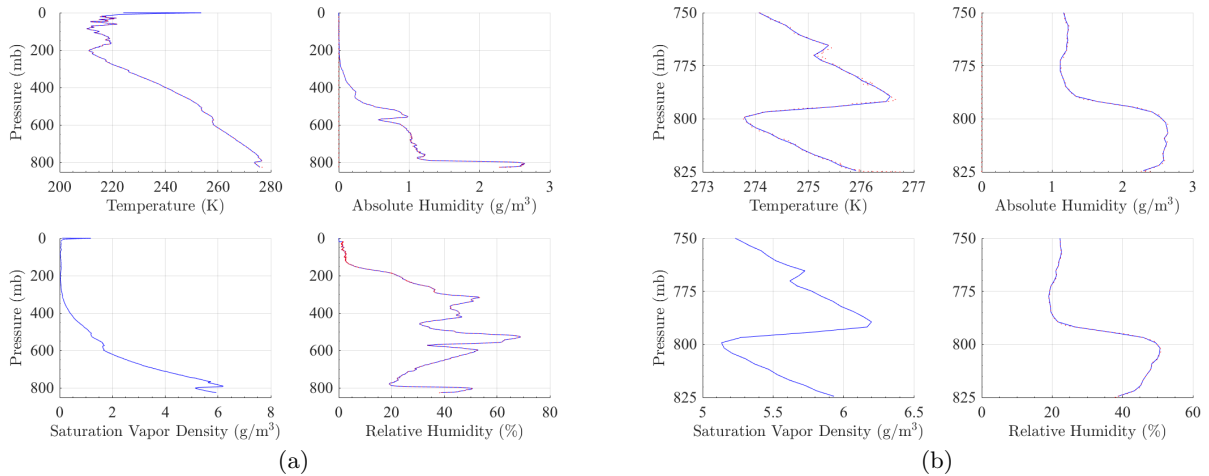


Figure 5.17: Radiosonde measurements of relevant atmospheric parameters taken at the NCAR Marshall field site in Boulder, CO (N39.9491°, W105.1973°, 1743 MASL) [5] are shown. The location is at an altitude of 1.743 km where the atmospheric pressure is 825.15 mb. Above 27.1 km, the sonde data has been appended with the TIGR mid latitude winter atmospheric profile [6] ensuring no discontinuity in pressure.

The Marshall experiment was conducted at the Marshall field site (N39.9491°, W105.1973°, 1743 MASL) of the National Center for Atmospheric Research (NCAR), a radiosonde launch location for the Earth System Research Laboratory (ESRL) Global Monitoring Division at the National Oceanic and Atmospheric Administration (NOAA). The first part of the experiment coincided with a water vapor and ozonesonde launched on a reasonably clear morning (Figure 5.16) on March 1, 2018 at ~10:55 AM MST, thanks to the cooperation of the team at NOAA ESRL [5]. Calibrated antenna temperatures obtained from this experiment were compared with those computed by an in-house microwave radiative transfer program [31].

It is noted that calibrated radiometer antenna temperatures are referred to the coordinate system of the antenna main aperture. Thus, these calibrated temperatures need to be transformed to the earth's coordinate system in order to determine sky scans as a function of zenith angle. For the two experiments described above, an Eulerian transformation was applied to the calibrated antenna temperatures. Approximate numbers for the Eulerian angles (pitch, roll and yaw) were determined from a Dassault Systèmes SolidWorks® model of the calibration chamber with the

radiometer.

5.6.1 Radiometer Antenna Step Response

The true radiation pattern of the MiniRad radiometer antenna system, comprising a scanning offset paraboloidal reflector supported on a single strut and a 3D-printed corrugated feed horn, could not be precisely measured in an antenna chamber due to cost and time constraints. During the bridge-scan experiment, as the MiniRad scanned across open clear-sky occulted by a far zone half-space concrete obstruction, it permitted the radiometer to observe a sharp far zone change in brightness temperature between the warm bridge and the cold sky. From this sudden brightness temperature change measured by the scanning radiometer, the step response of the radiometer system could be determined which helped verify important characteristics of the antenna subsystem.

An ideal step function was convolved with the simulated full wave antenna pattern for comparisons with the radiometer measurements obtained from the bridge-scan experiment (Figure 5.18). The step function for each radiometric channel was scaled based on the antenna temperatures observed by that channel. Measured responses show excellent agreement with computed curves for all channels. With an angular scanning rate $\omega_S \simeq 2\pi$ rad/s, and 3-dB beamwidth $\theta_{3\text{dB}} \simeq 2.2^\circ$, the time taken by the radiometer to scan through one beamwidth or the dwell time [29], is $\tau_d = \theta_{3\text{dB}}/\omega_S \simeq 6.1$ ms. With the MiniRad digital sampling and averaging integration time $\tau_i \simeq 4.096$ ms, the radiometer will register a change at the bridge-sky boundary in time τ_d , or a change in the zenith angle of ~ 1 3-dB beamwidth. Since the differentiation of an ideal step function is an impulse function, differentiating the computed and measured antenna gain convolved step responses provides a good estimate of the antenna main beamwidth. Figure 5.19 shows a comparison between the radiometer impulse responses derived from the measured step responses and the simulated far field antenna pattern at 118.75 GHz. It is seen that the MiniRad antenna main beamwidth is $\sim 0.1^\circ$ broader and slightly asymmetric about $\theta = 0^\circ$ when compared to the simulated main beam. This broadening could be due to the 3D-printed feed horn whose far field measurements indicated some broadening and asymmetry (Figure 3.4) compared to HFSS simulation results. It

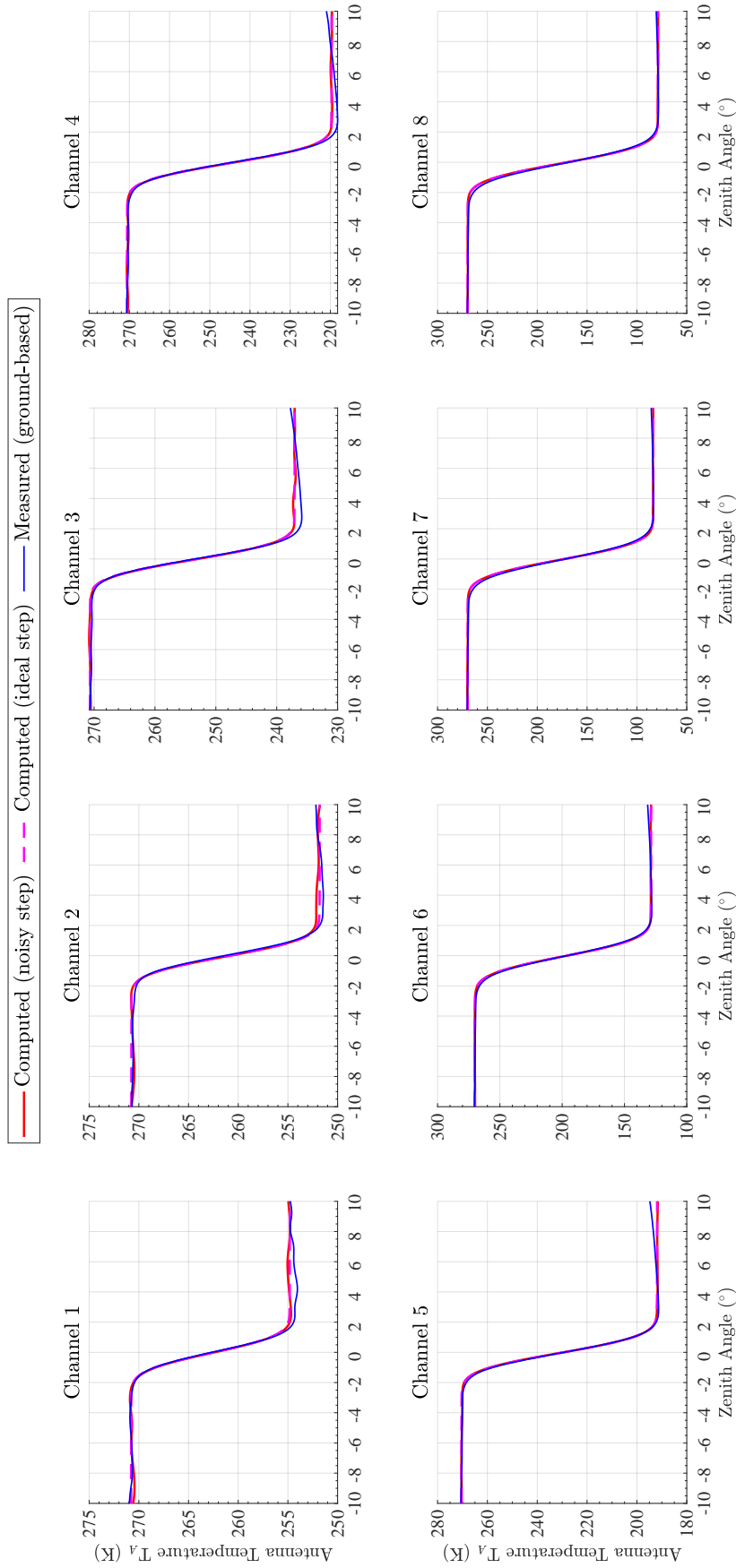


Figure 5.18: Step responses of the 8-channel radiometer measured during the bridge-scan experiment show excellent agreement with the simulated antenna-pattern-convolved step function.

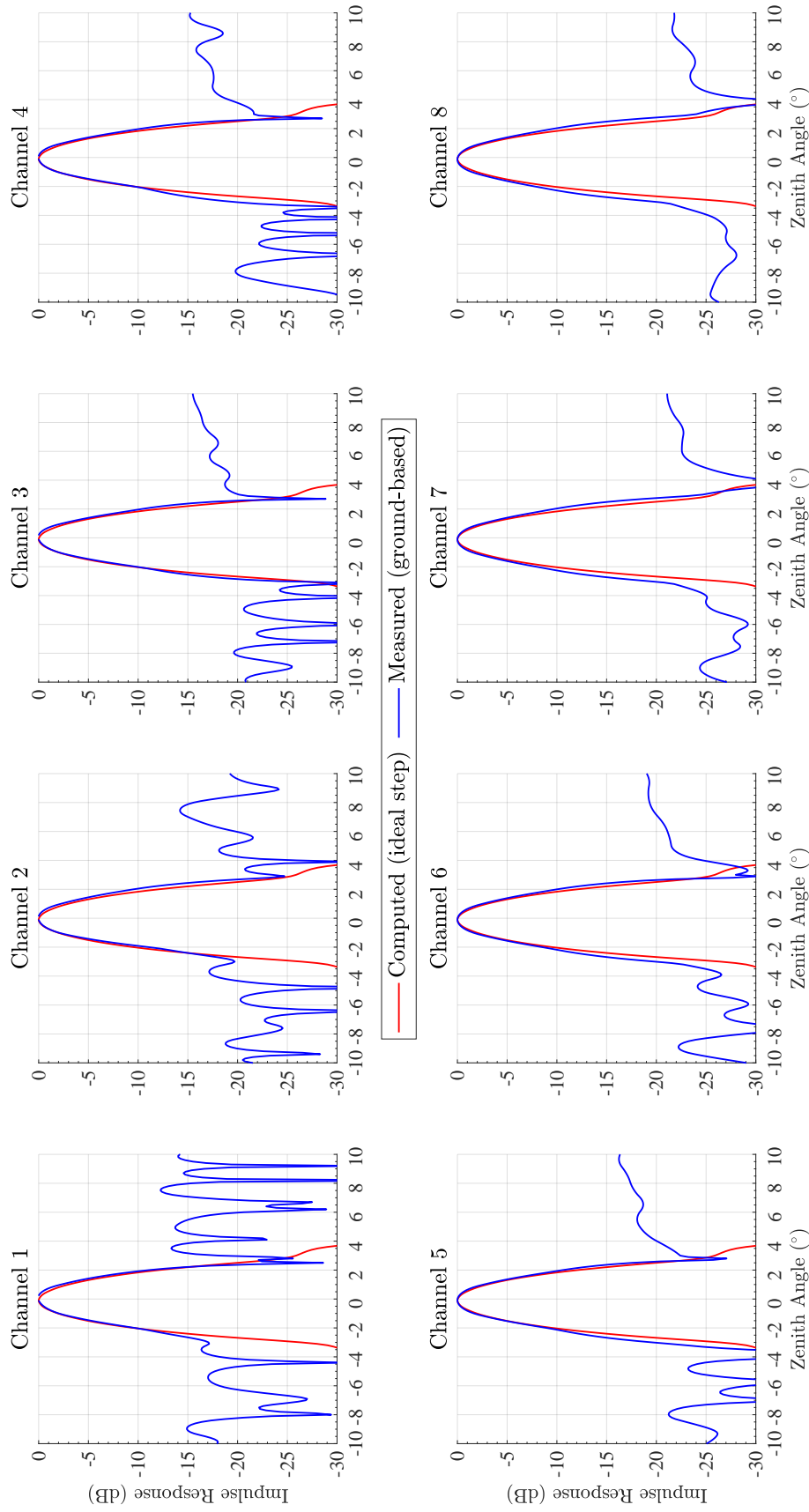


Figure 5.19: In this set of plots, derived impulse responses of the eight-channel radiometer antenna subsystem obtained from the measured step responses are compared with the simulated far field main beam. Data on either side of the main beam are *not* antenna side lobes but simply antenna temperature differences across the bridge (on the left side) and the sky (on the right side) away from the “step”.

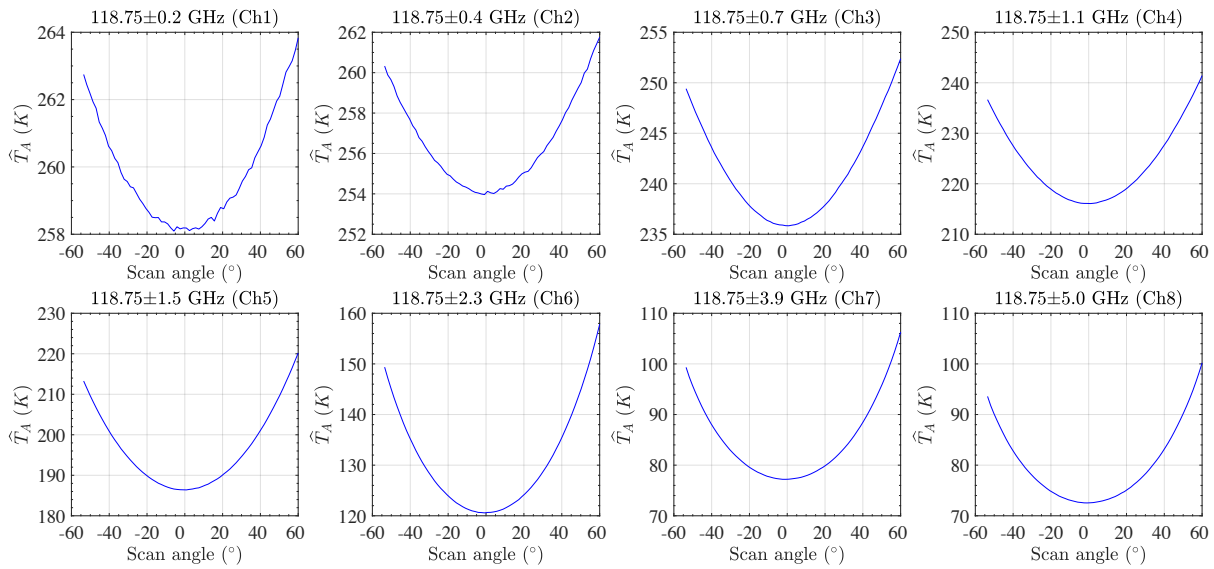
is important to discern the data on either side of the main beam in Figure 5.19: these are not antenna side lobes but simply antenna temperature differences across the bridge (on the left side) and the sky (on the right side).

5.6.2 Radiosonde-based Radiative Transfer Inter-comparisons

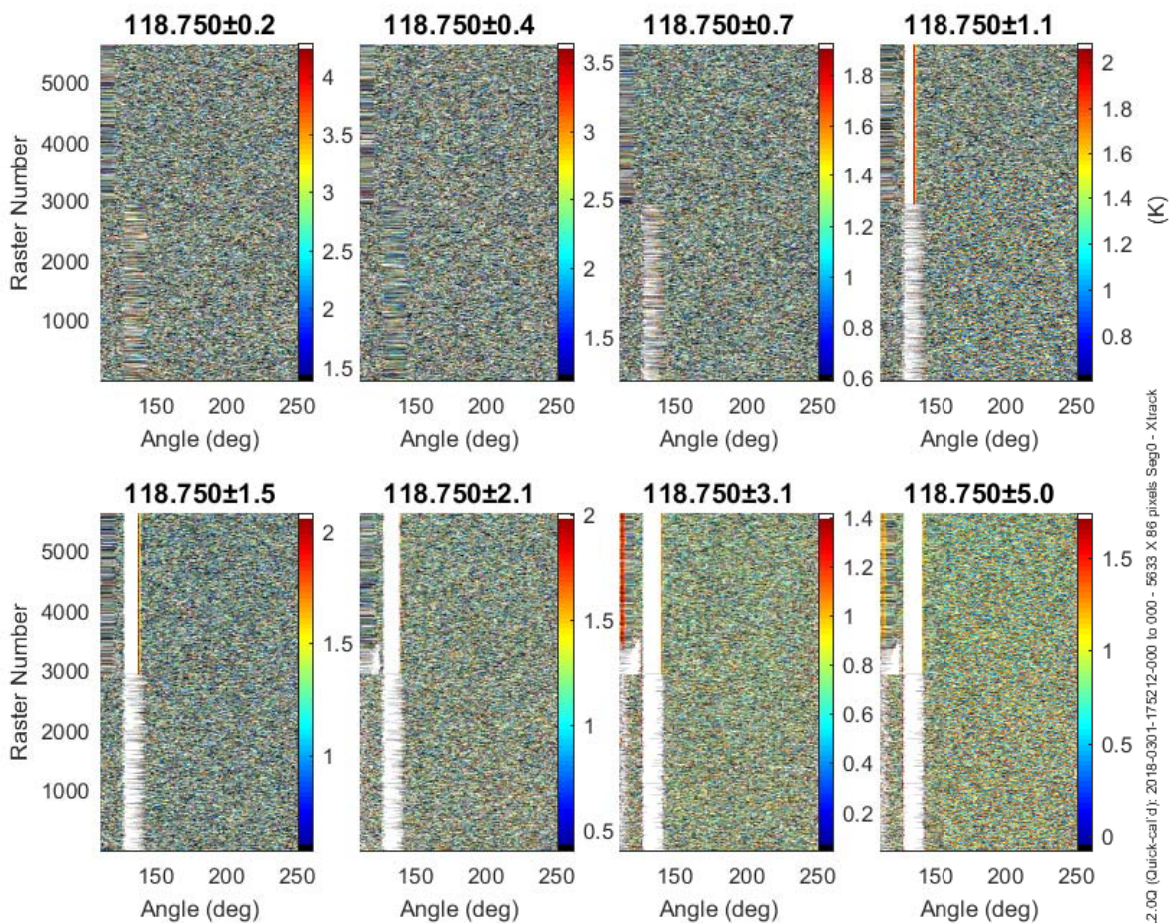
Sky scans measurements were taken during the Marshall field experiment for a period of ~ 1.5 hours after the radiosonde launch over three epochs, each epoch being ~ 30 minutes in duration. Estimates of the scene antenna temperatures, referred to the main aperture ((5.10)) can then be determined using the procedure delineated in §5.5. Time-averaged sky scan antenna temperatures obtained during the third epoch (averaged over ~ 30 minutes) are shown in Figure 5.21a. The sum-of-squares (SoS) measurements provide a useful means of direct determination of the radiometer sensitivity ΔT_{rms} (or noise temperature standard deviation). The SoS measurements (Figure 5.21b) obtained across multiple scans during the third epoch (~ 30 minute duration) show a strongly white Gaussian behavior, and no electromagnetic or radio frequency interference across all channels. Note that the PIN diode toggles states around zenith angle $\sim 40^\circ$ causing loss of data in this sky scan interval. For the radiometer integration time $\tau_i = NT_S = 16 \times 256 \mu s = 4.096$ ms, the measured radiometer sensitivities averaged over a 30-minute interval $\langle \Delta T_{rms} \rangle$ agree closely with theoretical calculations to within ~ 0.5 K across the eight channels (Table 5.20). A precisely calibrated 50-satellite constellation of similar radiometers will improve the overall sensitivity by a factor of $\sqrt{50}$.

Ch #	1	2	3	4	5	6	7	8
B_C (MHz)	265.72	204.22	674.29	563.00	665.85	676.14	2031.0	2708.7
ΔT_{rms} (K) (theoretical)	2.22	2.36	1.21	1.28	1.21	1.20	0.74	0.58
$\langle \Delta T_{rms} \rangle$ (K) (measured)	2.84	2.45	1.25	1.32	1.26	1.25	0.79	0.92

Figure 5.20: Comparisons between the average estimates of the radiometer ΔT_{rms} obtained from the sum-of-squares measurements and the theoretical calculations.



(a)



(b)

3AD L2.00 (Quick-cal): 2018-0301-175212-000 to 000 - 5633 X 86 pixels Seg0 - Xtrack

Figure 5.21: (a,b) Calibrated radiometric sky scan and sum-of-squares measurements obtained at the Marshall field experiment during the third 30-minute epoch.

The in-house microwave radiative transfer program (for clear-air observations in a planar-stratified non-scattering atmosphere) “Viewrad” [31] (see §1.3 for details) was used to obtain the computed brightness temperatures. The computed antenna temperatures were estimated using:

- (1) the atmospheric temperature profile and surface parameters obtained from the radiosonde launched at the beginning of the experiment (Figure 5.6),
- (2) the *measured* instrument passband responses as unitary weights (Figure 5.22), and
- (3) the *simulated* far field antenna pattern to obtain antenna temperatures from computed brightness temperatures.

As end-to-end swept RF frequency measurements of the PolarCube MiniRad radiometer were not acquired, the following two cases of instrument passband responses were used to determine the computed brightnesses for comparison with measurements:

- (a) the instrument IF spectral response obtained using a 50 MHz to 8 GHz swept frequency measurement at the IF LNA input (Figure 5.13). This measurement includes the true IF passband characteristics of the radiometer but does not take into account RF front end losses, spectral variations or port reflections, most importantly those due to the 3D-printed horn, the PIN diode, and the mixer. As a first order correction, manufacturer specifications of the PIN diode were used to incorporate its loss (as a function of frequency) into the measurement.
- (b) the RF spectral response measured on the GEMS-01A MiniRad instrument (Figure 5.13), a radiometer that uses an identical IF spectrometer and a 3D-printed horn from the same manufacturing batch as the PolarCube MiniRad. However, its RF front-end additionally includes an isolator and a waveguide section.

Brightness temperatures computed using both the above cases were convolved with the simulated main aperture radiated far field pattern directivity in order to obtain the computed antenna

temperatures. This radiated field, which does not include contributions due to the horn spillover, was used because the measured antenna temperatures are referred to the antenna main aperture instead of the horn aperture (See (5.10)).

Antenna temperature discrepancies, that is, differences between the computed and measured antenna temperatures are plotted in Figure 5.23. For plots on the left hand side, the computed antenna temperatures were obtained using the PolarCube IF passband response measurements whereas the right hand side plots used the GEMS-01A RF spectral response measurements. The PIN diode toggled states during part of the sky scan for epochs 1 and 2. This schedule was corrected at the start of the third epoch. Possible causes for the antenna temperature discrepancies seen in the left hand side plots that use the PolarCube IF passband response include:

- (a) Primarily, the IF passband response did not account for exact spectral variations in the RF front end, specifically loss in the 3D-printed horn (expected to be ~ 1 dB), measured PIN diode S-parameters (only approximate losses from specification sheets have been used), and mixer loss.
- (b) The scan curvature errors (i.e., the additional antenna temperature discrepancies at zenith

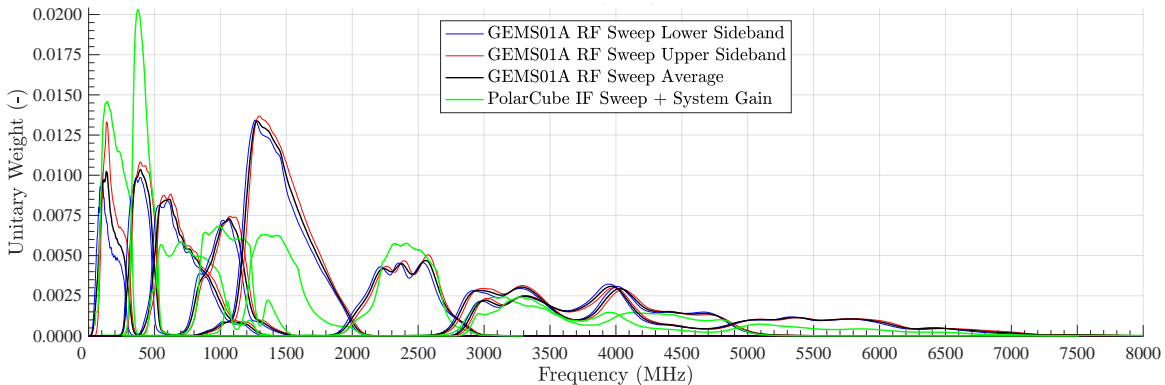


Figure 5.22: Comparisons between the unitary passband weights of the IF spectral response measured on the PolarCube MiniRad, and the RF spectral response measured on the GEMS-01A MiniRad instruments are depicted.

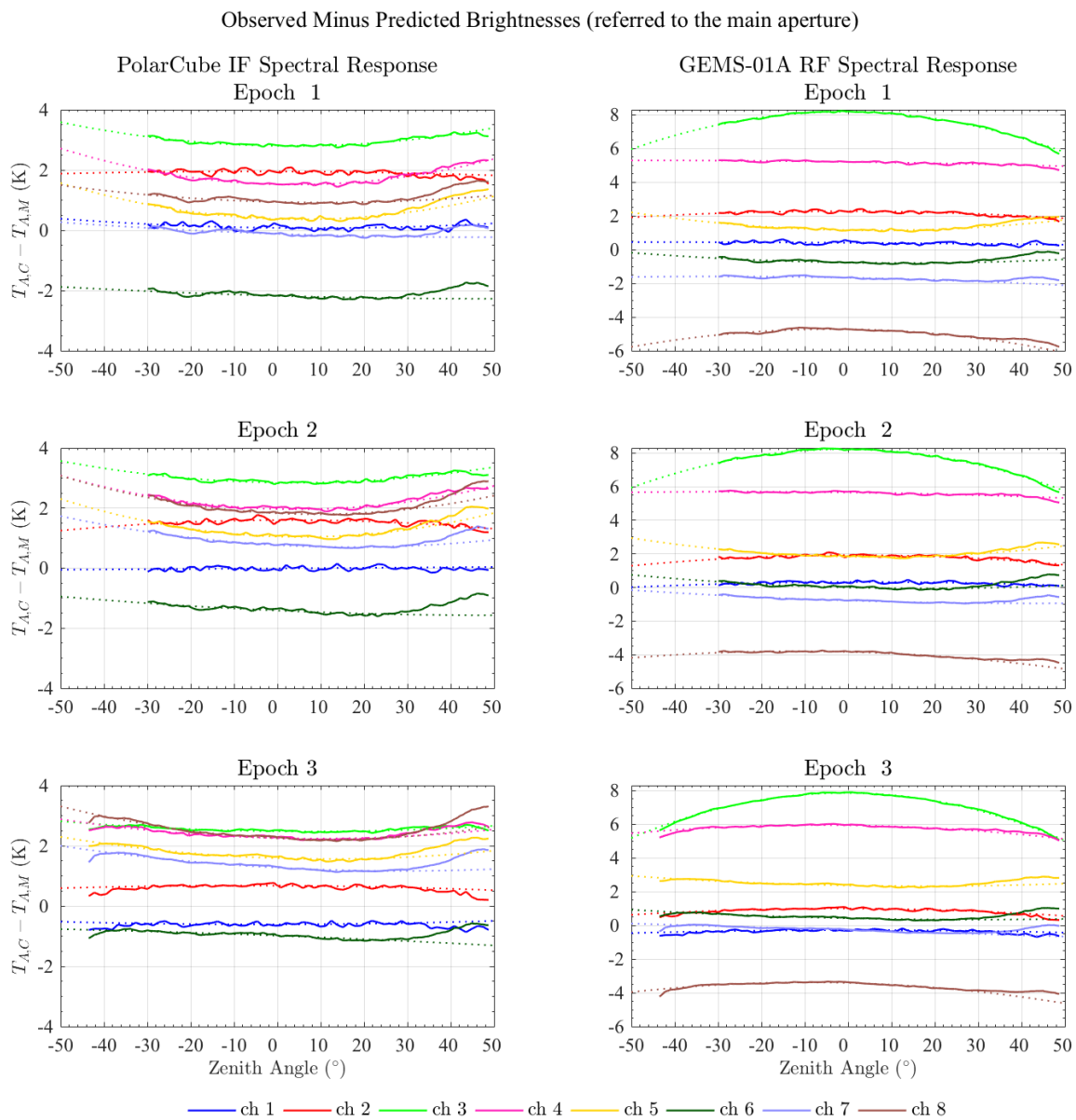


Figure 5.23: Antenna temperature discrepancies as a function of zenith angle (main beam pointing direction) are shown for skyscan measurements taken over three ~ 30 minute epochs for ~ 1.5 hours after the radiosonde launch.

angles away from 0°) arise largely due to an imprecise knowledge of the Eulerian angles which map the radiometer antenna spherical coordinate system and the earth's coordinate system. As the calibration chamber was not perfectly leveled during the experiment, an error of $\sim 2^\circ$ was estimated in the pitch angle obtained from a SolidWorks model of the calibration chamber and the instrument. This correction was incorporated into the coordinate system mapping to remove a ~ 2 K scan curvature error.

- (c) Other sources of brightness discrepancies < 1 K include use of the simulated rather than the true measured far field antenna pattern to compute the antenna temperatures from MRT brightnesses, and the presence of a ~ 3 mm thick sheet of S/MMW transparent Zotefoam window.

Further, a comparison between the IF and RF unitary passband weights (Figure 5.22) used in the MRT program clearly show gain variations that can cause differences of several Kelvin in the computed brightness temperatures obtained. The IF LNA gain used on the GEMS-01A instrument is not identical to that on the PolarCube MiniRad (which uses a much older Miteq amplifier). Additionally, its RF front-end includes a waveguide ferrite isolator and a ~ 5 cm waveguide section, both accounting for a front-end loss of ~ 0.6 dB. Such differences could cause brightness discrepancies of several Kelvin as seen in the right hand side plots of Figure 5.23.

5.6.3 PIN Diode Noise Temperature Calibration

The radiometer performance as a function of ambient temperature could not be measured in a standard thermal chamber. So, in order to determine the PIN diode noise characteristics with respect to physical temperatures of the RF front-end components, measurements from the bridge-scan and Marshall field experiments were used (Figure 5.25). The radiometer chassis temperature dropped from -10°C to -30°C during the bridge-scan test while the Marshall test caused the chassis temperature to swing between -10°C and $+6^\circ\text{C}$ (Table 5.1). The noise reference statistics clearly differ across channels, but follow a linear trend during both experiments. However, a 4 K offset is

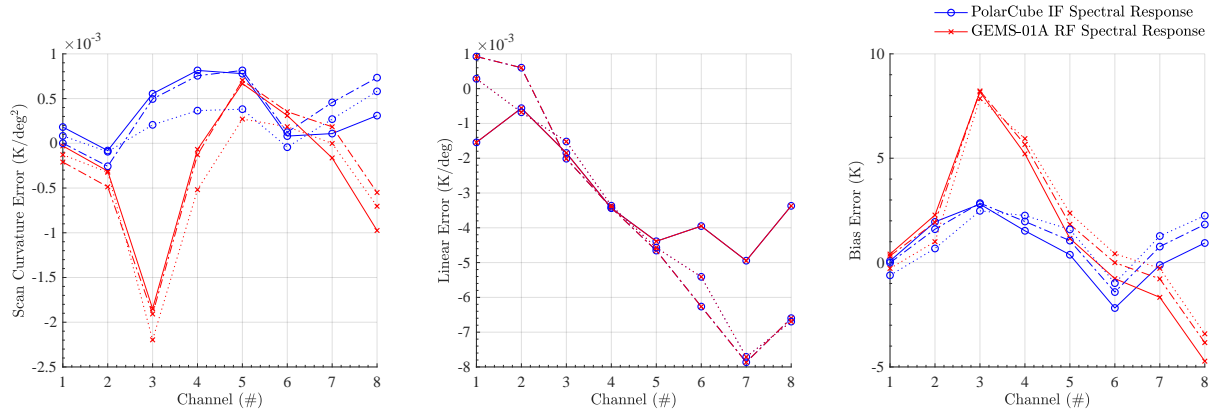


Figure 5.24: Plots of the second-order statistics of the brightness discrepancies for the eight radiometric channels.

seen between the datasets obtained from the two experiments (at ~ 10 °C) that were conducted a few days apart at different locations. The offset is roughly constant across all channels indicating that it is not frequency dependent, and could be a calibration offset error.

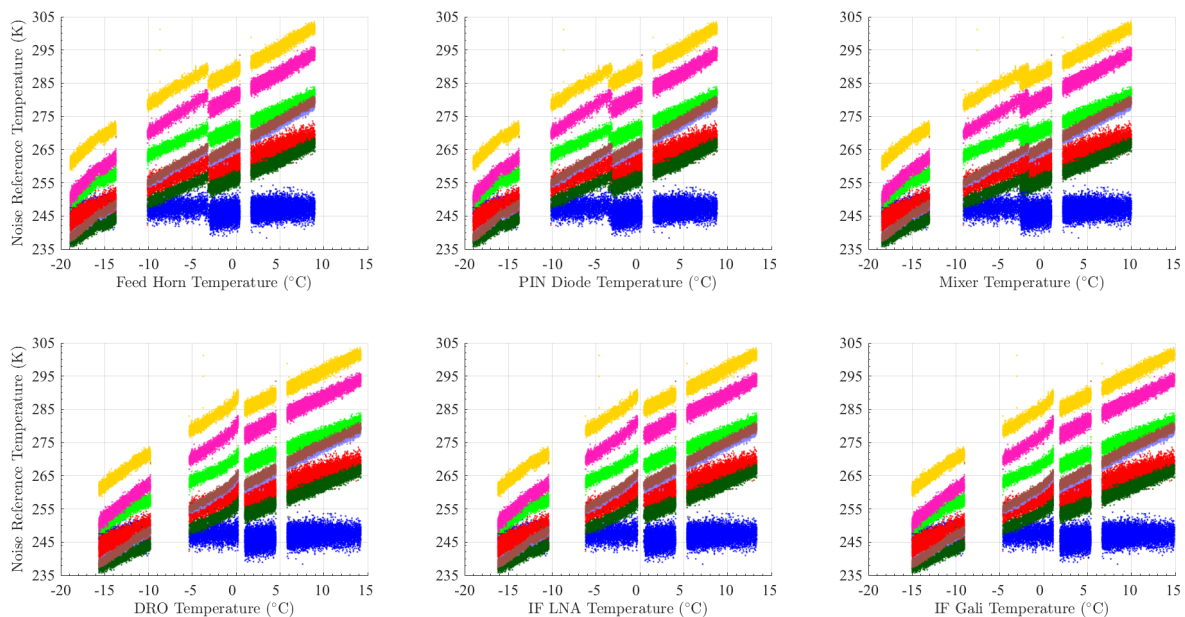


Figure 5.25: These set of plots combine data from the bridge-scan and Marshall field experiments in order to determine an estimate of noise reflected off the PIN diode as a function of physical temperature of front-end components.

Chapter 6

Conclusion

The electrical end-to-end design, development and prelaunch calibration of a low cost (< 0.25 million USD) 118.7503 GHz radiometer for CubeSat missions has been described in this dissertation. It is a demonstrator for a constellation of similar low earth orbit passive microwave sensors for weather forecasting at high spatial and temporal resolution. The radiometer has been built with limited funding, and many of its design challenges and manufacturing choices were associated with the project's limited budget, in addition to CubeSat 1.5U envelope constraints. The radiometer's performance has been successfully verified during two sky scan experiments in February 2018, as well as from images obtained during the NASA Operation Ice Bridge airborne experiment over Antarctica in Oct-Nov 2016.

6.1 Summary of Thesis

The overall design choices and specifications of the MiniRad radiometer are introduced in Chapter 1. A technical introduction to microwave radiative transfer theory, and the basics of atmosphere temperature profile retrieval using linear minimum mean square estimation has also been provided. Next, a thorough mathematical examination of radiometer received power, and MiniRad's hybrid two-point calibration scheme entails the key objectives of prelaunch calibration of the radiometer. These include precise estimation of antenna efficiencies, location of spillover lobes, reflector loss and thermal emission, RF+IF spectral response, LNA gain and insertion losses, and calibrated noise power measurements during the PIN diode ON state as a function of physical

temperature. Design and test procedures in the subsequent chapters mainly stem from these considerations.

The requirement for precise numerical analysis of the corrugated feed horn and offset reflector antenna system arises from the need to determine antenna main beam and spillover efficiencies, optimal feed horn and reflector geometry that maximizes these efficiencies, phase center location that maximizes phase efficiency, and finally the antenna's spatial radiometric response before launch. Chapter 2 describes a HE_{11} mode based full wave Fourier Bessel field analysis that has been developed to fulfill the aforementioned objectives with high accuracy on a standard desktop computer. It includes complete analytical derivation of radiated near and far zone electromagnetic fields, as well as the implementation of a Matlab-based software suite to compute these fields at the reflector and its main aperture at various scan angles. The full wave analysis provided a reliable and efficient means for estimating antenna parameters during the design phase. The computed main aperture spillover and main beam efficiencies at the 118.75 GHz center frequency using this analysis were 91.8% and 89.5% (respectively). The phase center of the antenna system was estimated to be 13.5 mm behind the feed horn aperture along its axis. The antenna system model was also implemented in ANSYS[®] HFSS, and both simulations show excellent agreement.

The feasibility of using a 3D-printed corrugated horn operating between 110 GHz and 126 GHz as feed for the 118.75 GHz 3U CubeSat temperature sounding radiometer was investigated primarily due to the very low cost and fast turn-around time of 3D printed components. The horn's corrugations were modified and optimized to enable the 3D printed process, and includes a rectangular to circular waveguide transition with a 17.28° bend to accommodate an offset paraboloidal reflector with maximum aperture area. A batch of five such horns were procured for $\lesssim 1000$ USD, a fraction of the cost of a single electroformed corrugated horn. Antenna measurements indicated a reflection coefficient below -15 dB and a far field pattern that compares closely with HFSS simulations. Although there is some asymmetry in the horn pattern, calculations of the measured beam efficiency function using the CROMMA measurements yield an average spillover of 89.08% at the 16° reflector half-angle. This number is indicative of the expected spillover efficiency of

the antenna subsystem with the 3D-printed horn. Since the reflector is in the near zone of the feed horn, a somewhat higher spillover efficiency could be expected since the beam remains partly collimated in the near zone.

An important contribution towards the development of this low cost radiometer is the IF-VA spectrometer, a four layer RO4350B and FR4 hybrid stack-up PCB that consists of an eight channel filterbank between 50 MHz to 8 GHz with bandwidths between 250 MHz and 2.2 GHz, as well as two-stage MMIC amplifiers, power detector diodes, chopper-stabilized op-amp circuitry and analog-to-digital conversion for each channel. The low cost and compact filterbank has been designed with seven contiguous cascaded diplexers implemented as coplanar waveguide and lumped-element combinations using off-the-shelf surface mount components taking into consideration all associated parasitics. The filterbank was first implemented as a two layer PCB during the design phase, and measured filterbank responses compared closely with simulation results obtained in the NI AWR circuit design environment. The IF and VA were then combined into a single 4-layer PCB. The VNA measurements of $|S_{21}|$ on four such PCBs were identical to within 0.1 dB indicating excellent repeatability in the filterbank design.

Detailed laboratory experiments and studies were conducted to precisely tune the GAT attenuators before the detector diodes, and the op-amp gain and offset resistors to maximize radiometer sensitivity (in mv/K) across all channels. The author also worked on the cross-talk estimation across the video amplifier channels, digital board power supply regulation circuitry design and output voltage accuracy, and thermistor circuitry design. A considerable amount of time was spent in debugging grounding issues at the ADC and digital board that caused millivolt level fluctuations between the analog and digital ground levels.

The radiometer was part of NASA's IceBridge mission as a 'piggyback' airborne instrument aboard the NASA DC-8 (Oct 24 - Nov 02, 2016). At an aircraft altitude of $\sim 33,000$ ft, images with resolution 380 m or better were captured over Antarctica. First light images obtained from the 118 GHz spectrometer during these airborne experiments depict sharp land and water boundaries, and indicate a well focused scanning reflector antenna system with high main beam efficiency.

Antenna temperature signatures obtained from 6 of 8 channels suggest the ability of the compact filterbank to separate channels around the 118.75 GHz oxygen resonance. The primary objective of this experiment was not to obtain science data, but to prove the functionality of this low-cost radiometer outside laboratory environment.

After the IceBridge mission, several hardware issues were identified and resolved on the radiometer including the interference of the PIN diode switching current and the mirror motor current with radiometric signals, and EMI and RFI issues on channels 2 and 3 whose IF bandwidths fall around the L-band frequency spectrum. Mechanical issues with the mirror motor bearing, the IF carriers, the mating connector between the IF and digital boards, etc. were also corrected. Laboratory experiments and studies carried out to estimate radiometer performance included bench-top and roof-top Y-factor tests, $1/f$ noise estimation, radiometer gain stability with temperature variations, Gaussianity of the data, and pressure cycling. After final integration of the radiometer to the CubeSat envelope, two field experiments were planned for its prelaunch calibration. To this end, a low budget measurement chamber was designed and built in the CET laboratory utilizing an existing freezer re-purposed to house the packaged instrument, as well as the hot and cold external calibration targets. Final sky-scan measurements before instrument delivery were conducted in Boulder, CO in Feb-Mar, 2018.

Measurements from the bridge-scan experiment helped determine the step response of MiniRad, and provided a good estimate of the antenna's performance, more so in the absence of true radiated antenna pattern measurements. In this experiment, the beam transitions the boundary between the warm bridge and the cold sky in ~ 1 beamwidth. Derived impulse responses of the 8-channel radiometer antenna system obtained from the measured step responses were compared with the simulated far field main beam. The measured 3 dB main beamwidths lie between 2.3° and 2.35° across the 8 channels, and agree closely with the 118.75 GHz simulated beamwidth of 2.2° .

The second sky-scan experiment at the UCAR Marshall field site coincided with a radiosonde launch. For integration time $\tau_i = NT_S = 16 \times 256 \mu s = 4.096$ ms, measured radiometer sensitivities averaged over a 30-minute interval $\langle \Delta T_{rms} \rangle$ vary between 0.92 K and 2.84 K, and agree closely

with theoretical calculations to within ~ 0.5 K across the eight channels. A precisely calibrated 50-satellite constellation of similar radiometers will improve the overall sensitivity by a factor of $\sqrt{50}$. Absolute antenna temperature (brightness) discrepancies, obtained by comparison with a simple non-scattering planar stratified MRT model using the instrument's IF spectral response are below 3 K. Causes for these discrepancies have been mainly attributed to the use of the IF passband response in the MRT calculations that did not account for exact spectral variations in the RF front end. Secondly, the scan curvature errors arise largely due to an imprecise knowledge of the Eulerian angle mapping between the radiometer main beam and earth spherical coordinate systems.

6.2 Future CubeSat Radiometer Constellations

Multiple CubeSat radiometer constellation concepts are presently being developed and demonstrated by OMS and CU-CET, MIT-LL, NASA-JPL and NASA-GSFC for sounding of atmospheric temperature and humidity. OMS intends to launch a fleet of such CubeSats as part of its Global Environmental Monitoring System (GEMS) constellation [96]. The MiniRad radiometer provides a basis for the development of similar low cost, quick turnaround CubeSat radiometers for this constellation that can provide cost-effective time-resolved global measurements of temperature, humidity, and precipitation at high spatial and temporal resolution. The overall ΔT_{rms} of a constellation of N such radiometers with precise inter-calibration will be better than that of a single CubeSat radiometer by a factor of \sqrt{N} , a substantial improvement! Although inter-calibration is challenging and an active area of research currently, it is easy to note the attractiveness of such a fleet compared to a single conventional satellite sensor not only in terms of improving spatial and temporal coverage, but also with respect to lower cost and provision for the inclusion of regularly updated radiometer technology. Important applications of such a constellation of millimeter wave radiometers include tropospheric temperature profiling in clear air, thick cloud and precipitation cell imaging, sea-ice edge mapping, and warm core hurricane imaging.

Bibliography

- [1] A. Murk, “Ticra[®] GRASP simulation of the PolarCube corrugated horn and reflector.” Personal communication, Sep. 2017.
- [2] M. L. Meeks and A. E. Lilley, “The Microwave Spectrum of Oxygen in the Earth’s Atmosphere,” *Journal of Geophysical Research*, vol. 68, no. 6, pp. 1683–1703, 1963.
- [3] D. H. Staelin, “Passive Remote Sensing at Microwave Wavelengths,” *Proceedings of the IEEE*, vol. 57, no. 4, pp. 427–439, 1969.
- [4] M. Klein and A. Gasiewski, “Nadir Sensitivity of Passive Millimeter and Submillimeter Wave Channels to Clear Air Temperature and Water Vapor Variations,” *Journal of Geophysical Research: Atmospheres*, vol. 105, no. D13, pp. 17 481–17 511, 2000.
- [5] Hall, E. and Jordan, A., “Ozone and Water Vapor Group, NOAA ESRL Global Monitoring Division.” Personal communication, Mar. 2018.
- [6] (1991) Thermodynamic Initial Guess Retrieval (TIGR) data set. [Online]. Available: <http://ara.abct.lmd.polytechnique.fr/index.php?page=tigr>
- [7] National Research Council, *Thriving on Our Changing Planet: A Decadal Strategy for Earth Observation from Space*. Washington, DC: The National Academies Press, 2017. [Online]. Available: <http://nap.edu/24938>
- [8] —, *Earth Science and Applications from Space: National Imperatives for the Next Decade and Beyond*. Washington, DC: The National Academies Press, 2007. [Online]. Available: <http://nap.edu/11820>
- [9] (2018) CubeSat Standard. [Online]. Available: <http://www.cubesat.org/>
- [10] Z. Li, J. Li, T. J. Schmitt, P. Wang, A. Lim, J. Li, F. W. Nagle, W. Bai, J. A. Otkin, R. Atlas et al., “The Alternative of CubeSat-based Advanced Infrared and Microwave Sounders for High Impact Weather Forecasting,” *Atmospheric and Oceanic Science Letters*, pp. 1–11, 2019.
- [11] A. Geer, M. Ahlgrimm, P. Bechtold, M. Bonavita, N. Bormann, S. English, M. Fielding, R. Forbes, R. Hogan, E. Hólm et al., *Assimilating observations sensitive to cloud and precipitation*. European Centre for Medium-Range Weather Forecasts, 2017.
- [12] A. J. Gasiewski, B. T. Sanders, and D. Gallaher, “Cubesat based sensors for global weather forecasting,” in *2013 US National Committee of URSI National Radio Science Meeting (USNC-URSI NRSM)*. IEEE, 2013, pp. 1–1.

- [13] (2017, Feb.) Application of a CubeSat-Based Passive Microwave Constellation to Operational Meteorology. [Online]. Available: <https://www.eumetsat.int/website/home/Data/ScienceActivities/VisitingScientists/ApplicationofaCubeSatBasedPassiveMicrowaveConstellationtoOperationalMeteorology/index.html?lang=EN>
- [14] J. Schoolcraft, A. T. Klesh, and T. Werne, "MarCO: Interplanetary Mission Development on a CubeSat Scale," in 14th International Conference on Space Operations, 2016, p. 2491.
- [15] A. J. Gasiewski, J. W. Barrett, P. G. Bonanni, and D. H. Staelin, "Aircraft-based Radiometric Imaging of Tropospheric Temperature and Precipitation using the 118.75 GHz Oxygen Resonance," *Journal of Applied Meteorology*, vol. 29, no. 7, pp. 620–632, 1990.
- [16] A. D. Ali, P. W. Rosenkranz, and D. H. Staelin, "Atmospheric Sounding Near 118 GHz," *Journal of Applied Meteorology*, vol. 19, no. 10, pp. 1234–1238, 1980.
- [17] M. J. Schwartz, J. W. Barrett, P. W. Fieguth, P. W. Rosenkranz, M. S. Spina, and D. H. Staelin, "Observations of Thermal and Precipitation Structure in a Tropical Cyclone by means of Passive Microwave Imagery near 118 GHz," *Journal of Applied Meteorology*, vol. 35, no. 5, pp. 671–678, 1996.
- [18] W. J. Blackwell, J. W. Barrett, F. W. Chen, R. V. Leslie, P. W. Rosenkranz, M. J. Schwartz, and D. H. Staelin, "NPOESS Aircraft Sounder Testbed- Microwave (NASt-M): Instrument Description and Initial Flight Results." *IEEE Transactions on Geoscience and Remote Sensing*, vol. 39, no. 11, pp. 2444–2453, Nov. 2001.
- [19] F. Weng, X. Zou, X. Wang, S. Yang, and M. Goldberg, "Introduction to Suomi National Polar Orbiting Partnership Advanced Technology Microwave Sounder for Numerical Weather Prediction and Tropical Cyclone Applications," *Journal of Geophysical Research: Atmospheres*, vol. 117, no. D19, 2012.
- [20] S. Padmanabhan, T. C. Gaier, S. C. Reising, B. H. Lim, R. Stachnik, R. Jarnot, W. Berg, C. D. Kummerow, and V. Chandrasekar, "Radiometer payload for the Temporal Experiment for Storms and Tropical Systems Technology Demonstration Mission," in 2017 IEEE International Geoscience and Remote Sensing Symposium (IGARSS). IEEE, 2017, pp. 1213–1215.
- [21] A. Crews, W. Blackwell, R. V. Leslie, M. Grant, I. Osaretin, M. DiLiberto, A. Milstein, and K. Cahoy, "Calibration and Validation of Small Satellite Passive Microwave Radiometers: MicroMAS-2A and TROPICS," in *Active and Passive Microwave Remote Sensing for Environmental Monitoring II*, vol. 10788. International Society for Optics and Photonics, 2018, p. 107880Y.
- [22] W. J. Blackwell, S. Braun, R. Bennartz, C. Velden, M. DeMaria, R. Atlas, J. Dunion, F. Marks, R. Rogers, B. Annane et al., "An Overview of the TROPICS NASA Earth Venture Mission," *Quarterly Journal of the Royal Meteorological Society*, vol. 144, pp. 16–26, 2018.
- [23] S. C. Reising, P. Kangaslahti, E. Schlecht, J. Jiang, X. Bosch-Lluis, M. Ogut, Y. Goncharenko, S. Padmanabhan, R. Cofield, N. Chahat et al., "Tropospheric Water and Cloud ICE (TWICE) Millimeter and Submillimeter-wave Radiometer Instrument for 6U-Class Nanosatellites," in 2016 41st International Conference on Infrared, Millimeter, and Terahertz waves (IRMMW-THz). IEEE, 2016, pp. 1–2.

- [24] Liebe, H.J. and Hufford, G.A. and Cotton, M.G., "Propagation Modeling of Moist Air and Suspended Water/Ice Particles at Frequencies below 1000 GHz," in AGARD, Atmospheric Propagation Effects Through Natural and Man-Made Obscurants for Visible to MM-Wave Radiation 11 p (See N94-30495 08-32), 1993.
- [25] J. D. Kraus, M. Tiuri, A. V. Räsänen, and T. D. Carr, Radio Astronomy. Powell, Ohio: Cygnus-Quasar Books, 1986, no. 69.
- [26] M. A. Janssen, Atmospheric Remote Sensing by Microwave Radiometry. John Wiley and Sons, 1994.
- [27] S. Chandrasekhar, Radiative Transfer. Dover, New York, 1960.
- [28] G. Rybicki and A. Lightman, Radiative Processes in Astrophysics. Wiley, New York, 1979.
- [29] F. T. Ulaby, R. K. Moore, and A. K. Fung, Remote Sensing: Active and Passive, vol. 1, Microwave Remote Sensing Fundamentals and Radiometry. Addison-Wesley, Boston, Mass, 1981, no. 1.
- [30] L. Tsang, J. A. Kong, and R. T. Shin, Theory of Microwave Remote Sensing. Wiley, New York, 1985.
- [31] A. J. Gasiewski, Atmospheric Temperature Sounding and Precipitation Cell Parameter Estimation using Passive 118 GHz O_2 Observations. PhD Thesis. Massachusetts Institute of Technology, Department of Electrical Engineering and Computer Science, 1988.
- [32] M. Dieml, The Thermal-Structure-Optical System Design and Analysis of the Satellite PolarCube. MS Thesis. Technical University of Munich, Institute of Astronautics, 2013.
- [33] M. Bukart, Integration and Test of the MiniRad Radiometer of the Satellite PolarCube. MS Thesis. Technical University of Munich, Institute of Astronautics, 2015.
- [34] A. Gasiewski and J. Johnson, "Statistical Temperature Profile Retrievals in Clear-air Using Passive 118-GHz O_2 Observations," IEEE Transactions on Geoscience and Remote Sensing, vol. 31, no. 1, pp. 106–115, Jan. 1993.
- [35] T. Mo, "Prelaunch Calibration of the Advanced Microwave Sounding Unit-A for NOAA-K," IEEE Transactions on Microwave Theory and Techniques, vol. 44, no. 8, pp. 1460–1469, Aug. 1996.
- [36] C. A. Balanis, Antenna Theory: Analysis and Design. John Wiley and Sons, 2015.
- [37] A. Stogryn, "Estimates of Brightness Temperatures from Scanning Radiometer Data," IEEE Transactions on Antennas and Propagation, vol. 26, no. 5, pp. 720–726, 1978.
- [38] E. G. Njoku, "Antenna Pattern Correction Procedures for the Scanning Multichannel Microwave Radiometer (SMMR)," Boundary-Layer Meteorology, vol. 18, no. 1, pp. 79–98, 1980.
- [39] D. A. Houtz, NIST Microwave Blackbody: The Design, Testing, and Verification of a Conical Brightness Temperature Source. Aerospace Engineering Sciences Graduate Theses and Dissertations. 164. University of Colorado at Boulder., 2017. [Online]. Available: https://scholar.colorado.edu/asen_gradetds/164

- [40] S. Sandeep, Broadband electromagnetic analysis of dispersive, periodic structures for radiometer calibration. Electrical, Computer and Energy Engineering Graduate Theses and Dissertations. 48. University of Colorado at Boulder., 2012. [Online]. Available: https://scholar.colorado.edu/ecen_gradetds/48
- [41] R. W. Saunders, T. J. Hewison, S. J. Stringer, and N. C. Atkinson, "The Radiometric Characterization of AMSU-B," *IEEE Transactions on Microwave Theory and Techniques*, vol. 43, no. 4, pp. 760–771, Apr. 1995.
- [42] E. Kim, C.-H. J. Lyu, K. Anderson, R. Vincent Leslie, and W. J. Blackwell, "S-NPP ATMS Instrument Prelaunch and On-orbit Performance Evaluation," *Journal of Geophysical Research: Atmospheres*, vol. 119, no. 9, pp. 5653–5670, 2014.
- [43] R. Wylde and D. Martin, "Gaussian Beam-Mode Analysis and Phase-Centers of Corrugated Feed Horns," *IEEE Transactions on Microwave Theory and Techniques*, vol. 41, no. 10, pp. 1691–1699, Oct. 1993.
- [44] R. E. Collin, *Antennas and Radiowave propagation*. McGraw-Hill, 1985.
- [45] G. Borgiotti, "Fourier Transforms Method of Aperture Antennas," *Alta Freq.*, vol. 32, pp. 196–204, Nov. 1963.
- [46] D. Pujara, S. Sharma, and S. Chakrabarty, "Historical and planned uses of antenna technology for space-borne microwave radiometers," *IEEE Antennas and Propagation Magazine*, vol. 53, no. 3, pp. 95–114, 2011.
- [47] J. Shiue and L. R. Dod, "Remote sensing and microwave radiometry," in *Antenna Handbook*. Springer, 1993, pp. 514–569.
- [48] P. J. B. Clarricoats and A. D. Olver, *Corrugated Horns for Microwave Antennas*. IEE Electromagnetic wave series, 1984, no. 18.
- [49] P. A. Ade, R. J. Wylde, and J. Zhang, "Ultra-Gaussian horns for CLOVER – a B-mode CMB experiment," in *Twentieth International Symposium on Space Terahertz Technology*, Apr. 2009, p. 128.
- [50] P. A. Cruickshank, D. R. Bolton, D. A. Robertson, R. J. Wylde, and G. M. Smith, "Reducing Standing Waves in Quasi-optical Systems by Optimal Feedhorn Design," in *Infrared and Millimeter Waves, 2007 and the 2007 15th International Conference on Terahertz Electronics. IRMMW-THz. Joint 32nd International Conference on*, Sep. 2007, pp. 941–942.
- [51] P. Potter, "A New Horn Antenna with Suppressed Sidelobes and Equal Beamwidths," *Microwave Journal*, pp. 71–78, Jun. 1963.
- [52] L. Zeng, C. L. Bennett, D. T. Chuss, and E. J. Wollack, "A Low Cross-polarization Smooth-walled Horn with Improved Bandwidth," *IEEE Transactions on Antennas and Propagation*, vol. 58, no. 4, pp. 1383–1387, Apr. 2010.
- [53] G. L. James, "Analysis and Design of TE₁₁-to-HE₁₁ Corrugated Cylindrical Waveguide Mode Converters," *IEEE Transactions on Microwave Theory and Techniques*, vol. 29, no. 10, pp. 1059–1066, 1981.

- [54] X. Zhang, "Design of Conical Corrugated Feed Horns for Wide-band High-frequency Applications," *IEEE Transactions on Microwave Theory and Techniques*, vol. 41, no. 8, pp. 1263–1274, Aug. 1993.
- [55] J. Lamb, "Optics Study for ALMA Receivers," ALMA Memo 359.1., 2001.
- [56] M. Abramowitz and I. A. Stegun, *Handbook of mathematical functions: with formulas, graphs, and mathematical tables*. Courier Corporation, 1965, vol. 55.
- [57] D. Levin, "Procedures for Computing One-and two-dimensional Integrals of Functions with Rapid Irregular Oscillations," *Mathematics of Computation*, vol. 38, no. 158, pp. 531–538, 1982.
- [58] J. Li, X. Wang, T. Wang, and S. Xiao, "An Improved Levin Quadrature Method for Highly Oscillatory Integrals," *Applied Numerical Mathematics*, vol. 60, no. 8, pp. 833–842, 2010.
- [59] G. A. Evans and K. Chung, "Some Theoretical Aspects of Generalised Quadrature Methods," *Journal of Complexity*, vol. 19, no. 3, pp. 272–285, 2003.
- [60] B. J. Butler, "Requirements for Subreflector and Feed Positioning for ALMA Antennas," Unpublished Note, 2003.
- [61] J. Ruze, "Small Displacements in Parabolic Reflectors," Lincoln Laboratory Memorandum, Feb. 1969.
- [62] (2016) IceBridge. [Online]. Available: <https://icebridge.gsfc.nasa.gov/>
- [63] (2016) IceBridge. [Online]. Available: https://espo.nasa.gov/oib/flight_reports/DC-8_10_24_16_-_10_25_16
- [64] J. A. Gordon, D. R. Novotny, M. H. Francis, R. C. Wittmann, M. L. Butler, A. E. Curtin, J. R. Guerrieri, L. Periasamy, and A. J. Gasiewski, "An All-Metal, 3-D-Printed CubeSat Feed Horn: An Assessment of Performance Conducted at 118.7503 GHz Using a Robotic Antenna Range," *IEEE Antennas and Propagation Magazine*, vol. 59, no. 2, pp. 96–102, Apr. 2017.
- [65] "Technical Description EOSINT M 280," EOS GmbH: Electro Optical Systems. [Online]. Available: www.eos.info
- [66] *Standard Terminology for Additive Manufacturing Technologies*, ASTM International, ASTM Committee F42 on Additive Manufacturing Technologies Subcommittee F42. 91 on Terminology, 2012.
- [67] A. Simchi, F. Petzoldt, and H. Pohl, "On the Development of Direct Metal Laser Sintering for Rapid Tooling," *Journal of Materials Processing Technology*, vol. 141, no. 3, pp. 319–328, Nov. 2003.
- [68] F. Calignano, D. Manfredi, E. Ambrosio, L. Iuliano, and P. Fino, "Influence of Process Parameters on Surface Roughness of Aluminum Parts produced by DMLS," *International Journal of Advanced Manufacturing Technology*, vol. 67, no. 9-12, pp. 2743–2751, Aug. 2013.
- [69] "EOS Aluminium AlSi10Mg: Material data sheet - Flexline," EOS GmbH: Electro Optical Systems.

- [70] “EOS Application Note: Design rules for DMLS,” White Paper, EOS GmBH: Electro Optical Systems, 1997.
- [71] J. A. Gordon, D. R. Novotny, M. H. Francis, R. C. Wittmann, M. L. Butler, A. E. Curtin, and J. R. Guerrieri, “Millimeter-wave Near-field Measurements using Coordinated Robotics,” *IEEE Transactions on Antennas and Propagation*, vol. 63, no. 12, pp. 5351–5362, Dec. 2015.
- [72] IEEE Standard Test Procedures for Antennas, ANSI/IEEE Std Antenna Standards Committee, 1949-1979.
- [73] Geometrical Product Specifications Surface Texture: Profile method terms, definitions and surface texture parameters, ISO/TC 213 Std. ISO 4287: 1997+ Cor 1: 1998+ Cor 2: 2005+ Amd 1: 2009, 2009.
- [74] “RO4000® Series High Frequency Circuit Materials,” Rogers Corporation. [Online]. Available: [”https://www.rogerscorp.com”](https://www.rogerscorp.com)
- [75] “Microwave Office utilized under the University License Program.” National Instruments. [Online]. Available: <https://www.awrcorp.com/products/ni-awr-design-environment/microwave-office-software>
- [76] G. Matthaei, “Microwave filters, impedance-matching networks and coupling structures,” Artech House Book, 1980.
- [77] H. W. Bode, *Network Analysis and Feedback Amplifier Design*. Van Nostrand, Princeton, N.J., 1945.
- [78] “Modelithics smc models for ni awr utilized under the university license program,” Modelithics Inc.
- [79] A. J. Gasiewski, “Remote Sensing Signals and Systems: Lecture 9,” University of Colorado at Boulder, 2014.
- [80] “Precision, Ultralow noise, RRIO, Zero-Drift Op Amp ADA4528-1/ADA4528-2,” Analog Devices Inc., 2017.
- [81] V. Wong, “Lowest Noise Zero-Drift Amplifier has $5.6 \text{ nV}/\sqrt{\text{Hz}}$ Voltage Noise Density,” Analog Devices Inc., 2014.
- [82] S. Nghiem, I. Rigor, D. Perovich, P. Clemente-Colón, J. Weatherly, and G. Neumann, “Rapid Reduction of Arctic Perennial Sea Ice,” *Geophysical Research Letters*, vol. 34, no. 19, 2007.
- [83] P. Z. Peebles, *Probability, Random Variables, and Random Signal Principles (Vol. 3)*. McGraw-Hill, New York, NY, USA., 2001.
- [84] D. Cramer, *Fundamental Statistics for Social Research: step-by-step calculations and computer techniques using SPSS for Windows*. Routledge., 2003, no. p85.
- [85] M. G. Bulmer, *Principles of Statistics*. Courier Corporation., 1979.
- [86] M. S. Keshner, “ $1/f$ Noise,” *Proceedings of the IEEE*, vol. 70, no. 3, pp. 212–218, Mar. 1982.

- [87] C. Dietlein, Z. Popović, and E. Grossman, “Broadband THz Aqueous Blackbody Calibration Source,” *Passive Millimeter-Wave Imaging Technology*. International Society for Optics and Photonics., vol. 6548, no. 2, p. 65480M, May 2007.
- [88] J. R. Piepmeier and A. J. Gasiewski, “Polarimetric Scanning Radiometer for Airborne Microwave Imaging Studies,” in *Geoscience and Remote Sensing Symposium, IGARSS’96*. IEEE., vol. 2, May 1996, pp. 1120–1122.
- [89] “Zotefoam Technical Information Sheet,” ZOTEFOAMS, Aug. 2002. [Online]. Available: <http://www.zotefoams.com/wp-content/uploads/2016/01/TIS07.pdf>
- [90] R. Finger, “ALMA RF Membrane Simulations,” ALMA Memo, 2007.
- [91] Y. Inoue, P. Ade, Y. Akiba, C. Aleman, K. Arnold, C. Baccigalupi, B. Barch, D. Barron, A. Bender, D. Boettger et al., “POLARBEAR-2: An Instrument for CMB Polarization Measurements,” in *Millimeter, Submillimeter, and Far-Infrared Detectors and Instrumentation for Astronomy VIII*, vol. 9914. International Society for Optics and Photonics, 2016, p. 99141I.
- [92] “Viewrad: Matlab-based Calibration Software Module, version = 2.0, year =,” Center for Environmental Technology, University of Colorado at Boulder.
- [93] A. J. Gasiewski, “Environmental Signal Processing: Lecture 13,” University of Colorado at Boulder, 2012.
- [94] A. V. Oppenheim and G. C. Verghese, *Signals, Systems and Inference*. Pearson., 2015.
- [95] M. K. Steven, *Fundamentals of Statistical Signal Processing*. Prentice-Hall, Englewood Cliffs, NJ., 1993.
- [96] “Space Newsfeed: Orbital Micro Systems delivers payload for UK’s Space Applications Catapult mission,” Space Newsfeed, Microcom Systems Ltd, Mar. 2017. [Online]. Available: <http://www.spacenewsfeed.com/index.php/news/2035-orbital-micro-systems-delivers-payload-for-uk-s-space-applications-catapult-mission>

Appendix A

List of Symbols

Constant	Value	Dimension	Description
c	2.99793×10^8	m/s	speed of light in vacuum
e	2.718281828...	-	Euler's number
π	3.314592654...	-	Archimedes' constant
h	6.6252×10^{-34}	J-s	Planck's constant
k_B	1.38046×10^{-23}	J/K	Boltzmann's constant
ϵ_o	8.854×10^{-12}	F/m	permittivity of free space
μ_o	$4\pi \times 10^{-7}$	H/m	permeability of free space
η_o	376.73031346...	Ω	wave impedance of free space

Table A.1: Table of constants.

Symbol	Dimension	Description
ϵ	-	relative permittivity
λ	m	free space wavelength
f	s^{-1}	frequency
θ	$^\circ$	elevation angle
ϕ	$^\circ$	azimuthal angle
Ω	st	solid angle
θ_{3dB}	$^\circ$	antenna 3-dB beamwidth
η_{ph}	%	antenna main aperture phase efficiency
$\eta_b(\theta)$	%	antenna main aperture beam efficiency function
η_{bm}	%	antenna main aperture main beam efficiency
η_s	%	antenna main aperture spillover efficiency
η_t	%	antenna main aperture taper efficiency
$\eta_{bh}(\theta)$	%	feed horn beam efficiency function
η_l	%	antenna system radiation efficiency
ψ_S	$^\circ$	reflector scan angle
ω_S	rad/s	angular velocity of scanning mirror
τ_S	s	scanning mirror time period
τ_i	s	radiometer integration time
τ_D	s	detector diode RC time constant
τ_d	s	radiometer dwell time

Table A.2: Table of Greek symbols.

Symbol	Dimension	Description
k	m^{-1}	free space wave number $\triangleq \frac{2\pi}{\lambda}$
$\langle \cdot \rangle$	-	statistical mean of \cdot .
$\hat{\cdot}$	-	estimate of \cdot .
$\hat{\cdot}$	-	\cdot is a unit vector
$\text{Re}\{\cdot\}$	-	real part of \cdot .
$\text{Im}\{\cdot\}$	-	imaginary part of \cdot .
$(\cdot)^*$	-	conjugate of \cdot .
$ \cdot $	-	modulus of \cdot .
\vec{E}	V/m	complex electric field with components along \hat{x} , \hat{y} and \hat{z}
\vec{H}	A/m	complex magnetic field with components along \hat{x} , \hat{y} and \hat{z}
\vec{E}_a	V/m	complex HE ₁₁ mode electric field at the feed horn aperture
\vec{H}_a	A/m	complex HE ₁₁ mode magnetic field at the feed horn aperture
J_n	-	n^{th} order Bessel function
T	K	physical temperature
T_B	K	brightness temperature
T_A	K	antenna temperature
B_f	$\text{Wm}^{-2}\text{Hz}^{-1}\text{st}^{-1}$	Planck function
$B_f^{R,J}$	$\text{Wm}^{-2}\text{Hz}^{-1}\text{st}^{-1}$	Planck function in the Rayleigh-Jeans approximation
B_f^W	$\text{Wm}^{-2}\text{Hz}^{-1}\text{st}^{-1}$	Planck function in the Wein approximation
\vec{I}	$\text{Wm}^{-2}\text{Hz}^{-1}\text{st}^{-1}$	modified Stokes' vector
B_{NE}	Hz	noise equivalent bandwidth
B_C	Hz	convolutional bandwidth
$\overline{\overline{R}}_{XY}$	K^2	temperature covariance matrix of temperature vectors \overline{X} and \overline{Y}
\overline{D}	-	LMMSE retrieval operator
H_{SYS}	-	radiometer spectral response excluding its antenna system
\overline{G}_p	-	antenna gain matrix inclusive of loss

Table A.3: Table of Roman symbols.

Appendix B

List of Acronyms

3D	3-Dimensional
ADC	Analog to Digital Converter
BPF	Band Pass Filter
BW	Bandwidth
CPW	Co-planar Waveguide
CROMMA	Configurable Robotic Millimeter-wave Antenna
DMLS	Direct Metal Laser Sintering
DRO	Dielectric resonator Oscillator
DSB	Double Side Band
EMI	ElectroMagnetic Interference
FEM	Finite Element Method
GEMS	Global Environmental Monitoring System
GPS	Global Positioning System
HPF	High Pass Filter
IF	Intermediate Frequency
LEO	Low Earth Orbit
L/C	Inductance/Capacitance
LMMSE	Linear Minimum Mean Square Error
LNA	Low Noise Amplifier

LN ₂	Liquid Nitrogen
LPF	Low Pass Filter
LSB	Lower Side Band
MASL	Meters Above Sea Level
MRT	Microwave Radiative Transfer
MMW	Milli-Meter Wave
MMIC	Monolithic Microwave Integrated Circuit
MST	Mountain Standard Time
NF	Noise Figure
NWP	Numerical Weather Prediction
NTC	Negative Temperature Coefficient
OIB	Operation Ice Bridge
PIN	(P)-type (I)nttrinsic (N)-type
PSR	Polarimetric Scanning Radiometer
PCB	Printed Circuit Board
RF	Radio Frequency
RFI	Radio Frequency Interference
RMS	Root Mean Square
RTD	Resistive Temperature Device
SMC	Surface Mount Component
SMMW	Sub Milli-Meter Wave
TIGR	Thermodynamic Initial Guess Retrieval data set
TL	Transmission Line
USB	Upper Side Band
VA	Video Amplifier
VCVA	Voltage Controlled Variable Attenuator
VNA	Vector Network Analyzer

Appendix C

118.75 GHz Polar Atmosphere Weighting Functions

In this appendix, theoretical atmospheric temperature weighting functions over Polar land and ocean for the 8-channel MiniRad 118 GHz space-borne radiometer during summer and winter for $\{0^\circ, 30^\circ, 60^\circ\}$ zenith angles are plotted. The weighting functions have been generated using an in-house microwave radiative transfer program that assumes a non-scattering planar stratified atmosphere [31].

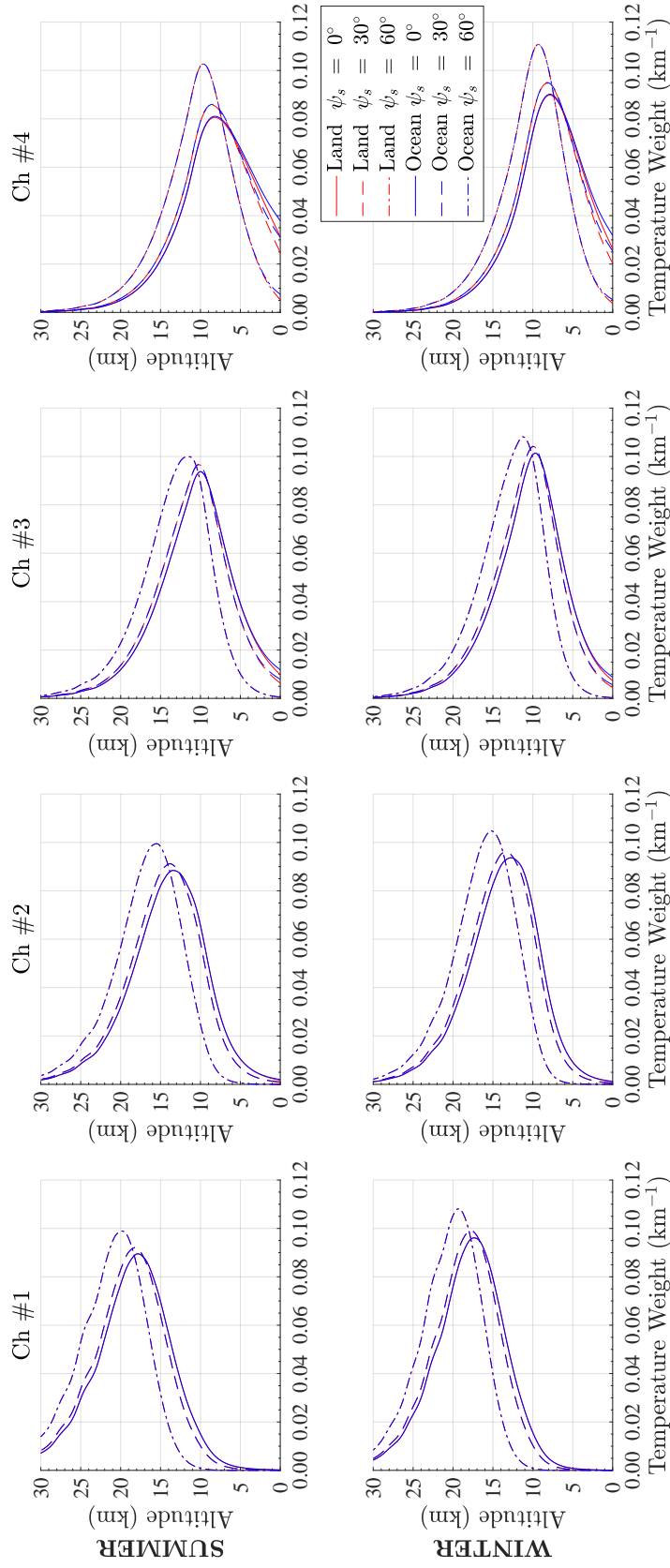


Figure C.1: Theoretical atmospheric temperature weighting functions for the four most opaque channels of the MiniRad 118 GHz spaceborne radiometer over Polar land and ocean during summer and winter for $\{0^\circ, 30^\circ, 60^\circ\}$ zenith angles.

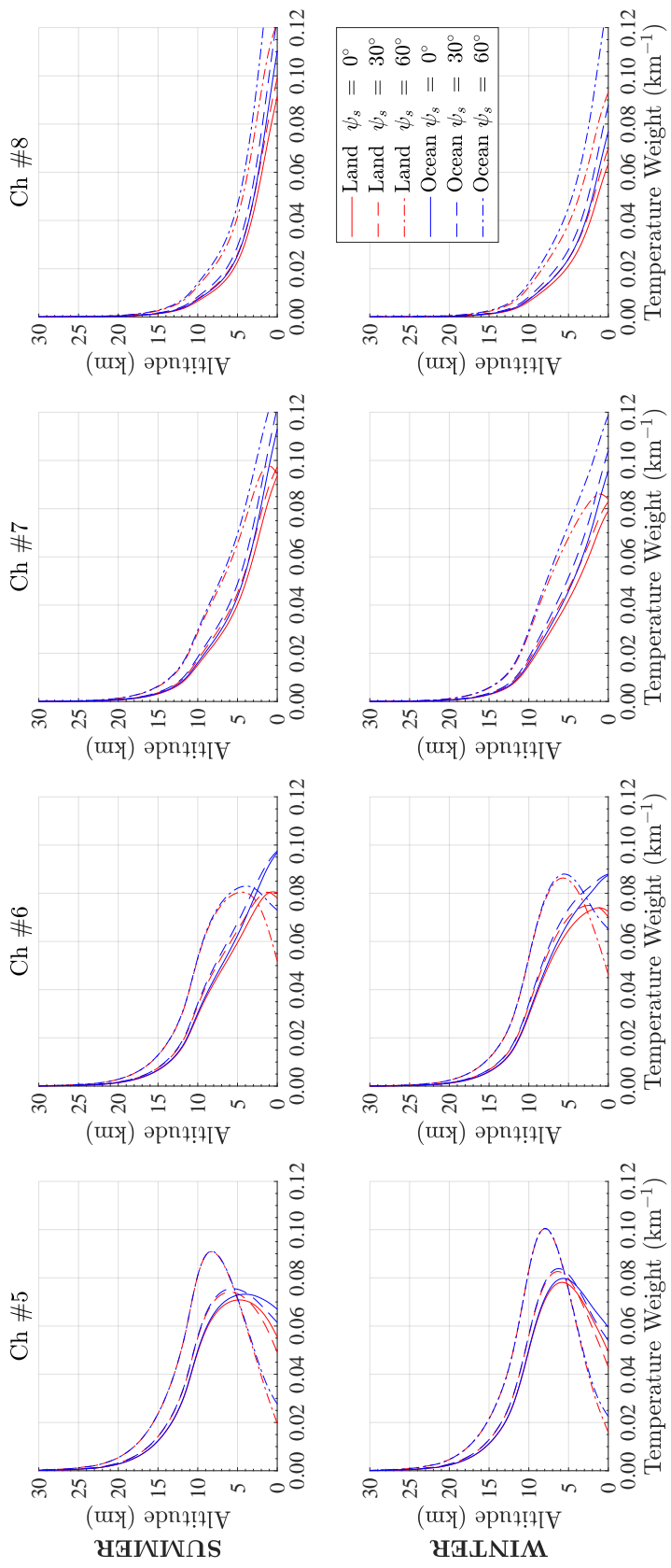


Figure C.2: Theoretical atmospheric temperature weighting functions for the four most transparent channels of the MiniRad 118 GHz space-borne radiometer over Polar land and ocean during summer and winter for $\{0^\circ, 30^\circ, 60^\circ\}$ zenith angles.

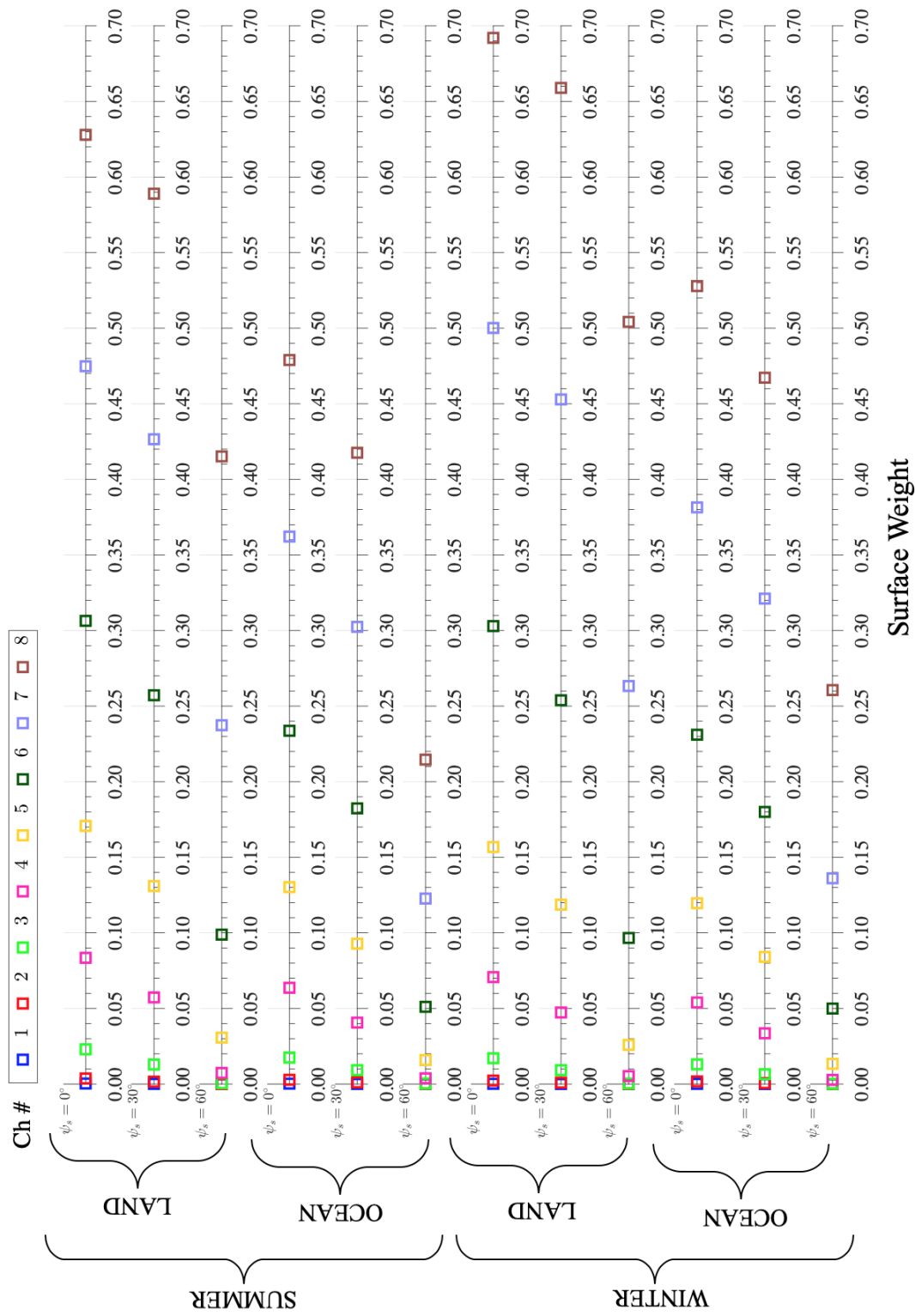


Figure C.3: Theoretical surface weights for the eight channels of the MiniRad 118 GHz space-borne radiometer over Polar land and ocean during summer and winter for $\{0^\circ, 30^\circ, 60^\circ\}$ zenith angles.

Appendix D

Antenna System Analytic Geometry

This appendix outlines the analytic geometry equations of the offset reflector and horn antenna developed in order to determine points in space at which the HE₁₁ mode based full wave analysis can be applied to compute the near and far zone electromagnetic fields.

The equation of the paraboloid, a section of which is the offset reflector, (see Figure 2.1) is given by:

$$(z \sin \psi_F + x \cos \psi_F)^2 + y^2 = 4f(f - z \cos \psi_F + x \sin \psi_F) \quad (\text{D.1})$$

Consider a cone of radiation from the focus of the reflector whose apex angle is θ_F . Initially, the reflector's focus or the radiation cone apex is assumed to be at the center of the feed horn's aperture, the origin of this cartesian coordinate system. The intersection of the paraboloid and the radiation cone will form the elliptic rim of the offset reflector on a plane tilted with respect to the feed horn axis. The equation of this elliptic rim can be determined in terms of the slope m_c of the line joining points P_1 and P_2 (Figure 2.1), the point z_{P_c} where this line intersects the feed horn axis, and the angle α between the normal to this line and the feed horn axis:

$$\frac{\left(x - \frac{z_{P_c} \tan \alpha}{\cot^2 \theta_F - \tan^2 \alpha}\right)^2}{\left(\frac{z_{P_c} \tan \theta_F \sec \alpha}{1 - \tan^2 \theta_F \tan^2 \alpha}\right)^2} + \frac{y^2}{\frac{(z_{P_c} \tan \theta_F)^2}{1 - \tan^2 \theta_F \tan^2 \alpha}} = 1 \quad (\text{D.2})$$

where $\alpha = \pi/2 - \tan^{-1}(m_c)$ and,

$$z_{P_c} = f \sec^2\left(\frac{\phi_2}{2}\right) \cos\left(\frac{\phi_2 - \phi_1}{2}\right) \left[1 - \frac{\tan\left(\frac{\phi_2 - \phi_1}{2}\right)}{m_c}\right]$$

Angles ϕ_1 and ϕ_2 are the angles between the axis of the paraboloid and points P_1 and P_2 respectively.

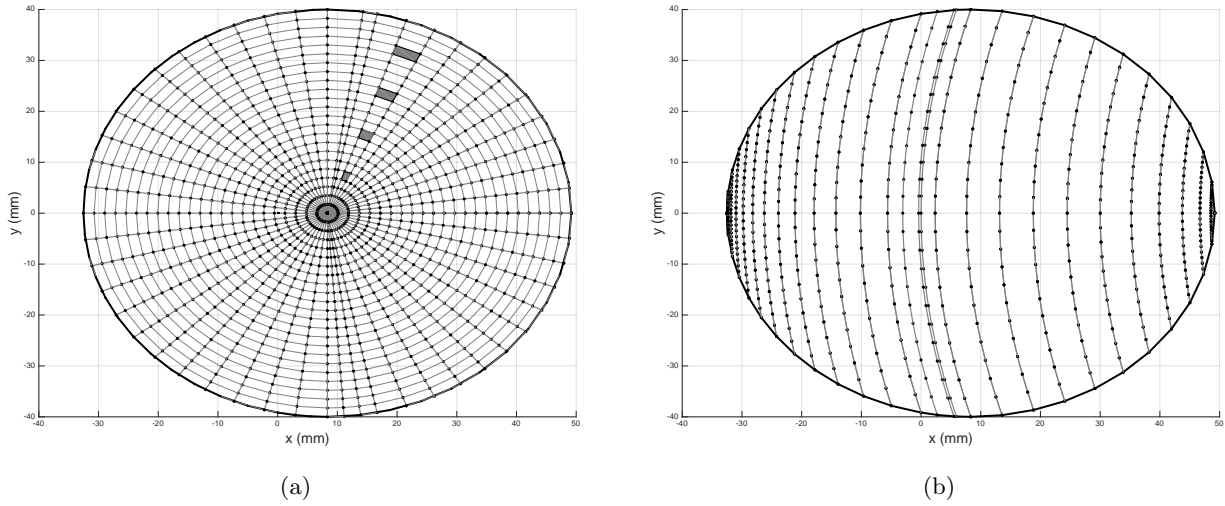


Figure D.1: The sampling schemes used on (a) the elliptic aperture, and (b) the reflector in order to determine the electromagnetic fields on their surfaces using the full wave Fourier transform method.

The elliptic aperture formed by the offset reflector is the area within this elliptic rim on the plane $z - x \tan \alpha = z_c$.

To accurately determine fields and power intercepted within this aperture, the elliptic area is sampled as a set of concentric ellipses (having identical eccentricity). Such a methodology achieved finer sampling near the aperture center, and allowed for minimum sampling error towards the edges of the elliptic aperture with coarser mesh sizes that could be handled on a desktop computer. Numerical integration of each quadrilateral element is carried out using nodal shape functions and Gaussian-Lobatto quadrature schemes. The inbuilt 2012-2014 Matlab quadrature functions for integration at the time of code development did not provide the level of accuracy needed for power conservation (below the -40 dB level).

Sample points on the reflector itself are determined by finding the locus of the intersection of closely spaced constant z -planes with the paraboloidal surface of the offset reflector (D.1) bounded by its elliptic rim (D.2). This locus is a set of elliptic contours whose parametric form is given in (D.3) where $\beta(z = z_o) \leq |\beta_{lim}(z = z_o)|$. The angular limit $\beta_{lim}(z = z_o)$ is found using the two points where the constant z -plane $z = z_o$ intersects the rim which are identical to the two extreme

points on the elliptic contour.

$$\begin{aligned}
 (x, y)_{(z=z_o)} &= (x^c + a \cos \beta, y^c + b \sin \beta)_{(z=z_o)} \\
 (x^c, y^c)_{(z=z_o)} &= (2f \tan \psi_F \sec \psi_F - z_o \tan \psi_F, 0) \\
 a_{(z=z_o)} &= 4f \sec^3 \psi_F (f \sec \psi_F - z_o) \\
 b_{(z=z_o)} &= 4f \sec \psi_F (f \sec \psi_F - z_o)
 \end{aligned}$$

where $(x^c, y^c)_{(z=z_o)}$ is the center of the ellipse of which the curve is a segment and, $a_{(z=z_o)}$ and $b_{(z=z_o)}$ its major and minor axes respectively.

D.1 Main Beam Scan Geometry

In Figure 2.1, the direction of the main beam is the normal to the main aperture plane containing the line $\overline{Q_1Q_2}$ (or the focal plane). The unit vector that represents the direction of the main beam for this reflector position is:

$$\hat{n} = \sin \psi_F \hat{x} + 0 \hat{y} - \cos \psi_F \hat{z} \quad (\text{D.3})$$

As the reflector scans, the main beam direction depends on the reflector scan angle ψ_S . The direction of the beam is then:

$$\begin{bmatrix} n_x^r \\ n_y^r \\ n_z^r \end{bmatrix} = \begin{bmatrix} \cos \psi_F & \sin \psi_F & 0 \\ -\sin \psi_F & \cos \psi_F & 0 \\ 0 & 0 & 1 \end{bmatrix} \begin{bmatrix} \sin \psi_F \\ 0 \\ -\cos \psi_F \end{bmatrix} \quad (\text{D.4})$$

Thus, the unit vector representing the main beam direction as a function of scan angle is:

$$\hat{n}^r = \cos \psi_S \sin \psi_F \hat{x} - \sin \psi_S \sin \psi_F \hat{y} - \cos \psi_F \hat{z} \quad (\text{D.5})$$

Appendix E

The Polar Fourier Transform

In the derivation of HE₁₁ mode based full wave electromagnetic fields, the Polar Fourier Bessel Transform was applied to the theoretical expressions for the aperture fields. For any non-radially symmetric function $f(r, \theta)$, its forward transform $F(\rho, \psi)$ is obtained as:

$$\begin{aligned}
 F(\rho, \psi) &= \int_{r=0}^{\infty} \int_{\theta=0}^{2\pi} f(r, \theta) e^{-jr\rho \cos(\psi-\theta)} r dr d\theta \\
 &= \left[\sum_{m=-\infty}^{\infty} f_m(r) e^{jm\theta} \right] \left[\sum_{n=-\infty}^{\infty} j^{-n} J_n(\rho r) e^{-jn(\theta-\psi)} \right] r dr d\theta \\
 &= \sum_{n=-\infty}^{\infty} \sum_{m=-\infty}^{\infty} j^{-n} \int_{r=0}^{\infty} f_m(r) J_n(\rho r) e^{jn\psi} \left[\int_0^{2\pi} e^{j\theta(m-n)} d\theta \right] r dr \\
 &= \sum_{n=-\infty}^{\infty} 2\pi j^{-n} e^{jn\psi} \int_{r=0}^{\infty} f_n(r) J_n(\rho r) r dr \tag{E.1}
 \end{aligned}$$

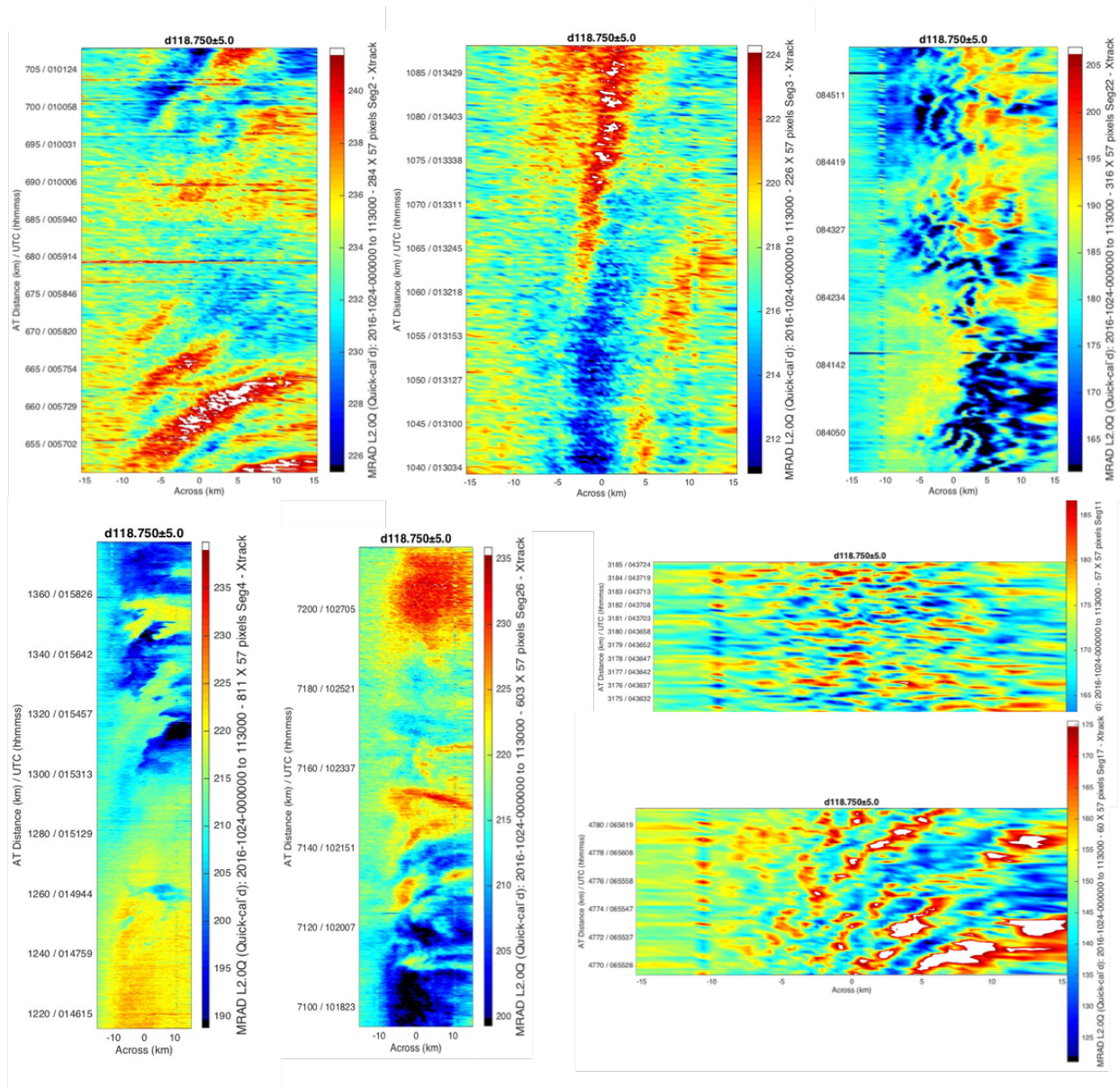
In (E.1), $f(r, \theta)$ and the exponential term are expanded in terms of their Fourier series. Also, it is to be noted that $\int_0^{2\pi} \exp(j(m-n)\theta) d\theta = 2\pi\delta_{mn}$ and equals 2π if $m = n$, and 0 otherwise. Similarly, the inverse transform is given by:

$$\begin{aligned}
 f(r, \theta) &= \frac{1}{(2\pi)^2} \int_{\rho=0}^{\infty} \int_{\psi=0}^{2\pi} F(\rho, \psi) e^{-jr\rho \cos(\psi-\theta)} \rho d\rho d\psi \\
 &= \frac{1}{(2\pi)^2} \sum_{n=-\infty}^{\infty} 2\pi j^n e^{jn\theta} \int_{\rho=0}^{\infty} F_n(\rho) J_n(\rho r) \rho d\rho \tag{E.2}
 \end{aligned}$$

Appendix F

Selected “First Light” Images from the OIB Experiment

A few antenna temperature maps obtained by the transparent channels of the MiniRad radiometer during the Ice Bridge experiment (Oct 24 to Nov 02, 2016) are reproduced here for representative purposes. The effect of the aircraft Rexolite[®] window has not been removed.



(a)

Figure F.1: Few antenna temperature maps obtained by the most transparent channel of the airborne MiniRad instrument aboard the NASA DC8 during the IceBridge experiment over Antarctica between Oct 24 and Nov 02, 2016. The effect of the aircraft Rexolite[®] window has not been removed. After this experiment, electrical and mechanical hardware corrections/improvements were made to the radiometer before its final integration in Feb 2018 (see Chapter 5)

Appendix G

Component Datasheets

Relevant manufacturer specifications of components used in the development of the MiniRad radiometer are included in this appendix.



46 Robezu str. • LV-1004 Riga • Latvia
 Phone: +371-7-065100
 Fax: +371-7-065102
 Mm-wave Division in St.Petersburg, Russia
 Phone: +7-812-326-59-24
 Fax: +7-812-326-10-60

CERTIFICATE

Voltage Controlled Variable Attenuator

Part No. VCVA-08

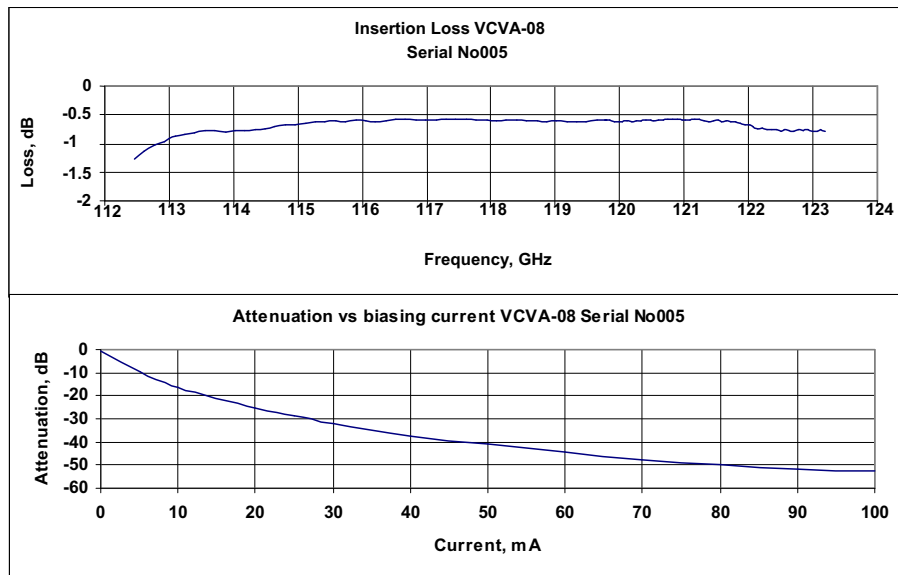
Serial No 005

Specifications.

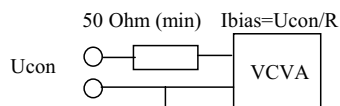
Frequency Band and Range, 113-123 GHz
 Insertion loss dB: 1
 Isolation dB (min): 50
 Power Handling (peak): 1.0
 Switching time mksec: 50
 DC max mA: 100
 Flanges: UG-387/U-M



Data of measuring



Scheme of control voltage feeding of VCVA attenuator:





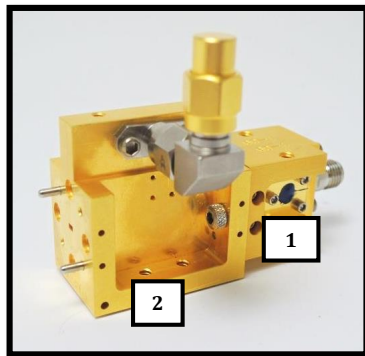
USER GUIDE

100-140 GHz Mixer Multiplier Chain (MixMC)

1 Product Overview

Product List (Quantity)	Serial Number(s)	Order No.	Date / Initials
100-140GHz MixMC (Mixer Multiplier Chain) (1)	VDI MixMC 131	14129 RSJ102014CO	11/17/2014 BTB

Product Description: This VDI product includes one 100-140GHz Mixer Multiplier Chain (MixMC).



VDI MixMC 131
WR16.0X3R1 1-09
WR8.0R5 1-15

Figure 1: Product photograph and listing is shown.

Note: Photographs and specifications of accessories (horns, waveguide straights, etc.) are not included in this user guide.

2 Warning and Caution Statements

WARNING AND CAUTION STATEMENTS	
WARNING	This product can be permanently damaged by Electrostatic Discharge (ESD). It is recommended that engineers and technicians wear a special grounded wrist strap when handling this component. In addition, the work environment around the component should be well grounded.
WARNING	Opening the blocks, parts, or components will damage the internal components. VDI is not responsible for the warranty or guaranty of products damaged as a result of improper handling, testing, biasing, or use by customer.
CAUTION	VDI assumes the customer is familiar with microwave, millimeter wave, and VDI products. The user and customer are expected to understand all safety guidelines, health hazards, and general advisories that may exist and are associated with the use of this device. VDI is not responsible for any human hazards that may exist or may occur while using this device.



Customer Code: CC1504
 PO Number: 11068874
 Job Number: 7257,RMA#151120-1

TEST DATA SHEET- DRO FREE RUNNING OSCILLATOR

Part Number: DRO-1070-19.79173	Customer P/N:
Serial Number: 7257-1419-001	Tester: MD5
Chassis NO(S):	Date: 12/14/2015

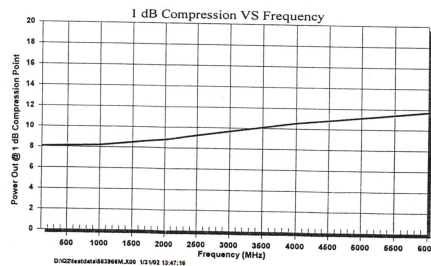
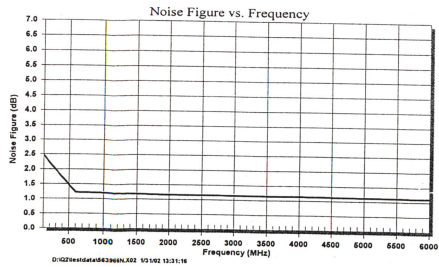
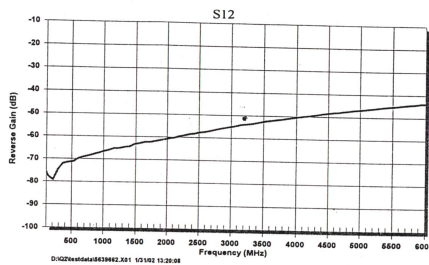
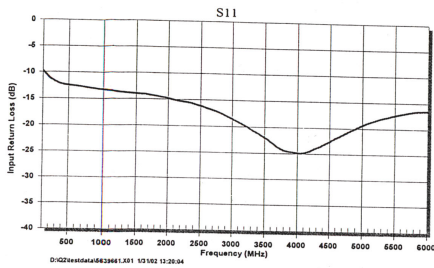
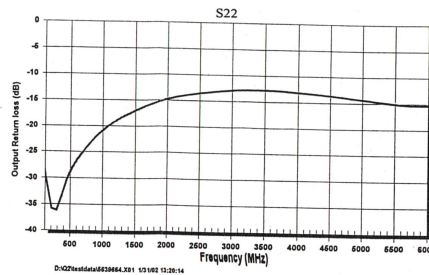
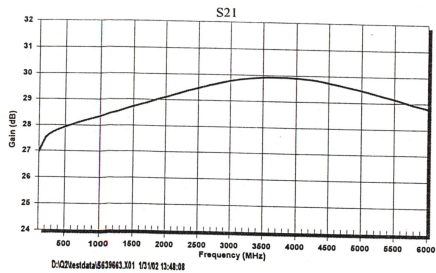
SPEC. PARA.	PARAMETER	TEST RESULTS	LIMITS	ACC	REJ
1.0	OUTPUT FREQUENCY	19.79173 (check)			
2.0	OUTPUT POWER at: +25°C	17.2 dBm	+16 dBm		
	+50°C	16.6 dBm			
	-20° C	17.2 dBm			
3.0	POWER FLATNESS (-20°C to +50°C)	+/-0.3 Db	+/- 2.0 dB		
4.0	TUNING RANGE (Mechanical)	OK (check)	+/-10 MHz		
5.0	SPURIOUS	OK (check)	-85 dBc		
6.0	HARMONICS	-29 dBc	-25 dBc		
7.0	DC CURRENT at +5 VDC	145 Ma	260 mA max		
8.0	FREQ. STABILITY	OK (check)	4 ppm/°C		
9.0	PHASE NOISE at:				
	10 KHz	-89 dBc/Hz			
	100 KHz	-107 dBc/Hz			
10.0	PUSHING	OK (check)	2 ppm/V, TYP		
11.0	PULLING	OK (check)	+/-90 ppm max		
12.0	MECHANICAL & MARKING	OK (check)	PER OUTLINE		



typo (mA)

EE APPROVED:  DATE: 12/14/15 INSPECTION:  DATE: 12/14/15

F 7.5.1-22
 DCC#:DCC-0001
 REV.:A



100 Davids Drive
Hauppauge NY 11788
Phone: (631) 439 - 9458

Model #: JS2-00100600-14-3A-SP
Customer: NOAA
Customer PO:
Serial #:563966
Project #:P114160
Housing:
StockNo:
Voltage:15V
Current:133mA
Temperature:23°C
Tested By:O.H.
Comment:

Freq (MHz)	Gain	Out. VSWR	In. VSWR	Rev. Gain	Noise Fig.	1 dB Comp.
100	26.97	1.08	1.96	-76.03	2.46	8.08
1000	28.35	1.20	1.56	-66.52	1.20	8.19
1500	28.73	1.33	1.50	-63.13	1.18	8.49
2000	29.11	1.45	1.45	-60.8	1.16	8.79
2500	29.47	1.53	1.37	-57.88	1.16	9.23
3000	29.76	1.58	1.27	-55.06	1.15	9.66
3500	29.91	1.59	1.17	-52.55	1.15	10.10
4000	29.90	1.57	1.12	-50.46	1.14	10.53
4500	29.74	1.52	1.16	-48.49	1.14	10.82
5000	29.47	1.47	1.24	-46.84	1.13	11.12
5500	29.14	1.43	1.31	-45.28	1.12	11.41
6000	28.79	1.42	1.35	-43.8	1.11	11.70

Surface Mount Monolithic Amplifier

DC-7 GHz

Features

- Miniature SOT-89 Package
- Frequency range, DC to 7 GHz
- Internally Matched to 50 Ohms
- Output power, 10.5 dBm typ.
- Excellent package for heat dissipation, exposed metal bottom
- Aqueous washable
- Protected by US Patent 6,943,629



Galii39+

CASE STYLE: DF782

Applications

- Cellular
- PCS
- Communication receivers & transmitters

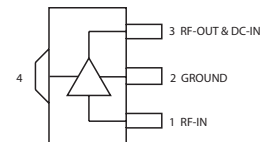
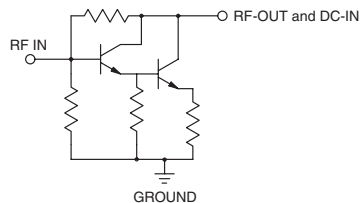
+RoHS Compliant

The +Suffix identifies RoHS Compliance. See our web site for RoHS Compliance methodologies and qualifications

General Description

Galii39+ (RoHS compliant) is a wideband amplifier offering high dynamic range. Lead finish is SnAgNi. It has repeatable performance from lot to lot, and is enclosed in a SOT-89 package. It uses patented Transient Protected Darlington configuration and is fabricated using InGaP HBT technology. Expected MTTF is 4,000 years at 85°C case temperature. Galii39+ is designed to be rugged for ESD and supply switch-on transients.

simplified schematic and pin description



Function	Pin Number	Description
RF IN	1	RF input pin. This pin requires the use of an external DC blocking capacitor chosen for the frequency of operation.
RF-OUT and DC-IN	3	RF output and bias pin. DC voltage is present on this pin; therefore a DC blocking capacitor is necessary for proper operation. An RF choke is needed to feed DC bias without loss of RF signal due to the bias connection, as shown in "Recommended Application Circuit".
GND	2,4	Connections to ground. Use via holes as shown in "Suggested Layout for PCB Design" to reduce ground path inductance for best performance.

Notes

- A. Performance and quality attributes and conditions not expressly stated in this specification document are intended to be excluded and do not form a part of this specification document.
 B. Electrical specifications and performance data contained in this specification document are based on Mini-Circuits' applicable established test performance criteria and measurement instructions.
 C. The parts covered by this specification document are subject to Mini-Circuits' standard limited warranty and terms and conditions (collectively, "Standard Terms"); Purchasers of this part are entitled to the rights and benefits contained therein. For a full statement of the Standard Terms and the exclusive rights and remedies thereunder, please visit Mini-Circuits' website at www.minicircuits.com/MCLStore/terms.jsp

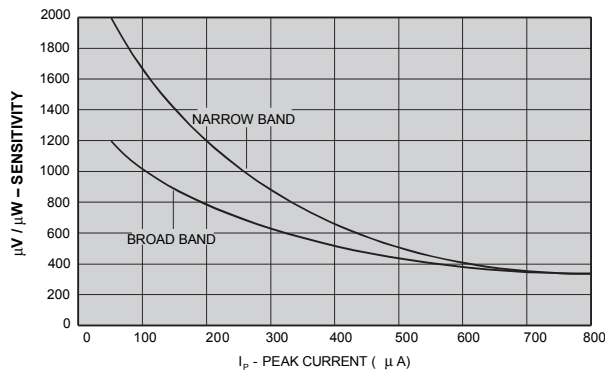
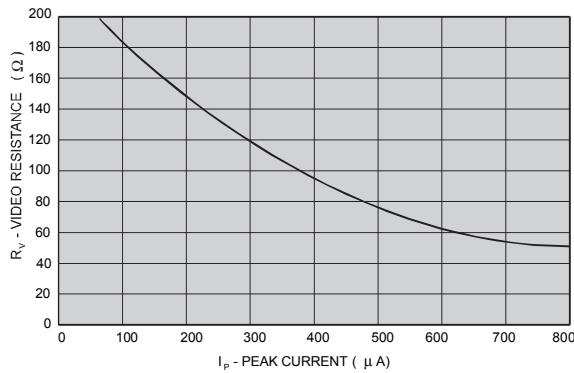
Mini-Circuits

www.minicircuits.com P.O. Box 350166, Brooklyn, NY 11235-0003 (718) 934-4500 sales@minicircuits.com

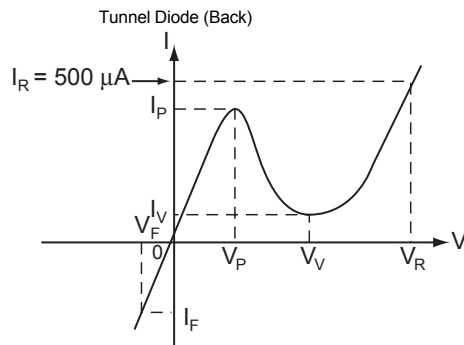
REV. K
 M151107
 D60-1117.DOC
 Q0201032
 GALI-39+
 PS/TD/CP/AM
 170927
 Page 1 of 4



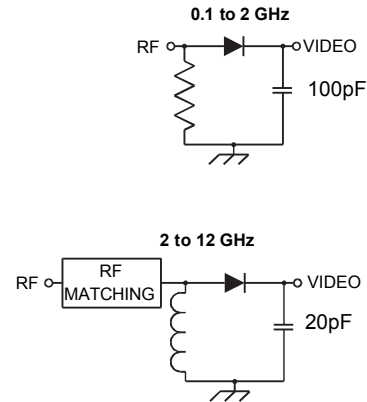
D I O D E S



Characteristic Curve



Typical Detector Circuits



Chip (C2) Assembly Notes

- ThermoCompression Wedge Bonding:
1. Use 0.7 mil gold wire.
 2. Tip temperature = 180°C MAX.
 3. Stage temperature = 160°C MAX.

Die attach

1. Silver epoxy with a maximum cure temperature of 125°C is recommended.

Package Assembly Notes

Lead Attach

1. 230°C Solder attach for 5 sec MAX.

CAUTION — Extremely Static Sensitive Devices

Notes

1. Chip top contact is cathode.
2. Detected output will be negative from the cathode.



ACTM-1007 TUNNEL DIODE DETECTOR MODULES

Frequency Range (min)	2 – 8	GHz
Sensitivity (min)	750	mV/mW
Flatness vs. Frequency (max)	0.5	±dB
Typical TSS	-50	dBm
Typical VSWR	2.5:1	Ratio
Nominal Video Capacitance	20	pF

NOTES:

Maximum input power: +14dBm (3dB guardband for +17dBm possible burnout)
 Sensitivity is measured into an open circuit load (>10k ohm).
 VSWR is measured at or below -20dBm input power level.
 Video capacitance is used for RF bypass. This value can be changed if required for video response time. Contact the factory for more information.

ENVIRONMENTAL SPECIFICATIONS:

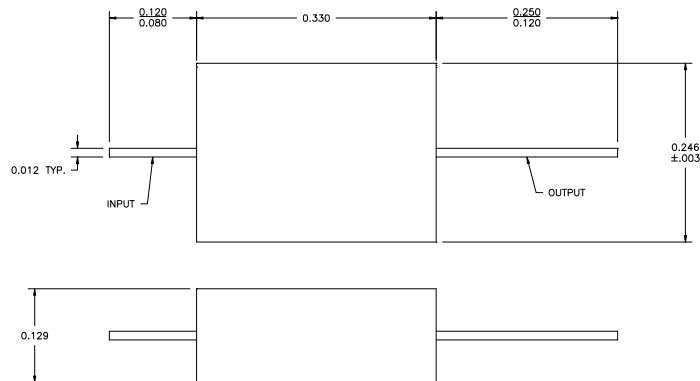
MIL-E-5400, MIL-STD-202, MIL-E-16400
 Operating Temp: -55°C to +100°C
 Storage Temp: -65°C to +100°C
 Humidity: MIL-STD-202F, M103, Cond B
 Shock: MIL-STD-202F, M213, Cond B
 Altitude: MIL-STD-202F, M105, Cond B
 Vibration : MIL-STD-202F, M204, Cond B
 Thermal Shock: MIL-STD-202F, M107, Cond A
 Temperature Cycle: MIL-STD-202F, M105C, Cond D

SCREENING:

Internal Visual per MIL-STD-883, Method 2017
 Temperature Cycle: -65°C to +100°C, 10 cycles

OPTIONAL HIGH-REL SCREENING (Ref MIL-PRF-38534):

Stabilization Bake per MIL-STD-883, Method 1008
 Temperature Cycle per MIL-STD-883, Method 1010
 Constant Acceleration per MIL-STD-883, Method 2001
 Burn-in per MIL-STD-883, Method 1015
 Leak Test per MIL-STD-883, Method 1014
 External Visual per MIL-STD-883, Method 2009



**STANDARD CASE STYLE M12
(Optional Case Styles – M51)**

PART NUMBER ORDERING INFORMATION:

- Add desired polarity suffix: "N" for Negative, "P" for Positive (Ex: ACTM-1007N)
- Add desired case style suffix: "M22" (Ex: ACTM-1007NM12)
- Add "-RC" suffix: RoHS-compliant (Ex: ACTM-1007NM12-RC)

0109

44031RC Precision Epoxy NTC Thermistor



- 10,000 ohm Resistance @ 25°C
- Interchangeable $\pm 0.1^\circ\text{C}$, 0°C to 70°C ,
- Pressed Disk Ceramic Sensor
- High sensitivity
- Thermally conductive epoxy coating
- 0.095" (2.4 mm) Maximum Diameter
- 32 AWG, 3" (7.6 cm) long Silver plated copper leads
- RoHS Compliant

DESCRIPTION

Epoxy Encapsulated Precision Interchangeable NTC Thermistor utilizing high stability pressed-disk ceramic sensor for general applications.

FEATURES

- 10,000 Ohm Resistance @ 25°C
- Interchangeability
- Good Long Term Stability
- High Sensitivity
- Thermally Conductive Epoxy Coating
- RoHS Compliance

APPLICATIONS

- Mid-range Temperature Applications
- Tight Tolerance Instrumentation
- General Applications Requiring Stability
- Applications Requiring Sensing Small Changes in Temperature
- Non-condensing Moisture Environments
- Allows use in Applications World-wide

PERFORMANCE SPECS

Parameter	Units	Value
Resistance @ 25°C	Ohms	10,000
tolerance 0°C to 70°C	$^\circ\text{C}$	± 0.1
Beta Value 25/85	K	3978
Tolerance on Beta Value	%	0.4
Time response in air	Seconds	< 10
Dissipation Constant in air	mW/ $^\circ\text{C}$	1
Insulation Resistance (Min. of 100Mohms for 1 Sec.)	Volts	500


www.vishay.com
NTCS0603E3.....T

Vishay BCcomponents

SMD 0603, Glass Protected NTC Thermistors


QUICK REFERENCE DATA		
PARAMETER	VALUE	UNIT
Resistance value at 25 °C	2.0K to 100K	Ω
Tolerance on R_{25} -value	± 1; ± 2; ± 3; ± 5	%
$B_{25/85}$ -value	3420 to 4100	K
Tolerance on $B_{25/85}$ -value	± 1	%
Maximum dissipation at 25 °C	125	mW
Thermal time constant τ	≈ 8	s
Dissipation factor D	3.0	mW/K
Operating temperature range at zero power	-40 to +150	°C
Weight	≈ 0.006	g

FEATURES

- TCR ranging from -7 %/K at -40 °C to -2 %/K at 150 °C
- Tolerance on R_{25} down to 1 %, and on $B_{25/85}$ down to 1 %
- Suitable for wave or reflow soldering
- NiSn terminations
- Fully glass coated and protected
- cUL recognized for safety applications (file E148885)
- AEC-Q200 qualified
- Material categorization: for definitions of compliance please see www.vishay.com/doc?99912

 AUTOMOTIVE
GRADE

 RoHS
COMPLIANT
HALOGEN
FREE

APPLICATIONS

- Temperature sensing, protection and compensation in automotive, industrial, telecom and consumer applications. Examples are:
 - Battery chargers
 - Power suppliers
 - Office equipment
 - LCD compensation
 - In-car entertainment

DESCRIPTION

Size 0603 (M1608) glass protected SMD chip thermistor with negative temperature coefficient (TCR) and tin (Sn) plated terminations. The device has no marking.

PACKAGING

Available in 8 mm punched paper tape on reel package of 4000 units.

DESIGN-IN SUPPORT

For complete curve computation, please visit:
www.vishay.com/thermistors/ntc-curve-list/

ELECTRICAL DATA AND ORDERING INFORMATION					
R_{25} (Ω)	R_{25} -TOL. (± %)	$B_{25/85}$ (K)	$B_{25/85}$ -TOL. (± %)	UL RECOGNIZED	SAP MATERIAL AND ORDERING NUMBER ⁽¹⁾
2000	5	3420	1	Y	NTCS0603E3202JLT
2200	1, 2, 3, 5	3520	1	Y	NTCS0603E3222*MT
2700	1, 2, 3, 5	3600	1	Y	NTCS0603E3272*MT
4700	1, 2, 3, 5	3830	1	Y	NTCS0603E3472*HT
10 000	1, 2, 3, 5	3435	1	Y	NTCS0603E3103*LT
10 000	1, 2, 3, 5	3610	1	Y	NTCS0603E3103*MT
10 000	1, 2, 3, 5	3960	1	Y	NTCS0603E3103*HT
15 000	1, 2, 3, 5	3600	1	N	NTCS0603E3153*MT
22 000	1, 2, 3, 5	3730	1	Y	NTCS0603E3223*MT
33 000	1, 2, 3, 5	3860	1	Y	NTCS0603E3333*HT
47 000	1, 2, 3, 5	3960	1	Y	NTCS0603E3473*HT
68 000	1, 2, 3, 5	3985	1	Y	NTCS0603E3683*HT
100 000	1, 2, 3, 5	4100	1	Y	NTCS0603E3104*XT

Note

⁽¹⁾ Replace * in SAP material number by J for ± 5 %, H for ± 3 %, G for ± 2 %, F for ± 1 % tolerance on R_{25}

Revision: 13-Jul-17

1

Document Number: 29056

 For technical questions, contact: nlr@vishay.com

THIS DOCUMENT IS SUBJECT TO CHANGE WITHOUT NOTICE. THE PRODUCTS DESCRIBED HEREIN AND THIS DOCUMENT ARE SUBJECT TO SPECIFIC DISCLAIMERS, SET FORTH AT www.vishay.com/doc?91000

TITLE: SPECIFICATION CONTROL DRAWING

PART IDENTIFIER: MTVAW3-CUSTOM [CUSTOMIZABLE MTVAW3 KIT]

**25 PIECES OF EACH PART NUMBER SELECTED.
12 MTVA0X00N0XW3 CUSTOMER TO PICK ATTENUATION AND SHIFT.
SEE BELOW FOR AVAILABLE VALUES.**

MTVA0X00N0XW3
 X = TEMPERATURE COEFFICIENT OF ATTEN. 1×10^{-3} DB/DB/°C.
 N = ATTENUATION SHIFT NEGATIVE.
 X DB VALUE SEE TABLE BELOW.

SHIFT (NEG)	DB VALUE
-003	1, 2, 3, 4, 5, 6, 7, 8
-004	1, 2, 3, 4, 5, 6
-005	1, 2, 3, 4, 5, 6, 8
-006	3, 4, 5, 6
-007	2, 3, 4, 5, 6
-009	1, 2, 3, 4, 5, 6, 8

DESCRIPTION: TEMPERATURE VARIABLE CHIP ATTENUATOR CUSTOM KIT.

ASSEMBLY DWG: 2402834

1.0 SPECIFICATIONS:

- 1.1 ELECTRICAL:
 - 1.1.1 IMPEDANCE: 50 OHMS NOMINAL.
 - 1.1.2 OPERATING FREQUENCY RANGE: DC - 12.4GHZ.
 - 1.1.3 ATTENUATION VALUES AVAILABLE: SEE TABLE ABOVE.
 - 1.1.4 ATTENUATION ACCURACY AT 25°C: $\pm 0.5\text{DB @ 1 GHZ}$.
 - 1.1.5 VSWR: 1.30:1 MAX. @ 1GHZ.
 - 1.1.6 INPUT POWER: 200 MILLIWATTS CW.
 - 1.1.6.1 FULL RATED POWER TO 125°C, DERATED LINEARLY TO 0 WATTS AT 150°C.
 - 1.1.7 TEMPERATURE COEFFICIENT OVER OPERATING TEMPERATURE RANGE:
SEE TABLE ABOVE. TEMPERATURE COEFFICIENT TOLERANCE: $\pm 0.001 \text{ DB/DB/°C}$.
- 1.2 MECHANICAL:
 - 1.2.1 OUTLINE DWG: SEE SHEET 2.
 - 1.2.2 WORKMANSHIP: PER MIL-PRF-55342.
- 1.3 ENVIRONMENTAL:
 - 1.3.1 OPERATING TEMPERATURE RANGE: -55°C TO +150°C.

2.0 UNIT MARKING: DB VALUE (X), DIRECTION OF SHIFT (N) AND TCA SHIFT (X).
LEGIBILITY AND PERMANENCY PER MIL-STD-130.

3.0 QUALITY ASSURANCE:

- 3.1 SAMPLE INSPECT PER ANSI/ASQC Z1.4 GENERAL INSPECTION, LEVEL II, AQL = 1.0.
 - 3.1.1 VISUAL AND MECHANICAL EXAMINATION FOR CONFORMANCE TO OUTLINE DRAWING REQUIREMENTS.
- 3.2 SAMPLE INSPECTION (DESTRUCTIVE TESTING).
 - 3.2.1 SELECT THREE (3) UNITS FROM LOT AND MEASURE DCA EVERY 20°C OVER THE TEMPERATURE RANGE -55°C TO +125°C.
 - 3.2.1.1 CALCULATE, USING LINEAR REGRESSION, THE SLOPE OF THE CURVE.
 - 3.2.1.2 CALCULATE TCA USING THE FOLLOWING FORMULA:

$$TCA = \frac{\text{SLOPE}}{\text{ATTENUATION @ } 25^\circ\text{C}}$$
 - 3.2.1.3 ACCEPTANCE LIMITS: PER 1.1.7.
- 3.3 INSPECTION IN ACCORDANCE WITH 824W170 AND 824F036 FOR COMMERCIAL GRADE PRODUCT.
- 3.4 TEST DATA REQUIREMENTS:
 - 3.4.1 NO TEST DATA REQUIRED FOR CUSTOMER.
 - 3.4.2 DATA RETENTION - 24 MONTHS.

4.0 PACKAGING: STANDARD PACK PER 755W002.

EMC TECHNOLOGY 8851 SW OLD KANSAS AVE. STUART, FL 34997	CAGE CODE # 24602		DWG #	1012075000
	CHANGE NOTICE	EN 09-E0726	REV LVL	-
			SHEET	1 OF 2

Brushless DC-Servomotors

2 Pole Technology

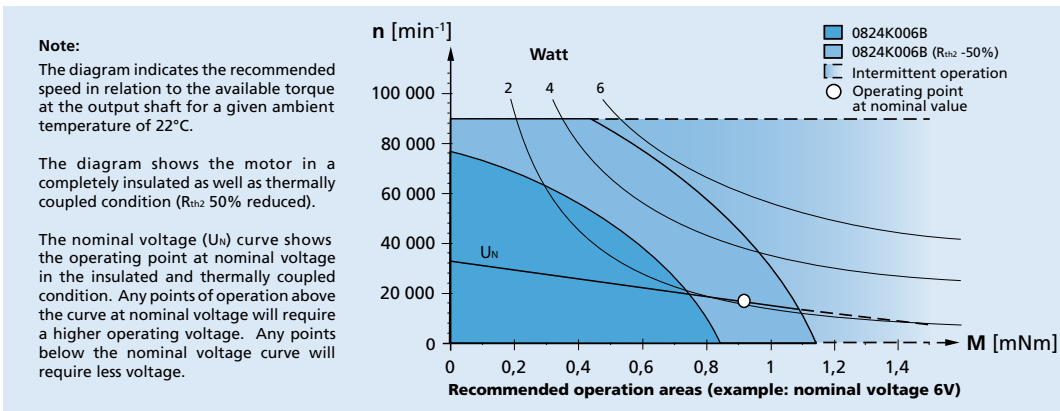
1,1 mNm

5,8 W

Series 0824 ... B

Values at 22°C and nominal voltage	0824 K	006 B	012 B	
1 Nominal voltage	U_N	6	12	V
2 Terminal resistance, phase-phase	R	2,91	10,7	Ω
3 Efficiency, max.	η_{max}	70	70	%
4 No-load speed	n_0	35 100	37 500	min^{-1}
5 No-load current, typ. (with shaft \varnothing 1 mm)	I_0	0,055	0,031	A
6 Stall torque	M_H	3,28	3,34	mNm
7 Friction torque, static	C_0	0,021	0,021	mNm
8 Friction torque, dynamic	C_V	$1,89 \cdot 10^{-6}$	$1,89 \cdot 10^{-6}$	mNm/min ⁻¹
9 Speed constant	k_n	5 968	3 183	min^{-1}/V
10 Back-EMF constant	k_E	0,168	0,314	$\text{mV}/\text{min}^{-1}$
11 Torque constant	k_M	1,6	3	mNm/A
12 Current constant	k_I	0,625	0,333	A/mNm
13 Slope of n-M curve	$\Delta n / \Delta M$	10 855	11 353	$\text{min}^{-1}/\text{mNm}$
14 Terminal inductance, phase-phase	L	30	107	μH
15 Mechanical time constant	τ_m	2,4	2,5	ms
16 Rotor inertia	J	0,0285	0,0285	gcm^2
17 Angular acceleration	α_{max}	1 561	1 592	$\cdot 10^3 \text{rad}/\text{s}^2$
18 Thermal resistance	R_{th1} / R_{th2}	11,2 / 55,2		K/W
19 Thermal time constant	τ_{w1} / τ_{w2}	3,5 / 112		s
20 Operating temperature range:				
- motor		-20 ... +100		°C
- winding, max. permissible		+125		°C
21 Shaft bearings		ball bearings, preloaded		
22 Shaft load max.:				
- with shaft diameter		1		mm
- radial at 10 000 min^{-1} (4 mm from mounting flange)		1,5		N
- axial at 10 000 min^{-1} (push only)		0,4		N
- axial at standstill (push only)		10		N
23 Shaft play:				
- radial	\leq	0,012		mm
- axial	$=$	0		mm
24 Housing material		aluminium, black anodized		
25 Mass		5,2		g
26 Direction of rotation		electronically reversible		
27 Speed up to	n_{max}	90 000		min^{-1}
28 Number of pole pairs		1		
29 Hall sensors		digital		
30 Magnet material		NdFeB		
Rated values for continuous operation				
31 Rated torque	M_N	0,89	0,86	mNm
32 Rated current (thermal limit)	I_N	0,66	0,341	A
33 Rated speed	n_N	22 120	24 560	min^{-1}

Note: Rated values are calculated with nominal voltage and at a 22°C ambient temperature. The R_{th2} value has been reduced by 25%.



NEW

Encoder

magnetic Encoder, digital outputs
3 channels, 32 - 1024 lines per revolution

For combination with
Brushless DC-Servomotors

Series IEM3 – 1024

		IEM3 – 32	IEM3 – 64	IEM3 – 128	IEM3 – 256	IEM3 – 512	IEM3 – 1024	
Lines per revolution	N	32	64	128	256	512	1024	
Frequency range, up to ¹⁾	f	64	128	256	500	500	500	kHz
Signal output, square wave		2+1 Index						channels
Supply voltage	U _{DD}	4,5 ... 5,5						V DC
Current consumption, typical ²⁾	I _{DD}	typ. 16, max. 23						mA
Output current, max. allowable ³⁾	I _{OUT}	4						mA
Index Pulse width ⁴⁾	P ₀	90 ± 45			90 ± 75			°e
Phase shift, channel A to B ⁴⁾	Φ	90 ± 45			90 ± 75			°e
Signal rise/fall time, max. (C _{LOAD} = 50 pF)	tr/tf	0,1 / 0,1						µs
Operating temperature range		– 20 ... + 100						°C

¹⁾ speed (rpm) = f(Hz) x 60/N

²⁾ U_{DD Enc} = 5V: with unloaded outputs

³⁾ U_{DD Enc} = 5V: low logic level < 0,4V, high logic level > 4,5V: CMOS- and TTL compatible

⁴⁾ at 5 000 rpm

For combination with motor

Dimensional drawing A	L1 [mm]		
0824K...B	24,1		
Dimensional drawing B	L1 [mm]		
1028S...B	28,1		

Features

These incremental encoders in combination with the FAULHABER motors are used for the indication and control of both velocity and direction of rotation as well as for positioning.

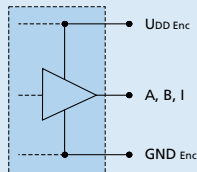
The encoder is available in a variety of different resolutions and is suitable for speed control and positioning applications.

Motor and encoder are connected via a common flexboard.

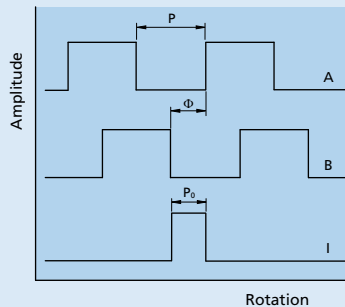
A permanent magnet on the shaft creates a moving magnetic field which is captured using a single-chip angular sensor and further processed. At the encoder outputs, two 90° phase-shifted rectangular signals are available with up to 1024 impulses and an index impulse per motor revolution.

Circuit diagram / Output signals

Output circuit



Output signals with clockwise rotation as seen from the shaft end



Admissible deviation of phase shift:

$$\Delta\Phi = \left| 90^\circ - \frac{\Phi}{P} * 180^\circ \right|$$

Admissible deviation of Index pulse:

$$\Delta P_0 = \left| 90^\circ - \frac{P_0}{P} * 180^\circ \right|$$



Precision, Ultralow Noise, RRIO, Zero-Drift Op Amp

Data Sheet

ADA4528-1/ADA4528-2

FEATURES

- Low offset voltage:** 2.5 μV maximum
- Low offset voltage drift:** 0.015 $\mu\text{V}/^\circ\text{C}$ maximum
- Low noise**
 - 5.6 nV/ $\sqrt{\text{Hz}}$ at $f = 1$ kHz, $A_v = +100$
 - 97 nV p-p at $f = 0.1$ Hz to 10 Hz, $A_v = +100$
- Open-loop gain:** 130 dB minimum
- CMRR:** 135 dB minimum
- PSRR:** 130 dB minimum
- Unity-gain crossover:** 4 MHz
- Gain bandwidth product:** 3 MHz at $A_v = +100$
- 3 dB closed-loop bandwidth:** 6.2 MHz
- Single-supply operation:** 2.2 V to 5.5 V
- Dual-supply operation:** ± 1.1 V to ± 2.75 V
- Rail-to-rail input and output**
- Unity-gain stable**

APPLICATIONS

- Thermocouple/thermopile
- Load cell and bridge transducers
- Precision instrumentation
- Electronic scales
- Medical instrumentation
- Handheld test equipment

GENERAL DESCRIPTION

The ADA4528-1/ADA4528-2 are ultralow noise, zero-drift operational amplifiers featuring rail-to-rail input and output swing. With an offset voltage of 2.5 μV , offset voltage drift of 0.015 $\mu\text{V}/^\circ\text{C}$, and typical noise of 97 nV p-p (0.1 Hz to 10 Hz, $A_v = +100$), the ADA4528-1/ADA4528-2 are well suited for applications in which error sources cannot be tolerated.

The ADA4528-1/ADA4528-2 have a wide operating supply range of 2.2 V to 5.5 V, high gain, and excellent CMRR and PSRR specifications, which make it ideal for applications that require precision amplification of low level signals, such as position and pressure sensors, strain gages, and medical instrumentation.

The ADA4528-1/ADA4528-2 are specified over the extended industrial temperature range (-40°C to $+125^\circ\text{C}$). The ADA4528-1 and ADA4528-2 are available in 8-lead MSOP and 8-lead LFCSP packages.

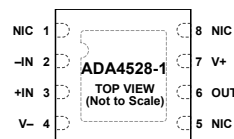
For more information about the ADA4528-1/ADA4528-2, see the AN-1114 Application Note, *Lowest Noise Zero-Drift Amplifier Has 5.6 nV/ $\sqrt{\text{Hz}}$ Voltage Noise Density*.

PIN CONNECTION DIAGRAMS



NOTES
1. NIC = NO INTERNAL CONNECTION.

Figure 1. ADA4528-1 Pin Configuration, 8-Lead MSOP



NOTES
1. NIC = NO INTERNAL CONNECTION.
2. CONNECT THE EXPOSED PAD TO V- OR LEAVE IT UNCONNECTED.

Figure 2. ADA4528-1 Pin Configuration, 8-Lead LFCSP

For ADA4528-2 pin connections and for more information about the pin connections for these products, see the Pin Configurations and Function Descriptions section.

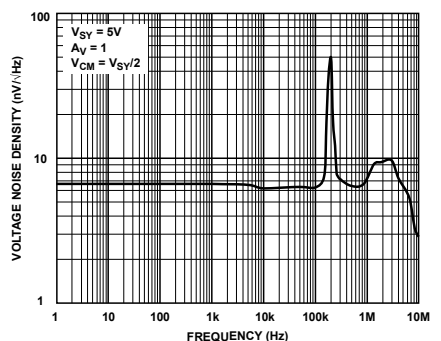


Figure 3. Voltage Noise Density vs. Frequency

Table 1. Analog Devices, Inc., Zero-Drift Op Amp Portfolio¹

Type	Ultralow Noise	Micropower (<20 μA)	Low Power (<1 mA)	16 V Operating Voltage	30 V Operating Voltage
Single	ADA4528-1	ADA4051-1	AD8628 AD8538	AD8638	ADA4638-1
Dual	ADA4528-2	ADA4051-2	AD8629 AD8539	AD8639	
Quad			AD8630		

¹ See www.analog.com for the latest selection of zero-drift operational amplifiers.

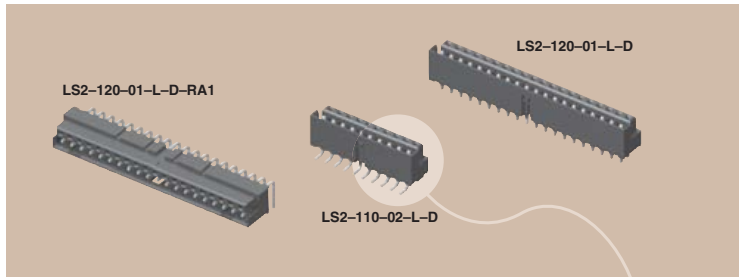
Rev. D [Document Feedback](#)
Information furnished by Analog Devices is believed to be accurate and reliable. However, no responsibility is assumed by Analog Devices for its use, nor for any infringements of patents or other rights of third parties that may result from its use. Specifications subject to change without notice. No license is granted by implication or otherwise under any patent or patent rights of Analog Devices. Trademarks and registered trademarks are the property of their respective owners.

One Technology Way, P.O. Box 9106, Norwood, MA 02062-9106, U.S.A.
Tel: 781.329.4700 ©2011–2013 Analog Devices, Inc. All rights reserved.
Technical Support www.analog.com



(2,00 mm) .0787"

LS2 SERIES



SELF MATING HERMAPHRODITIC STRIP

SPECIFICATIONS

For complete specifications and recommended PCB layouts see www.samtec.com?LS2

Insulator Material: Black Liquid Crystal Polymer



Contact Material: Phosphor Bronze

Plating: Au or Sn over

50µ" (1.27 µm) Ni

Voltage Rating: 475 VAC mated with LS2

Operating Temp Range: -55°C to +125°C

Insertion Force: (Single contact only)

4 oz (1,11 N) avg.

Withdrawal Force: (Single contact only)

3 oz (0,83 N) avg.

RoHS Compliant: Yes

CURRENT RATING (PER CONTACT)	
AMBIENT TEMP	6 Contacts
20°C	5A
40°C	4.3A
60°C	3.6A
80°C	2.7A

Processing: Lead-Free Solderable:

Yes

SMT Lead Coplanarity:

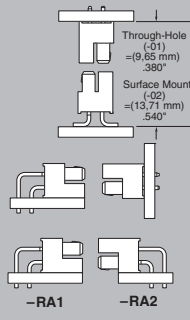
(0,15 mm) .006" max

APPLICATION SPECIFIC OPTION

Alignment pin.
Call Samtec.

Mates with:
LS2

APPLICATION



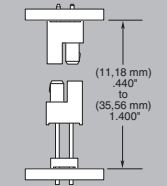
Shrouded Terminals

Align & Latch™

Polarized



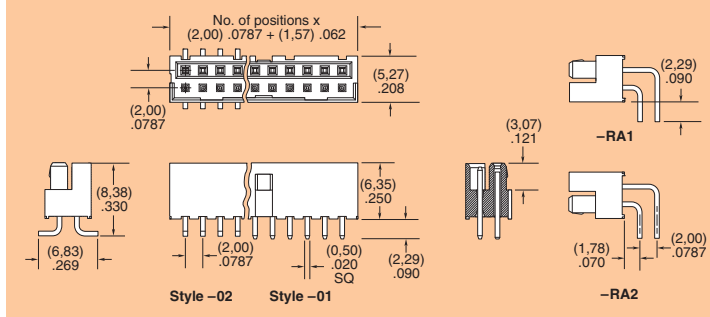
APPLICATION SPECIFIC



Call Samtec for elevated board stacking applications.

LS2	1	NO. PINS PER ROW	LEAD STYLE	PLATING OPTION	D	TAIL OPTION	OPTION
		05, 10, 15, 20, 25, 30	-01 = Through-hole -02 = Surface Mount	-F = Gold flash on contact, Matte Tin on tail -L = 10µ" (0,25 µm) Gold on contact, Matte Tin on tail		-01 only -RA1 = Right Angle (Shroud Down) -RA2 = Right Angle (Shroud Up)	-K = (6,30 mm) .248" DIA Polyimide Film Pick & Place Pad (-02 only) -TR = Tape & Reel Packaging

Note: Other Gold plating options available. Contact Samtec.



Note: Some lengths, styles and options are non-standard, non-returnable.

Due to technical progress, all designs, specifications and components are subject to change without notice.

WWW.SAMTEC.COM

SAMTEC USA • Tel: 1-800-SAMTEC-9 or 812-944-8733 SAMTEC NORTHERN CALIFORNIA • Tel: 408-395-5900 SAMTEC SOUTHERN CALIFORNIA • Tel: 1-800-726-8329
 SAMTEC AMERICA LATINA COMERCIO EXTERIOR LTDA • Tel: (+55 31) 3786 3227 SAMTEC UNITED KINGDOM • Tel: 44 01236 739292 SAMTEC GERMANY • Tel: +49 (0) 89 / 89460-0
 SAMTEC FRANCE • Tel: 33 01 69 35 06 80 SAMTEC ITALY • Tel: 39 039 6890367 SAMTEC NOROCCIDENTAL • Tel: 46-84477280 SAMTEC BENELUX • Tel: 44 01236 739292
 SAMTEC ISRAEL • Tel: 972-5-7529920 SAMTEC INDIA • Tel: +91-80-3272 1912 SAMTEC ASIA PACIFIC • Tel: 65 6745-5955 SAMTEC JAPAN • Tel: 045-4761-1955 SAMTEC CHINA • Tel: 86-21-6083 3766
 SAMTEC TAIWAN • Tel: 886-2-2735-6109 SAMTEC HONG KONG • Tel: 852-26904658 SAMTEC KOREA • Tel: 82-31-717-5685 SAMTEC ANZ • Tel: 613 9580 0683